1998

FLUID INERTIA AND END EFFECTS IN RHEOMETER FLOWS

HUGHES, JASON PETER

http://hdl.handle.net/10026.1/1889

http://dx.doi.org/10.24382/4091
University of Plymouth

FLUID INERTIA AND END EFFECTS IN RHEOMETER FLOWS

by

JASON PETER HUGHES
B.Sc. (Hons)

A thesis submitted to the University of Plymouth
in partial fulfilment for the degrèe of

DOCTOR OF PHILOSOPHY

School of Mathematics and Statistics
Faculty of Technology
University of Plymouth

April 1998

ACKNOWLEDGEMENTS

I would like to thank my supervisors Dr. J.M. Davies, Prof. T.E.R. Jones and Dr. K. Golden for their continued support and guidance throughout the course of my studies. I also gratefully acknowledge the receipt of a H.E.F.C.E research studentship during the period of my research.

AUTHORS DECLARATION

At no time during the registration for the degree of Doctor of Philosophy has the author been registered for any other University award.

This study was financed with the aid of a H.E.F.C.E studentship and carried out in collaboration with T.A. Instruments Ltd.

Publications:

1. J.P. Hughes, T.E.R Jones, J.M. Davies, 'End effects in concentric cylinder rheometry', Proc. 12th Int. Congress on Rheology, (1996) 391.
2. J.P. Hughes, J.M. Davies, T.E.R. Jones, 'Concentric cylinder end effects and fluid inertia effects in controlled stress rheometry, Part I: Numerical simulation', accepted for publication in J.N.N.F.M.

Signed J. Hughes

Date 14.04.98

FLUID INERTIA AND END EFFECTS IN RHEOMETER FLOWS

Jason Peter Hughes

Abstract

This thesis is concerned with the characterisation of the flow behaviour of inelastic and viscoelastic fluids in steady shear and oscillatory shear flows on commercially available rheometers.

The first part of this thesis is concerned with a linear viscoelastic theory to describe the oscillatory shear flow behaviour of fluids on a Weissenberg rheogoniometer. A fluid inertia perturbation analysis is used to produce analytical formulae for correcting complex viscosity data for first and second order fluid inertia effects. In order to validate the perturbation theory we perform a simulation of the oscillatory shear flow behaviour of Newtonian and single element Maxwell fluids on a Weissenberg rheogoniometer.

A theoretical prediction of end effects and fluid inertia effects on steady shear viscosity measurements of Newtonian fluids in a recessed concentric cylinder geometry is developed for a CSR controlled stress rheometer and a Weissenberg rheogoniometer. The relevant equations are solved using a perturbation analysis which is valid for low Reynolds number flows. From this theory correction formulae are produced to compensate for end effects and second order fluid inertia effects in steady shear flows on these instruments. End effects and fluid inertia effects are also investigated for power law shear thinning fluids.

The final part of the thesis is concerned with a theoretical prediction of the end effect of a recessed concentric cylinder geometry on complex viscosity measurements of a generalised linear viscoelastic fluid. The linear viscoelastic theory is carried out for oscillatory shear flows on a CSR controlled stress rheometer and a Weissenberg rheogoniometer. A fluid inertia perturbation analysis is used to produce analytical formulae to correct complex viscosity data for end effects and second order fluid inertia effects. Numerically simulated oscillatory shear data is used to establish the limitations of the second order fluid inertia correction formulae which include end effects.

CONTENTS

CHAPTER 1

INTRODUCTION

Rheology is defined as 'the study of the deformation and flow of matter'. The term was invented by E.C. Bingham and was first accepted when the first Society of Rheology (American) was formed in 1929. This organisation brought together workers from the fields of chemistry, engineering, mathematics and physics. The scope of rheology is now extremely wide and is of importance to many industries, such as food, pharmaceutical, plastics, petroleum and rubber.

In classical mechanics the deformation of solids was governed by Hooke's law for elastic deformations and the flow of fluids was governed by Newton's Law describing viscous flow. However the flow behaviour of the majority of materials lies between these two extremes and the material exhibits both solid-like and fluid-like properties. Such materials are described as viscoelastic. In this thesis we shall consider steady shear and oscillatory shear theories that can be used to characterise the flow properties of inelastic and viscoelastic materials respectively.

Rheometry is an important area of rheological study which is concerned with the measurement of material properties in simple shear flow situations. These measurements can be used to characterise the flow behaviour of non-Newtonian fluids using suitably defined material functions. The rheological data obtained from the simple flow situations can also be used in the development of constitutive equations. These constitutive equations can then be used in conjunction with the stress equations of motion and the continuity equation to predict the behaviour of materials in more complex flow situations. The simple shear flow situations can be generated on an instrument known as a rheometer. In this thesis two different types of rheometer are considered, one being the CSR controlled stress rheometer

where the material under test is subjected to a stress and the subsequent deformation is measured. The other type of rheometer is the controlled strain Weissenberg rheogoniometer where a deformation is applied to the material and the subsequent forces are measured.

This thesis is concerned with a theoretical investigation of some of the simple flow situations that can be generated on the CSR controlled stress rheometer and the Weissenberg rheogoniometer. The main purpose of the work is to modify current rheometer formulae to give improved material data. This involves extending the existing theories to include fluid inertia effects and/or end effects.

In chapter 2 we present the equations of motion and equations of state required to describe the rheometer flows considered in this thesis. The equations of conservation of mass and conservation of momentum are presented and a brief description of their derivation is given. For the theoretical fluid models considered in this thesis we describe the formulation of the equations of state. In this chapter we also define the complex viscosity function which is used to characterise the oscillatory shear flow behaviour of viscoelastic fluids.

In chapter 3 we introduce the numerical methods that are used to solve the equations of motion for concentric cylinder flows. A description of the finite difference approximation of partial differential equations is given and iterative methods for solving the resulting linear system of algebraic equations are discussed. The method of transforming an irregular finite difference mesh in the physical domain to meshpoints with uniform spacing in a computational plane is described. In the analysis of steady shear concentric cylinder flow the authors numerical results will be compared with those obtained using the Polyflow package. We give a brief description of this package and discuss the relevant Polyflow boundary conditions for steady shear concentric cylinder flow.

Chapter 4 is concerned with the linear viscoelastic theory for oscillatory shear flow

on a controlled strain Weissenberg rheogoniometer. The oscillatory shear theory is presented for the parallel plate, concentric cylinder and cone and plate geometries where the upper platen is constrained by a torsion bar. At present the calculation of complex viscosity in these geometries is based on a theory in which fluid inertia effects are ignored. A perturbation analysis, which is valid for small values of a non-dimensional fluid inertia parameter, is carried out to second order accuracy. Using this analysis formulae are produced for calculating the complex viscosity of a fluid which include first and second order fluid inertia effects. We also consider the case where the upper platen is connected to a strain gauge torsion head and present the relevant fluid inertia correction formulae. These correction formulae are compared to those for oscillatory shear flow on a CSR controlled stress rheometer.

In chapter 5 we perform a numerical simulation of the oscillatory shear flow behaviour of Newtonian fluids and single element Maxwell fluids on a Weissenberg rheogoniometer. Simulations are carried out for the case where the upper platen is constrained by a torsion bar and the case where the upper platen is connected to a strain gauge torsion head. The complex viscosity data generated from these simulations is used to establish the effect of fluid inertia on complex viscosity predictions in the three geometries. We also simulate the oscillatory shear flow behaviour of Newtonian fluids and single element Maxwell fluids on a CSR controlled stress rheometer. From these simulations complex viscosity data is generated and compared with the corresponding data obtained when a strain gauge torsion head is used on the Weissenberg rheogoniometer.

Chapter 6 is concerned with a theoretical prediction of end effects and fluid inertia effects on steady shear viscosity predictions obtained using a recessed concentric cylinder geometry on the CSR controlled stress rheometer. For Newtonian fluids the equations of motion are solved using a perturbation analysis which is valid for low Reynolds number

flows. The perturbation equations are solved numerically using a finite difference method with an irregular mesh. From the perturbation theory we produce correction formulae to compensate for end effects and second order fluid inertia effects in steady shear concentric cylinder flows on a CSR rheometer. End effects and fluid inertia effects are also investigated for shear thinning fluids using the Polyflow package. Numerically simulated steady shear data is generated for a Newtonian fluid to establish the limitations of the perturbation theory.

In chapter 7 we consider steady shear end effects and fluid inertia effects for a recessed concentric cylinder geometry on the Weissenberg rheogoniometer. The analysis follows the same procedure to that in chapter 6 for steady shear concentric cylinder flow on a CSR controlled stress rheometer. Formulae which include end effects and second order fluid inertia effects are produced for calculating the steady shear viscosity of a fluid on the Weissenberg rheogoniometer. The limitations of the second order fluid inertia perturbation theory is investigated by simulating the steady shear concentric cylinder flow of Newtonian fluids on a Weissenberg rheogoniometer.

Chapter 8 is concerned with a theoretical prediction of the end effect of a recessed concentric cylinder geometry on complex viscosity measurements of a generalised linear viscoelastic fluid. The relevant equations are solved using a perturbation analysis which will be valid when fluid inertia effects are small. A finite difference method with an irregular mesh is used to solve the perturbation equations. Using the perturbation theory the existing oscillatory shear formulae which include second order fluid inertia effects are modified to compensate for end effects. Numerically simulated data is generated for Newtonian fluids and single element Maxwell fluids and a comparison is made between the standard and modified formulae. The simulated data is also used to establish the limitations of the perturbation theory.

Formulae for calculating the complex viscosity of a fluid in a concentric cylinder geometry on the Weissenberg rheogoniometer, which include first and second order fluid inertia effects, are presented in chapter 4. In chapter 9 these formulae are modified to include end effects. The analysis follows a similar procedure to that of chapter 8 and formulae, which include end effects and second order fluid inertia effects, are produced for calculating the complex viscosity of a fluid on a Weissenberg rheogoniometer with a torsion bar system. These equations are adapted to give the fluid inertia correction formulae for the case where the inner cylinder is connected to a strain gauge torsion head. A numerical simulation of the oscillatory shear flow behaviour of Newtonian fluids and single element Maxwell fluids is performed to generate complex viscosity data. Using this simulated data a comparison is made between the formulae of chapter 4 and the formulae modified to include end effects. We also generate simulated complex viscosity data for the Weissenberg rheogoniometer set up where the upper platen is connected to a strain gauge torsion head. This data is compared with the corresponding simulated data obtained for a CSR controlled stress rheometer.

CHAPTER 2

RHEOLOGICAL EQUATIONS OF STATE AND EQUATIONS OF MOTION

2.1 The characterisation of fluids

A fluid is defined as a substance which deforms when subjected to an applied force. However the fluid will offer resistance to the deformation and the fluid viscosity is a measure of this resistance. Fluids can be classified as being either a liquid or a gas. A liquid possesses intermolecular forces of attraction which hold it together with a definite volume but no regular shape. Whereas a gas consists of molecules in random motion such that it has no definite volume, no regular shape and is highly compressible. In this thesis we will only be concerned with the characterisation of the flow properties of incompressible fluids which have constant density.

A fluid can be categorised as being either Newtonian or non-Newtonian. The vast majority of fluids such as paints, lubricating greases and facial creams which possess a complex structure fall into the non-Newtonian category. Examples of Newtonian fluids are air, water and mineral oils.

The work presented in this thesis is concerned with the characterisation of the flow properties of fluids using commercially available rheometers. In chapters 4, 5, 8 and 9 we consider the characterisation of the flow behaviour of viscoelastic fluids in small amplitude oscillatory shear flow. A theory for the characterisation of Newtonian fluids and inelastic non-Newtonian fluids in steady shear flow is considered in chapters 6 and 7. In order to develop these theories we require a set of equations which describe the flow behaviour of a fluid. These equations are referred to as the 'equations of change' and indicate how the mass, momentum and energy of the fluid change with position and time (Bird *et al* [1]). In

addition to these equations we require rheological equations of state which describe the relationship between the stress tensor and the fluid viscosity. A brief description for the derivation of the equation of mass and the equation of momentum is given in section 2.2. The equations of state for the theoretical model fluids considered in this thesis are presented in section 2.3.

2.2 Equations of motion

The physical laws that govern the motion of a fluid are described by the equations of conservation of mass, momentum and energy. These equations are derived by considering an arbitrary fixed infinitesimal control volume V, bounded by the surface S, within a flowing fluid. The fluid is able to flow across the boundary S and through the control volume V.

2.2.1 Equation of conservation of mass

A fluid flows across the surface of the infinitesimal control volume with velocity vector $\boldsymbol{v}$. The law of conservation of mass states that the total mass of fluid within a volume V will only increase because of a net influx of fluid across the bounding surface S. On applying this law and using Gauss's divergence theorem it can be shown (Bird *et al* [1]) that the equation for the conservation of mass can be written in conventional vector notation as

$$\frac{\partial \rho}{\partial t} = -(\nabla \cdot \rho \boldsymbol{v}) \tag{2.2.1}$$

where ρ is the local density of the fluid, $\nabla\cdot$ is the divergence operator and $\partial/\partial t$ is the time derivative. It should be noted that the equation of conservation of mass is usually known as 'the equation of continuity'.

For an incompressible fluid which has constant density ρ equation (2.2.1) reduces to

$$\nabla \cdot \boldsymbol{v} = 0 \tag{2.2.2}$$

In this thesis cylindrical polar coordinates (r, θ, z) and spherical polar coordinates (r, θ, φ) will be used for the analysis of rheometer flows. The equation of conservation of mass for these coordinate systems is given by Bird *et al* [1].

2.2.2 Equation of conservation of momentum

The fluid flowing across the surface S will have momentum due to the bulk flow of the fluid and momentum due to the molecular motions and interactions within the fluid. In addition there is momentum due to the force of gravity acting on the fluid. The law of conservation of momentum states that the total momentum of the fluid within the control volume V will increase because of a net influx of momentum across S, by both the bulk flow and the molecular motions, and because of the gravitational force. Using this law and Gauss's divergence theorem it can be shown (Bird *et al* [2]) that the equation for the conservation of momentum can be written in conventional vector notation as

$$\rho \frac{D\boldsymbol{v}}{Dt} = \nabla \cdot \boldsymbol{\tau} - \nabla p + \rho \boldsymbol{g} \tag{2.2.3}$$

where ρ is the fluid density, D/Dt is the substantial derivative, $\boldsymbol{\tau}$ is the extra stress tensor, p is the pressure and $\boldsymbol{g}$ is the gravitational acceleration.

In equation (2.2.3) the opposite sign convention for stress, as adopted by Walters [3], is used. This stress sign convention will be used throughout the thesis. The equations embodied in equation (2.2.3) are also referred to as the stress equations of motion (Walters [3]). Bird *et al* [1] and Walters [3] give the equation of conservation of mass for both a cylindrical polar coordinate (r, θ, z) system and a spherical polar (r, θ, φ) coordinate system.

2.3 Equations of state

In this thesis we will be concerned with the flow behaviour of Newtonian fluids, inelastic power law fluids and viscoelastic fluids. These fluids fall into the category of either a generalised Newtonian fluid or a generalised linear viscoelastic fluid. The equations of state for these fluids will be presented in this section.

A viscoelastic fluid may exhibit the behaviour of both a Newtonian fluid and a Hookean solid. It has the ability to store energy and will therefore partially recover to its initial state on the removal of any stress it has been subjected to. Viscoelastic fluids also have the ability to remember past events. In presenting the equation of state for a generalised linear viscoelastic fluid we shall firstly consider a single element Maxwell model fluid (Maxwell [4]), which is the simplest form of all linear viscoelastic models.

2.3.1 The generalised Newtonian fluid

A fluid is defined to be Newtonian if the viscosity is independent of time and unaffected by any shearing force or deformation the fluid is subjected to. The equation of state for an incompressible Newtonian fluid gives the relationship between the shear stress tensor τ and the shear rate tensor $\dot{\gamma}$ $(= \nabla v + (\nabla v)^{\mathrm{T}})$ as

$$\tau = \eta_0 \dot{\gamma} \tag{2.3.1}$$

where η_0 is the Newtonian viscosity

The generalised Newtonian model is obtained by modifying the equation of state for a Newtonian fluid to give a shear rate dependent viscosity $\eta(\dot{\gamma})$. Therefore for the generalised Newtonian model we have

$$\tau = \eta(\dot{\gamma})\dot{\gamma} \tag{2.3.2}$$

where $\dot{\gamma}$ is the magnitude of the shear rate tensor $\dot{\gamma}$, given by

$$\dot{\gamma} = \left(\frac{I_2}{2}\right)^{1/2} \tag{2.3.3}$$

In this equation I_2 is the second invariant of the shear rate tensor, which in tensor notation is given by

$$I_2 = \sum_i \sum_j \dot{\gamma}_{ij} \dot{\gamma}_{ji} \tag{2.3.4}$$

Many formulae have been produced in order to model the dependence of the shear viscosity on the shear rate. In this thesis the Newtonian model (constant viscosity) and the power law model (Bird *et al* [1]), described below, will be used.

Power law model fluid

The shear viscosity of a power law model fluid is given by

$$\eta(\dot{\gamma}) = k\dot{\gamma}^{\,n-1} \tag{2.3.5}$$

where k is the fluid consistency index and n is the power law index.

It is noted that on setting $n = 1$ equation (2.3.5) becomes the equation of state for a Newtonian fluid. In equation (2.3.5) $n < 1$ represents a shear thinning fluid whereas $n > 1$ represents a shear thickening fluid.

2.3.2 The Maxwell model fluid

The characterisation of the flow behaviour of viscoelastic fluids is greatly simplified by imposing the restriction that an arbitrary element of the fluid can only be subjected to a small deformation from its initial position. Under this restriction non-linear effects can be ignored. The single element Maxwell model (Maxwell [4]) is obtained from the relationship between the stress tensor τ and the strain tensor γ of a spring and dashpot in series. A spring behaves as an elastic solid and the stress/strain relationship is given by

$$\tau = G\gamma \tag{2.3.6}$$

where G is the rigidity modulus of the spring.

A dashpot consists of a piston moving in a cylinder containing a fluid of constant viscosity η_1 and the relationship between the stress and the rate of strain (shear rate) is given by

$$\tau = \eta_1 \dot{\gamma} \tag{2.3.7}$$

The single element Maxwell model can be expressed as (Bird *et al* [1])

$$\tau + \lambda_1 \frac{\partial}{\partial t}\tau = \eta_1 \dot{\gamma} \tag{2.3.8}$$

where $\lambda_1 = \eta_1 / G$ is a time constant referred to as the relaxation time.

Assuming that τ is zero at time $t = -\infty$ equation (2.3.8) can be expressed as

$$\tau(t) = \int_{-\infty}^{t} \left[\frac{\eta_1}{\lambda_1} e^{-(t-t')/\lambda_1} \right] \dot{\gamma}(t')\, dt \tag{2.3.9}$$

where t now represents the present time and t' represents the past time.

The function within the [ ] brackets is referred to as the relaxation modulus for the single element Maxwell model fluid. It can be seen from equation (2.3.9) that the stress $\tau(t)$ is dependent on the shear rate at the present time t as well as on the shear rate at all past times t'. The exponential decaying form of the relaxation modulus in this equation implies that the most recent events have the greatest influence on the current stress and that the influence of past events decays exponentially as we go back in time. Therefore the single element Maxwell model in equation (2.3.9) contains the notion of a fading memory, where the fluid clearly remembers what it has experienced in the recent past but remembers very little of events in the distant past.

The single element Maxwell model can be generalised by considering a linear superposition of an infinite number of Maxwell elements. The differential form of the generalised Maxwell model is given by

$$\tau_k + \lambda_k \frac{\partial}{\partial t} \tau_k = \eta_k \dot{\gamma}_k \tag{2.3.10}$$

where τ_k is the stress in the kth Maxwell element which has the parameters λ_k and η_k.

The stress for the generalised Maxwell model is given by

$$\tau = \sum_{k=1}^{\infty} \tau_k \tag{2.3.11}$$

and hence we can write

$$\tau(t) = \int_{-\infty}^{t} \left[\sum_{k=1}^{\infty} \frac{\eta_k}{\lambda_k} e^{-(t-t')/\lambda_k} \right] \dot{\gamma}(t')\, dt' \tag{2.3.12}$$

This model has been found to describe the flow behaviour of linear viscoelastic fluids reasonably well (Bird *et al* [1]).

2.3.3 The generalised linear viscoelastic model fluid

The linear viscoelastic models represented by equations (2.3.9) and (2.3.12) are both of the same form, an integral over all past times where the integrand consists of a relaxation modulus multiplied by the rate of strain tensor. These models are contained within a more general equation of state known as the generalised linear viscoelastic model, which is described by the equation

$$\tau(t) = \int_{-\infty}^{t} G(t-t')\, \dot{\gamma}(t')\, dt' \tag{2.3.13}$$

where $G(t-t')$ is the relaxation modulus.

It should be noted that as for the Maxwell models the integrand in equation (2.3.13) consists of the product of two functions. The first function, the relaxation modulus $G(t-t')$, depends on the nature of the fluid and the second function, the rate of strain tensor $\dot{\gamma}(t')$, is dependent on the nature of the flow.

2.3.4 Definition of complex viscosity

In chapters 4, 5, 8 and 9 theories for the determination of the complex viscosity of a fluid in small amplitude oscillatory shear flow will be considered. For small amplitude oscillatory shear flow the shear rate tensor can be expressed as

$$\dot{\gamma}(t') = \dot{\gamma}_0 \, e^{i\omega t'} \tag{2.3.14}$$

where $\dot{\gamma}_0$ is the shear rate amplitude, ω is the angular frequency of oscillation and the real part of these quantities is implied.

On using equations (2.3.13) and (2.3.14) and making the substitution $s = t - t'$ we can write

$$\tau(t) = \eta^* \, \dot{\gamma}_0 \, e^{i\omega t} \tag{2.3.15}$$

where η^*, known as the complex viscosity function, is given by (Bird *et al* [1])

$$\eta^* = \int_0^\infty G(s) e^{-i\omega s} ds \tag{2.3.16}$$

The complex viscosity function can be expressed in terms of its real and imaginary parts as

$$\eta^* = \eta' - i G'/\omega \tag{2.3.17}$$

where η' is defined as the dynamic viscosity function and G' is defined as the dynamic rigidity function. These two functions describe the relative viscous and elastic components in any fluid under small amplitude oscillatory shear flow conditions. Alternatively the dynamic viscosity and dynamic rigidity functions are respectively interpreted as describing the energy dissipated and the energy stored by the fluid in the cyclic deformation. A knowledge of the complex viscosity function provides a complete characterisation of the oscillatory shear flow behaviour of viscoelastic fluids.

In this thesis we consider theories for determining the complex viscosity of linear viscoelastic fluids on both a Weissenberg rheogoniometer and a CSR controlled stress rheometer. The oscillatory shear flow behaviour of single element Maxwell fluids on these

instruments will be numerically simulated. From equation (2.3.9) the relaxation modulus $G(t-t')$ for a single element Maxwell fluid is given by

$$G(t-t') = \frac{\eta_1}{\lambda_1} e^{-(t-t')/\lambda_1} \tag{2.3.18}$$

On making the substitution $s = t - t'$ in equation (2.3.18) and using equation (2.3.16) the complex viscosity of a single element Maxwell fluid can be expressed as

$$\eta^* = \frac{\eta_1}{\lambda_1} \int_0^\infty e^{-s(1+i\omega\lambda_1)/\lambda_1} ds \tag{2.3.19}$$

Evaluating the integral in equation (2.3.19) gives

$$\eta^* = \frac{\eta_1}{(1+i\lambda_1\omega)} \tag{2.3.20}$$

CHAPTER 3

NUMERICAL METHODS USED FOR THE SOLUTION OF THE EQUATIONS OF MOTION

3.1 Introduction to numerical methods

An analytical solution to the stress equations of motion (equation (2.2.4)) for a given equation of state can only be obtained for a very limited number of fluid flow problems, usually in simple flow geometries. For the majority of problems encountered a numerical method must be used in order to solve the relevant partial differential equations (PDEs). In chapters 6 to 9 numerical methods will be used to obtain solutions to the governing equations for the flow of fluids in a finite concentric cylinder geometry.

The two most commonly used numerical methods for the solution of PDEs are the finite difference and finite element methods. An analytical solution to a PDE will provide a continuous solution over the whole flow domain, whereas these numerical methods give the solution at only a discrete number of points. The finite difference and finite element methods approximate the original PDE by an algebraic equation which is then solved at specified meshpoints within the flow domain. Descriptions of the finite difference and finite element methods which are aimed at readers working in fluid dynamics can be found in Wendt [5] and Crochet *et al* [6]. A more comprehensive description of the finite difference and finite element methods is given by Smith [7] and Huebner and Thornton [8] respectively. In the analysis of end effects and fluid inertia effects, in both steady shear and oscillatory shear concentric cylinder flows, we will use a finite difference method to solve the governing equations. The commercially available package Polyflow [9], which uses finite elements, will also be used in the analysis of steady shear concentric cylinder flow.

For the analysis of concentric cylinder flows the finite difference method will be used

to solve elliptic equations over an irregular L shaped geometry. In order to give a brief introduction to this method we consider the finite difference solution of Laplace's elliptic equation over a simple rectangular geometry. A description of the Polyflow package will be given in section 3.3.

3.2 The finite difference method

In order to describe the finite difference method we consider a regularly spaced mesh placed over a closed flow domain in the xy-plane. The mesh consists of regularly spaced parallel lines placed in both the x-direction and the y-direction as shown in figure 3.1.

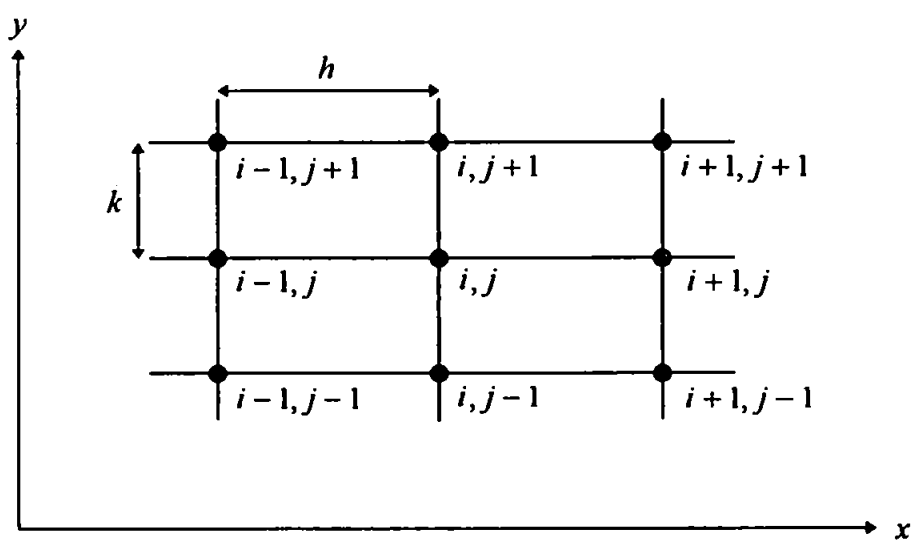

Figure 3.1:- Discrete meshpoints for the finite difference method

The regular spacing between meshpoints in the x and y directions is denoted by h and k respectively. In figure 3.1 the meshpoints are identified by using an index i in the x-direction and an index j in the y-direction. The finite difference method is based on replacing the partial derivatives in a PDE with algebraic difference quotients to give a system of algebraic equations. These equations are then solved at the specified discrete meshpoints.

3.2.1 Finite difference representation of partial derivatives

Finite difference representations for the partial derivatives are obtained using Taylor series expansions. We consider a velocity field $u(x,y)$ over the xy-plane shown in figure 3.1 and denote the velocity at the meshpoint (i,j) by $u_{i,j}$. The velocity $u_{i+1,j}$ at the meshpoint $(i+1,j)$ can be expressed in terms of a Taylor series expanded about the meshpoint (i,j) as

$$u_{i+1,j} = u_{i,j} + h\left(\frac{\partial u}{\partial x}\right)_{i,j} + \frac{h^2}{2!}\left(\frac{\partial^2 u}{\partial x^2}\right)_{i,j} + \frac{h^3}{3!}\left(\frac{\partial^3 u}{\partial x^3}\right)_{i,j} + \ldots \tag{3.2.1}$$

Similarly for the velocity $u_{i-1,j}$ at the meshpoint $(i-1,j)$ we have

$$u_{i-1,j} = u_{i,j} - h\left(\frac{\partial u}{\partial x}\right)_{i,j} + \frac{h^2}{2!}\left(\frac{\partial^2 u}{\partial x^2}\right)_{i,j} - \frac{h^3}{3!}\left(\frac{\partial^3 u}{\partial x^3}\right)_{i,j} + \ldots \tag{3.2.2}$$

On using equations (3.2.1) and (3.2.2) we obtain

$$\left(\frac{\partial u}{\partial x}\right)_{i,j} = \frac{u_{i+1,j} - u_{i-1,j}}{2h} + O(h^2) \tag{3.2.3}$$

This equation is referred to as the second order central difference representation for the derivative $\partial u/\partial x$ at the meshpoint (i,j). Equations (3.2.1) and (3.2.2) can also be used to give a second order central difference representation for the derivative $\partial^2 u/\partial x^2$ at the meshpoint (i,j) as

$$\left(\frac{\partial^2 u}{\partial x^2}\right)_{i,j} = \frac{u_{i+1,j} - 2\,u_{i,j} + u_{i-1,j}}{h^2} + O(h^2) \tag{3.2.4}$$

It can be shown that the second order central difference representation for the derivative $\partial u/\partial y$ at the meshpoint (i,j) is given by

$$\left(\frac{\partial u}{\partial y}\right)_{i,j} = \frac{u_{i,j+1} - u_{i,j-1}}{2k} + O(k^2) \tag{3.2.5}$$

For the second order central difference representation of the derivative $\partial^2 u/\partial y^2$ at the meshpoint (i, j) we have

$$\left(\frac{\partial^2 u}{\partial y^2}\right)_{i,j} = \frac{u_{i,j+1} - 2u_{i,j} + u_{i,j-1}}{k^2} + O(k^2) \tag{3.2.6}$$

Equations (3.2.2) to (3.2.6) can therefore be used to represent the first and second order partial derivatives of $u(x, y)$ in terms of discrete meshpoints (i, j) within the flow domain.

3.2.2 Finite difference boundary conditions

If a finite difference method is to be used to solve an elliptic PDE then the PDE must apply over a closed domain which is surrounded by a closed boundary. For an elliptic PDE the solution at any point P influences the solution at any other point within the closed domain. In turn the solution at P is influenced by any point on the closed boundary. Therefore boundary conditions must be specified over the entire boundary surrounding the closed domain. Considering the velocity $u(x, y)$ over a closed domain in the xy-plane these boundary conditions usually take one of the following forms

1. *Dirichlet condition*

   Specifying the value of the variable $u(x, y)$ along the boundary.

2. *Neumann condition*

   Specifying the derivative in the outward normal direction to the boundary. e.g.

   $\partial u/\partial y = 0$ along the boundary

3.2.3 The finite difference method applied to Laplace's equation

In chapters 6 to 9 we will be using a finite difference method to solve $\zeta[u(x, y)] = g(x, y)$ over an L shaped flow domain for various operators ζ. Some of the boundary conditions for $u(x, y)$ will be of the Dirichlet type and others will be of the

Neumann type. In order to demonstrate the formation of a finite difference scheme to solve these type of equations we consider the solution of Laplace's equation, with a mixture of Dirichlet and Neumann boundary conditions, over the rectangular region shown in figure 3.2.

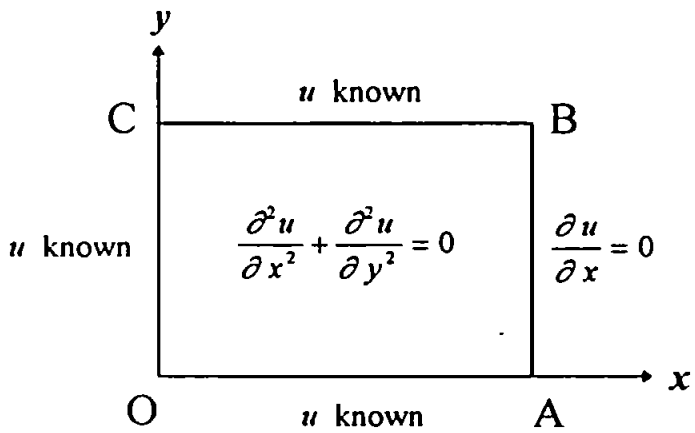

Figure 3.2:- Solution domain for Laplace's equation.

A mesh is placed over the region OABC with m divisions in the x-direction and n divisions in the y-direction. The number of divisions m and n can be chosen to give a square mesh which has steplength h in both the x and y directions, *i.e.* $h = A/m = B/n$. For a square mesh equations (3.2.4) and (3.2.6) can be used to discretise Laplace's equation as

$$\frac{u_{i+1,j} - 2\,u_{i,j} + u_{i-1,j}}{h^2} + \frac{u_{i,j+1} - 2\,u_{i,j} + u_{i,j-1}}{h^2} = 0 \qquad (3.2.7)$$

It is noted that the meshpoint node notation in the x-direction runs from $i = 0$ on boundary OC to $i = m$ on boundary AB. Similarly in the y-direction the meshpoints are labelled from $j = 0$ on boundary OA to $j = n$ on boundary BC. On rearranging equation (3.2.7) the velocity $u_{i,j}$ at a meshpoint (i, j) can be expressed as

$$u_{i,j} = \frac{1}{4}\left[u_{i-1,j} + u_{i,j-1} + u_{i+1,j} + u_{i,j+1}\right] \qquad (3.2.8)$$

for $i = 1$ to m and $j = 1$ to $n-1$.

Note that equation (3.2.8) is not applied at meshpoints on boundaries OA, OC and BC where the value of $u(x,y)$ is known. However the boundary condition on boundary BC is of the Neumann type, where the derivative in the outward normal direction is specified, and equation (3.2.8) must be applied at meshpoints on this boundary. Using equation (3.2.8) to evaluate $u_{m,j}$ on boundary BC will involve the meshpoints $(m+1,j)$ which lie outside the solution domain. Such points are known as 'fictitious points' and are assigned a value by using the boundary condition. On boundary BC we have the condition $\partial u/\partial x = 0$ and therefore from equation (3.2.3) $u_{i,j}$ must satisfy the condition $u_{m+1,j} = u_{m-1,j}$ on this boundary.

3.2.4 Iterative methods for solving the finite difference equations

Equation (3.2.8) represents a system of linear equations which can be solved numerically using a suitable iterative method. Three such methods are the Jacobi, Gauss-Seidel and successive over relaxation (SOR) methods (Smith [7]) which will be described briefly. In the computed solution the values of $u_{i,j}$ over the whole flow domain are stored as a matrix and a single iteration of the iterative method uses equation (3.2.8) to update each matrix entry. Note that for the example considered we have the 'fictitious points' $(m+1,j)$ which are also stored in the matrix. Hence the values of $u_{i,j}$ are stored in a $(m+2)\times(n+1)$ matrix where the entries for $i=0$ to $m+1$ and $j=0$ to n correspond to the meshpoints in the flow domain.

The system of linear equations represented by equation (3.2.8) can be solved numerically using the Jacobi method which gives the iterative procedure

$$u_{i,j}^{(r+1)} = \frac{1}{4}\left[u_{i-1,j}^{(r)} + u_{i,j-1}^{(r)} + u_{i+1,j}^{(r)} + u_{i,j+1}^{(r)}\right] \tag{3.2.9}$$

For this method $i=1$ to m and $j=1$ to $n-1$ gives one complete iteration and

$r = 0, 1, 2, \ldots$ performs the iteration process until a specified convergence criteria is reached.

Rather than waiting until the next iteration to use the $(r+1)^{\text{th}}$ approximations the Gauss-Seidel method uses them as soon as they are available giving the iterative procedure

$$u_{i,j}^{(r+1)} = \frac{1}{4}\left[u_{i-1,j}^{(r+1)} + u_{i,j-1}^{(r+1)} + u_{i+1,j}^{(r)} + u_{i,j+1}^{(r)}\right] \tag{3.2.10}$$

The rate of convergence of the Gauss-Seidel method can be improved by over-correcting the $u_{i,j}^{(r+1)}$ estimate at each iteration, known as the successive over relaxation method (SOR) method. If $\bar{u}_{i,j}^{(r+1)}$ is the Gauss-Seidel estimate then the SOR estimate $u_{i,j}^{(r+1)}$ is obtained by correcting $\bar{u}_{i,j}^{(r+1)}$ using the formula

$$u_{i,j}^{(r+1)} = u_{i,j}^{(r)} + w\left[\bar{u}_{i,j}^{(r+1)} - u_{i,j}^{(r)}\right] \tag{3.2.11}$$

where w is the relaxation parameter.

From equations (3.2.10) and (3.2.11) the SOR method for solving the system of linear equations represented by equation (3.2.8) is given by the iterative procedure

$$u_{i,j}^{(r+1)} = \frac{w}{4}\left[u_{i-1,j}^{(r+1)} + u_{i,j-1}^{(r+1)} + u_{i+1,j}^{(r)} + u_{i,j+1}^{(r)}\right] + (1-w)\, u_{i,j}^{(r)} \tag{3.2.12}$$

The SOR method is divergent unless $0 < w < 2$ and the optimum value, denoted as w_b, usually lies in the range $1 < w < 2$ (Smith [7]). However it is not possible to determine w_b for an arbitrary system of linear equations (Smith [7]). It should be noted that formulae for determining w_b have been obtained for linear systems of equations where the matrix satisfies specific conditions.

3.2.5 Irregular finite difference meshes and transformations

In figure 3.1 the meshpoints are regularly spaced in both the x and y directions where the spacing is given by h and k respectively. However it is not necessary that the meshpoints are regularly spaced and it is possible to use irregularly spaced meshpoints in

both directions. In this case h will have a different value between each successive pair of meshpoints in the x-direction and similarly k will have a different value between each successive pair of meshpoints in the y-direction. The majority of finite difference solutions are obtained on a mesh which has regularly spaced meshpoints, since this simplifies the programming of the solution and results in greater accuracy (Jones and Thompson [10]). However the regular spacing of meshpoints does not have to occur in the physical domain. Instead the finite difference solutions can be obtained in a transformed computational space, which has uniformly spaced meshpoints in the transformed independent variables corresponding to the irregular mesh in the physical domain. A general discussion of the transformation of variables is given by Anderson [11]. In this thesis the governing equations of both steady shear and oscillatory shear flow will be transformed to a computational plane in order to determine solutions using a finite difference method with a regular mesh.

3.3 The Polyflow package

The Polyflow package [9] is a finite element program which has primarily been designed for simulating viscous and viscoelastic flows which occur in processing applications. It can be used to solve flow problems within the categories of isothermal or non-isothermal, two- or three- dimensional and steady state or time dependent. In this thesis Polyflow will be used to solve the governing equations of steady shear concentric cylinder flow for fluids which obey isothermal viscosity laws. Steady shear concentric cylinder flow is axisymmetric about the axis of rotation of the cylinders and has three velocity components. This type of flow is classed by Polyflow as a $2\frac{1}{2}$D axisymmetric problem (Polyflow [9]).

Polyflow is a self contained package which is divided into several modules. In the analysis of steady shear concentric cylinder flow we use three of the Polyflow modules

which will now be briefly described. The geometry and the finite element mesh are generated using the Polymesh module where sub-domains and boundary sets can be defined. The material properties, boundary conditions and numerical parameters of the problem are specified using Polydata which generates a complex data file. This data file activates the central Polyflow server which also uses the mesh file generated by Polymesh. For the applications considered in this thesis Polyflow generates a results data file which contains the finite element meshpoint coordinates and values for the velocity components, streamfunction, pressure and shear stress tensors at each meshpoint. The results generated by Polyflow can be viewed graphically using the Polyplot module which displays contour lines, velocity vectors, streamlines and cross sections. In the steady shear concentric cylinder flow simulations we require the value of the shear stress tensors along the inner cylinder wall. These stresses can be obtained from the Polyflow results data file and used to determine the torque exerted on the inner cylinder due to the motion of the fluid. A description of the Polyflow boundary conditions used in the steady shear concentric cylinder flow problem is now given.

3.3.1 Polyflow boundary conditions

It has previously been stated that concentric cylinder flow is axisymmetric about the axis of rotation of the cylinders and therefore only half the flow domain needs to be considered. This is classed by Polyflow as a $2\frac{1}{2}$ D problem and one of the boundaries of the Polyflow flow domain will be a line of symmetry along the line $r = 0$.

On solid boundaries of the flow domain we use the condition 'Normal and tangential velocities imposed'. The normal velocity component along a boundary is denoted by v_n and the tangential component by v_t. When the 'Normal and tangential velocities imposed' condition is used for a $2\frac{1}{2}$ D axisymmetric problem the user must also specify whether to

impose the w-velocity or the w-force. This represents the angular velocity or angular force about the axis of rotation. For the steady shear concentric cylinder flow problem we set $v_n = v_s = 0$ and impose the w-velocity on the solid boundaries whether they are fixed ($w = 0$) or moving ($w \neq 0$).

For free surface boundaries which remain in their initial positions the condition 'Normal velocity and tangential force imposed' is used. The normal velocity component along a boundary is denoted by v_n and the tangential force component by f_s. When the 'Normal velocity and tangential force imposed' condition is used for a $2\frac{1}{2}$ D axisymmetric problem the w-velocity or w-force on the boundary must be specified. Setting $v_n = f_s = 0$ and the w-force to be zero gives the boundary conditions required for a horizontal free surface which remains in its initial position.

3.4 Non-dimensional form of the equations of motion

In chapters 6 and 7 we will be concerned with obtaining numerical solutions to the relevant equations of motion for steady shear concentric cylinder flow. End effects and fluid inertia effects will be considered for various Newtonian and power law fluids. Obtaining solutions numerically involves a large amount of arithmetic and computational time. It is therefore advantageous to obtain a numerical solution which is applicable to more than one specific case of concentric cylinder flow. This can be achieved by expressing the equations of motion in terms of non-dimensional variables and obtaining a numerical solution to the equations in their non-dimensional form. For steady shear concentric cylinder flow the equations of motion can be expressed in non-dimensional form by defining a Reynolds number (Bird *et al* [2]), denoted R_e. The Reynolds number provides the ratio of the inertial forces to the viscous forces in the flow. We now briefly consider the relationship between Reynolds number and the behaviour of steady shear concentric cylinder flow.

At very low Reynolds numbers the inertial forces are negligible and the flow is dominated by the viscous forces. In this case the concentric cylinder flow can be considered to be laminar about the axis of rotation. As the Reynolds number increases secondary inertial flows occur and the flow becomes more unstable with increasing Reynolds number up to a critical value (Bird *et al* [2]). Above the critical Reynolds number the inertial forces dominate the viscous forces and the flow becomes unstable. It is noted that the critical value of the Reynolds number is dependent on the ratio between the inner and outer cylinder radii, the angular speed of rotation and the fluid density and viscosity. Hence the description 'very low Reynolds number' is relative to the specified flow conditions and fluid properties.

CHAPTER 4

THE EFFECT OF FLUID INERTIA ON COMPLEX VISCOSITY PREDICTIONS OBTAINED FROM A WEISSENBERG RHEOGONIOMETER

4.1 Introduction

This chapter is concerned with the characterisation of linear viscoelastic fluids using a controlled strain Weissenberg rheogoniometer in its oscillatory shear mode. At present the formulae incorporated into the rheogoniometer software for calculating the complex viscosity of a fluid are based on a theory in which fluid inertia effects are ignored.

Oldroyd [12] produced a theory for the oscillatory shear flow of a viscoelastic fluid in a concentric cylinder geometry on an elastoviscometer. On this instrument the amplitudes of the inner and outer cylinders can be measured in which case the amplitude ratio can then be determined. A formula for the amplitude ratio, as a function of the geometry and fluid parameters, has been produced by Oldroyd [12] in terms of Bessel functions of the first and second kind. Markovitz [13] developed a method for expanding these Bessel functions and produced an approximate formula for the amplitude ratio. From this formula the complex viscosity of a fluid could be obtained by solving a quadratic equation with complex coefficients. Walters [14] modified the theory of Oldroyd [12] to include the phase lag of the inner cylinder behind the outer cylinder. An equation of motion in terms of the phase lag and the amplitude ratio is given by Walters [14] and it is concluded that both of these quantities should be included if a complete characterisation of viscoelastic fluids is required. Series approximations to this formula for both large arguments of the Bessel functions and small arguments of the Bessel functions are given by Walters [15]. It is proposed that the approximation for small arguments of the Bessel functions is rapidly convergent if the

quantity αh is small, where α is a parameter that governs the magnitude of fluid inertia effects and h is the gap between the inner and outer cylinders.

Weissenberg [16] produced a theory for oscillatory shear flow in a small angle cone and plate geometry which assumed that the shear rate across the gap between the cone and plate is a constant at all frequencies of oscillation. On making this assumption this worker was effectively ignoring fluid inertia effects. A solution to the equation of motion for oscillatory shear flow in a cone and plate geometry which does not assume a constant shear rate across the gap was obtained by Maude and Walters [17]. The solution given by these workers was valid for small values of α provided that the gap between the cone and plate is small enough for edge effects to be ignored. Using a separation of variables method Nally [18] obtained an exact solution to the equation of motion for oscillatory shear cone and plate flow in terms of Bessel functions of the first kind and Legendre's associated functions of the first and second kind. From this solution Nally [18] produced an equation for a cone and plate rheogoniometer which, for a given frequency, expresses the amplitude ratio and phase lag in terms of the variable α. Numerical results obtained by Nally [18] for small cone angles ($\leq 3°$) showed that the shear stress can vary considerably along the radius of the cone. It was concluded that the assumption of constant shear stress across the gap can only be made for a narrow range of frequencies and materials and the exact theory should be used if experiments are to be conducted for a wide range of frequencies and materials. However the exact equation of Nally [18] was too complicated to be useful for experimentalists wishing to determine α from the measured amplitude ratio and phase lag. An approximation to this equation, which is valid for small α, is obtained by Walters and Kemp [19] for the case where the gap between the cone and plate is small ($\leq 4°$). A formula including first order fluid inertia effects is produced, which can be used to determine α from the experimentally measured amplitude ratio and phase lag.

Walters and Kemp [20] developed a theory for oscillatory shear flows in the parallel plate geometry on a Weissenberg rheogoniometer and produced a non-linear equation which expresses α in terms of the measured amplitude ratio and phase lag. An iterative procedure to determine the exact value of α from this equation is given by these workers. Walters and Kemp [20] also determined a series approximation to the exact equation which is valid when αh is very small, where h is the gap between the parallel plates. The exact equation for the parallel plate geometry is much simpler than the corresponding exact equations for the concentric cylinder and cone and plate geometries (Walters [15] and Nally [18]). From both a theoretical and experimental point of view it is concluded by Walters and Kemp [20] that the parallel plate geometry is the most suitable for oscillatory shear testing on a Weissenberg rheogoniometer.

If fluid inertia effects are ignored in the theory the complex viscosity can easily be determined from the measured amplitude ratio and phase lag on a Weissenberg rheogoniometer for all three geometries. However determining the complex viscosity, when fluid inertia effects are included in the theory, from the exact equations (Walters [15], Nally [18], Walters and Kemp [20]) requires the use of suitable iterative techniques. Iterative methods can be time consuming and since the equations have multiple solutions convergence to the correct solution is not guaranteed. Therefore iterative solutions are by no means a suitable method for experimentalists to interpret experimental measurements into complex viscosity predictions and other techniques will be considered. Fluid inertia effects in the cone and plate, parallel plate and concentric cylinder geometries have been considered by Golden [21] for oscillatory shear flows on a CSR controlled stress rheometer. If fluid inertia effects are ignored in the theory complex viscosity data can easily be calculated from experimental measurements made on the CSR controlled stress rheometer. Using a perturbation analysis Golden [21] has produced formulae which can be used to

correct the complex viscosity prediction for both first and second order fluid inertia effects. It is concluded that these corrections should be used when complex viscosity predictions are made, especially for concentric cylinder geometries and wide gap parallel plate geometries.

In this chapter we consider fluid inertia effects in oscillatory shear flows on a controlled strain Weissenberg rheogoniometer. The oscillatory shear theory for linear viscoelastic fluids is presented for the parallel plate, concentric cylinder and cone and plate geometries. Using a fluid inertia perturbation analysis (Golden [21]), which is valid for small fluid inertia effects, we develop formulae for determining the complex viscosity of a fluid which include both first and second order fluid inertia effects. These formulae will take a similar form to those produced by Golden [21] and can be used as on line corrections for complex viscosity data obtained experimentally from a Weissenberg rheogoniometer.

For all three geometries simulated oscillatory shear data will be generated for a Newtonian fluid and a single element Maxwell fluid and used to consider the validity of the second order fluid inertia perturbation theory. The simulated data, presented in chapter 5, will also be used to establish the frequency range of applicability of the second order fluid inertia corrections for Newtonian and single element Maxwell fluids.

The oscillatory shear theory presented in this chapter is developed for the case of the upper platen of the geometry being constrained by a torsion bar of finite stiffness. However this theory can easily be adapted to the case where the upper platen of the geometry is connected to a strain gauge torsion head by assuming that the upper platen remains stationary for this torsion head system. Therefore we consider the strain gauge torsion head to be infinitely stiff and when it is used on a Weissenberg rheogoniometer the upper platen of the geometry will be stationary as the lower platen oscillates. This is in contrast to the oscillatory shear flow conditions on a CSR controlled stress rheometer where the upper platen oscillates and the lower platen is stationary, which is considered for comparison

purposes.

Simulated oscillatory shear data for Newtonian and single element Maxwell fluids will be generated for the case where a strain gauge torsion head is used on the Weissenberg rheogoniometer. This data, which is presented in chapter 5, will be compared with the corresponding simulated oscillatory shear data obtained for a CSR controlled stress rheometer. Comparisons will be made, for a given geometry, between the fluid inertia effects on the Weissenberg and CSR instruments and the limitations of the second order fluid inertia perturbation theory for each instrument will also be discussed.

4.2 Parallel plate geometry

4.2.1 Governing equations

With reference to a set of cylindrical polar coordinates (r,θ,z) a viscoelastic fluid occupies the region between two coaxial parallel plates of radius a, separated by a vertical distance h as shown in figure 4.1. The lower plate is forced to perform small amplitude angular oscillations of amplitude θ_2 and frequency f (cycles/sec) about the z-axis. The resulting motion of the fluid causes the upper plate, which is constrained by a torsion bar of stiffness K, to perform oscillations about the z-axis of amplitude θ_1 with a phase lag c behind the motion of the lower plate. It is assumed that the amplitude of oscillation of the driven lower plate is sufficiently small to ensure that the flow is in the linear viscoelastic region and hence non-linear fluid inertia terms can be neglected in the equations of motion. On neglecting edge effects we assume a velocity distribution, which satisfies the equation of continuity for incompressible fluids, of the form

$$v_r = 0 \quad , \quad v_\theta = r\,f(z)\,e^{i\omega t} \quad , \quad v_z = 0 \tag{4.2.1}$$

where $\omega = 2\pi f$ (radians/sec) is the angular frequency of oscillation and the real part of

these quantities is implied.

This velocity distribution gives one non-zero component of the shear stress tensor as

$$\tau_{\theta z} = \eta^{*} r \frac{d f(z)}{dz} e^{i\omega t} \tag{4.2.2}$$

where η^{*} is the complex viscosity of the fluid.

Substituting equations (4.2.1) and (4.2.2) into the relevant stress equations of motion (Bird *et al* [1]) and noting that the flow is axi-symmetric we obtain the second order ordinary differential equation

$$\frac{d^2 f(z)}{dz^2} + \alpha^2 f(z) = 0 \tag{4.2.3}$$

In this equation α^2 is a complex parameter, which governs the magnitude of fluid inertia effects, defined as (Walters [3])

$$\alpha^2 = \frac{-i\rho\omega}{\eta^{*}} \tag{4.2.4}$$

where ρ is the fluid density.

On using equation (4.2.1) the boundary conditions for the function $f(z)$ are given by

$$f(0) = \theta_2 \, i\omega \, e^{ic} \tag{4.2.5}$$

$$f(h) = \theta_1 \, i\omega \tag{4.2.6}$$

The solution of equation (4.2.3) subject to these boundary conditions is

$$f(z) = i\omega[\theta_1 \operatorname{cosec}(\alpha h) - \theta_2 e^{ic} \cot(\alpha h)] \sin(\alpha z) + i\omega\theta_2 e^{ic} \cos(\alpha z) \tag{4.2.7}$$

By the principle of conservation of angular momentum the equation of motion of the upper plate can be expressed as

$$C_F - K\theta = I\ddot{\theta} \tag{4.2.8}$$

where θ is the angular displacement of the upper plate, C_F is the torque exerted on the upper plate due to the motion of the fluid and I is the moment of inertia of the member

constrained by the torsion bar. The angular displacement of the upper plate is given by $\theta = \theta_1 e^{i\omega t}$ and hence in equation (4.2.8) we have

$$C_F = (K - I\omega^2)\theta_1 e^{i\omega t} \tag{4.2.9}$$

The torque C_F exerted on the upper plate due to the motion of the fluid is given by

$$C_F = -2\pi \int_0^a r^2 \tau_{\theta z}\big|_{z=h} dr \tag{4.2.10}$$

Using equations (4.2.2) and (4.2.7) the $\tau_{\theta z}$ shear stress on the upper plate can be determined and on substituting into equation (4.2.10) we have

$$C_F = \frac{\pi i \omega a^4 \alpha}{2}\left(\theta_1 \cot(\alpha h) - \frac{\theta_2 e^{ic}}{\sin(\alpha h)}\right) e^{i\omega t} \tag{4.2.11}$$

On combining equations (4.2.9) and (4.2.11) the equation of motion of the upper plate can be expressed as

$$\frac{e^{ic}}{\vartheta} = \cos(\alpha h) + \frac{S}{\rho h^2 \omega}(\alpha h)\sin(\alpha h) \tag{4.2.12}$$

where S is a geometrical parameter given by

$$S = \frac{2h(K - I\omega^2)}{\pi a^4 \omega} \tag{4.2.13}$$

and $\vartheta (= \theta_1/\theta_2)$ is defined as the amplitude ratio.

The frequency ω and amplitude θ_2 of the lower plate are prescribed by the Weissenberg rheogoniometer operator and the resulting amplitude θ_1 and phase lag c of the upper plate are measured. Therefore in equation (4.2.12) the amplitude ratio ϑ, phase lag c and geometrical parameter S are known and the complex viscosity η^* can then be determined. However equation (4.2.12) which includes full fluid inertia effects is non-linear in terms of the non-dimensional quantity αh and a full solution can only be obtained using a suitable numerical iterative technique. In this thesis we shall consider a perturbation method of

solution which will be valid for the case when fluid inertia effects are small. From the perturbation theory we will produce formulae which can be incorporated into the rheogoniometer software to provide an on line correction of experimental data for first and second order fluid inertia effects.

4.2.2 Perturbation method of solution to predict complex viscosity

Equation (4.2.12) is the equation of motion of the upper plate and on using equation (4.2.4) it can be expressed as

$$\frac{e^{ic}}{\vartheta} = \cos(\alpha h) - \frac{iS}{\eta^*}\frac{\sin(\alpha h)}{\alpha h} \tag{4.2.14}$$

For oscillatory shear parallel plate flow in which fluid inertia effects are small, we consider a Taylor series expansion of equation (4.2.14) in terms of the non-dimensional parameter αh about the point $\alpha h = 0$. On working to second order terms in the non-dimensional parameter $(\alpha h)^2$ the right hand side of equation (4.2.14) can be expanded to give

$$\frac{e^{ic}}{\vartheta} = 1 - \frac{iS}{\eta^*} - \left[\frac{1}{2} - \frac{1}{6}\frac{iS}{\eta^*}\right](\alpha h)^2 + \left[\frac{1}{24} - \frac{1}{120}\frac{iS}{\eta^*}\right](\alpha h)^4 \tag{4.2.15}$$

We define η_0^* to be the complex viscosity of the fluid when fluid inertia effects are ignored. The equation of motion of the upper plate when fluid inertia effects are ignored is then obtained from equation (4.2.15) by setting $\alpha = 0$ and replacing η^* by η_0^* to give

$$\frac{e^{ic}}{\vartheta} = 1 - \frac{iS}{\eta_0^*} \tag{4.2.16}$$

The measured amplitude ratio ϑ and phase lag c are then used to calculate the complex viscosity η_0^*, when fluid inertia effects are ignored, by expressing equation (4.2.16) in the form

$$\eta_0^* = \frac{iS}{\left(1 - e^{ic}/\vartheta\right)} \tag{4.2.17}$$

On considering the real and imaginary components of equation (4.2.17) formulae for calculating the dynamic viscosity η_0' and the dynamic rigidity G_0' of a fluid, when fluid inertia effects are ignored, are given by (Walters [3])

$$\eta_0' = \frac{-S\vartheta \sin(c)}{[\vartheta^2 - 2\vartheta\cos(c) + 1]} \tag{4.2.18}$$

$$G_0' = \frac{\omega S\vartheta\,[\cos(c) - \vartheta]}{[\vartheta^2 - 2\vartheta\cos(c) + 1]} \tag{4.2.19}$$

We define the complex parameter α_0^2 as

$$\alpha_0^2 = \frac{-i\rho\omega}{\eta_0^*} \tag{4.2.20}$$

On using equations (4.2.15), (4.2.16) and (4.2.20) we obtain a relationship between η_0^* and η^* given by

$$-\frac{iS}{\eta_0^*} = -\frac{iS}{\eta^*} - \frac{\eta_0^*}{\eta^*}\left[\frac{1}{2} - \frac{1}{6}\frac{iS}{\eta^*}\right](\alpha_0 h)^2 + \frac{\eta_0^{*2}}{\eta^{*2}}\left[\frac{1}{24} - \frac{1}{120}\frac{iS}{\eta^*}\right](\alpha_0 h)^4 \tag{4.2.21}$$

In order to determine an expression for η^* in terms of η_0^* from this equation we expand η^* as a second order power series in the non-dimensional parameter $(\alpha_0 h)^2$ given by

$$\eta^* = \eta_0^* + (\alpha_0 h)^2 \eta_1^* + (\alpha_0 h)^4 \eta_2^* \tag{4.2.22}$$

On substituting equation (4.2.22) into equation (4.2.21) we obtain

$$-\frac{iS}{\eta_0^*} = -\frac{iS}{\eta_0^*} - \left[\frac{1}{2} - \frac{iS}{\eta_0^*}\left\{\frac{1}{6} + \frac{\eta_1^*}{\eta_0^*}\right\}\right](\alpha_0 h)^2$$

$$+\left[\frac{1}{24} + \frac{1}{2}\frac{\eta_1^*}{\eta_0^*} - \frac{iS}{\eta_0^*}\left\{\frac{1}{120} - \frac{1}{3}\frac{\eta_1^*}{\eta_0^*} - \frac{\eta_1^{*2}}{\eta_0^{*2}} + \frac{\eta_2^*}{\eta_0^*}\right\}\right](\alpha_0 h)^4 \tag{4.2.23}$$

where terms of order $(\alpha_0 h)^6$ and higher have been neglected.

Comparing coefficients of the $(\alpha_0 h)^2$ terms gives

$$\eta_1^* = -\frac{\eta_0^*}{2}\left[\frac{1}{3}+\frac{i\eta_0^*}{S}\right] \tag{4.2.24}$$

On comparing coefficients of the $(\alpha_0 h)^4$ terms and using equation (4.2.24) we have

$$\eta_2^* = -\frac{\eta_0^*}{24}\left[\frac{7}{15}+\frac{i\eta_0^*}{S}\right] \tag{4.2.25}$$

Substituting these expressions for η_1^* and η_2^* into equation (4.2.22) gives

$$\eta^* = \eta_0^*\left[1-\frac{1}{2}\left\{\frac{1}{3}+\frac{i\eta_0^*}{S}\right\}(\alpha_0 h)^2-\frac{1}{24}\left\{\frac{7}{15}+\frac{i\eta_0^*}{S}\right\}(\alpha_0 h)^4\right] \tag{4.2.26}$$

On using equation (4.2.20) we can express equation (4.2.26) in the form

$$\eta^* = \eta_0^* + \frac{i\rho h^2\omega}{2}\left\{\frac{1}{3}+\frac{i\eta_0^*}{S}\right\}+\frac{\rho^2 h^4\omega^2}{24\eta_0^*}\left\{\frac{7}{15}+\frac{i\eta_0^*}{S}\right\} \tag{4.2.27}$$

Equation (4.2.27) is the formula for calculating the complex viscosity of a fluid which corrects for first and second order fluid inertia effects. In this equation it should be noted that η_0^* is known from equation (4.2.17).

In order to establish the limitations of the second order fluid inertia perturbation theory we shall simulate the oscillatory shear flow behaviour of a Newtonian fluid and a single element Maxwell fluid in the parallel plate geometry. The simulated data will be presented in chapter 5.

4.2.3 Complex viscosity prediction for a strain gauge torsion head system on the Weissenberg rheogoniometer

On a Weissenberg rheogoniometer instead of constraining the upper plate with a torsion bar it is possible to connect the upper plate to a strain gauge torsion head. The strain gauge measures the torque exerted on the upper plate due to the motion of the fluid and in relation to a torsion bar has a stiffness K of approximately 5,000 Nm/rad. This stiffness

results in minute amplitudes of oscillation in comparison to those obtained using a torsion bar. Therefore it is assumed that the upper plate is stationary and in the theory we consider the strain gauge to have a stiffness K of infinity. It is noted that if K is infinite then the geometrical parameter S defined in equation (4.2.13) will also be infinite. For this type of oscillatory shear flow a relationship between η_0^* and η^* is obtained by combining equations (4.2.12) and (4.2.16) and setting $S = \infty$ to give

$$\eta_0^* = \frac{\alpha h}{\sin(\alpha h)} \eta^* \tag{4.2.28}$$

Setting $S = \infty$ in equation (4.2.26) gives the second order fluid inertia correction for complex viscosity data obtained using a strain gauge torsion head as

$$\eta^* = \eta_0^* \left[1 - \frac{1}{6}(\alpha_0 h)^2 - \frac{7}{360}(\alpha_0 h)^4 \right] \tag{4.2.29}$$

If the stiffness of the strain gauge is considered to be infinite we have the lower plate oscillating with small amplitude at a prescribed frequency and the upper plate stationary. This is a similar situation to parallel plate oscillatory shear flow on a CSR controlled stress rheometer, where the upper plate oscillates with small amplitude and the lower plate is stationary, which is now considered for comparison purposes.

4.2.4 Complex viscosity prediction for a CSR controlled stress rheometer

On a CSR controlled stress rheometer an oscillatory torque of amplitude C_0 and frequency f is applied to the upper plate, forcing it to make small amplitude oscillations of amplitude X_0 with a phase lag c behind the applied torque. The lower plate remains stationary. An equation of motion for the upper plate is determined by considering the torque exerted on the upper plate due to the motion of the fluid. Using the equations given by Golden [21] for this type of oscillatory shear flow we obtain a relationship between η_0^*

and η^* as

$$\eta_0^* = \alpha h \cot(\alpha h)\eta^* \tag{4.2.30}$$

An expression to correct complex viscosity data obtained from a CSR controlled stress rheometer for second order fluid inertia effects is given by Golden [21] as

$$\eta^* = \eta_0^*\left[1+\frac{1}{3}(\alpha_0 h)^2+\frac{1}{45}(\alpha_0 h)^4\right] \tag{4.2.31}$$

It should be noted from equations (4.2.28) and (4.2.30) that the relationship between η^* and η_0^* on a CSR controlled stress rheometer is different to that on a Weissenberg rheogoniometer fitted with a strain gauge torsion head. The difference in these relationships is due to the torque being measured on the stationary plate on the Weissenberg rheogoniometer, whereas on the CSR controlled stress rheometer the torque is measured on the moving plate. It should be noted that on both instruments the strain is measured on the moving surface.

The difference in complex viscosity predictions obtained from the Weissenberg rheogoniometer fitted with a strain gauge torsion head and the CSR controlled stress rheometer will be demonstrated, in chapter 5, by simulating the oscillatory shear flow behaviour of a Newtonian fluid and a single element Maxwell fluid in the parallel plate geometry on each instrument. The simulated data will also be used to establish the frequency range of applicability of the respective second order fluid inertia corrections given in equations (4.2.29) and (4.2.31).

4.3 Concentric cylinder geometry

4.3.1 Governing equations

With reference to a set of cylindrical polar coordinates (r,θ,z) a viscoelastic fluid

occupies the region between two coaxial cylinders as shown in figure 4.2. The inner and outer cylinders have radii r_i and r_o respectively and the fluid is considered to be in contact with the cylinders, which are assumed to be infinitely long in the z direction, over a length h. Therefore end effects are ignored in the theory (end effects in concentric cylinder oscillatory shear flow on a Weissenberg rheogoniometer will be considered in chapter 9). The outer cylinder is forced to perform small amplitude angular oscillations of amplitude θ_2 and frequency f (cycles/sec) about the z-axis. The resulting motion of the fluid causes the inner cylinder, which is constrained by a torsion bar of stiffness K, to perform oscillations about the z-axis of amplitude θ_1 with a phase lag c behind the motion of the outer cylinder. It is assumed that the amplitude of oscillation of the driven outer cylinder is sufficiently small to ensure that the flow is in the linear viscoelastic region and hence non-linear terms can be neglected in the equations of motion. On neglecting end effects we assume a velocity distribution, which satisfies the equation of continuity for incompressible fluids, of the form

$$v_r = 0 \quad , \quad v_\theta = r\,f(r)\,e^{i\omega t} \quad , \quad v_z = 0 \tag{4.3.1}$$

where $\omega = 2\pi f$ (radians/sec) is the angular frequency of oscillation and the real part of these quantities is implied.

This velocity distribution gives one non-zero component of the shear stress tensor as

$$\tau_{r\theta} = \eta^* r \frac{d\,f(r)}{dr} e^{i\omega t} \tag{4.3.2}$$

where η^* is the complex viscosity of the fluid.

Substituting equations (4.3.1) and (4.3.2) into the relevant stress equations of motion (Bird *et al* [1]) and noting that the flow is axisymmetric we obtain the second order ordinary differential equation

$$\frac{d}{dr}\left[r^3 \frac{d\,f(r)}{dr}\right] + \alpha^2 r^3 f(r) = 0 \tag{4.3.3}$$

where α^2 is defined in equation (4.2.4)

On considering equation (4.3.1) it can be shown that the function $f(r)$ is subject to the boundary conditions

$$f(r_i) = \theta_1 i\omega \tag{4.3.4}$$

$$f(r_o) = \theta_2 i\omega\, e^{ic} \tag{4.3.5}$$

Making the substitution $g(r) = r\,f(r)$ in equation (4.3.3) gives

$$r^2 \frac{d^2 g(r)}{dr^2} + r\frac{d\,g(r)}{dr} + (\alpha^2 r^2 - 1)g(r) = 0 \tag{4.3.6}$$

This is a parametric Bessel equation for which the general solution is known and therefore the solution of equation (4.3.3) is given by

$$f(r) = \frac{1}{r}[A\,J_1(\alpha r) + B\,Y_1(\alpha r)] \tag{4.3.7}$$

where A and B are constants to be determined.

On applying the boundary conditions of equations (4.3.4) and (4.3.5) to equation (4.3.7) the constants A and B are given by

$$A = \frac{i\omega\,[\theta_1\, r_i\, Y_1(\alpha r_o) - \theta_2\, e^{ic}\, r_o\, Y_1(\alpha r_i)]}{[J_1(\alpha r_i)\, Y_1(\alpha r_o) - J_1(\alpha r_o)\, Y_1(\alpha r_i)]} \tag{4.3.8}$$

$$B = \frac{i\omega\,[\theta_1\, r_i\, J_1(\alpha r_o) - \theta_2\, e^{ic}\, r_o\, J_1(\alpha r_i)]}{[Y_1(\alpha r_i)\, J_1(\alpha r_o) - Y_1(\alpha r_o)\, J_1(\alpha r_i)]} \tag{4.3.9}$$

The equation of motion of the inner cylinder can be expressed as

$$C_F = (K - I\omega^2)\theta_1 e^{i\omega t} \tag{4.3.10}$$

where C_F is the torque exerted on the inner cylinder due to the motion of the fluid and I is the moment of inertia of the member constrained by the torsion bar.

The torque C_F exerted on the inner cylinder due to the motion of the fluid is given by

$$C_F = 2\pi r_i^2 \int_0^h \tau_{r\theta}\big|_{r=r_i} dz \tag{4.3.11}$$

On using equation (4.3.2) the torque C_F can be expressed as

$$C_F = 2\pi h r_i^3 \eta^* \left.\frac{df}{dr}\right|_{r=r_i} e^{i\omega t} \tag{4.3.12}$$

From equation (4.3.7) we have

$$\left.\frac{df}{dr}\right|_{r=r_i} = \frac{\alpha}{2r_i}\left[A\{J_0(\alpha r_i) - J_2(\alpha r_i)\} + B\{Y_0(\alpha r_i) - Y_2(\alpha r_i)\}\right]$$

$$-\frac{1}{r_i^2}\left[A\, J_1(\alpha r_i) + B\, Y_1(\alpha r_i)\right] \tag{4.3.13}$$

Using equations (4.3.8) to (4.3.10), (4.3.12) and (4.3.13) and the properties of Bessel functions given in Appendix 4.1 the equation of motion of the inner cylinder can be expressed as

$$\frac{e^{ic}}{\vartheta} = \frac{\pi r_i^2}{2r_o}\left[\alpha\{J_2(\alpha r_i)Y_1(\alpha r_o) - Y_2(\alpha r_i)J_1(\alpha r_o)\}\right.$$

$$\left. + \frac{2Sr_o^2}{r_i(r_o^2 - r_i^2)\rho\omega}\alpha^2\{J_1(\alpha r_i)Y_1(\alpha r_o) - Y_1(\alpha r_i)J_1(\alpha r_o)\}\right] \tag{4.3.14}$$

where S is a geometrical parameter given by

$$S = \frac{(r_o^2 - r_i^2)(K - I\omega^2)}{4\pi h r_i^2 r_o^2 \omega} \tag{4.3.15}$$

and $\vartheta\ (= \theta_1/\theta_2)$ is defined as the amplitude ratio.

On a Weissenberg rheogoniometer the frequency ω, amplitude ratio ϑ, phase lag c and geometrical parameter S are all known quantities. Therefore α, and hence the complex viscosity η^*, can be obtained from the solution to equation (4.3.14). This equation, which includes full fluid inertia effects, is non-linear in terms of α and a full solution can only be obtained using a suitable numerical iterative technique. However iterative methods of solution may lead to incorrect complex viscosity predictions. Therefore, as for the parallel plate geometry, we shall consider solving equation (4.3.14) using a perturbation method

which will be valid for the case when fluid inertia effects are small. Formulae will be produced from the perturbation theory which can be incorporated into the rheogoniometer software to provide an on line correction of concentric cylinder complex viscosity data for first and second order fluid inertia effects.

4.3.2 Perturbation method of solution to predict complex viscosity

Equation (4.3.14) is the equation of motion of the inner cylinder and on using equation (4.2.4) it can be expressed as

$$\frac{e^{ic}}{\vartheta} = \frac{\pi r_i^2}{2r_o}\left[\alpha\{J_2(\alpha r_i)Y_1(\alpha r_o) - Y_2(\alpha r_i)J_1(\alpha r_o)\}\right.$$

$$\left. - \frac{2iSr_o^2}{r_i(r_o^2 - r_i^2)\eta^*}\{J_1(\alpha r_i)Y_1(\alpha r_o) - Y_1(\alpha r_i)J_1(\alpha r_o)\}\right] \qquad (4.3.16)$$

For concentric cylinder oscillatory shear flows in which fluid inertia effects are small we consider a Taylor series expansion of equation (4.3.16) in terms of the non-dimensional parameter αr_o about the point $\alpha r_o = 0$. On working to second order terms in the non-dimensional parameter $(\alpha r_o)^2$ the right hand side of equation (4.3.16) can be expanded to give

$$\frac{e^{ic}}{\vartheta} = 1 - \frac{iS}{\eta^*} - \left[B - \frac{iS}{\eta^*}C\right](\alpha r_o)^2 + \left[D - \frac{iS}{\eta^*}E\right](\alpha r_o)^4 \qquad (4.3.17)$$

where B, C, D and E are non-dimensional geometry dependent constants given by

$$B = \frac{(r_o^2 - r_i^2)^2}{8r_o^4}$$

$$C = \frac{r_i^2}{8(r_o^2 - r_i^2)}\left[4\ln(r_i/r_o) + \frac{r_o^2}{r_i^2} - \frac{r_i^2}{r_o^2}\right]$$

$$D = \frac{1}{192r_o^6}\left[(r_o^2 - r_i^2)(r_o^4 - 5r_i^2r_o^2 - 2r_i^4) + 12r_o^2r_i^4\ln(r_i/r_o)\right]$$

$$E = \frac{1}{192 r_o^4 (r_o^2 - r_i^2)} \left[(r_o^2 - r_i^2)(r_i^4 + 10 r_i^2 r_o^2 + r_o^4) + 12 r_i^2 r_o^2 (r_i^2 + r_o^2) \ln\left(r_i / r_o\right) \right] \qquad (4.3.18)$$

The equation of motion of the inner cylinder when fluid inertia effects are ignored is obtained from equation (4.3.17) by setting $\alpha = 0$ and replacing η^* with η_0^*, the complex viscosity when fluid inertia effects are ignored, to give

$$\frac{e^{ic}}{\vartheta} = 1 - \frac{iS}{\eta_0^*} \qquad (4.3.19)$$

This equation is of identical form to the equation of motion for the upper plate of the parallel plate geometry when fluid inertia effects are ignored (equation (4.2.16)). However it should be noted that the definition of the geometrical parameter S is now given by equation (4.3.15). The complex viscosity η_0^* when fluid inertia effects are ignored can therefore be calculated for the concentric cylinder geometry by using equation (4.2.17) with the geometrical parameter S defined in equation (4.3.15). Using equations (4.3.17), (4.3.19) and the definition of α_0^2 in equation (4.2.20) we obtain a relationship between η_0^* and η^* given by

$$-\frac{iS}{\eta_0^*} = -\frac{iS}{\eta^*} - \frac{\eta_0^*}{\eta^*}\left[B - \frac{iS}{\eta^*}C\right](\alpha_0 r_o)^2 + \frac{\eta_0^{*2}}{\eta^{*2}}\left[D - \frac{iS}{\eta^*}E\right](\alpha_0 r_o)^4 \qquad (4.3.20)$$

In order to determine an expression for η^* in terms of η_0^* from this equation we expand η^* as a second order power series in the non-dimensional parameter $(\alpha_0 r_o)^2$ given by

$$\eta^* = \eta_0^* + (\alpha_0 r_o)^2 \eta_1^* + (\alpha_0 r_o)^4 \eta_2^* \qquad (4.3.21)$$

On substitution of equation (4.3.21) into equation (4.3.20) we obtain

$$-\frac{iS}{\eta_0^*} = -\frac{iS}{\eta_0^*} - \left[B - \frac{iS}{\eta_0^*}\left\{C + \frac{\eta_1^*}{\eta_0^*}\right\}\right](\alpha_0 r_o)^2$$

$$+\left[D + B\frac{\eta_1^*}{\eta_0^*} - \frac{iS}{\eta_0^*}\left\{E - 2C\frac{\eta_1^*}{\eta_0^*} - \frac{\eta_1^{*2}}{\eta_0^{*2}} + \frac{\eta_2^*}{\eta_0^*}\right\}\right](\alpha_0 r_o)^4 \qquad (4.3.22)$$

where terms of order $(\alpha_0 r_o)^6$ and higher have been neglected.

Comparing coefficients of the $(\alpha_0 r_o)^2$ terms we obtain

$$\eta_1^* = -\eta_0^*\left[C + \frac{i\eta_0^*}{S}B\right] \tag{4.3.23}$$

On comparing coefficients of the $(\alpha_0 r_o)^4$ terms and using equation (4.3.23) we have

$$\eta_2^* = -\eta_0^*\left[\left(C^2 - E\right) + \frac{i\eta_0^*}{S}\left(BC - D\right)\right] \tag{4.3.24}$$

Substituting these expressions for η_1^* and η_2^* into equation (4.3.21) and using the definition of the non-dimensional geometry constants B, C, D and E in equation (4.3.18) gives

$$\eta^* = \eta_0^*\left[1 - \left\{C_1 + \frac{i\eta_0^*}{S}C_2\right\}(\alpha_0 r_o)^2 - \left\{C_3 + \frac{i\eta_0^*}{S}C_4\right\}(\alpha_0 r_o)^4\right] \tag{4.3.25}$$

where C_1, C_2, C_3 and C_4 are non-dimensional geometry dependent factors given by

$$C_1 = \frac{r_i^2}{8(r_o^2 - r_i^2)}\left[4\ln(r_i/r_o) + \frac{r_o^2}{r_i^2} - \frac{r_i^2}{r_o^2}\right]$$

$$C_2 = \frac{(r_o^2 - r_i^2)^2}{8r_o^4}$$

$$C_3 = \frac{1}{96r_o^4(r_o^2 - r_i^2)^2}\left[(r_o^2 - r_i^2)^4 + 6r_i^2r_o^2\left\{r_o^4 - r_o^4 + 4r_i^2r_o^2\ln(r_i/r_o)\right\}\ln(r_i/r_o)\right]$$

$$C_4 = \frac{1}{192r_o^6}\left[(2r_o^6 + 3r_i^2r_o^4 - 6r_i^4r_o^2 + r_i^6 + 12r_o^4r_i^2\ln(r_i/r_o)\right] \tag{4.3.26}$$

On using equation (4.2.20) we can express equation (4.3.25) as

$$\eta^* = \eta_0^* + i\rho r_o^2\omega\left\{C_1 + \frac{i\eta_0^*}{S}C_2\right\} + \frac{\rho^2 r_o^4\omega^2}{\eta_0^*}\left\{C_3 + \frac{i\eta_0^*}{S}C_4\right\} \tag{4.3.27}$$

Equation (4.3.27) is the formula for calculating the complex viscosity of a fluid which includes first and second order fluid inertia effects. In this equation it should be noted that η_0^* is known from equation (4.2.17) where the geometrical parameter S is defined by

equation (4.3.15). It is also noted that the formulae in equations (4.2.18) and (4.2.19), to respectively calculate the zero order dynamic viscosity η_0' and dynamic rigidity G_0', can be used for the concentric cylinder geometry where the geometrical parameter S is defined by equation (4.3.15). In order to establish the limitations of the second order fluid inertia perturbation theory we shall simulate the oscillatory shear flow behaviour of a Newtonian fluid and a single element Maxwell fluid in the concentric cylinder geometry. This simulation will be presented in chapter 5.

4.3.3 Complex viscosity prediction for a strain gauge torsion head system on the Weissenberg rheogoniometer

On a Weissenberg rheogoniometer instead of constraining the inner cylinder with a torsion bar it is possible to connect the inner cylinder to a strain gauge torsion head. As for the parallel plate geometry, we assume that the strain gauge is infinitely stiff and therefore the geometrical parameter S defined in equation (4.3.15) will also be infinite. A relationship between η_0^* and η^* for oscillatory shear flow with a strain gauge torsion head is then obtained by combining equations (4.3.14) and (4.3.19) and setting $S = \infty$ to give

$$\eta_0^* = \frac{(r_o^2 - r_i^2)\eta^*}{\pi r_i r_o \{J_1(\alpha r_i)Y_1(\alpha r_o) - Y_1(\alpha r_i)J_1(\alpha r_o)\}} \tag{4.3.28}$$

On setting $S = \infty$ in equation (4.3.25) we obtain the second order fluid inertia correction for complex viscosity data obtained using a strain gauge torsion head as

$$\eta^* = \eta_0^*\left[1 - C_1(\alpha_0 r_o)^2 - C_3(\alpha_0 r_o)^4\right] \tag{4.3.29}$$

where C_1 and C_3 are defined in equation (4.3.26).

If the stiffness of the strain gauge is considered to be infinite we have the outer cylinder oscillating with small amplitude at a prescribed frequency and the inner cylinder stationary. This is similar to concentric cylinder oscillatory shear flow on a CSR controlled stress

rheometer, where the inner cylinder oscillates with small amplitude and the outer cylinder is stationary, which is now considered for comparison purposes.

4.3.4 Complex viscosity prediction for a CSR controlled stress rheometer

On a CSR controlled stress rheometer an oscillatory torque of amplitude C_0 and frequency f is applied to the inner cylinder, forcing it to make small amplitude oscillations of amplitude X_0 with a phase lag c behind the applied torque. The outer cylinder remains stationary. An equation of motion for the inner cylinder is determined by considering the torque exerted on the inner cylinder due to the motion of the fluid. The equations for CSR concentric cylinder oscillatory shear flow, given by Golden [21], can be used to obtain a relationship between η_0^* and η^* as

$$\eta_0^* = \frac{r_i(r_o^2 - r_i^2)}{2r_o^2} \frac{\alpha\{J_1(\alpha r_o)Y_2(\alpha r_i) - Y_1(\alpha r_o)J_2(\alpha r_i)\}}{\{J_1(\alpha r_o)Y_1(\alpha r_i) - Y_1(\alpha r_o)J_1(\alpha r_i)\}}\eta^* \tag{4.3.30}$$

Complex viscosity obtained from a CSR controlled stress rheometer can be corrected for second order fluid inertia effects using the expression (Golden [21])

$$\eta^* = \eta_0^*\left[1 + B_1(\alpha_0 r_o)^2 + B_2(\alpha_0 r_o)^4\right] \tag{4.3.31}$$

where B_1 and B_2 are non-dimensional geometry dependent factors given by

$$B_1 = \frac{r_i^2}{2r_o^2}\left[\frac{\left(r_i^2 - 3r_o^2\right)}{4r_o^2} - \frac{r_o^2 \ln(r_i/r_o)}{\left(r_o^2 - r_i^2\right)}\right] \tag{4.3.32}$$

$$B_2 = \frac{r_i^2}{32r_o^2}\left[\frac{(7r_o^2 - r_i^2)(r_o^2 - r_i^2)}{6r_o^4} - \frac{4r_i^2 \ln(r_i/r_o)}{(r_o^2 - r_i^2)}\left\{1 + \frac{2r_o^2 \ln(r_i/r_o)}{(r_o^2 - r_i^2)}\right\}\right] \tag{4.3.33}$$

The difference in complex viscosity data obtained from the Weissenberg rheogoniometer fitted with a strain gauge torsion head and the CSR controlled stress rheometer will be demonstrated by simulating the oscillatory shear flow behaviour of a Newtonian fluid and a single element Maxwell fluid in the concentric cylinder geometry on

each instrument. The simulated data, presented in chapter 5, will also used to establish the frequency range of applicability of the respective second order fluid inertia corrections given in equations (4.3.29) and (4.3.31).

4.4 Cone and plate geometry

4.4.1 Governing equations

With reference to a set of spherical polar coordinates (r,θ,φ) a viscoelastic fluid occupies the region between a cone of semi-vertical angle θ_c and a flat circular plate as shown in figure 4.3. The plate and the cone base are coaxial and both have radius a. As seen in figure 4.3 the tip of the cone is truncated to prevent contact between the cone and the plate. We denote the small angle between the cone and the plate by $\theta_0 = (\pi/2 - \theta_c)$. The plate is forced to perform small amplitude angular oscillations of amplitude ψ_2 and frequency f (cycles/sec) about the z-axis. The resulting motion of the fluid causes the cone, which is constrained by a torsion bar of stiffness K, to perform small amplitude oscillations of amplitude ψ_1 with a phase lag c behind the motion of the plate. It is assumed that the amplitude of oscillation of the driven plate is sufficiently small to ensure that the flow is in the linear viscoelastic region and hence non-linear fluid inertia terms can be neglected in the relevant equations of motion. On neglecting edge effects we assume a velocity distribution, which satisfies the equation of continuity for incompressible fluids, of the form

$$v_r = 0 \quad , \quad v_\theta = 0 \quad , \quad v_\varphi = f(r,\theta)\, e^{i\omega t} \tag{4.4.1}$$

where $\omega = 2\pi f$ (radians/sec) is the angular frequency of oscillation and the real part of these quantities is implied.

This velocity distribution gives two non-zero components of the shear stress tensor as

$$\tau_{\theta\varphi} = \frac{\eta^*}{r}\left[\frac{\partial f(r,\theta)}{\partial\theta} - \cot\theta\, f(r,\theta)\right]e^{i\omega t} \tag{4.4.2}$$

$$\tau_{\varphi r} = \eta^*\left[\frac{\partial f(r,\theta)}{\partial r} - \frac{f(r,\theta)}{r}\right]e^{i\omega t} \tag{4.4.3}$$

where η^* is the complex viscosity of the fluid.

Substituting equations (4.4.1) to (4.4.3) into the relevant stress equations of motion (Bird *et al* [11]) and noting that the flow is axi-symmetric we obtain the second order partial differential equation

$$\frac{1}{r^2}\frac{\partial}{\partial r}\left(r^2\frac{\partial f(r,\theta)}{\partial r}\right) + \frac{1}{r^2\sin\theta}\frac{\partial}{\partial\theta}\left(\sin\theta\frac{\partial f(r,\theta)}{\partial\theta}\right) - \frac{f(r,\theta)}{r^2\sin^2\theta} + \alpha^2 f(r,\theta) = 0 \tag{4.4.4}$$

where α^2 is defined in equation (4.2.4)

On considering equation (4.4.1) it can be shown that the function $f(r,\theta)$ is subject to the boundary conditions

$$f(r,\theta_c) = r i\omega\psi_1 \sin\theta_c \tag{4.4.5}$$

$$f(r,\pi/2) = r i\omega\psi_2 e^{ic} \tag{4.4.6}$$

Using the separation of variables method a general solution of equation (4.4.4) has been obtained by Nally [18] as

$$f(r,\theta) = r^{-1/2}\sum_{n=1}^{\infty}\left[A_n P_n^1(\cos\theta) + B_n Q_n^1(\cos\theta)\right]J_{n+1/2}(\alpha r) \tag{4.4.7}$$

where $P_n^1(\cos\theta)$ and $Q_n^1(\cos\theta)$ are associated Legendre functions of the first and second kind respectively of degree n and order 1 and $J_{n+1/2}(\alpha r)$ is a Bessel function of the first kind of order $(n+1/2)$. In equation (4.4.7) A_n and B_n are arbitrary constants to be determined from the boundary conditions in equations (4.4.5) and (4.4.6).

From Watson [22] a series expansion for $(\alpha r)^{3/2}$ can be expressed in the form

$$(\alpha r)^{3/2} = \sum_{n=1,3,..}^{\infty} a_n J_{n+1/2}(\alpha r) \tag{4.4.8}$$

In this equation the coefficients a_n are given by

$$a_n = \frac{2^{3/2}(n+1/2)\Gamma(1+n/2)}{((n-1)/2)!} \tag{4.4.9}$$

where Γ is the Gamma function (Abramowitz and Stegun [23]).

Using equations (4.4.6) and (4.4.8) the boundary condition for the plate can be expressed as

$$f(r,\pi/2) = r^{-1/2}\alpha^{-3/2} i\omega\psi_2 e^{ic} \sum_{n=1,3,..}^{\infty} a_n J_{n+1/2}(\alpha r) \tag{4.4.10}$$

Similarly the boundary condition for the cone can be written in the form

$$f(r,\theta_c) = r^{-1/2}\alpha^{-3/2} i\omega\psi_1 \sin\theta_c \sum_{n=1,3,..}^{\infty} a_n J_{n+1/2}(\alpha r) \tag{4.4.11}$$

On using equations (4.4.10) and (4.4.11) with the general solution in equation (4.4.7) the constants A_n and B_n are given by

$$A_n = B_n = 0 \qquad \text{for } n \text{ even} \tag{4.4.12}$$

$$A_n = \frac{a_n i\omega}{\alpha^{3/2}}\left[\frac{\psi_2 e^{ic} Q_n^1(\cos\theta_c) - \sin\theta_c\, \psi_1 Q_n^1(\cos\pi/2)}{P_n^1(\cos\pi/2)Q_n^1(\cos\theta_c) - P_n^1(\cos\theta_c)Q_n^1(\cos\pi/2)}\right] \qquad \text{for } n \text{ odd} \tag{4.4.13}$$

$$B_n = \frac{a_n i\omega}{\alpha^{3/2}}\left[\frac{\sin\theta_1\, \psi_1 P_n^1(\cos\pi/2) - \psi_2 e^{ic} P_n^1(\cos\theta_c)}{P_n^1(\cos\pi/2)Q_n^1(\cos\theta_c) - P_n^1(\cos\theta_c)Q_n^1(\cos\pi/2)}\right] \qquad \text{for } n \text{ odd} \tag{4.4.14}$$

Hence the general solution in equation (4.4.7) becomes

$$f(r,\theta) = r^{-1/2} \sum_{n=1,3,..}^{\infty} \left[A_n P_n^1(\cos\theta) + B_n Q_n^1(\cos\theta)\right] J_{n+1/2}(\alpha r) \tag{4.4.15}$$

where A_n and B_n are given in equations (4.4.13) and (4.4.14) respectively.

The equation of motion of the cone can be expressed as

$$C_F = (K - I\omega^2)\psi_1 e^{i\omega t} \tag{4.4.16}$$

where C_F is the torque exerted on the cone due to the motion of the fluid and I is the

moment of inertia of the member constrained by the torsion bar.

The torque C_F exerted on the cone due to the motion of the fluid is given by

$$C_F = 2\pi \sin^2\theta_c \int_0^a r^2 \tau_{\theta\varphi}\Big|_{\theta=\theta_c} dr \tag{4.4.17}$$

Abramowitz and Stegun [23] give the result

$$\frac{d}{d\theta} P_n^1(\cos\theta) - \cot\theta\, P_n^1(\cos\theta) = P_n^2(\cos\theta) \tag{4.4.18}$$

Substituting equations (4.4.13) to (4.4.15) into equation (4.4.2) and using equation (4.4.18) we have

$$\tau_{\theta\varphi}\Big|_{\theta=\theta_c} = \eta^* i\omega\, \psi_1 (\alpha r)^{-3/2} \sum_{n=1,3,..}^{\infty} a_n \left[D_n \frac{\psi_2}{\psi_1} e^{ic} - F_n \right] e^{i\alpha t} \tag{4.4.19}$$

where D_n and F_n are given by

$$D_n = \frac{Q_n^1(\cos\theta_c)\, P_n^2(\cos\theta_c) - P_n^1(\cos\theta_c)\, Q_n^2(\cos\theta_c)}{P_n^1(\cos\pi/2)\, Q_n^1(\cos\theta_c)} \tag{4.4.20}$$

$$F_n = -\frac{Q_n^2(\cos\theta_c)}{Q_n^1(\cos\theta_c)} \sin\theta_c \tag{4.4.21}$$

On using equations (4.4.16), (4.4.17) and (4.4.19) the equation of motion of the cone can be expressed as

$$\frac{e^{ic}}{\vartheta} \sum_{n=1,3,..}^{\infty} a_n D_n \beta_n = -\frac{iS}{\eta^*} \frac{1}{M} + \sum_{n=1,3,..}^{\infty} a_n F_n \beta_n \tag{4.4.22}$$

where

$$M = \frac{3\,\theta_0 \sin^2\theta_c}{a^3} \tag{4.4.23}$$

$$\beta_n = \alpha^{-3/2} \int_0^a r^{1/2} J_{n+1/2}(\alpha r)\, dr \tag{4.4.24}$$

S is a geometrical parameter given by

$$S = \frac{3\,\theta_0 (K - I\omega^2)}{2\pi a^3 \omega} \tag{4.4.25}$$

and $\vartheta\,(=\psi_1/\psi_2)$ is defined as the amplitude ratio.

If an oscillatory shear experiment is performed on a Weissenberg rheogoniometer the angular frequency ω, amplitude ratio ϑ, phase lag c and geometrical parameter S will all be known. Therefore in theory α, and hence the complex viscosity η^*, can be obtained by solving equation (4.4.22). A full solution to this equation, which includes full fluid inertia effects, can be obtained using a suitable numerical iterative technique. However equation (4.4.22) has multiple solutions and therefore iterative methods cannot be guaranteed to give convergence to the correct solution. We shall therefore solve this equation using a perturbation method which will be valid for the case when fluid inertia effects are small and the cone angle is small ($\theta_0 \leq 4^\circ$). Formulae will be produced from the perturbation theory which can be incorporated into the rheogoniometer software to provide an on line correction of cone and plate complex viscosity data for first and second order fluid inertia effects.

4.4.2 Perturbation method of solution to predict complex viscosity

In order to solve equation (4.4.22) using a perturbation method, we must express this equation in the form of a power series expansion in terms of the non-dimensional quantity $(\alpha a)^2$. On working to second order terms in the non-dimensional quantity $(\alpha a)^2$ we consider an expansion of equation (4.4.22) in the form

$$\frac{e^{ic}}{\vartheta}\left[b_0 + b_2(\alpha a)^2 + b_4(\alpha a)^4 + \ldots\right] = -\frac{iS}{\eta^*}\frac{1}{M} + \left[c_0 + c_2(\alpha a)^2 + c_4(\alpha a)^4 + \ldots\right] \qquad (4.4.26)$$

where the coefficients b_i and c_i for $i = 0, 2, 4$ are to be determined.

From equations (4.4.20) to (4.4.25) it can be seen that α only appears within the β_n terms. We therefore consider a Taylor series expansion for β_n in terms of the non-dimensional quantity $(\alpha a)^2$ about the point $\alpha a = 0$. Up to terms of order $(\alpha a)^4$ we have

$$\beta_1 = a^3\sqrt{\frac{2}{\pi}}\left[\frac{1}{9} - \frac{1}{150}(\alpha a)^2 + \frac{1}{5880}(\alpha a)^4\right] \tag{4.4.27}$$

$$\beta_3 = a^3\sqrt{\frac{2}{\pi}}\left[\frac{1}{525}(\alpha a)^2 - \frac{1}{13230}(\alpha a)^4\right] \tag{4.4.28}$$

$$\beta_5 = a^3\sqrt{\frac{2}{\pi}}\left[\frac{1}{72765}(\alpha a)^4\right] \tag{4.4.29}$$

It should be noted that since we are only considering terms up to order $(\alpha a)^4$ we have $\beta_n = 0$ for $n \geq 7$. Therefore only the first three terms ($n = 1, 3, 5$) need to be considered in equation (4.4.22). On considering equation (4.4.22) and equations (4.4.27) to (4.4.29) the coefficients b_i and c_i (for $i = 0, 2, 4$) in equation (4.4.26) are given by

$$b_0 = a^3\sqrt{2/\pi}\,(1/9a_1 D_1)$$

$$c_0 = a^3\sqrt{2/\pi}\,(1/9a_1 F_1)$$

$$b_2 = a^3\sqrt{2/\pi}\,(-1/150a_1 D_1 + 1/525a_3 D_3)$$

$$c_2 = a^3\sqrt{2/\pi}\,(-1/150a_1 F_1 + 1/525a_3 F_3)$$

$$b_4 = a^3\sqrt{2/\pi}\,(1/5870a_1 D_1 - 1/13230a_3 D_3 + 1/72765a_5 D_5)$$

$$c_4 = a^3\sqrt{2/\pi}\,(1/5870a_1 F_1 - 1/13230a_3 F_3 + 1/72765a_5 F_5) \tag{4.4.30}$$

Substituting these coefficients into equation (4.4.26) and expanding the resulting equation as a Taylor series in terms of the small cone angle θ_0 about the angle $\theta_0 = 0$ gives

$$\frac{e^{ic}}{\vartheta} = 1 - \frac{iS}{\eta^*}A - \left[B - \frac{iS}{\eta^*}C\right](\alpha a)^2 + \left[D - \frac{iS}{\eta^*}E\right](\alpha a)^4 \tag{4.4.31}$$

where terms of order $(\alpha a)^6$ and higher have been neglected.

In this equation A, B, C, D and E are non-dimensional geometry dependent constants given by

$$A = 1 + \frac{1}{2}\theta_0^2 + \frac{11}{4}\theta_0^4 \qquad B = \frac{3}{10}\theta_0^2 + \frac{1}{10}\theta_0^4$$

$$C = \frac{1}{10}\theta_0^2 + \frac{53}{300}\theta_0^4 \qquad D = \frac{17}{1400}\theta_0^4$$

$$E = \frac{1}{600}\theta_0^4 \tag{4.4.32}$$

where terms of order θ_0^6 and higher are considered small enough to be neglected.

The equation of motion of the cone when fluid inertia effects are ignored is obtained from equation (4.4.31) by setting $\alpha = 0$ and replacing η^* with η_0^*, the complex viscosity when fluid inertia effects are ignored, to give

$$\frac{e^{ic}}{\vartheta} = 1 - \frac{iS}{\eta_0^*}A \tag{4.4.33}$$

For a cone of small angle $(\theta_0 \leq 4°)$, terms of order θ_0^2 and higher in the non-dimensional geometry dependent constant A are considered small enough to be neglected (*i.e.* $A = 1$). Therefore the equation of motion of the cone when fluid inertia effects are ignored reduces to equation (4.2.16), where the geometrical parameter S is defined by equation (4.4.25). The complex viscosity η_0^*, when fluid inertia effects are ignored, can then be calculated for the cone and plate geometry by using equation (4.2.17) with S defined in equation (4.4.25).

Using equations (4.4.31), (4.4.33) and the definition of α_0^2 in equation (4.2.20) we obtain a relationship between η_0^* and η^* given by

$$-\frac{iS}{\eta_0^*}A = -\frac{iS}{\eta^*}A - \frac{\eta_0^*}{\eta^*}\left[B - \frac{iS}{\eta^*}C\right](\alpha_0 a)^2 + \frac{\eta_0^{*2}}{\eta^{*2}}\left[D - \frac{iS}{\eta^*}E\right](\alpha_0 a)^4 \tag{4.4.34}$$

In order to determine an expression for η^* in terms of η_0^* from this equation we expand η^* as a second order power series in the non-dimensional parameter $(\alpha_0 a)^2$ given by

$$\eta^* = \eta_0^* + (\alpha_0 a)^2 \eta_1^* + (\alpha_0 a)^4 \eta_2^* \tag{4.4.35}$$

On substitution of equation (4.4.35) into equation (4.4.34) we obtain

$$-\frac{iS}{\eta_o^*}A = -\frac{iS}{\eta_0^*}A - \left[B - \frac{iS}{\eta_0^*}\left\{C + \frac{\eta_1^*}{\eta_0^*}\right\}\right](\alpha_0 a)^2$$

$$+\left[D + B\frac{\eta_1^*}{\eta_0^*} - \frac{iS}{\eta_0^*}\left\{E - 2C\frac{\eta_1^*}{\eta_0^*} - \frac{\eta_1^{*2}}{\eta_0^{*2}} + \frac{\eta_2^*}{\eta_0^*}\right\}\right](\alpha_0 a)^4 \qquad (4.4.36)$$

where terms of order $(\alpha_0 a)^6$ and higher have been neglected.

The coefficients of the $(\alpha_0 a)^2$ and $(\alpha_0 a)^4$ terms in equation (4.4.36) are of identical form to the coefficients of the $(\alpha_0 r_o)^2$ and $(\alpha_0 r_o)^4$ terms in equation (4.3.22) for the concentric cylinder geometry. Hence in equation (4.4.35) η_1^* and η_2^* are given by equations (4.3.23) and (4.3.24) respectively, where the non-dimensional geometry dependent constants B, C, D and E are now defined by equation (4.4.32). Substituting these expressions for η_1^* and η_2^* into equation (4.4.35) and using equation (4.4.32) gives

$$\eta^* = \eta_0^*\left[1 - \theta_0^2\left\{\frac{1}{10} + \frac{i\eta_0^*}{S}\frac{3}{10}\right\}(\alpha_0 a)^2 - \theta_0^4\left\{\frac{1}{120} + \frac{i\eta_0^*}{S}\frac{1}{56}\right\}(\alpha_0 a)^4\right] \qquad (4.4.37)$$

In forming this equation terms of order θ_0^4 and higher in the coefficient of the $(\alpha_0 a)^2$ term are considered small enough to be neglected. Similarly terms of order θ_0^6 and higher are considered small enough to be neglected in the coefficient of the $(\alpha_0 a)^4$ term. On using equation (4.2.20) we can express equation (4.4.37) as

$$\eta^* = \eta_0^* + i\rho\omega a^2\theta_0^2\left\{\frac{1}{10} + \frac{i\eta_0^*}{S}\frac{3}{10}\right\} + \frac{\rho^2\omega^2 a^4\theta_0^4}{\eta_0^*}\left\{\frac{1}{120} + \frac{i\eta_0^*}{S}\frac{1}{56}\right\} \qquad (4.4.38)$$

Equation (4.4.38) is the formula for calculating the complex viscosity of a fluid which corrects for first and second order fluid inertia effects. In this equation it should be noted that, for small cone angles ($\theta_0 \le 4°$), η_0^* is known from equation (4.2.17) where the geometrical parameter S is defined by equation (4.4.25). It is also noted that the formulae in equations (4.2.18) and (4.2.19), to calculate the zero order dynamic viscosity η_0' and

dynamic rigidity G_0' respectively, can be used for the cone and plate geometry with the geometrical parameter S defined by equation (4.4.25). In order to establish the limitations of the second order fluid inertia perturbation theory we shall simulate the oscillatory shear flow behaviour of a Newtonian fluid and a single element Maxwell fluid in the cone and plate geometry. This oscillatory shear flow simulation will be presented in chapter 5.

4.4.3 Complex viscosity prediction for a strain gauge torsion head system on the Weissenberg rheogoniometer

On a Weissenberg rheogoniometer instead of constraining the cone with a torsion bar it is possible to connect the cone to a strain gauge torsion head. As before we consider the strain gauge to have infinite stiffness ($K = \infty$) and therefore the geometrical parameter S defined in equation (4.4.25) will be infinite. For this type of oscillatory shear flow a relationship between η_0^* and η^* is obtained by combining equations (4.4.22) and (4.4.33) (with $A = 1$) and setting $S = \infty$ to give

$$\eta_0^* = \eta^* M \sum_{n=1,3,\ldots}^{\infty} a_n D_n \beta_n \tag{4.4.39}$$

Setting $S = \infty$ in equation (4.4.37) gives the second order fluid inertia correction formula for complex viscosity data obtained using a strain gauge torsion head as

$$\eta^* = \eta_0^* \left[1 - \frac{1}{10}(\alpha_0 a \theta_0)^2 - \frac{1}{120}(\alpha_0 a \theta_0)^4 \right] \tag{4.4.40}$$

If the stiffness of the strain gauge is considered to be infinite we have the flow situation where the plate oscillates with small amplitude at a prescribed frequency and the cone is stationary. This is similar to cone and plate oscillatory shear flow on a CSR controlled stress rheometer, where the cone oscillates with small amplitude and the plate is stationary. Oscillatory shear flow on a CSR controlled stress rheometer is now considered for comparison purposes.

4.4.4 Complex viscosity prediction for a CSR controlled stress rheometer

On a CSR controlled stress rheometer an oscillatory torque of amplitude C_0 and frequency f is applied to the cone forcing, it to make small amplitude oscillations of amplitude X_0 with a phase lag c behind the applied torque. The plate remains stationary. An equation of motion for the cone is determined by considering the torque exerted on the cone due to the motion of the fluid. The equations for cone and plate oscillatory shear flow on a CSR controlled stress rheometer are given by Golden [21]. On using these equations we obtain a relationship between η_0^* and η^* as

$$\eta_0^* = \eta^* M \sum_{n=1,3,..}^{\infty} a_n F_n \beta_n \tag{4.4.41}$$

where a_n, F_n, M and β_n are defined in equations (4.4.9), (4.4.21), (4.4.23) and (4.4.24) respectively.

An expression to correct complex viscosity data obtained from a CSR controlled stress rheometer for second order fluid inertia effects is given by Golden [21] as

$$\eta^* = \eta_0^* \left[1 + \frac{1}{5}(\alpha_0 a\theta_0)^2 + \frac{1}{105}(\alpha_0 a\theta_0)^4 \right] \tag{4.4.42}$$

In chapter 5 the difference in complex viscosity predictions obtained from the Weissenberg rheogoniometer fitted with a strain gauge and the CSR controlled stress rheometer will be demonstrated by simulating the oscillatory shear flow behaviour of a Newtonian fluid and a single element Maxwell in the cone and plate geometry on each instrument. The simulated data is also used to establish the frequency range of applicability of the respective second order fluid inertia corrections given in equations (4.4.40) and (4.4.42).

4.5 Inaccuracies in complex viscosity predictions near the natural frequency of the constrained member

The member constrained by the torsion bar has a natural angular frequency of oscillation denoted ω_0. When subjected to a displacement and released this member will oscillate freely at the natural frequency which is equal in magnitude to the quantity $\sqrt{K/I}$. At the natural frequency ω_0 we therefore have $(K - I\omega^2) = 0$ and hence for all three geometries considered the geometrical parameter S is equal to zero. As an example we consider the equations for the parallel plate geometry when $\omega = \omega_0$.

From equation (4.2.12) it can be seen that at the natural frequency the equation of motion of the upper plate reduces to

$$\frac{e^{ic}}{\vartheta} = \cos(\alpha h) \qquad (4.5.1)$$

Therefore for parallel plate oscillatory shear flows in which fluid inertia effects are small ($i.e.\ \alpha h \approx 0$) we have $e^{ic}/\vartheta \approx 1$ at the natural frequency. The complex viscosity η_0^*, when fluid inertia effects are ignored, is calculated using the value of the geometrical parameter S and the measured quantity e^{ic}/ϑ in equation (4.2.17). At the natural frequency ω_0 the right hand side of this equation is not defined and hence η_0^* cannot be determined at this frequency. For frequencies of oscillation close to the natural frequency we will also obtain $S \approx 0$ and $e^{ic}/\vartheta \approx 1$ and hence small errors in these quantities can lead to large errors in complex viscosity predictions (Walters [3]).

4.6 Comments

Second order fluid inertia corrections have been produced for complex viscosity data obtained using a strain gauge torsion head on the Weissenberg rheogoniometer. When a strain gauge torsion head is used, it is assumed in the oscillatory shear theory that the

upper platen of the geometry is stationary as the lower platen performs small amplitude oscillations. This is in contrast to the oscillatory shear flow conditions on a CSR controlled stress rheometer where the upper platen of the geometry performs small amplitude oscillations and the lower platen is stationary. It has previously been noted that the torque is measured on the stationary platen on the Weissenberg rheogoniometer whereas on the CSR rheometer the torque is measured on the moving plate. For a given fluid and geometry there will be a difference between the complex viscosity η_0^*, when fluid inertia effects are ignored, obtained from each instrument. It has also been noted that for a given geometry the second order fluid inertia corrections for each instrument are different. However a relationship, which applies for all three geometries, has been observed between the second order corrections for the two instruments.

For all three geometries, on both instruments, the second order fluid inertia corrections are expressed as a power series in terms of a non dimensional parameter that we shall denote by N. Note that the non dimensional parameter N is equal to $(\alpha_0 h)$, $(\alpha_0 r_o)$ and $(\alpha_0 a \theta_0)$ for the parallel plate, concentric cylinder and cone and plate geometries respectively. When the upper platen is constrained by a strain gauge on the Weissenberg rheogoniometer the second order fluid inertia corrections, for all three geometries, can be expressed in the form

$$\eta^* = \eta_0^* \left[1 + W_1 N^2 + W_2 N^4\right] \tag{4.6.1}$$

where W_1 and W_2 are non-dimensional geometry dependent factors.

Similarly on the CSR controlled stress rheometer the second order fluid inertia corrections, for all three geometries, can be expressed as

$$\eta^* = \eta_0^* \left[1 + C_1 N^2 + C_2 N^4\right] \tag{4.6.2}$$

where C_1 and C_2 are non-dimensional geometry dependent factors.

From the fluid inertia corrections previously determined it can be seen that for both the parallel plate and cone and plate geometries we have $W_1/C_1 = -1/2$ and $W_2/C_2 = -7/8$. Furthermore on considering a very narrow gap concentric cylinder geometry we obtain $\lim_{r_i \to r_o} W_1/C_1 = -1/2$ and $\lim_{r_i \to r_o} W_2/C_2 = -7/8$. It should be emphasised that for a given geometry the value of η_0^*, and hence the value of N in equations (4.6.1) and (4.6.2), which is obtained from each instrument will be different. However the W_1/C_1 and W_2/C_2 ratios indicate that a relationship, which applies for all three geometries, exists between the second order fluid inertia corrections on each instrument.

CHAPTER 5

SIMULATION OF OSCILLATORY SHEAR FLOW ON A WEISSENBERG RHEOGONIOMETER AND A CSR CONTROLLED STRESS RHEOMETER

5.1 Introduction

In this chapter we simulate the small amplitude oscillatory shear flow behaviour of theoretical model fluids, for which the complex viscosity and density are known, on a Weissenberg rheogoniometer. Simulations are performed for the parallel plate, concentric cylinder and cone and plate geometries.

For a Newtonian fluid and a single element Maxwell fluid the complex viscosity of the fluid is given by $\eta^* = \eta_0$ and $\eta^* = \eta_0/(1+i\lambda\omega)$ respectively, where η_0 is the Newtonian viscosity and λ is the relaxation time. The complex viscosity of these theoretical model fluids will be referred to as the exact viscosity data throughout this chapter. At a prescribed frequency of oscillation the amplitude ratio ϑ and phase lag c for the theoretical model fluids can be calculated analytically. Using these calculated values the complex viscosity η_0^* when fluid inertia effects are ignored can be analytically determined. This complex viscosity data is equivalent to the data that would be obtained from the rheogoniometer software which ignores fluid inertia effects. On comparing the analytically simulated η_0^* data with the exact viscosity data for the theoretical model fluids we can establish the influence of fluid inertia effects on complex viscosity predictions. The complex viscosity prediction can be corrected for first and second order fluid inertia effects using the correction formulae determined in chapter 4. Since the exact viscosity data is known we can consider the frequency range of applicability of the second order fluid inertia corrections for the theoretical model fluids. In this chapter we shall discuss both complex viscosity data

corrected for first order fluid inertia effects and complex viscosity data corrected for second order fluid inertia effects. It should be noted that if data is corrected for second order fluid inertia effects then it is implied that first order fluid inertia effects are also included.

For each geometry the simulations will be performed for the oscillatory shear flow situations where the upper platen is constrained by a torsion bar and the upper platen is connected to a strain gauge torsion head. Simulations are also considered for the oscillatory shear flow of a Newtonian fluid and a single element Maxwell fluid on the CSR controlled stress rheometer. The complex viscosity data obtained from these simulations will be compared to the corresponding simulated data obtained for a Weissenberg rheogoniometer with the upper platen connected to a strain gauge torsion head.

5.2 Parallel plate geometry constrained by a torsion bar

We simulate the oscillatory shear flow behaviour of a Newtonian fluid and a single element Maxwell fluid in the parallel plate geometry where the upper plate is constrained by a torsion bar. At a prescribed angular frequency of oscillation ω the known fluid parameters (η^*, ρ) and geometry parameters (a, h, I, K) can be used in equation (4.2.12) to evaluate the expression e^{ic}/ϑ analytically. On using this value in equation (4.2.17) the complex viscosity η_0^*, when fluid inertia effects are ignored, is then known. It is noted that this simulated complex viscosity data is equivalent to the data obtained when the rheogoniometer software does not include fluid inertia effects. The simulated η_0^* data can then be used in equation (4.2.27) to correct the complex viscosity prediction for first and second order fluid inertia effects.

For the simulations we consider a parallel plate geometry in which the coaxial plates have radius $a = 37 \cdot 5\,\text{mm}$ and are separated by a vertical distance $h = 500\,\mu m$. The upper plate is constrained by a torsion bar of stiffness $K = 5 \cdot 005\,\text{Nm/rad}$ and the member

constrained by this torsion bar has moment of inertia $I = 164\ \mu\text{Ns}^2$. For these values of K and I the member constrained by the torsion bar will have a natural angular frequency of $\omega_0 = 174 \cdot 695\ \text{rad/s}$.

5.2.1 Newtonian fluids

For a given parallel plate geometry and torsion bar (*i.e.* a, h, I, K known) it can be shown that the normalised complex viscosity (η^*/η_0) of a Newtonian fluid can be represented as a function of the two non-dimensional quantities $R\,(=\rho h^2\omega_0/\eta_0)$ and the normalised frequency (ω/ω_0). We simulate the oscillatory shear flow behaviour of Newtonian fluids over the angular frequency range $0 < \omega < 2\omega_0$.

In figures 5.1 and 5.2 we present fluid inertia corrections for simulated dynamic viscosity and dynamic rigidity data respectively of a Newtonian fluid when $R = 2$. The uncorrected data in these figures is obtained from the standard formula (equation (4.2.17)) in which fluid inertia effects are ignored. Figures 5.1 and 5.2 also include data corrected for first order fluid inertia effects and data corrected for second order fluid inertia effects. It is seen in figure 5.1 that the first order fluid inertia correction for dynamic viscosity gives very little improvement in accuracy over the uncorrected data. However when corrected for second order fluid inertia effects, good agreement is obtained with the exact dynamic viscosity data over the full normalised frequency range considered. Figure 5.2 shows an apparent positive dynamic rigidity when fluid inertia effects are ignored and an apparent negative dynamic rigidity when fluid inertia effects are included in the theory. It should be noted that in this figure a more accurate prediction of the dynamic rigidity is obtained when the data is only corrected for first order fluid inertia effects. Correcting for second order fluid inertia effects increases the error in the dynamic rigidity prediction. Therefore for Newtonian fluids higher order fluid inertia terms may need to be considered in order to

obtain improved dynamic rigidity predictions. This will be discussed in section 5.8. In figure 5.2 it is seen that the first order fluid inertia correction and the second order fluid inertia correction give good agreement with the exact dynamic rigidity data up to normalised frequencies of 1 and 0·6 respectively. It is noted that in figure 5.1, the corresponding second order fluid inertia correction for dynamic viscosity data gives good agreement with the exact data over the full normalised frequency range considered.

We now consider the normalised frequency range of applicability of the second order fluid inertia corrections for various values of the non-dimensional quantity R. The dynamic viscosity and dynamic rigidity corrections are presented in figures 5.3 and 5.4 respectively. It can be seen in figure 5.3 that when R has a value below 8 good agreement is obtained with the exact dynamic viscosity data up to normalised frequencies of 0·7. However the corresponding dynamic rigidity data in figure 5.4 shows that when R has a value below 8 good agreement with the exact data is only obtained up to a normalised frequency of 0·2. If R has a value below 2 then the dynamic viscosity data is in good agreement with the exact data up to a normalised frequency of 2, whereas the corresponding dynamic rigidity data only gives good agreement for normalised frequencies below 1. In figures 5.3 and 5.4 it is seen that for all values of R, the second order fluid inertia correction for dynamic viscosity gives good agreement with the exact data up to a higher normalised frequency than the corresponding correction for dynamic rigidity.

5.2.2 Single element Maxwell fluids

For a given parallel plate geometry and torsion bar (*i.e.* a, h, I, K known) it can be shown that the normalised complex viscosity (η^*/η_0) of a single element Maxwell fluid, with a specific relaxation time λ, can be represented as a function of the two non-dimensional quantities $R(=\rho h^2\omega_0/\eta_0)$ and the normalised frequency (ω/ω_0). We

consider the oscillatory shear flow behaviour of single element Maxwell fluids over the frequency range $0 < \omega < 2\omega_0$ and choose the relaxation time λ such that $\lambda\ \omega_0 = 1$.

In figures 5.5 and 5.6 we present fluid inertia corrections for simulated dynamic viscosity and dynamic rigidity data respectively of a single element Maxwell fluid when $R = 1$. In these figures we present the uncorrected data (obtained from equation (4.2.17)), data corrected for first order fluid inertia effects and data corrected for second order fluid inertia effects. It is seen in figure 5.5 that first and second order fluid inertia effects are not very significant in dynamic viscosity predictions, except when close to the natural frequency ($\omega/\omega_0 = 1$). However the corresponding dynamic rigidity data in figure 5.6 shows that both first order and second order fluid inertia effects are important in dynamic rigidity predictions. In this figure it is seen that the first order fluid inertia correction gives good agreement with the exact dynamic rigidity data up to normalised frequencies of 0·6 and correcting for second order fluid inertia effects gives good agreement up to a normalised frequency of 1·2.

We now consider the normalised frequency range of applicability of the second order fluid inertia corrections for various values of the non-dimensional quantity R. The dynamic viscosity and dynamic rigidity corrections are presented in figures 5.7 and 5.8 respectively. It can be seen in these figures that when R has a value below 4 good agreement with the exact data is obtained up to normalised frequencies of 0·3. However if R has a value below 1 then good agreement is obtained with the exact data up to a normalised frequency of 1·6. In figures 5.7 and 5.8 it is seen that for all values of R the second order fluid inertia corrections for dynamic viscosity and dynamic rigidity both give agreement with the exact data up to approximately the same normalised frequency. It should be noted that this was not the case for Newtonian fluids where the second order fluid inertia correction for dynamic viscosity data is valid up to higher normalised frequencies than the

corresponding correction for dynamic rigidity data.

5.3 Parallel plate geometry connected to a strain gauge torsion head

We simulate the oscillatory shear flow behaviour of a Newtonian fluid and a single element Maxwell fluid in the parallel plate geometry, where the upper plate is connected to a strain gauge torsion head. It is noted that when a strain gauge torsion head is used the upper plate is assumed to be stationary. For comparison purposes the oscillatory shear flow behaviour of a Newtonian fluid and a single element Maxwell fluid is also simulated for the parallel plate geometry on a CSR controlled stress rheometer. At a prescribed lower plate angular frequency of oscillation ω the known fluid parameters (η^*, ρ) and the geometry parameters (a, h) can be used in equation (4.2.28) and the complex viscosity η_0^*, when fluid inertia effects are ignored, is then known. Similarly at a prescribed upper plate angular frequency of oscillation ω the known geometry and fluid parameters can be used in equation (4.2.30) and the complex viscosity η_0^*, when fluid inertia effects are ignored, for a CSR controlled stress rheometer is also known. Using the two sets of simulated η_0^* data and the exact viscosity data the influence of fluid inertia effects on complex viscosity predictions for each instrument can be compared. The simulated η_0^* data can be used to correct the complex viscosity prediction for first and second order fluid inertia effects using equations (4.2.29) and (4.2.31) respectively. Therefore the frequency range of applicability of the second order fluid inertia corrections given in equations (4.2.29) and (4.2.31) can be established for the theoretical model fluids.

As before we consider a parallel plate geometry in which the coaxial plates have radius $a = 37 \cdot 5$ mm and are separated by a vertical distance $h = 500\,\mu m$.

5.3.1 Newtonian fluids

For a Newtonian fluid in a given parallel plate geometry (*i.e.* a, h known) it can be shown that, on both the Weissenberg rheogoniometer fitted with a strain gauge and the CSR controlled stress rheometer, the normalised complex viscosity (η^*/η_0) can be represented as a function of the non-dimensional normalised frequency ($= \rho h^2\omega/\eta_0$).

In figures 5·9 and 5·10 we present fluid inertia corrections for simulated dynamic viscosity and dynamic rigidity data respectively of a Newtonian fluid on both the Weissenberg rheogoniometer fitted with a strain gauge and the CSR controlled stress rheometer. These figures include, for both instruments, uncorrected data and data corrected for second order fluid inertia effects. It is noted that the uncorrected data in these figures is obtained from equations (4.2.28) and (4.2.30) for the Weissenberg rheogoniometer and the CSR controlled stress rheometer respectively. From equations (4.2.29) and (4.2.31) it can be seen that, for both instruments, the dynamic viscosity data is not influenced by first order fluid inertia effects. Therefore first order fluid inertia corrections are only presented for the dynamic rigidity data in figure 5.10. In figure 5.9 it is seen that the Weissenberg rheogoniometer dynamic viscosity data corrected for second order fluid inertia effects gives good agreement with the exact data up to a normalised frequency of 6. However in this figure the corresponding CSR controlled stress rheometer dynamic viscosity data corrected for second order fluid inertia effects is only in good agreement for normalised frequencies below 1·5. Figure 5.10 shows that when fluid inertia effects are ignored an apparent positive dynamic rigidity is obtained on the Weissenberg rheogoniometer and an apparent negative dynamic rigidity is obtained on the CSR controlled stress rheometer. In this figure it is also seen that the Weissenberg rheogoniometer second order fluid inertia correction for dynamic rigidity only gives good agreement with the exact data for normalised frequencies below 1·5, whereas the corresponding correction for the CSR controlled stress rheometer is in

good agreement up to a normalised frequency of 5. It is noted that the Weissenberg rheogoniometer dynamic rigidity data presented in figure 5.10 is more accurate if only first order fluid inertia effects are included. Correcting for second order fluid inertia effects introduces greater inaccuracies in the dynamic rigidity prediction. This behaviour is consistent with the results presented in figure 5.2 for Newtonian fluids where the parallel plate geometry is used with a torsion bar on the Weissenberg rheogoniometer. From the second order fluid inertia corrections presented in figures 5.9 and 5.10, it can be concluded that for dynamic viscosity predictions the Weissenberg rheogoniometer gives good agreement with the exact data up to higher normalised frequencies than the CSR controlled stress rheometer. However for dynamic rigidity predictions good agreement with the exact data is obtained up to higher normalised frequencies by the CSR controlled stress rheometer.

5.3.2 Single element Maxwell fluids

For a single element Maxwell fluid in a given parallel plate geometry (*i.e.* a and h known) it can be shown that, on both the Weissenberg rheogoniometer fitted with a strain gauge and the CSR controlled stress rheometer, the normalised complex viscosity (η^*/η_0) can be represented as a function of the two non-dimensional quantities $R\,(=\rho h^2/(\lambda\eta_0))$ and the Deborah number $De\,(=\lambda\omega)$.

In figures 5·11 and 5·12 we present fluid inertia corrections for simulated dynamic viscosity and dynamic rigidity data respectively of a single element Maxwell fluid when $R = 0\cdot5$. Data is presented for both the Weissenberg rheogoniometer fitted with a strain gauge torsion head and the CSR controlled stress rheometer. Figures 5.11 and 5.12 include, for both instruments, uncorrected data (obtained using equations (4.2.28) and (4.2.30)) and data corrected for second order fluid inertia effects. Dynamic rigidity data corrected for first

order fluid inertia effects is also presented in figure 5.12. It is seen in figure 5.11 that when fluid inertia effects are ignored the dynamic viscosity is underestimated by the Weissenberg rheogoniometer and overestimated by the CSR controlled stress rheometer. However it should be noted that the error in dynamic viscosity predictions when fluid inertia effects are ignored is relatively small over the Deborah number range considered. In figure 5.12 it is seen that when fluid inertia effects are ignored the dynamic rigidity is overestimated by the Weissenberg rheogoniometer and underestimated by the CSR controlled stress rheometer. The error in dynamic rigidity predictions when fluid inertia effects are ignored is significant and it is seen that, for both instruments, correcting for second order fluid inertia effects gives good agreement with the exact data up to Deborah numbers of 1·6. It is noted that for both instruments, the corresponding dynamic viscosity data corrected for second order fluid inertia effects is also in good agreement with the exact data up to Deborah numbers of 1.6, as shown in figure 5.11.

We now consider the Deborah number range of applicability of the second order fluid inertia corrections for various values of the non-dimensional quantity R, for both the Weissenberg rheogoniometer fitted with a strain gauge and the CSR controlled stress rheometer. The dynamic viscosity and dynamic rigidity corrections are presented in figures 5.13 and 5.14 respectively. It can be seen in these figures that when R has a value below 4 good agreement with the exact viscosity data is obtained up to Deborah numbers of 0·3 for both instruments. However if R has a value below 0·5 then good agreement is obtained with the exact viscosity data, for both instruments, up to Deborah numbers of 1·6.

5.4 Concentric cylinder geometry constrained by a torsion bar

The oscillatory shear flow behaviour of a Newtonian fluid and a single element Maxwell fluid is simulated in the concentric cylinder geometry, where the inner cylinder is

constrained by a torsion bar. At a prescribed outer cylinder angular frequency of oscillation ω the known fluid parameters (η^*, ρ) and the geometry parameters (r_i, r_o, h, I, K) can be used in equation (4.3.14) to evaluate the expression e^{ic}/ϑ analytically. On using this value in equation (4.2.17), where the geometrical parameter S is given by equation (4.3.15), the complex viscosity η_0^*, when fluid inertia effects are ignored, is then known. This value of η_0^* can then be used in equation (4.3.27) to obtain the complex viscosity prediction which includes first and second order fluid inertia effects.

For the simulations we consider a concentric cylinder geometry with the dimensions $r_i = 15\,\text{mm}$, $r_o = 20{\cdot}75\,\text{mm}$ and $h = 50\,\text{mm}$. This geometry is commercially available for the CSR controlled stress rheometer (TA Instruments [24]) and attachments have been manufactured, at the University of Plymouth, which enable it to be used on a Weissenberg rheogoniometer. For the concentric cylinder simulations we choose the moment of inertia of the member constrained by the torsion bar to be $I = 164\,\mu\text{Ns}^2$ and a torsion bar of stiffness $K = 5{\cdot}005\,\text{Nm/rad}$. It is noted that these values are identical to those used for the parallel plate geometry simulations and the natural frequency of the member constrained by the torsion bar is $\omega_0 = 174{\cdot}695\,\text{rad/s}$.

5.4.1 Newtonian fluids

For a given concentric cylinder geometry and torsion bar (*i.e.* r_i, r_o, h, I, K known) it can be shown that the normalised complex viscosity (η^*/η_0) of a Newtonian fluid can be represented as a function of the two non-dimensional quantities $R\,(=\rho r_i^2\omega_0/\eta_0)$ and the normalised frequency (ω/ω_0). As for the parallel plate simulations we consider the oscillatory shear flow behaviour of Newtonian fluids over the frequency range $0 < \omega < 2\omega_0$.

In figures 5.15 and 5.16 we present fluid inertia corrections for simulated dynamic

viscosity and dynamic rigidity data respectively of a Newtonian fluid when $R = 10$. The uncorrected data in these figures is obtained from equation (4.2.17) where the geometrical parameter S is defined by equation (4.3.15). Figures 5.15 and 5.16 also include data corrected for first order fluid inertia effects and data corrected for second order fluid inertia effects. It is seen in figure 5.16 that an apparent positive dynamic rigidity is obtained when fluid inertia effects are ignored and if first and second order fluid inertia effects are included in the theory we obtain an apparent negative dynamic rigidity, except near the natural frequency ($\omega/\omega_0 = 1$). The dynamic rigidity data corrected for second order fluid inertia effects gives good agreement with the exact data up to a normalised frequency of 0·6. However it is seen in figure 5.15 that the corresponding dynamic viscosity data corrected for second order fluid inertia effects is in good agreement with the exact data over the full normalised frequency range considered. It is noted that in figure 5.16 the dynamic rigidity data corrected for first order fluid inertia effects gives a more accurate prediction of the dynamic rigidity than the data corrected for second order fluid inertia effects. This behaviour of the dynamic rigidity first order and second order fluid inertia corrections is consistent with the simulated data presented in figure 5.2 for a Newtonian fluid in the parallel plate geometry.

The normalised frequency range of applicability of the second order fluid inertia corrections is now considered for various values of the non-dimensional quantity R. We present the dynamic viscosity and dynamic rigidity corrections in figures 5.17 and 5.18 respectively. It is seen in figure 5.17 that when R has a value below 40 good agreement is obtained with the exact dynamic viscosity data up to a normalised frequency of 0·7. However if R has a value below 5 then good agreement with the exact dynamic viscosity data is obtained over the full normalised frequency range considered. The corresponding dynamic rigidity data presented in figure 5.18 shows that when R has a value below 40 good

agreement with the exact data is obtained up to a normalised frequency of 0·2 and if R has a value below 5 then good agreement is obtained up to normalised frequencies of 1·6. From the Newtonian fluid data presented in figures 5.17 and 5.18 it can be concluded that for all values of R the second order fluid inertia correction for dynamic viscosity gives good agreement with the exact data up to higher normalised frequencies than the corresponding correction for dynamic rigidity. This is consistent with the behaviour seen in figures 5.3 and 5.4 for the complex viscosity prediction of Newtonian fluids in the parallel plate geometry.

5.4.2 Single element Maxwell fluids

For a given concentric cylinder geometry and torsion bar (*i.e.* r_i, r_o, h, I, K known) it can be shown that the normalised complex viscosity (η^*/η_0) of a single element Maxwell fluid, with a specific relaxation time λ, can be represented as a function of the two non-dimensional quantities $R\,(=\rho r_i^2\omega_0/\eta_0)$ and the normalised frequency (ω/ω_0). As for the parallel plate simulations we consider the oscillatory shear flow behaviour of single element Maxwell fluids over the frequency range $0<\omega<2\omega_0$ and choose the relaxation time λ such that $\lambda\,\omega_0=1$.

Figures 5.19 and 5.20 show fluid inertia corrections for the simulated dynamic viscosity and dynamic rigidity data respectively of a single element Maxwell fluid when $R=5$. In these figures we present the uncorrected data (equation (4.2.17) with S given by equation (4.3.15)), data corrected for first order fluid inertia effects and data corrected for second order fluid inertia effects. It is seen in figure 5.19 that except near the natural frequency ($\omega/\omega_0=1$) dynamic viscosity predictions are not significantly improved by correcting for second order fluid inertia effects. For the corresponding dynamic rigidity data in figure 5.20 it is seen that the second order fluid inertia correction gives good agreement with the exact data up to a normalised frequency of 1·4 whereas, the uncorrected data is

only in agreement for normalised frequencies below 0·05.

The normalised frequency range of applicability of the second order fluid inertia corrections is now considered for various values of the non-dimensional quantity R. Dynamic viscosity and dynamic rigidity data for various values of R is presented in figures 5.21 and 5.22 respectively. In these figures it is seen that when R has a value below 40 good agreement with the exact complex viscosity data is only obtained up to a normalised frequency of 0·2, whereas if R has a value below 2 then good agreement is obtained over the full normalised frequency range considered. It is noted that the frequency range of applicability of the second order fluid inertia corrections for the single element Maxwell fluid is approximately the same for both dynamic viscosity and dynamic rigidity data. This is consistent with the results presented in figures 5.7 and 5.8 for a single element Maxwell fluid in the parallel plate geometry constrained by a torsion bar.

5.5 Concentric cylinder geometry connected to a strain gauge torsion head

We simulate the oscillatory shear flow behaviour of a Newtonian fluid and a single element Maxwell fluid in a concentric cylinder geometry, where the inner cylinder is connected to a strain gauge torsion head. It is noted that we consider the inner cylinder to be stationary and assume that the strain gauge has infinite stiffness. For comparison purposes we also simulate the concentric cylinder oscillatory shear flow behaviour of a Newtonian fluid and a single element Maxwell fluid on a CSR controlled stress rheometer. At a prescribed outer cylinder angular frequency of oscillation ω the known fluid parameters (η^*, ρ) and the geometry parameters (r_i, r_o) can be used in equation (4.3.28) and the complex viscosity η_0^*, when fluid inertia effects are ignored, is then known. Similarly at a prescribed inner cylinder angular frequency of oscillation ω the known geometry and fluid parameters can be used in equation (4.3.30) and the complex viscosity

η_0^*, when fluid inertia effects are ignored, for a CSR controlled stress rheometer is also known. The two sets of simulated η_0^* data will be used to establish the frequency range of applicability of the respective second order fluid inertia corrections for the Weissenberg and CSR instruments.

As before we consider a CSR concentric cylinder geometry in which the coaxial inner and outer cylinders have radii $r_i = 15$ mm and $r_o = 20 \cdot 75$ mm respectively.

5.5.1 Newtonian fluids

For a Newtonian fluid in a given concentric cylinder geometry (*i.e.* r_i, r_o known) it can be shown that, on both the Weissenberg rheogoniometer fitted with a strain gauge and the CSR controlled stress rheometer, the normalised complex viscosity (η^*/η_0) can be represented as a function of the non-dimensional normalised frequency ($= \rho r_i^2 \omega / \eta_0$).

Figures 5.23 and 5.24 respectively show fluid inertia corrections for the simulated dynamic viscosity and dynamic rigidity data of a Newtonian fluid on both the Weissenberg rheogoniometer fitted with a strain gauge and the CSR controlled stress rheometer. In these figures we present, for both instruments, uncorrected data (obtained from equations (4.3.28) and (4.3.30)) and data corrected for second order fluid inertia effects. It can be seen from equations (4.3.29) and (4.3.31) that, for both instruments, the dynamic viscosity is not influenced by first order fluid inertia effects. Therefore first order fluid inertia corrections are only presented for the dynamic rigidity data in figure 5.24. It can be seen in figure 5.23 that the Weissenberg rheogoniometer dynamic viscosity data corrected for second order fluid inertia effects gives good agreement with the exact data up to a higher normalised frequency than the corresponding data for the CSR controlled stress rheometer. However the corresponding second order fluid inertia corrections for dynamic rigidity, presented in figure 5.24, show that the CSR controlled stress rheometer gives good

agreement with the exact data up to higher normalised frequencies than the Weissenberg rheogoniometer. It is noted that this behaviour of the second order fluid inertia corrections is consistent with the results presented in figures 5.9 and 5.10 for Newtonian fluids in the parallel plate geometry. In figure 5.24 it should also be noted that the first order fluid inertia correction gives better agreement with the exact dynamic rigidity data than the second order correction. Again this is consistent with the results presented in figure 5.10 for Newtonian fluids in the parallel plate geometry.

5.5.2 Single element Maxwell fluids

For a single element Maxwell fluid in a given concentric cylinder geometry (*i.e.* r_i, r_o known) it can be shown that, on both the Weissenberg rheogoniometer fitted with a strain gauge and the CSR controlled stress rheometer, the normalised complex viscosity (η^*/η_0) can be represented as a function of the two non-dimensional quantities $R\,(=\rho r_i^2/(\lambda\eta_0))$ and the Deborah number $De\,(=\lambda\omega)$.

In figures 5.25 and 5.26 we present fluid inertia corrections for simulated dynamic viscosity and dynamic rigidity data respectively of a single element Maxwell fluid when $R=5$, on both the Weissenberg rheogoniometer fitted with a strain gauge and the CSR controlled stress rheometer. These figures include, for both instruments, uncorrected data (obtained from equations (4.3.28) and (4.3.30)) and data corrected for second order fluid inertia effects. Figure 5.26 also shows dynamic rigidity data corrected for first order fluid inertia effects. It is seen in figure 5.25 that when fluid inertia effects are ignored the dynamic viscosity is underestimated by the Weissenberg rheogoniometer and overestimated by the CSR controlled stress rheometer. The corresponding dynamic rigidity data presented in figure 5.26 shows that when fluid inertia effects are ignored, the dynamic rigidity will be overestimated by the Weissenberg rheogoniometer and underestimated by the CSR

controlled stress rheometer. It is noted that when fluid inertia effects are ignored the behaviour of the complex viscosity data in figures 5.25 and 5.26, for each instrument, is consistent with that observed in figures 5.11 and 5.12 for a single element Maxwell fluid in the parallel plate geometry. In figures 5.25 and 5.26 it is seen that when corrected for second order fluid inertia effects both instruments give good agreement with the exact complex viscosity data up to a Deborah number of 1·4.

For both the Weissenberg rheogoniometer fitted with a strain gauge and the CSR controlled stress rheometer we now consider the Deborah number range of applicability of the second order fluid inertia corrections for various values of the non-dimensional quantity R. The dynamic viscosity and dynamic rigidity corrections are presented in figures 5.27 and 5.28 respectively. In these figures it is seen that if R has a value below 40 then good agreement with the exact complex viscosity data is obtained up to Deborah numbers of 0·3, for both instruments. Whereas when R has a value below 2 both instruments give good agreement with the exact data for the full normalised frequency range considered.

5.6 Cone and plate geometry constrained by a torsion bar

The oscillatory shear flow behaviour of a Newtonian fluid and a single element Maxwell fluid is simulated for the cone and plate geometry, where the cone is constrained by a torsion bar. At a prescribed angular frequency of oscillation ω the known fluid parameters (η^*, ρ) and the geometry parameters (a, θ_0, I, K) can be used in equation (4.4.22) to evaluate the expression e^{ic}/ϑ analytically. It is noted that in order to determine e^{ic}/ϑ analytically the two infinite series in equation (4.4.22) must be evaluated. Therefore the analytically calculated value of e^{ic}/ϑ must be checked to ensure that a sufficient number of terms in these series have been taken to give a converged solution. On using the

calculated value for e^{ic}/ϑ in equation (4.2.17), where the geometrical parameter S is given by equation (4.4.25), the complex viscosity η_0^*, when fluid inertia effects are ignored, is then known. This value of η_0^* can be used in equation (4.4.38) to obtain the complex viscosity prediction which includes first and second order fluid inertia effects.

In order to perform the analytical simulations the integral β_n in equation (4.4.24) must be evaluated over a range of α values and for many values of n at each α. Computational time can be significantly reduced by using a recursive formula to evaluate these integrals. From equation (4.4.24) we let $\beta_n = \alpha^{-3/2} H_{n+1/2}$ where

$$H_{n+1/2} = \int_0^a r^{1/2} J_{n+1/2}(\alpha r)\, dr \tag{5.6.1}$$

From Watson [22] a recursive formula for evaluating the Bessel function $J_{n+1/2}(\alpha r)$ is given by

$$J_{n+1/2}(\alpha r) = \frac{(2n-1)}{\alpha r} J_{n-1/2}(\alpha r) - J_{n-3/2}(\alpha r) \tag{5.6.2}$$

This formula is stable when recursing in the backward direction, but unstable when recursing forwards. On substituting equation (5.6.2) into equation (5.6.1) and integrating by parts we obtain a recursive formula for evaluating the integral $H_{n+1/2}$, which is stable when recursing in the backward direction, as

$$H_{n+1/2} = \frac{(n+1)}{(n+2)} H_{n+3/2} + \frac{(2n+3)}{(n+2)} \frac{a^{1/2}}{\alpha} J_{n+3/2}(\alpha a) \tag{5.6.3}$$

For the simulations we consider a cone and plate geometry with the dimensions $a = 37 \cdot 5\,\text{mm}$ and $\theta_0 = 2^\circ$, where a is the radius of the cone base and the plate and θ_0 is the small angle between the cone and the plate. The moment of inertia of the member constrained by the torsion bar is chosen to be $I = 164\,\mu\text{Ns}^2$ and a torsion bar with stiffness

$K = 5 \cdot 005\,\mathrm{Nm/rad}$ is used. It is noted that these values are identical to those used for both the parallel pate and concentric cylinder simulations and the natural frequency of the member constrained by the torsion bar is $\omega_0 = 174 \cdot 695\,\mathrm{rad/s}$.

5.6.1 Newtonian fluids

For a given cone and plate geometry and torsion bar (*i.e.* a, θ_0, I, K known) it can be shown that the normalised complex viscosity (η^*/η_0) of a Newtonian fluid can be represented as a function of the two non-dimensional quantities $R\,(=\rho a^2\omega_0/\eta_0)$ and the normalised frequency (ω/ω_0). As for the previous simulations we consider the oscillatory shear flow behaviour of Newtonian fluids over the frequency range $0 < \omega < 2\omega_0$.

In figures 5.29 and 5.30 we present fluid inertia corrections for simulated dynamic viscosity and dynamic rigidity data respectively of a Newtonian fluid when $R = 1000$. The uncorrected data in these figures is obtained from equation (4.2.17) where the geometrical parameter S is defined by equation (4.4.25). Figures 5.29 and 5.30 also include data corrected for first order fluid inertia effects and data corrected for second order fluid inertia effects. It is seen in figure 5.29 that the second order fluid inertia correction for dynamic viscosity gives good agreement with the exact data over the full normalised frequency range considered. Figure 5.30 shows that an apparent positive dynamic rigidity is obtained when fluid inertia effects are ignored and if second order fluid inertia effects are taken into account the expected zero dynamic rigidity is obtained for normalised frequencies below 0·8.

5.6.2 Single element Maxwell fluids

For a given cone and plate geometry and torsion bar (*i.e.* a, θ_0, I, K known) it can

be shown that the normalised complex viscosity (η^*/η_0) of a single element Maxwell fluid, with a specific relaxation time λ, can be represented as a function of the two non-dimensional quantities $R(=\rho a^2\omega_0/\eta_0)$ and the normalised frequency (ω/ω_0). As for the previous simulations we consider the oscillatory shear flow behaviour of single element Maxwell fluids over the frequency range $0<\omega<2\omega_0$ and choose the relaxation time λ such that $\lambda\,\omega_0=1$.

Figures 5.31 and 5.32 show fluid inertia corrections for the simulated dynamic viscosity and dynamic rigidity data respectively of a single element Maxwell fluid when $R=1000$. In these figures we present the uncorrected data (equation (4.2.17) with S given by equation (4.4.25)), data corrected for first order fluid inertia effects and data corrected for second order fluid inertia effects. Figure 5.31 shows that except near the natural frequency ($\omega/\omega_0=1$) the dynamic viscosity prediction is not significantly improved by correcting for first and second order fluid inertia effects. However the corresponding dynamic rigidity data presented in figure 5.32 shows that the second order fluid inertia correction gives good agreement with the exact data up to a normalised frequency of 1·4, whereas the uncorrected data is only in agreement for normalised frequencies very close to zero.

5.7 Cone and plate geometry connected to a strain gauge torsion head

We simulate the oscillatory shear flow behaviour of a Newtonian fluid and a single element Maxwell fluid in the cone and plate geometry, where the cone is connected to a strain gauge torsion head. It is noted that the cone is considered to remain stationary and the strain gauge is assumed to be infinitely stiff. For comparison purposes we shall also simulate the oscillatory shear flow behaviour of a Newtonian fluid and a single element Maxwell fluid in the cone and plate geometry on a CSR controlled stress rheometer. For a

prescribed angular frequency of oscillation ω of the plate the known fluid parameters (η^*, ρ) and the geometry parameters (a, θ_0) can be used in equation (4.4.39) and the complex viscosity η_0^*, when fluid inertia effects are ignored, is then known. Similarly for a prescribed angular frequency of oscillation ω of the cone the known geometry and fluid parameters can be used in equation (4.4.41) and the complex viscosity η_0^*, when fluid inertia effects are ignored, for a CSR controlled stress rheometer is also known. Using the two sets of simulated η_0^* data the respective complex viscosity predictions can be corrected for first and second order fluid inertia effects using equations (4.4.40) and (4.4.42) and the frequency range of applicability of these corrections can be established.

As before the simulations are performed for a cone and plate geometry with the dimensions $a = 37 \cdot 5$ mm and $\theta_0 = 2°$.

5.7.1 Newtonian fluids

For a Newtonian fluid in a given cone and plate geometry (*i.e.* a, θ_0 known) it can be shown that, on both the Weissenberg rheogoniometer fitted with a strain gauge and the CSR controlled stress rheometer, the normalised complex viscosity (η^*/η_0) can be represented as a function of the non-dimensional normalised frequency ($= \rho a^2 \omega / \eta_0$).

Figures 5.33 and 5.34 show, for both the Weissenberg rheogoniometer fitted with a strain gauge and the CSR controlled stress rheometer, fluid inertia corrections for the simulated dynamic viscosity and dynamic rigidity data of a Newtonian fluid. In these figures we present, for both instruments, uncorrected data (obtained from equations (4.4.39) and (4.4.41)) and data corrected for second order fluid inertia effects. It is seen in figure 5.33 that for normalised frequencies below 2000 fluid inertia effects on either instrument only have a small influence on the dynamic viscosity prediction. The corresponding dynamic

rigidity data presented in figure 5.34 shows that when second order fluid inertia effects are taken into account good agreement with the exact data is obtained, on both instruments, for normalised frequencies below 1400.

5.7.2 Single element Maxwell fluids

For a single element Maxwell fluid in a given cone and plate geometry (*i.e.* a, θ_0 known) it can be shown that, on both the Weissenberg rheogoniometer fitted with a strain gauge and the CSR controlled stress rheometer, the normalised complex viscosity (η^*/η_0) can be represented as a function of the two non-dimensional quantities $R\,(=\rho a^2/(\lambda\eta_0))$ and the Deborah number $De\,(=\lambda\omega)$.

In figures 5.35 and 5.36 we present fluid inertia corrections for simulated dynamic viscosity and dynamic rigidity data respectively of a single element Maxwell fluid when $R = 1000$, on both the Weissenberg rheogoniometer fitted with a strain gauge and the CSR controlled stress rheometer. For both instruments these figures include uncorrected data (obtained from equations (4.4.39) and (4.4.41)) and data corrected for second order fluid inertia effects. Figure 5.36 also includes dynamic rigidity data corrected for first order fluid inertia effects. It is seen in figure 5.35 that for both instruments the dynamic viscosity prediction is not significantly improved by correcting for second order fluid inertia effects. However for the corresponding dynamic rigidity data in figure 5.36, it is seen that fluid inertia effects are important and that for both instruments the second order fluid inertia correction gives good agreement with the exact dynamic rigidity data for Deborah numbers below 1·2.

5.8 Comments

In the Newtonian fluid simulations for a Weissenberg rheogoniometer it has been

observed that, for all three geometries, the first order fluid inertia correction for dynamic rigidity gives better agreement with the exact data than the second order correction. It should be noted that for all of the single element Maxwell fluid simulations the second order fluid inertia correction, as expected, gives a more accurate prediction of the dynamic rigidity data than the first order correction. From the figures presented it appears that when either a torsion bar system or a strain gauge torsion head system is used the inclusion of second order fluid inertia effects will increase the error in the dynamic rigidity prediction of a Newtonian fluid. We shall investigate this behaviour for the parallel plate geometry on a Weissenberg rheogoniometer where the upper plate is connected to a strain gauge torsion head. The simulated dynamic viscosity and dynamic rigidity data for Newtonian fluids in this geometry was presented in figures 5.9 and 5.10 respectively. In these figures the complex viscosity data is also compared with the corresponding simulated data obtained for a CSR controlled stress rheometer. In figure 5.10 it is seen that for the Weissenberg rheogoniometer the first order fluid inertia correction gives a more accurate dynamic rigidity prediction than the second order correction. From this figure it is not possible to verify this behaviour for low normalised frequencies, however inspection of the dynamic rigidity data reveals that the first order correction is more accurate than the second order correction even at very low normalised frequencies. Therefore higher order fluid inertia terms will need to be considered in order to improve on the first order dynamic rigidity prediction. It is noted that for normalised frequencies below 2·25 on the CSR controlled stress rheometer the first order fluid inertia correction is in better agreement with the exact dynamic rigidity data than the second order correction. The dynamic viscosity data presented in figure 5.9 is not influenced by first order fluid inertia effects and it is seen that, for both instruments, the data corrected for second order fluid inertia effects gives a more accurate dynamic viscosity prediction than the uncorrected data.

Third order fluid inertia corrections have been determined for the parallel plate geometry on both the Weissenberg rheogoniometer fitted with a strain gauge torsion head and the CSR controlled stress rheometer as

Weissenberg:- $$\eta^* = \eta_0^*\left[1 - \frac{1}{6}(\alpha_0 h)^2 - \frac{7}{360}(\alpha_0 h)^4 - \frac{1}{189}(\alpha_0 h)^6\right] \tag{5.8.1}$$

CSR;- $$\eta^* = \eta_0^*\left[1 + \frac{1}{3}(\alpha_0 h)^2 + \frac{1}{45}(\alpha_0 h)^4 - \frac{1}{189}(\alpha_0 h)^6\right] \tag{5.8.2}$$

It should be noted that the value of η_0^* and hence the value of α_0 obtained from each instrument will be different (see equations (4.2.28) and (4.2.30)). The third order fluid inertia corrections in equations (5.8.1) and (5.8.2) have been applied to the Newtonian data in figures 5.9 and 5.10. On the Weissenberg rheogoniometer the third order fluid inertia correction gives a more accurate prediction of the dynamic rigidity than the first or second order corrections for normalised frequencies below 3. However for the corresponding dynamic viscosity data the third order correction is less accurate than the second order correction for all frequencies of oscillation. For normalised frequencies below 5 on the CSR controlled stress rheometer, both the dynamic viscosity and dynamic rigidity second order predictions are improved by correcting for third order fluid inertia effects.

It has been shown that for Newtonian fluids on a Weissenberg rheogoniometer the first order dynamic rigidity prediction can be improved by including both second and third order fluid inertia effects in the theory. However for the corresponding dynamic viscosity data the third order fluid inertia correction is less accurate than the second order correction. It is also noted that for a non-Newtonian single element Maxwell fluid the second order correction behaves as expected, giving better agreement with the exact dynamic rigidity data than the first order correction. In practice experiments will be performed on fluids whose viscosity behaviour is unknown and therefore experimentalists should correct both the dynamic viscosity and dynamic rigidity data of all fluids for second order fluid inertia

effects. However complex viscosity measurements using the second order fluid inertia corrections should only be taken over the frequency ranges of applicability that have been determined in this chapter.

5.9 Conclusions

We have shown that including first and second order fluid inertia effects in the Weissenberg rheogoniometer theory gives a more accurate complex viscosity prediction than that obtained from the standard theory in which fluid inertia effects are ignored. The simulated oscillatory shear data has shown the importance of these fluid inertia corrections when characterising the flow properties of mobile fluids at high frequencies of oscillation. When a torsion bar system is used the second order fluid inertia correction gives a significant improvement in the complex viscosity prediction when the frequency of oscillation is near the natural frequency of the member constrained by the torsion bar. If fluid inertia effects are not taken into account for Newtonian fluids, the Weissenberg rheogoniometer gives rise to an apparent positive dynamic rigidity as opposed to the CSR controlled stress rheometer which gives an apparent negative dynamic rigidity.

For the simulated complex viscosity data on a Weissenberg rheogoniometer, with a strain gauge torsion head, the standard theory underestimates the dynamic viscosity and overestimates the dynamic rigidity. This is in contrast to the CSR controlled stress rheometer in which the standard theory overestimates the dynamic viscosity and underestimates the dynamic rigidity.

The conclusions for each geometry and torsion head system are now given individually.

i) Parallel plate geometry ($h = 500\mu$m, $a = 0 \cdot 0375$ m) with torsion bar

For normalised frequencies below 2 the oscillatory shear flow simulations of Newtonian fluids show the validity of the second order fluid inertia correction formulae for R values below 1. The single element Maxwell fluid simulations show that for R values below 1 the correction formulae are valid up to normalised frequencies of 1·6.

ii) Parallel plate geometry ($h = 500\mu$m, $a = 0 \cdot 0375$ m) with strain gauge

Results for Newtonian fluids have shown the validity of the second order fluid inertia correction formulae up to normalised frequencies of 1·5 for both the Weissenberg and CSR instruments. For R values below 0·5, oscillatory shear flow simulations of single element Maxwell fluids have shown the validity of the correction formulae on both instruments up to a Deborah number of 1·6.

iii) Concentric cylinder geometry ($r_i = 15$ mm, $r_o = 20 \cdot 75$ mm) with torsion bar

Oscillatory shear flow simulations of Newtonian fluids show that for R values below 5 the second order fluid inertia correction formulae are valid for normalised frequencies below 2. Results for single element Maxwell fluids have shown that for for R values below 2 the second order correction formulae give good agreement with the exact viscosity data up to normalised frequencies of 2.

iv) Concentric cylinder geometry ($r_i = 15$ mm, $r_o = 20 \cdot 75$ mm) with strain gauge

On both the Weissenberg and CSR instruments the second order fluid inertia correction formulae give good agreement with the exact Newtonian data for normalised frequencies below 10. For R values below 2, oscillatory shear flow simulations of single element Maxwell fluids have shown the validity of the second order fluid inertia correction

formulae up to Deborah numbers of 2 on both instruments.

v) Cone and plate geometry ($a = 0 \cdot 0375$ m, $\theta_0 = 2^\circ$) with torsion bar

Oscillatory shear flow simulations of Newtonian fluids and single element Maxwell fluids when $R = 1000$ have shown the validity of the second order fluid inertia correction formulae up to normalised frequencies of 0·8.

vi) Cone and plate geometry ($a = 0 \cdot 0375$ m, $\theta_0 = 2^\circ$) with strain gauge

For Newtonian fluids we have shown that the second order fluid inertia correction formulae are valid for normalised frequencies below 1400 on both the Weissenberg and CSR instruments. Oscillatory shear flow simulations of a single element Maxwell fluid when $R = 1000$ show the validity of the correction formulae on both instruments for Deborah numbers below 1·2.

CHAPTER 6

CONCENTRIC CYLINDER END EFFECTS AND FLUID INERTIA EFFECTS ON STEADY SHEAR VISCOSITY PREDICTIONS IN CONTROLLED STRESS RHEOMETRY

6.1 Introduction

The theory for the characterisation of the flow properties of fluids, in commercially available rheometers, generally ignores geometry edge or end effects (Walters [3]). Griffiths and Walters [25] analysed edge effects in both cone and plate and parallel plate geometries for Newtonian fluids and second order fluids. These edge effects give rise to secondary flows which can affect the characterisation of a fluid. However for commercially available CSR geometries their results indicate that edge effects on viscosity predictions are negligible. Olagunju [26] reached a similar conclusion for the flow of a viscoelastic fluid in a parallel plate geometry. Walters [3] comments on secondary flows appearing in wide gap concentric cylinder geometries which are generated by the ends of the finite cylinders. In a concentric cylinder geometry the cylinders are not infinite in length as required by the standard theory. It is suggested by Walters [3] that the gap between the cylinders is made as narrow as possible in order to reduce end effects. The magnitude of end effects in concentric cylinder flow is dependent on the ratio between the length of the cylinders h and the gap between the cylinders $(r_2 - r_1)$. Short [27] suggests that the flow in the centre of the test length can be influenced by end effects for $h/(r_2 - r_1)$ ratios less than 10.

Taylor [28] and Kataoka [29] have studied the flow of Newtonian fluids between concentric cylinders where the inner cylinder is rotated at a constant speed and the outer cylinder is stationary. Both workers considered cylinders of infinite length and used a linear stability theory to predict a critical Taylor number at which the flow becomes turbulent. A

numerical study was carried out by Lockett *et al* [30] to predict a critical Taylor number for inelastic non-Newtonian fluids. The flow between infinite cylinders is free of secondary flows and Taylor vortices until the critical Taylor number is reached. However in a finite concentric cylinder geometry the end effect produces secondary flows which result in the formation of Taylor like vortex cells for any non-zero Reynolds number (Hughes *et al* [31]). The effect of these Taylor like vortices on the prediction of shear viscosity will be discussed in this chapter.

In a commercially available CSR controlled stress rheometer the calculation of the shear viscosity of a fluid, in a concentric cylinder geometry, is based on a theory in which end effects and fluid inertia effects are ignored (T.A. Instruments [24]). This theory assumes the fluid under test occupies the region between two infinitely long coaxial cylinders and will be referred to as the standard theory throughout chapters 6 and 7. The concentric cylinder geometry consists of two coaxial cylinders as shown in figure 6.1. In order to reduce the end effect on viscosity prediction the bottom of the inner cylinder is usually recessed so that air is trapped underneath the cylinder (T.A. Instruments [24]). Concentric cylinder end effects can be reduced by increasing the cylinder lengths or decreasing the gap between the inner and outer cylinders. It may be possible to compensate experimentally for end effects by considering a range of immersed cylinder lengths. However it is not a simple task to produce an accurate extrapolation formula to correct shear viscosity data for end effects.

In this chapter the theory for predicting the shear viscosity in a recessed concentric cylinder geometry will be developed to include end effects. Fluid inertia effects in steady shear can no longer be ignored and must be taken into account in the theory. For Newtonian fluids these effects are included by using a perturbation analysis which is valid for low Reynolds number flows. Using this theory existing steady shear formulae are modified to

include end effects and second order fluid inertia effects. These modified formulae can be incorporated into the CSR software to give an on line correction for shear viscosity data obtained from a CSR controlled stress rheometer. The second order fluid inertia perturbation theory will be compared with results obtained using the Polyflow package [9]. This package is also used to investigate end effects and fluid inertia effects for inelastic power law fluids. Simulated steady shear data will be generated for a Newtonian fluid to establish the limitations of the second order perturbation theory. It is noted that the simulated data will be equivalent to the data obtained from the CSR software which ignores end effects and fluid inertia effects.

Throughout this chapter the perturbation theory equations will be solved using a finite difference scheme with an irregular mesh. This allows a finer mesh to be used near the recessed end where the greatest shear stress variation occurs.

6.2 Steady shear theory

On a CSR controlled stress rheometer a constant torque C_0 is applied to the inner cylinder of a concentric cylinder geometry, forcing it to rotate at a constant angular velocity Ω. The outer cylinder remains stationary. The angular velocity of the inner cylinder is measured and together with the applied torque C_0 can be used to calculate the steady shear viscosity of a fluid. At present the formulae for predicting the shear viscosity of a fluid are determined from infinite cylinder theory which is now described.

6.2.1 Shear viscosity prediction using infinite cylinder theory

The theory considers the fluid under test to occupy the region between two infinitely long coaxial cylinders and to be in contact with the cylinders over a length h. With respect to a set of cylindrical polar coordinates (r,θ,z) the torque exerted on the inner cylinder due

to the motion of the fluid is given by

$$C_F = -2\pi\, r_1^2 \int_0^h \tau_{r\theta}\big|_{r=r_1} dz \tag{6.2.1}$$

When infinite cylinder theory is assumed the $\tau_{r\theta}$ shear stress on the inner cylinder wall is given by

$$\tau_{r\theta} = \frac{2r_2^2\,\Omega\eta}{(r_1^2 - r_2^2)} \tag{6.2.2}$$

where η is the steady shear viscosity of the fluid.

It is noted that equation (6.2.2) is based on Newtonian theory, however it can be shown that it is also valid for any inelastic fluid in narrow gap geometries. By the principle of equal and opposite forces the torque exerted on the inner cylinder due to the motion of the fluid C_F is equal in magnitude to the applied torque C_0. Therefore on using equation (6.2.2) in equation (6.2.1) we obtain

$$\eta = \frac{(r_2^2 - r_1^2)}{4\pi h r_1^2 r_2^2}\frac{C_0}{\Omega} \tag{6.2.3}$$

This is the formula employed by the CSR software to calculate the steady shear viscosity of a fluid. It is noted that the calculation of shear viscosity data using formulae based on infinite length concentric cylinders will be referred to as the standard theory throughout chapters 6 and 7. For Newtonian fluids a low Reynolds number perturbation analysis will be used to produce a formula for calculating the shear viscosity of a fluid which includes end effects and second order fluid inertia effects.

6.2.2 Governing equations and boundary conditions

In the analysis we shall assume that the inner cylinder rotates at a prescribed constant angular velocity Ω. The torque exerted on the inner cylinder due to the motion of the inner cylinder can then be calculated and compared with that obtained when infinite

cylinder theory is assumed.

The physical dimensions of the flow domain are referred to a set of cylindrical polar coordinates (r,θ,z). Figure 6.2 shows a schematic diagram of a concentric cylinder geometry which is axisymmetric about the inner cylinder axis of rotation.

In figure 6.2 the boundary CD is a 'free surface' and for a recessed inner cylinder the boundary AB is also a 'free surface'. For the CSR geometries considered in this chapter these free surfaces have been observed experimentally, by the author, to remain in a horizontal position except for highly elastic liquids or high rotational speeds. For highly elastic liquids the Weissenberg effect will distort the free surface and at high rotational speeds the free surface will be distorted by fluid inertia effects. However these opposing forces counteract each other to a certain degree. In this study elastic effects and high rotational speeds are not considered in the steady shear theory and therefore we will impose the condition that the 'free surface' boundaries remain in their horizontal positions . On these surfaces the tangential shear force f_s, the shear force in the θ direction f_θ and the normal velocity v_n to the free surface is zero. On the remaining boundaries OE, DE and BC the tangential velocity v_s and the velocity component v_θ satisfy the no slip condition. The normal velocity v_n on these boundaries is zero.

The equation of continuity and the equation of motion of the fluid are respectively given by

$$\nabla \cdot v = 0 \tag{6.2.4}$$

$$\rho \frac{Dv}{Dt} = -\nabla p + \nabla \cdot \tau \tag{6.2.5}$$

where v is the velocity vector, p is the pressure, τ is the extra stress tensor, ρ is the fluid density, D/Dt is the substantial derivative and body forces have been neglected.

The equation of state for an inelastic power law fluid is given by

$$\tau = k\left(\frac{I_2}{2}\right)^{n-1}\dot{\gamma} \tag{6.2.6}$$

where $\dot{\gamma} = \nabla v + (\nabla v)^{\mathrm{T}}$ is the rate of strain tensor, I_2 is the second invariant of the rate of strain tensor, k and n are power law constants. When $n = 1$ equation (6.2.6) is the equation of state for a Newtonian fluid.

An analytical solution of equations (6.2.4), (6.2.5) and (6.2.6) subject to the steady shear boundary conditions is not possible over the L shaped flow domain shown in figure 6.2. Therefore these equations will be solved numerically, subject to the steady shear boundary conditions.

In determining the steady shear viscosity of a fluid using a concentric cylinder geometry we are effectively concerned with the torque exerted on the inner cylinder due to the motion of the fluid. With reference to figure 6.2 this torque is given by

$$C_F = -2\pi r_1^2 \int_{z_1}^{z_2} \tau_{r\theta}\big|_{r=r_1} dz \tag{6.2.7}$$

The $\tau_{r\theta}$ shear stress component for the axisymmetric flow is

$$\tau_{r\theta} = \eta r \frac{\partial}{\partial r}\left(\frac{v_\theta}{r}\right) \tag{6.2.8}$$

where η is the steady shear viscosity of the fluid.

At a prescribed inner cylinder angular velocity Ω equations (6.2.4), (6.2.5) and (6.2.6) can be solved numerically and the $\tau_{r\theta}$ shear stresses along the inner cylinder wall can then be determined. On using these stresses in equation (6.2.7) the torque exerted on the inner cylinder due to the motion of the fluid, when end effects and fluid inertia effects are included, can be calculated. The value of this torque will then be compared to the value obtained from infinite cylinder theory and we can establish the magnitude of end effects and fluid inertia effects in steady shear concentric cylinder flows.

For a power law fluid it can be shown that the $\tau_{r\theta}$ shear stress on the inner cylinder

wall is given by

$$\tau_{r\theta}\Big|_{r=r_1} = k\left[\frac{2\Omega\left(r_2/r_1\right)^{(2/n)}}{n\left\{\left(r_2/r_1\right)^{(2/n)}-1\right\}}\right]^n \tag{6.2.9}$$

On using equation (6.2.9) in equation (6.2.1) the torque exerted on the inner cylinder due to the motion of a power law fluid when end effects are ignored is given by

$$C_F = 2\pi h k\left[\frac{2\Omega}{n\left\{1-\left(r_1/r_2\right)^{2/n}\right\}}\right]^n \tag{6.2.10}$$

6.3 Fluid inertia perturbation theory for a Newtonian fluid

In this analysis we consider a Newtonian fluid in a concentric cylinder geometry where the inner cylinder rotates at a constant angular velocity Ω and the outer cylinder remains stationary. With reference to a set of cylindrical polar coordinates (r,θ,z) we let the velocity components in the r, θ and z directions be v_r, v_θ and v_z respectively. Since steady shear flow is time independent and the flow is axisymmetric we assume a velocity distribution of the form

$$v_r = v_r(r,z) \quad , \quad v_\theta = v_\theta(r,z) \quad , \quad v_z = v_z(r,z) \tag{6.3.1}$$

From Bird *et al* [1] the equation of continuity is given by

$$\frac{1}{r}\frac{\partial}{\partial r}\left(r\,v_r\right)+\frac{\partial v_z}{\partial z} = 0 \tag{6.3.2}$$

The velocity distribution in equation (6.3.1) gives six non-zero components of the shear stress tensor as

$$\tau_{rr} = 2\eta_0\frac{\partial v_r}{\partial r} \qquad \tau_{\theta\theta} = 2\eta_0\frac{v_r}{r} \qquad \tau_{zz} = 2\eta_0\frac{\partial v_z}{\partial z}$$

$$\tau_{r\theta} = \eta_0 r \frac{\partial}{\partial r}\left(\frac{v_\theta}{r}\right) \qquad \tau_{\theta z} = \eta_0 \frac{\partial v_\theta}{\partial z} \qquad \tau_{rz} = \eta_0\left(\frac{\partial v_r}{\partial z} + \frac{\partial v_z}{\partial r}\right) \tag{6.3.3}$$

where η_0 is the Newtonian shear viscosity of the fluid.

The stress equations of motion for axisymmetric steady shear flow, which is independent of θ and time t, are given by

$$\rho\left(v_r \frac{\partial v_r}{\partial r} - \frac{v_\theta^2}{r} + v_z \frac{\partial v_r}{\partial z}\right) = \eta\left[\frac{1}{r}\frac{\partial}{\partial r}(r\tau_{rr}) + \frac{\partial}{\partial z}\tau_{rz} - \frac{\tau_{\theta\theta}}{r}\right] - \frac{\partial p}{\partial r} \tag{6.3.4}$$

$$\rho\left(v_r \frac{\partial v_\theta}{\partial r} + \frac{v_r v_\theta}{r} + v_z \frac{\partial v_\theta}{\partial z}\right) = \eta\left[\frac{1}{r^2}\frac{\partial}{\partial r}(r^2\tau_{r\theta}) + \frac{\partial}{\partial z}\tau_{\theta z}\right] \tag{6.3.5}$$

$$\rho\left(v_r \frac{\partial v_z}{\partial r} + v_z \frac{\partial v_z}{\partial z}\right) = \eta\left[\frac{1}{r}\frac{\partial}{\partial r}(r\tau_{rz}) + \frac{\partial}{\partial z}\tau_{zz}\right] - \frac{\partial p}{\partial z} \tag{6.3.6}$$

where body forces have been neglected.

With reference to figure 6.2 the boundary conditions for the three velocity components (v_r, v_θ, v_z) are now considered. On boundaries OE and DE the normal and tangential velocities are zero and the no slip condition is imposed, hence $v_r = v_\theta = v_z = 0$. These conditions also apply on the moving boundary BC, hence $v_r = v_z = 0$ and $v_\theta = r_1\Omega$. The 'free surface' boundaries AB and CD do not exert any shear force and hence $\tau_{\theta z} = \tau_{rz} = 0$ on these boundaries. We also impose that these 'free surface' boundaries remain in their horizontal positions and using equation (6.3.3) gives the conditions $\partial v_r/\partial z = 0$, $\partial v_\theta/\partial z = 0$ and $v_z = 0$ on boundaries AB and CD. There is no fluid motion across the line of symmetry and no θ-direction fluid motion on the line of symmetry. Therefore on boundary OA we have $v_r = 0$ and $v_\theta = 0$. Boundary OA is at $r = 0$ and we must impose that the velocity v_z is bounded as $r \to 0$, hence on this boundary we have the condition that $\lim_{r\to 0} v_z$ is bounded.

On taking r_1 to be a typical dimension of length and $r_1\Omega$, the velocity of the inner

cylinder, to be a typical velocity we define the following non-dimensional variables

$$r^+ = \frac{r}{r_1} \quad , \quad z^+ = \frac{z}{r_1} \quad , \quad z_1^+ = \frac{z_1}{r_1} \quad , \quad z_2^+ = \frac{z_2}{r_1} \quad ,$$

$$v_r^+ = \frac{v_r}{r_1\Omega} \quad , \quad v_\theta^+ = \frac{v_\theta}{r_1\Omega} \quad , \quad v_z^+ = \frac{v_z}{r_1\Omega} \quad , \quad p^+ = \frac{p}{\eta_0\,\Omega} \tag{6.3.7}$$

A non-dimensional Reynolds number (Bird *et al* [2]) for the Newtonian flow is defined as

$$R_e = \frac{\rho r_1^2 \Omega}{\eta_0} \tag{6.3.8}$$

where ρ is the fluid density and η_0 is the Newtonian viscosity.

Substituting the stress components of equation (6.3.3) into equations (6.3.4) to (6.3.6) and using equation (6.3.7) gives the non-dimensional equations

$$R_e\left(v_r \frac{\partial v_r}{\partial r} - \frac{v_\theta^2}{r} + v_z \frac{\partial v_r}{\partial z}\right) = \frac{\partial^2 v_r}{\partial r^2} + \frac{1}{r}\frac{\partial v_r}{\partial r} - \frac{v_r}{r^2} + \frac{\partial^2 v_r}{\partial z^2} - \frac{\partial p}{\partial r} \tag{6.3.9}$$

$$R_e\left(v_r \frac{\partial v_\theta}{\partial r} + \frac{v_r v_\theta}{r} + v_z \frac{\partial v_\theta}{\partial z}\right) = \frac{\partial^2 v_\theta}{\partial r^2} + \frac{1}{r}\frac{\partial v_\theta}{\partial r} - \frac{v_\theta}{r^2} + \frac{\partial^2 v_\theta}{\partial z^2} \tag{6.3.10}$$

$$R_e\left(v_r \frac{\partial v_z}{\partial r} + v_z \frac{\partial v_z}{\partial z}\right) = \frac{\partial^2 v_z}{\partial r^2} + \frac{1}{r}\frac{\partial v_z}{\partial r} + \frac{\partial^2 v_z}{\partial z^2} - \frac{\partial p}{\partial z} \tag{6.3.11}$$

where the $^+$ notation is implied but has been omitted for convenience.

Using equation (6.3.7) the boundary conditions for the non-dimensional functions $v_r(r,z)$, $v_\theta(r,z)$ and $v_z(r,z)$ are given by equations (6.3.12), (6.3.13) and (6.3.14) respectively

$$\left.\begin{aligned} v_r &= 0 \quad \text{on boundaries OA, BC, DE and OE.} \\ \partial v_r/\partial z &= 0 \quad \text{on free surface boundaries AB and CD.} \end{aligned}\right\} \tag{6.3.12}$$

$$\left.\begin{aligned} v_\theta &= 0 \quad \text{on boundaries OA, OE and DE.} \\ \partial v_\theta/\partial z &= 0 \quad \text{on free surface boundaries AB and CD.} \\ v_\theta &= 1 \quad \text{on the moving boundary BC.} \end{aligned}\right\} \tag{6.3.13}$$

$$\left.\begin{array}{ll} v_z = 0 & \text{on boundaries BC, DE and OE.} \\ v_z = 0 & \text{on free surface boundaries AB and CD.} \\ \lim\limits_{r\to 0} v_z & \text{is bounded on the line of symmetry OA} \end{array}\right\} \tag{6.3.14}$$

On working to second order terms in Reynolds number the non-dimensional velocity components can be expanded in terms of the Reynolds number R_e as

$$v_r(r,z) = R_e\, v_{r1}(r,z) + O(R_e^3) \tag{6.3.15}$$

$$v_\theta(r,z) = v_{\theta 0}(r,z) + R_e^2\, v_{\theta 2}(r,z) + O(R_e^3) \tag{6.3.16}$$

$$v_z(r,z) = R_e\, v_{z1}(r,z) + O(R_e^3) \tag{6.3.17}$$

where the suffices 0, 1 and 2 refer to the zero order, first order and second order velocity components respectively. It can be shown that the first order Reynolds number component in v_θ and the second order Reynolds number components in v_r and v_z are equal to zero and hence are omitted in equations (6.3.15) to (6.3.17). The pressure term is also expanded as a second order power series in terms of the Reynolds number R_e. On considering equation (6.3.9) together with equation (6.3.15) and equation (6.3.11) together with equation (6.3.17) the pressure term can be expanded as

$$p = R_e\, p_1(r,z) + O(R_e^3) \tag{6.3.18}$$

On substituting equations (6.3.15) to (6.3.18) into equations (6.3.9) to (6.3.11) and comparing the Reynolds number coefficients we have

R_e^0 *terms*:-

$$L\left[v_{\theta 0}\right] = 0 \tag{6.3.19}$$

where $$L = \frac{\partial^2}{\partial r^2} + \frac{1}{r}\frac{\partial}{\partial r} - \frac{1}{r^2} + \frac{\partial^2}{\partial z^2} = \nabla^2 - \frac{1}{r^2}$$

is the θ component of the Laplacian operator of a vector field

R_e^1 *terms*:-

$$L[v_{r1}] - \frac{\partial p_1}{\partial r} = -\frac{v_{\theta 0}^2}{r} \tag{6.3.20}$$

$$\nabla^2 v_{z1} - \frac{\partial p_1}{\partial z} = 0 \tag{6.3.21}$$

R_e^2 *terms*:-

$$L[v_{\theta 2}] = v_{r1}\frac{\partial v_{\theta 0}}{\partial r} + \frac{v_{r1}v_{\theta 0}}{r} + v_{z1}\frac{\partial v_{\theta 0}}{\partial z} \tag{6.3.22}$$

The boundary conditions given in equations (6.3.12) to (6.3.14) are also expanded in terms of the Reynolds number R_e using equations (6.3.15) to (6.3.17). Each set of equations and their respective boundary conditions is now considered.

6.3.1 Zero order equations and boundary conditions

The only non-zero R_e^0 velocity component is $v_{\theta 0}(r,z)$, which can be obtained by solving equation (6.3.19) subject to the relevant boundary conditions. On considering equations (6.3.13) and (6.3.16) the boundary conditions for $v_{\theta 0}(r,z)$ are

$$\left.\begin{aligned} v_{\theta 0} &= 0 \quad \text{on boundaries OA, OE and DE.} \\ \partial v_{\theta 0}/\partial z &= 0 \quad \text{on free surface boundaries AB and CD.} \\ v_{\theta 0} &= 1 \quad \text{on the moving boundary BC.} \end{aligned}\right\} \tag{6.3.23}$$

6.3.2 First order equations and boundary conditions

On differentiating equation (6.3.20) with respect to z and differentiating equation (6.3.21) with respect to r, the first order pressure term p_1 can be eliminated to give

$$\frac{\partial}{\partial z}L[v_{r1}] - \frac{\partial}{\partial r}\nabla^2 v_{z1} = -\frac{2v_{\theta 0}}{r}\frac{\partial v_{\theta 0}}{\partial z} \tag{6.3.24}$$

The first order streamfunction $\psi(r,z)$ of the axisymmetric flow is defined as (Bird *et al* [1])

$$v_{r1} = \frac{1}{r}\frac{\partial \psi}{\partial z} \qquad v_{z1} = -\frac{1}{r}\frac{\partial \psi}{\partial r} \tag{6.3.25}$$

Substitution of equation (6.3.25) into equation (6.3.24) gives

$$E^4\psi = E^2(E^2\psi) = -2v_{\theta 0}\frac{\partial v_{\theta 0}}{\partial z} \tag{6.3.26}$$

where E^4 is the bi-harmonic operator and E^2 is defined by

$$E^2 = \frac{\partial^2}{\partial r^2} - \frac{1}{r}\frac{\partial}{\partial r} + \frac{\partial^2}{\partial z^2} \tag{6.3.27}$$

It is convenient to introduce the variable $\phi(r,z)$ which enables equation (6.3.28) to be expressed as the two coupled equations

$$E^2\phi = -2v_{\theta 0}\frac{\partial v_{\theta 0}}{\partial z} \tag{6.3.28}$$

$$E^2\psi = \phi \tag{6.3.29}$$

On considering equations (6.3.12) and (6.3.15) the boundary conditions for $v_{r1}(r,z)$ can be determined and similarly the boundary conditions for $v_{z1}(r,z)$ can be obtained from equations (6.3.15) and (6.3.18). Using the boundary conditions for $v_{r1}(r,z)$ and $v_{z1}(r,z)$ in equation (6.3.25) we can set $\psi = 0$ on all six boundaries of the flow domain presented in figure 6.2. Equations (6.3.27) and (6.3.29) give

$$\phi = \frac{\partial^2\psi}{\partial r^2} - \frac{1}{r}\frac{\partial \psi}{\partial r} + \frac{\partial^2\psi}{\partial z^2} \tag{6.3.30}$$

Therefore on using equation (6.3.30) the boundary conditions for $\phi(r,z)$ can be expressed in terms of the streamfunction $\psi(r,z)$. The boundary conditions for $\phi(r,z)$ on each of the six boundaries of the flow domain are now considered.

Boundary OE

$v_{r1} = 0$ and $v_{z1} = 0$ therefore using equation (6.3.25) gives $\partial\psi/\partial z = 0$ and

$\partial\psi/\partial r = 0$. Also since the boundary lies in the r-direction and $\psi = 0$ along its length we have $\partial^2\psi/\partial r^2 = 0$. Hence from equation (6.3.30) we have $\phi = \partial^2\psi/\partial z^2$.

Boundaries BC and DE

$v_{r1} = 0$ and $v_{z1} = 0$ therefore using equation (6.3.25) gives $\partial\psi/\partial z = 0$ and $\partial\psi/\partial r = 0$. Also since these boundaries lie in the z-direction and $\psi = 0$ along their length we have $\partial^2\psi/\partial z^2 = 0$. Hence from equation (6.3.30) we have $\phi = \partial^2\psi/\partial r^2$.

Boundaries AB and CD

$\partial v_{r1}/\partial z = 0$ and $v_{z1} = 0$ therefore using equation (6.3.25) gives $\partial^2\psi/\partial z^2 = 0$ and $\partial\psi/\partial r = 0$. Also since these boundaries lie in the r-direction and $\psi = 0$ along their length we have $\partial^2\psi/\partial r^2 = 0$. Hence from equation (6.3.30) we have $\phi = 0$.

Boundary OA

The boundary lies in the z-direction and $v_{r1} = 0$ along its length, therefore from equation (6.3.25) $\partial^2\psi/\partial z^2 = 0$. Hence in equation (6.3.30) we have

$$\phi = \partial^2\psi/\partial r^2 - (1/r)\partial\psi/\partial r \tag{6.3.31}$$

Considering the limit of ϕ in equation (6.3.31) as $r \to 0$ gives $\phi = 0$ on boundary OA.

The boundary conditions for $\psi(r,z)$ and $\phi(r,z)$ in the coupled equations (6.3.28) and (6.3.29) are summarised in figure 6.3.

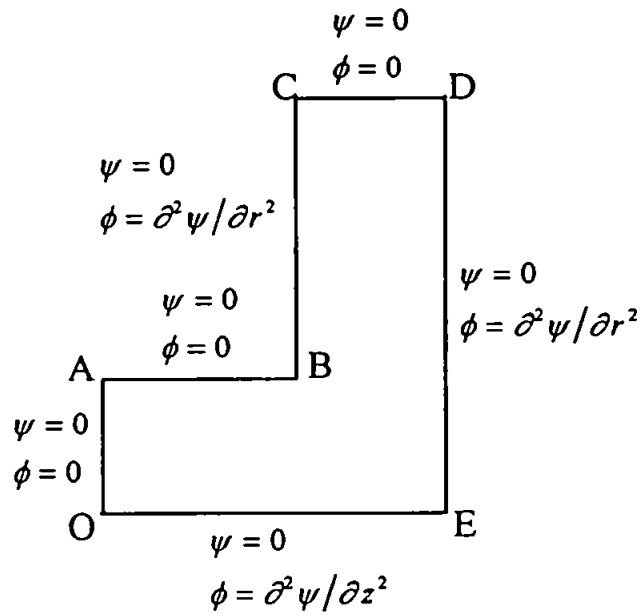

Figure 6.3:- Boundary conditions for the functions $\psi(r,z)$ and $\phi(r,z)$.

It is noted that when solving the coupled equations (6.3.28) and (6.3.29) for the streamfunction $\psi(r,z)$ the values of $v_{\theta 0}(r,z)$ are known from the solution to equation (6.3.19). On using the solution obtained for the streamfunction $\psi(r,z)$ the secondary velocity components $v_{r1}(r,z)$ and $v_{z1}(r,z)$ can be determined from equation (6.3.25).

6.3.3 Second order equations and boundary conditions

The only non-zero R_e^2 velocity component is $v_{\theta 2}(r,z)$, which is obtained from the solution of equation (6.3.22) subject to the relevant boundary conditions. On using equations (6.3.13) and (6.3.16) the boundary conditions for $v_{\theta 2}(r,z)$ are given by

$$\left.\begin{aligned} v_{\theta 2} &= 0 \quad \text{on boundaries OA, BC, DE and OE.} \\ \partial v_{\theta 2}/\partial z &= 0 \quad \text{on free surface boundaries AB and CD.} \end{aligned}\right\} \qquad (6.3.32)$$

It is noted that when solving equation (6.3.22) the values of $v_{\theta 0}(r,z)$ are known from the solution to equation (6.3.19) and the values of $v_{r1}(r,z)$ and $v_{z1}(r,z)$ can be determined from the solution to the coupled equations (6.3.28) and (6.3.29).

It has been shown that equation (6.3.19), the coupled equations (6.3.28) and (6.3.29) and equation (6.3.22) must be solved, subject to the relevant boundary conditions, in order to determine the non-zero velocity components ($v_{\theta 0}$, v_{r1}, v_{z1} and $v_{\theta 2}$) of the Newtonian second order fluid inertia perturbation theory. Due to the shape of the flow domain shown in figure 6.2 it is not possible to obtain an analytical solution to these equations. Therefore the equations will be solved numerically using a finite difference method, which will be described in section 6.4.

6.3.4 Modified formulae for predicting the shear viscosity of a Newtonian fluid

The torque C_F exerted on the inner cylinder due to the motion of the fluid is given in equation (6.2.7). Using the $\tau_{r\theta}$ shear stress component given in equation (6.3.3) and the non-dimensional variables of equation (6.3.7) the torque C_F is given by

$$C_F = -2\pi r_1^3 \eta_0 \Omega \int_{z_1}^{z_2} \left(\frac{\partial v_\theta}{\partial r} - \frac{v_\theta}{r} \right)\Bigg|_{r=1} dz \tag{6.3.33}$$

On substituting the second order power series expansion of $v_\theta(r,z)$ in equation (6.3.16) into equation (6.3.33) the torque C_F exerted on the inner cylinder due to the motion of the fluid can be expressed in the form

$$C_F = 2\pi r_1^3 \eta_0 \Omega \left(\beta_0 + \beta_2 R_e^2 \right) \tag{6.3.34}$$

where

$$\beta_m = -\int_{z_1}^{z_2} \left(\frac{\partial v_{\theta m}}{\partial r} - \frac{v_{\theta m}}{r} \right)\Bigg|_{r=1} dz \qquad m = 0,2 \tag{6.3.35}$$

are non-dimensional geometry dependent constants.

On a CSR controlled stress rheometer the applied torque C_0 is equal in magnitude to the torque C_F exerted on the inner cylinder due to the motion of the fluid. On replacing

C_F by C_0 in equation (6.3.34) and working to second order terms in Reynolds number we obtain a formula for calculating the Newtonian shear viscosity of a fluid given by

$$\eta_0 = \frac{C_0}{2\pi r_1^3 \Omega \beta_0}\left(1 - \frac{\beta_2}{\beta_0} R_a^2\right) \tag{6.3.36}$$

It is convenient to write equation (6.3.36) in the form

$$\eta_0 = f_0 \frac{(r_2^2 - r_1^2) C_0}{4\pi h r_1^2 r_2^2 \Omega}\left(1 - f_2 R_a^2\right) \tag{6.3.37}$$

where f_0 $(=2hr_2^2/[\beta_0 r_1(r_2^2 - r_1^2)])$ and f_2 $(=\beta_2/\beta_0)$ are geometry dependent factors and h is the height of the inner cylinder. It should be noted that in this form setting $f_0 = 1$ and $f_2 = 0$ gives the standard concentric cylinder formula (T.A. Instruments [24]) for determining the shear viscosity of a fluid on a CSR controlled stress rheometer.

The non-dimensional geometry dependent constants β_0 and β_2, and therefore the geometry dependent factors f_0 and f_2, can be determined from the numerical solution of equations (6.3.19), (6.3.28), (6.3.29) and (6.3.22) subject to the relevant boundary conditions.

6.4 Finite difference method of solution for the equations obtained from the fluid inertia perturbation theory

In this chapter we shall consider three CSR concentric cylinder geometries with inner cylinder radii $r_1 = 12\cdot5$ mm, $r_1 = 15$ mm and $r_1 = 18\cdot5$ mm which we shall refer to as the wide, medium and narrow gap CSR geometries respectively. All three geometries have outer cylinder radii $r_2 = 20\cdot75$ mm and axial dimensions $z_1 = 1$ mm and $z_2 = 51$ mm. The medium gap and narrow gap geometries are commercially available (TA instruments [24]). The specially constructed wide gap geometry has previously been used to determine the

flow properties of large particle sewage suspensions.

With reference to figure 6.2 the gap between $z = 0$ and $z = z_1$ below the recessed inner cylinder is very small in comparison to the inner cylinder height $(z_2 - z_1)$. Also, particularly for the narrow gap geometry, the gap $(r_2 - r_1)$ between the inner and outer cylinders is small in relation to the inner cylinder radius r_1. It is therefore impractical and computationally inefficient to consider solving the equations using a finite difference method with a regular mesh over the whole flow domain. For example the use of regularly spaced meshpoints in the z-direction would dictate that 50 times more meshpoints are required between $z = z_1$ and $z = z_2$ than in the small gap between $z = 0$ and $z = z_1$. Hence very large meshes would be required in order to achieve a reasonable degree of mesh refinement in the small gap between $z = 0$ and $z = z_1$.

The greatest variation in the velocity and streamfunction profiles is expected near the recessed end (corner B in figure 6.2) and therefore a fine mesh is required in this area of the flow domain. We shall therefore use a finite difference method with an irregular mesh where the steplength varies with a geometric progression ratio. This will allow the degree of mesh refinement to be varied over the flow domain with a finer mesh near corner B.

In this section, finite difference equations will be produced for solving the equations obtained from the perturbation theory. The finite difference equations represent a system of linear equations which will be solved using the SOR iterative method described in section 3.2.4.

6.4.1 Transformation from physical domain to a computational space

In order to use a finite difference method with an irregular mesh, enabling meshpoints to be concentrated near the recessed end (corner B in figure 6.2), the flow domain is separated into three rectangular sub-domains as shown in figure 6.4.

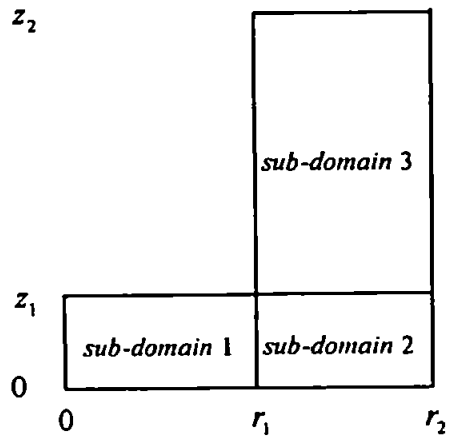

Figure 6.4:- Division of flow domain into three sub-domains.

In each sub-domain the finite difference mesh gives:-

Sub-domain 1: m_1 intervals in the r-direction and n_1 intervals in the z-direction.

Sub-domain 2: m_2 intervals in the r-direction and n_2 intervals in the z-direction.

Sub-domain 3: m_3 intervals in the r-direction and n_3 intervals in the z-direction.

In order to be able to match the finite difference equations across the interfaces between each sub-domain the conditions $n_1 = n_2$ and $m_2 = m_3$ must be imposed.

The equations obtained from the fluid inertia perturbation theory are to be solved using a finite difference method with an irregular mesh in the physical domain (r,z). However the second order accuracy of central difference formulae for a regular mesh is reduced to first order accuracy for an irregular mesh (Jones and Thompson [10]). Therefore the equations are transformed to a computational space which has uniform spacing in the transformed independent variables, corresponding to the irregular mesh in the physical plane (Anderson [32]). The transformed equations can then be discretised using central difference formulae and since a regular mesh is used in the computational space the accuracy of the finite difference approximation will be second order (Jones and Thompson [10]).

For all three sub-domains in figure 6.4 an irregular mesh, in the physical domain, is chosen with a steplength which varies with a geometric progression ratio. The irregular

mesh in each of the three sub-domains in the physical plane (r,z) is to be transformed to a regular mesh in a computational plane (x,y), where all meshpoints are separated by a unit distance of 1. With reference to figure 6.4 the origin of the computational plane (x,y) is taken to be at the bottom left hand corner of each sub-domain. Noting that we are working with the non-dimensional variables defined in equation (6.3.7) the transformation for each of the three sub-domains is given by

Sub-domain 1:- $$r = \frac{h_1(1-\delta_1^x)}{(1-\delta_1)} \qquad z = \frac{k_1(1-\varepsilon_1^y)}{(1-\varepsilon_1^y)} \tag{6.4.1}$$

where $x = 0$ to m_1 and $y = 0$ to n_1

Sub-domain 2:- $$r = 1 + \frac{h_2(1-\delta_2^x)}{(1-\delta_2)} \qquad z = \frac{k_2(1-\varepsilon_2^y)}{(1-\varepsilon_2)} \tag{6.4.2}$$

where $x = 0$ to m_2 and $y = 0$ to n_2

Sub-domain 3:- $$r = 1 + \frac{h_3(1-\delta_3^x)}{(1-\delta_3)} \qquad z = z_1 + \frac{k_3(1-\varepsilon_3^y)}{(1-\varepsilon_3)} \tag{6.4.3}$$

where $x = 0$ to m_3 and $y = 0$ to n_3

In equations (6.4.1) to (6.4.3) h_s for $s = 1,2,3$, in sub-domains 1, 2 and 3 respectively denotes the steplength from the origin of the sub-domain to the first meshpoint in the r-direction. Similarly k_s for $s = 1,2,3$ in equations (6.4.1) to (6.4.3) denotes the steplength from the origin of the sub-domain to the first meshpoint in the z-direction. The geometric progression ratios δ_s and ε_s determine the degree of non-uniformity in the finite difference mesh. It has already been noted that we must set $n_1 = n_2$ and $m_2 = m_3$. Similarly in order to

be able to match the finite difference equations across the interfaces between each sub-domain we must also set $k_1 = k_2$, $\varepsilon_1 = \varepsilon_2$, $h_2 = h_3$ and $\delta_2 = \delta_3$. On considering the limit of equations (6.4.1) to (6.4.3) as δ_s and ε_s tend to 1 we return to a regular finite difference mesh. For example the limit of equation (6.4.1) as $\delta_s \to 1$ and $\varepsilon_s \to 1$ gives $r = h_1 x$ for $x = 0$ to m_1 and $z = k_1 y$ for $y = 0$ to n_1.

6.4.2 Transformations of the derivative terms

We consider the transformation of a function $u(r,z)$ from the physical plane (r,z) to the computational plane (x,y) by letting $u(r,z)$ be transformed to $u_s(x,y)$ for $s = 1,2 \text{ and } 3$ in sub-domains 1, 2 and 3 respectively. Note that it is only the independent variables which are transformed. The value of the function $u_s(x,y)$ in the computational plane (x,y) is identical to the value of the function $u(r,z)$ at the corresponding meshpoint in the physical plane (r,z). Using equations (6.4.1) to (6.4.3) the transformations for the first and second order derivatives of $u(r,z)$ are given by

$$\frac{\partial u}{\partial r} = A_s \frac{\partial u_s}{\partial x} \tag{6.4.4}$$

$$\frac{\partial^2 u}{\partial r^2} = A_s^2 \frac{\partial^2 u_s}{\partial x^2} + B_s \frac{\partial u_s}{\partial x} \tag{6.4.5}$$

$$\frac{\partial u}{\partial z} = D_s \frac{\partial u_s}{\partial y} \tag{6.4.6}$$

$$\frac{\partial^2 u}{\partial z^2} = D_s^2 \frac{\partial^2 u_s}{\partial y^2} + E_s \frac{\partial u_s}{\partial y} \tag{6.4.7}$$

for $s = 1,2,3$, where the coefficients A_s, B_s, D_s and E_s are given by

$$A_s = \frac{-(1-\delta_s)}{h_s \ln(\delta_s)\delta_s^x} \qquad B_s = \frac{-(1-\delta_s)^2}{h_s^2 \ln(\delta_s)\delta_s^{2x}} \tag{6.4.8}$$

$$D_s = \frac{-(1-\varepsilon_s)}{k_s \ln(\varepsilon_s)\varepsilon_s^{\,y}} \qquad E_s = \frac{-(1-\varepsilon_s)^2}{k_s^2 \ln(\varepsilon_s)\varepsilon_s^{2y}} \tag{6.4.9}$$

for $s = 1,2,3$.

It is also convenient to define a coefficient (denoted by C_s) which represents the transformation of the quantity $1/r$ from the physical plane (r,z) to the computational plane (x,y). On using equations (6.4.1) to (6.4.3) the coefficient C_s is given in each sub-domain by

Sub-domain 1:- $$C_1 = \frac{(1-\delta_1)}{h_1(1-\delta_1^x)} \tag{6.4.10}$$

Sub-domains 2 *and* 3:- $$C_s = \frac{(1-\delta_s)}{[1-\delta_s + h_s(1-\delta_s^x)]} \qquad s = 2,3 \tag{6.4.11}$$

6.4.3 Finite difference equations for the zero order component of the primary velocity $v_{\theta 0}(r,z)$

We let the primary velocity function $v_{\theta 0}(r,z)$ be transformed to $v_{0_s}(x,y)$ for $s = 1,2,3$ in sub-domains 1, 2 and 3 respectively. Therefore, from equations (6.4.4) to (6.4.11), equation (6.3.19) can be transformed to the computational plane (x,y) to give a partial differential equation for $v_{0_s}(x,y)$ as

$$A_s^2 \frac{\partial^2 v_{0_s}}{\partial x^2} + (B_s + A_s C_s)\frac{\partial v_{0_s}}{\partial x} - C_s^2 v_{0_s} + D_s^2 \frac{\partial^2 v_{0_s}}{\partial y^2} + E_s \frac{\partial v_{0_s}}{\partial y} = 0 \tag{6.4.12}$$

for $s = 1,2,3$, where the coefficients A_s, B_s, C_s, D_s and E_s for each of the three sub-domains are given in equations (6.4.8) to (6.4.11).

The velocity $v_{0_s}(x,y)$ over the xy-plane is denoted at each meshpoint (i,j) by $v_{0_s\,i,j}$ where i denotes its position in the x-direction and j denotes its position in the y-direction. It is seen in equations (6.4.8) to (6.4.11) that the coefficients A_s, B_s and C_s are

functions of x only and the coefficients D_s and E_s are functions of y only. Therefore for the meshpoint node notation used the coefficients A_s, B_s and C_s are only dependent on the discrete variable i and the coefficients D_s and E_s are only dependent on the discrete variable j. It is noted that all meshpoints in the computational plane (x,y) are separated by a unit distance of 1 in both the x-direction and the y-direction. Therefore on using central difference formulae for regularly spaced meshpoints, as described in section 3.2.1, to represent the derivative terms in equation (6.4.12) it can be discretised as

$$v_{0s\ i,j} = \frac{1}{e_s(i,j)}\left[a_s(i)\, v_{0s\ i+1,j} + b_s(i)\, v_{0s\ i-1,j} + c_s(j)\, v_{0s\ i,j+1} + d_s(j)\, v_{0s\ i,j-1}\right] \tag{6.4.13}$$

where $i = 1$ to $m_s - 1$ and $j = 1$ to n_s for $s = 1,3$
$i = 1$ to $m_s - 1$ and $j = 1$ to $n_s - 1$ for $s = 2$

and

$$a_s(i) = A_s^2 + (B_s + A_s C_s)/2 \qquad b_s(i) = A_s^2 - (B_s + A_s C_s)/2$$

$$c_s(j) = D_s^2 + E_s/2 \qquad d_s(j) = D_s^2 - E_s/2$$

$$e_s(i,j) = (2A_s^2 + 2D_s^2 + C_s^2) \tag{6.4.14}$$

are discrete functions which can be determined using equations (6.4.8) to (6.4.11).

Since all meshpoints in the xy-plane are separated by a unit distance of 1, the discrete functions $a_s(i)$, $b_s(i)$, $c_s(j)$, $d_s(j)$ and $e_s(i,j)$ can be calculated at each meshpoint (i,j) by making the substitutions $x = i$ and $y = j$ in equations (6.4.8) to (6.4.11). Therefore for a given geometry and finite difference mesh the discrete functions $a_s(i)$, $b_s(i)$, $c_s(j)$, $d_s(j)$ and $e_s(i,j)$ can be evaluated at each meshpoint (i,j) and stored as an array to reduce the computational time.

In sub-domains 1 and 3 equation (6.4.13) is to be applied on the free surface boundaries (for $j = n_1$ and $j = n_3$). Therefore a row of 'fictitious points' (for $j = n_1 + 1$ and $j = n_3 + 1$) must be introduced above these boundaries. On these free surface boundaries the

boundary condition $\partial v_{\theta 0}/\partial z = 0$ is to be applied, which from equation (6.4.6) transforms to $\partial v_{0_s}/\partial y = 0$ for $s = 1, 3$, in the computational plane (x, y). Using central difference formulae to represent the derivative $\partial v_{0_s}/\partial y$ the velocity $v_{0_s\ i,j}$ on the 'free surface' boundaries will satisfy the condition

$$v_{0_s\ i,n_s+1} = v_{0_s\ i,n_s-1} \tag{6.4.15}$$

for $i = 1$ to $m_s - 1$ $(s = 1, 3)$.

Equation (6.4.15) is used to update the values of $v_{0_s\ i,n_s+1}$ at the 'fictitious points' after equation (6.4.13) has been applied for $j = 1$ to n_s $(s = 1, 3)$. These updated values for $v_{0_s\ i,n_s+1}$ will be required when equation (6.4.13) is applied at $j = n_s$ in the next iteration of the SOR method.

Unless the steplengths h_s and k_s and the geometric ratios δ_s and ε_s are specifically chosen the coefficients A_s, B_s, C_s, D_s and E_s will be different in each of the three sub-domains. It then follows that the partial differential equation for $v_{0_s}(x, y)$, given by equation (6.4.12), will also be different in each sub-domain. Therefore equation (6.4.13) is not applicable at meshpoints which lie on the interfaces between the sub-domains defined in figure 6.4. In order to produce a finite difference method where the choice of mesh is as flexible as possible, we consider the finite difference equations at meshpoints on the interfaces between sub-domains in terms of irregularly spaced meshpoints in the physical plane (r, z).

Interface between sub-domains 1 and 2

Meshpoints on the interface between sub-domains 1 and 2 are considered to lie in both sub-domain 1 (where $i = m_1$) and in sub-domain 2 (where $i = 0$). The velocity

$v_{\theta 0}(r,z)$ on this interface is then denoted at each meshpoint by $v_{01\ m_1,j}$ (for $j=1$ to n_1-1) to correspond to the meshpoint notation for sub-domain 1 and by $v_{02\ 0,j}$ (for $j=1$ to n_2-1) to correspond to the meshpoint notation for sub-domain 2. A typical meshpoint lying on the interface between sub-domains 1 and 2 is presented in figure 6.5.

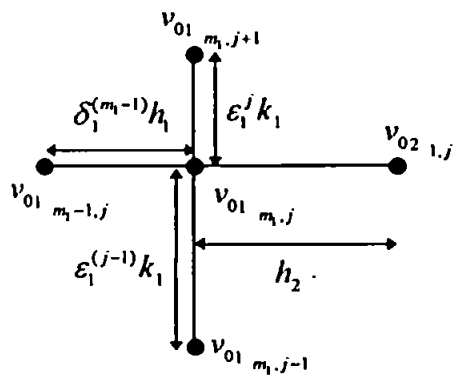

Figure 6.5:- Surrounding meshpoints and steplengths for a typical meshpoint lying on the interface between sub-domains 1 and 2.

A finite difference representation for the derivatives of $v_{\theta 0}(r,z)$, on the interface between sub-domains 1 and 2, is obtained by considering Taylor series expansions of the derivatives in terms of the four meshpoints and steplengths surrounding the meshpoints (m_1,j) shown in figure 6.5. It can be shown that

$$\frac{\partial v_{\theta 0}}{\partial r}=\frac{\delta_1^{2(m_1-1)}h_1^2\,v_{02\ 1,j}+(h_2^2-\delta_1^{2(m_1-1)}h_1^2)\,v_{01\ m_1,j}-h_2^2\,v_{01\ m_1-1,j}}{\delta_1^{(m_1-1)}h_1\,h_2(\delta_1^{(m_1-1)}h_1+h_2)} \tag{6.4.16}$$

Similar finite difference formulae for the representation of the derivatives $\partial^2 v_{\theta 0}/\partial r^2$ and $\partial^2 v_{\theta 0}/\partial z^2$ can be obtained and on substituting these formulae into equation (6.3.19) the finite difference equations at meshpoints lying on the interface between sub-domains 1 and 2 are given by

$$v_{01\ m_1,j}=\frac{1}{e_{m_1}(j)}\left[a_{m_1}\,v_{02\ 1,j}+b_{m_1}\,v_{01\ m_1-1,j}+c_{m_1}(j)\,v_{01\ m_1,j+1}+d_{m_1}(j)\,v_{01\ m_1,j-1}\right] \tag{6.4.17}$$

for $j=1$ to n_1-1, where

$$a_{m_1} = \frac{2+\delta_1^{(m_1-1)}h_1}{h_2(\delta_1^{(m_1-1)}h_1+h_2)} \qquad b_{m_1} = \frac{2-h_2}{\delta_1^{(m_1-1)}h_1(\delta_1^{(m_1-1)}h_1+h_2)}$$

$$c_{m_1}(j) = \frac{2}{\varepsilon_1^j(\varepsilon_1^{(j-1)}+\varepsilon_1^j)k_1^2} \qquad d_{m_1}(j) = \frac{2}{\varepsilon_1^{(j-1)}(\varepsilon_1^{(j-1)}+\varepsilon_1^j)k_1^2}$$

$$e_{m_1}(j) = 1+\frac{2+\delta_1^{(m_1-1)}h_1-h_2}{\delta_1^{(m_1-1)}h_1h_2}+\frac{2}{\varepsilon_1^{(j-1)}\varepsilon_1^j k_1^2} \tag{6.4.18}$$

It is noted that in order to match the finite difference equations across the interface between sub-domains 1 and 2 we let

$$v_{02\ 0,j} = v_{01\ m_1,j} \qquad \text{for} \qquad j=1 \text{ to } n_1-1 \tag{6.4.19}$$

when the values of $v_{01\ m_1,j}$ have been obtained from equation (6.4.17).

Interface between sub-domains 2 and 3

The velocity $v_{\theta 0}(r,z)$ is denoted at each meshpoint on this interface by $v_{02\ i,n_2}$ (for $i=1$ to m_2-1) and $v_{03\ i,0}$ (for $i=1$ to m_3-1). Finite difference formulae for the representation of the derivatives of $v_{\theta 0}(r,z)$ can be obtained by considering the surrounding meshpoints and steplengths of a typical meshpoint on the interface between sub-domains 2 and 3. On substitution of these formulae into equation (6.3.19) we obtain finite difference equations at meshpoints on this interface as

$$v_{02\ i,n2} = \frac{1}{e_{n_2}(i)}\left[a_{n_2}(i)\,v_{02\ i+1,n_2}+b_{n_2}(i)\,v_{02\ i-1,n_2}+c_{n_2}\,v_{03\ i,1}+d_{n_2}\,v_{02\ i,n_2-1}\right] \tag{6.4.20}$$

for $i=1$ to m_2-1, where

$$a_{n_2}(i) = \frac{2r+\delta_2^{(i-1)}h_2}{\delta_2^i h_2^2(\delta_2^{(i-1)}+\delta_2^i)r} \qquad b_{n_2}(i) = \frac{2r-\delta_2^i h_2}{\delta_2^{(i-1)}h_2^2(\delta_2^{(i-1)}+\delta_2^i)r}$$

$$c_{n_2} = \frac{2}{k_3(\varepsilon_2^{(n_2-1)}+k_3)} \qquad d_{n_2} = \frac{2}{\varepsilon_2^{(n_2-1)}k_2(\varepsilon_2^{(n_2-1)}+k_3)}$$

$$e_{n_2}(i) = \frac{1}{r^2} + \frac{2r + h_2(\delta_2^{(i-1)} - \delta_2^i)}{\delta_2^{(i-1)}\delta_2^i h_2^2 r} + \frac{2}{\varepsilon_2^{(n_2-1)} k_2 k_3} \tag{6.4.21}$$

On making the substitution $x = i$ in equation (6.4.2) the value of r in the discrete functions $a_{n_2}(i)$, $b_{n_2}(i)$ and $e_{n_2}(i)$ can be obtained using $r = 1 + h_2(1-\delta_2^i)/(1-\delta_2)$. It is noted that in order to match the finite difference equations across the interface between sub-domains 2 and 3 we let

$$v_{03\ i,0} = v_{02\ i,n_2} \qquad \text{for} \qquad i = 1 \text{ to } m_2 - 1 \tag{6.4.22}$$

when the values of $v_{02\ i,n_2}$ have been obtained from equation (6.4.20).

The iterative procedure for solving the finite difference equations presented in this section is given in appendix 6.1

6.4.4 Finite difference equations for the streamfunction $\psi(r,z)$

Transforming from the physical plane (r,z) to the computational plane (x,y), we let the streamfunction $\psi(r,z)$ be transformed to $\psi_s(x,y)$ and the variable $\phi(r,z)$ be transformed to $\phi_s(x,y)$ for $s = 1,2,3$ in sub-domains 1, 2 and 3 respectively. Therefore, from equations (6.4.4) to (6.4.11), the coupled equations (6.3.28) and (6.3.29) can be transformed to the computational plane (x,y) to give partial differential equations for $\phi_s(x,y)$ and $\psi_s(x,y)$ as

$$A_s^2 \frac{\partial^2 \phi_s}{\partial x^2} + (B_s - A_s C_s)\frac{\partial \phi_s}{\partial x} + D_s^2 \frac{\partial^2 \phi_s}{\partial y^2} + E_s \frac{\partial \phi_s}{\partial y} = -2 D_s v_{0s} \frac{\partial v_{0s}}{\partial y} \tag{6.4.23}$$

$$A_s^2 \frac{\partial^2 \psi_s}{\partial x^2} + (B_s - A_s C_s)\frac{\partial \psi_s}{\partial x} + D_s^2 \frac{\partial^2 \psi_s}{\partial y^2} + E_s \frac{\partial \psi_s}{\partial y} = \phi_s \tag{6.4.24}$$

for $s = 1, 2, 3$, where the coefficients A_s, B_s, C_s, D_s and E_s are given in equations (6.4.8) to (6.4.11).

In equation (6.4.23) $v_{0_s}(x,y)$ is known at each meshpoint from the finite difference solution of $v_{0_s\ i,j}$. Therefore, on using central difference formulae for regularly spaced meshpoints, the right hand side of equation (6.4.23) (denoted by the discrete function $f_s(i,j)$) can be calculated at each meshpoint using the formula

$$f_s(i,j) = g_s(j)\, v_{0_s\ i,j}\left[v_{0_s\ i,j+1} - v_{0_s\ i,j-1}\right] \tag{6.4.25}$$

where $i = 1$ to $m_s - 1$ and $j = 1$ to $n_s - 1$ for $s = 1, 2, 3$

The discrete function $g_s(j) = -D_s$ in equation (6.4.25) can be calculated at each meshpoint by making the substitution $y = j$ in the D_s coefficients given in equation (6.4.9). The streamfunction $\psi_s(x,y)$ and the variable $\phi_s(x,y)$ over the xy-plane are denoted at each meshpoint (i,j) by $\psi_{s\ i,j}$ and $\phi_{s\ i,j}$ respectively. On using central difference formulae for regularly spaced meshpoints to represent the derivative terms in equations (6.4.23) and (6.4.24) the coupled equations can be discretised as

$$\phi_{s\ i,j} = \frac{1}{e_s(i,j)}\left[a_s(i)\,\phi_{s\ i+1,j} + b_s(i)\,\phi_{s\ i-1,j} + c_s(j)\,\phi_{s\ i,j+1} + d_s(j)\,\phi_{s\ i,j-1} - f_s(i,j)\right] \tag{6.4.26}$$

$$\psi_{s\ i,j} = \frac{1}{e_s(i,j)}\left[a_s(i)\,\psi_{s\ i+1,j} + b_s(i)\,\psi_{s\ i-1,j} + c_s(j)\,\psi_{s\ i,j+1} + d_s(j)\,\psi_{s\ i,j-1} - \phi_{s\ i,j}\right] \tag{6.4.27}$$

where $i = 1$ to $m_s - 1$ and $j = 1$ to $n_s - 1$ for $s = 1, 2, 3$

and

$$a_s(i) = A_s^2 + (B_s - A_s C_s)/2 \qquad b_s(i) = A_s^2 - (B_s - A_s C_s)/2$$

$$c_s(j) = D_s^2 + E_s/2 \qquad d_s(j) = D_s^2 - E_s/2$$

$$e_s(i,j) = 2A_s^2 + 2D_s^2 \tag{6.4.28}$$

are discrete functions which can be calculated at each meshpoint (i,j) by making the substitutions $x = i$ and $y = j$ in equations (6.4.8) to (6.4.11).

As for $v_{\theta 0}(r,z)$, we consider finite difference equations for $\psi(r,z)$ and $\phi(r,z)$ at meshpoints on the interfaces between sub-domains in terms of irregularly spaced meshpoints in the physical plane (r,z).

Interface between sub-domains 1 and 2

The streamfunction $\psi(r,z)$ is denoted at each meshpoint on this interface by $\psi_{1\ m_1,j}$ (for $j=1$ to n_1-1) and $\psi_{2\ 0,j}$ (for $j=1$ to n_2-1). Similarly the variable $\phi(r,z)$ is denoted by $\phi_{1\ m_1,j}$ (for $j=1$ to n_1-1) and $\phi_{2\ 0,j}$ (for $j=1$ to n_2-1). Finite difference formulae for the representation of derivatives of $\phi(r,z)$ and $\psi(r,z)$ can be obtained by considering the surrounding meshpoints and steplengths of a typical meshpoint on the interface between sub-domains 1 and 2. On substitution of these formulae into equations (6.3.28) and (6.3.29) the finite difference equations at meshpoints lying on this interface are given by

$$\phi_{1\ m_1,j} = \frac{1}{e_{m_1}(j)}\left[a_{m_1}\,\phi_{2\ 1,j} + b_{m_1}\,\phi_{1\ m_1-1,j} + c_{m_1}(j)\phi_{1\ m_1,j+1} + d_{m_1}(j)\,\phi_{1\ m_1,j-1} - f_{m1}(i,j)\right] \quad (6.4.29)$$

$$\psi_{1\ m_1,j} = \frac{1}{e_{m_1}(j)}\left[a_{m_1}\,\psi_{2\ 1,j} + b_{m_1}\,\psi_{1\ m_1-1,j} + c_{m_1}(j)\psi_{1\ m_1,j+1} + d_{m_1}(j)\,\psi_{1\ m_1,j-1} - \phi_{1\ m_1,j}\right] \quad (6.4.30)$$

for $j=1$ to n_1-1, where

$$a_{m_1} = \frac{2-\delta_1^{(m_1-1)}h_1}{h_2(\delta_1^{(m_1-1)}h_1+h_2)} \qquad b_{m_1} = \frac{2+h_2}{\delta_1^{(m_1-1)}h_1(\delta_1^{(m_1-1)}h_1+h_2)}$$

$$c_{m_1}(j) = \frac{2}{\varepsilon_1^j(\varepsilon_1^{(j-1)}+\varepsilon_1^j)k_1^2} \qquad d_{m_1}(j) = \frac{2}{\varepsilon_1^{(j-1)}(\varepsilon_1^{(j-1)}+\varepsilon_1^j)k_1^2}$$

$$e_{m_1}(j) = \frac{2+h_2-\delta_1^{(m_1-1)}h_1}{\delta_1^{(m_1-1)}h_1\,h_2} + \frac{2}{\varepsilon_1^{(j-1)}\varepsilon_1^j k_1^2}$$

$$f_{m_1}(j) = -\frac{2\,v_{01\ m_1,j}\left[\varepsilon_1^{2(j-1)}\,v_{01\ m_1,j+1} + (\varepsilon_1^{2j}-\varepsilon_1^{2(j-1)})\,v_{01\ m_1,j} - \varepsilon_1^2\,v_{01\ m_1,j-1}\right]}{\varepsilon_1^j\varepsilon_1^{(j-1)}(\varepsilon_1^j+\varepsilon_1^{(j-1)})k_1} \quad (6.4.31)$$

The discrete function $f_{m_1}(j)$ can be calculated at each meshpoint on the interface using the values obtained from the finite difference solution of $v_{01\ m_1,j}$. It is noted that in order to match the finite difference equations across the interface between sub-domains 1 and 2 we set $\phi_{2\ 0,j} = \phi_{1\ m_1,j}$ for $j = 1$ to $n_1 - 1$ when the value of $\phi_{1\ m_1,j}$ is obtained from equation (6.4.29). Similarly we set $\psi_{2\ 0,j} = \psi_{1\ m_1,j}$ for $j = 1$ to $n_1 - 1$ when the value of $\psi_{1\ m_1,j}$ is obtained from equation (6.4.30).

Interface between sub-domains 2 and 3

The streamfunction $\psi(r,z)$ is denoted at each meshpoint on this interface by $\psi_{2\ i,n_2}$ (for $i = 1$ to $m_2 - 1$) and by $\psi_{3\ i,0}$ (for $i = 1$ to $m_3 - 1$). Similarly the variable $\phi(r,z)$ is denoted by $\phi_{2\ i,n_2}$ (for $i = 1$ to $m_2 - 1$) and $\phi_{3\ i,0}$ (for $i = 1$ to $m_3 - 1$). The finite difference equations at meshpoints on the interface between sub-domains 2 and 3 are given by

$$\phi_{2\ i,n_2} = \frac{1}{e_{n_2}(i)}\left[a_{n_2}(i)\,\phi_{2\ i+1,n_2} + b_{n_2}(i)\,\phi_{2\ i-1,n_2} + c_{n_2}\,\phi_{3\ i,1} + d_{n_2}\,\phi_{2\ i,n_2-1} - f_{n_2}(i)\right] \tag{6.4.32}$$

$$\psi_{2\ i,n_2} = \frac{1}{e_{n_2}(i)}\left[a_{n_2}(i)\,\psi_{2\ i+1,n_2} + b_{n_2}(i)\,\psi_{2\ i-1,n_2} + c_{n_2}\,\psi_{3\ i,1} + d_{n_2}\,\psi_{2\ i,n_2-1} - \phi_{2\ i,n_2}\right] \tag{6.4.33}$$

for $i = 1$ to $m_2 - 1$, where

$$a_{n_2}(i) = \frac{2r - \delta_2^{(i-1)} h_2}{\delta_2^i\, h_2^2 (\delta_2^{(i-1)} + \delta_2^i)\, r} \qquad b_{n_2}(i) = \frac{2r + \delta_2^i\, h_2}{\delta_2^{(i-1)} h_2^2 (\delta_2^{(i-1)} + \delta_2^i)\, r}$$

$$c_{n_2} = \frac{2}{k_3(\varepsilon_2^{(n_2-1)} + k_3)} \qquad d_{n_2} = \frac{2}{\varepsilon_2^{(n_2-1)} k_2 (\varepsilon_2^{(n_2-1)} + k_3)}$$

$$e_{n_2}(i) = \frac{2r + h_2(\delta_2^i - \delta_2^{(i-1)})}{\delta_2^{(i-1)} \delta_2^i\, h_2^2\, r} + \frac{2}{\varepsilon_2^{(n_2-1)} k_2 k_3}$$

$$f_{n_2}(i) = -\frac{2v_{02\ i,n_2}\left[\varepsilon_2^{2(n_2-1)}k_2^2 v_{03\ i,1} + (k_3^2 - \varepsilon_2^{2(n_2-1)}k_2^2)v_{02\ i,n_2} - k_3^2 v_{02\ i,n_2-1}\right]}{\varepsilon_2^{(n_2-1)}k_2k_3(\varepsilon_2^{(n_2-1)}k_2 + k_3)r} \tag{6.4.34}$$

On making the substitution $x = i$ in equation (6.4.2) the value of r in the discrete functions $a_{n_2}(i)$, $b_{n_2}(i)$, $e_{n_2}(i)$ and $f_{n_2}(i)$ can be obtained using $r = 1 + h_2(1-\delta_2^i)/(1-\delta_2)$. The discrete function $f_{n_2}(i)$ can be evaluated at each meshpoint on the interface using the values obtained from the finite difference solution of $v_{02\ i,j}$ and $v_{03\ i,j}$. In order to match the finite difference equations across the interface between sub-domains 2 and 3 we set $\phi_{3\ i,0} = \phi_{2\ i,n_2}$ for $i = 1$ to $m_2 - 1$ when the value of $\phi_{2\ i,n_2}$ is obtained from equation (6.4.32). Similarly we set $\psi_{3\ i,0} = \psi_{2\ i,n_2}$ for $i = 1$ to $m_2 - 1$ when the value of $\psi_{2\ i,n_2}$ is obtained from equation (6.4.33).

As presented in figure 6.3 the boundary conditions for the variable $\phi(r,z)$ on boundaries BC, DE and OE are dependent on the streamfunction $\psi(r,z)$. Therefore once each iteration of the SOR method is completed, the boundary conditions for $\phi_{s\ i,j}$ on these boundaries must be re-calculated using the most recent values obtained for $\psi_{s\ i,j}$. Using the transformations for derivative terms in equations (6.4.4) to (6.4.7) we consider the boundary conditions for $\phi_{s\ i,j}$ on boundaries BC, DE and OE.

Boundary OE

On this boundary $\partial\psi/\partial z = 0$ and therefore from equation (6.4.6) we have $\partial\psi_s/\partial y = 0$. Using this result in equation (6.4.7) the boundary condition $\phi = \partial^2\psi/\partial z^2$ is transformed to the xy-plane as

$$\phi_s = D_s^2 \frac{\partial^2 \psi_s}{\partial y^2} \tag{6.4.35}$$

for $s = 1, 2$ where the coefficient D_s is given in equation (6.4.9).

To evaluate $\partial^2 \psi_s / \partial y^2$ on the boundary a quadratic function is fitted through the finite difference values $\psi_{s\ i,j}$ at the three meshpoints closest to the boundary (*i.e.* $j = 0, 1, 2$). Using this quadratic function and noting that on this boundary $\psi_s = 0$ and $\partial \psi_s / \partial y = 0$, the boundary condition for $\phi_{s\ i,j}$ is given by

$$\phi_{s\ i,0} = d_s(0)\, \psi_{s\ i,1} \tag{6.4.36}$$

where $i = 1$ to m_s for $s = 1$ and $i = 0$ to $m_s - 1$ for $s = 2$

The discrete function $d_s(j) = 2\, D_s^2$ can be calculated at each meshpoint on the boundary by making the substitution $y = j$ in the D_s coefficient in equation (6.4.9).

Boundary DE

On this boundary $\partial \psi / \partial r = 0$ and therefore from equation (6.4.4) we have $\partial \psi_s / \partial x = 0$. Using this result in equation (6.4.5) the boundary condition $\phi = \partial^2 \psi / \partial r^2$ is transformed to the *xy*-plane as

$$\phi_s = A_s^2 \frac{\partial^2 \psi_s}{\partial x^2} \tag{6.4.37}$$

for $s = 2, 3$ where the coefficient A_s is given in equation (6.4.8).

To evaluate $\partial^2 \psi_s / \partial x^2$ on the boundary a quadratic function is fitted through the finite difference values $\psi_{s\ i,j}$ at the three meshpoints closest to the boundary (*i.e.* $i = m_s,\ m_s - 1,\ m_s - 2$). Using this quadratic function and noting that on this boundary $\psi_s = 0$ and $\partial \psi_s / \partial x = 0$, the boundary condition for $\phi_{s\ i,j}$ is given by

$$\phi_{s\ m_s,j} = a_s(m_s)\,\psi_{s\ m_s-1,j} \tag{6.4.38}$$

where $j = 1$ to n_s for $s = 2$ and $j = 0$ to $n_s - 1$ for $s = 3$

The discrete function $a_s(i) = 2\,A_s^2$ can be calculated at each meshpoint on the boundary by making the substitution $x = i$ in the A_s coefficient in equation (6.4.8).

Boundary BC

We have $\partial\psi/\partial r = 0$ on this boundary which lies in the same direction as boundary OE. Therefore in the transformed xy-plane the boundary condition for boundary BC is given by equation (6.4.37) (for $s = 3$).

To evaluate the value of $\partial^2\psi_s/\partial x^2$ on the boundary a quadratic function is fitted through the finite difference values $\psi_{s\ i,j}$ at the three meshpoints closest to the boundary (*i.e.* $i = 0,1,2$). Using this quadratic function and noting that on this boundary $\psi_s = 0$ and $\partial\psi_s/\partial x = 0$, the boundary condition for $\phi_{s\ i,j}$ is given by

$$\phi_{3\ 0,j} = a_3(0)\,\psi_{3\ 1,j} \tag{6.4.39}$$

where $j = 1$ to $n_3 - 1$

The discrete function $a_3(i) = 2\,A_3^2$ can be calculated at each meshpoint on the boundary by making the substitution $x = i$ in the A_3 coefficient of equation (6.4.8).

Meshpoint at the corner point B

Equation (6.4.39) is not applicable at the meshpoint ($j = 0$) which lies on corner B in figure 6.2 and the boundary condition for $\phi(r,z)$ at this corner must be calculated using equation (6.3.30). It is noted that the meshpoint on this corner is considered to lie in sub-domains 1, 2 and 3 (at meshpoints (m_1,n_1), $(0,n_2)$ and $(0,0)$ respectively). The conditions

$\partial\psi/\partial r = 0$ and $\partial\psi/\partial z = 0$ apply at the corner and therefore from equations (6.4.4) and (6.4.6) we respectively have $\partial\psi_s/\partial x = 0$ and $\partial\psi_s/\partial y = 0$. On using these results in equations (6.4.5) and (6.4.7) and using equation (6.3.30), the boundary condition for ϕ_s on corner B is transformed to the xy-plane as

$$\phi_s = A_s^2 \frac{\partial^2 \psi_s}{\partial x^2} + D_s^2 \frac{\partial^2 \psi_s}{\partial y^2} \tag{6.4.40}$$

where the coefficients A_s (for $s = 2,3$) and D_s (for $s = 1,2$) are given in equations (6.4.8) and (6.4.9) respectively.

To evaluate $\partial^2\psi_s/\partial x^2$ on corner B, from the finite difference values $\psi_{s\ i,j}$, a quadratic function is fitted through the three meshpoints in sub-domain 2 at $j = n_2$ which are closest to the corner (*i.e.* at $i = 0,1,2$). Similarly $\partial^2\psi_s/\partial y^2$ is evaluated on corner B, from the finite difference values $\psi_{s\ i,j}$, by fitting a quadratic function through the three meshpoints in sub-domain 2 at $i = 0$ which are closest to the corner (*i.e.* at $j = n_2, n_2 - 1, n_2 - 2$). On using these quadratic functions and noting that on corner B $\psi_s = 0$, $\partial\psi_s/\partial x = 0$ and $\partial\psi_s/\partial y = 0$ the boundary condition for $\phi_{s\ i,j}$ is given by

$$\phi_{2\ 0,n_2} = a_2(0)\,\psi_{2\ 1,n_2} + d_2(n_2)\,\psi_{2\ 0,n_2-1} \tag{6.4.41}$$

where the discrete functions $a_2(i) = 2\,A_2^2$ and $d_2(j) = 2\,D_2^2$ can be calculated by making the substitutions $x = i$ and $y = j$ in the A_2 and D_2 coefficients of equations (6.4.8) and (6.4.9) respectively. When the boundary condition for $\phi_{2\ 0,n_2}$ has been calculated we set $\phi_{1\ m_1,n_1} = \phi_{2\ 0,n_2}$ and $\phi_{3\ 0,0} = \phi_{2\ 0,n_2}$.

The iterative procedure for solving the finite difference equations presented in this section is given in appendix 6.2

6.4.5 Determination of the secondary flow velocities $v_{r1}(r,z)$ and $v_{z1}(r,z)$ from the finite difference solution for the streamfunction $\psi(r,z)$

Transforming from the physical plane (r,z) to the computational plane (x,y), we let $v_{r1}(r,z)$ and $v_{z1}(r,z)$ be transformed to $v_{rs}(x,y)$ and $v_{zs}(x,y)$ respectively for $s=1,2,3$. Using equations (6.4.4) to (6.4.11), equation (6.3.25) is transformed to the xy-plane to give expressions for $v_{rs}(x,y)$ and $v_{zs}(x,y)$ as

$$v_{rs} = C_s D_s \frac{\partial \psi_s}{\partial y} \qquad\qquad v_{zs} = -A_s C_s \frac{\partial \psi_s}{\partial x} \tag{6.4.42}$$

for $s=1,2,3$, where the coefficients A_s, C_s and D_s are given in equations (6.4.8) to (6.4.11).

The secondary velocities $v_{rs}(x,y)$ and $v_{zs}(x,y)$ over the xy-plane are denoted at each meshpoint (i,j) by $v_{rs\ i,j}$ and $v_{zs\ i,j}$ respectively. On using central difference formulae to represent the derivative terms in equation (6.4.42) it can be discretised to give

$$v_{rs\ i,j} = a_s(i,j)\left[\psi_{s\ i,j+1} - \psi_{s\ i,j-1}\right] \tag{6.4.43}$$

$$v_{zs\ i,j} = b_s(i)\left[\psi_{s\ i+1,j} - \psi_{s\ i-1,j}\right] \tag{6.4.44}$$

where $i=1$ to m_s-1 and $j=1$ to n_s-1 for $s=1,2,3$

The discrete functions $a_s(i,j)=C_s D_s/2$ and $b_s(i)=-A_s C_s/2$ can be calculated at each meshpoint (i,j) by making the substitutions $x=i$ and $y=j$ in equations (6.4.8) to (6.4.11).

It is noted that equation (6.4.43) cannot be applied on the free surface boundaries ($j=n_1$ and $j=n_3$) where the value of $v_{rs\ i,j}$ is non-zero. Also, equation (6.4.44) cannot be applied on the line of symmetry ($i=0$ in sub-domain 1) where the value of $v_{zs\ i,j}$ is non-zero. The method used to calculate $v_{rs\ i,j}$ and $v_{zs\ i,j}$ on these boundaries and on the

interfaces between sub-domains is now described.

Boundary OA

Since the flow is axisymmetric $\partial\psi/\partial r = 0$ on this boundary. Therefore from equation (6.3.25) we must consider the limit of $-(1/r)\,\partial\psi/\partial r$ as r tends to zero to evaluate $v_{z1}(r,z)$ on this boundary. Using L'Hopital's rule gives

$$\lim_{r\to 0} v_{z1} = -\left.\frac{\partial^2\psi}{\partial r^2}\right|_{r=0} \tag{6.4.45}$$

Since $\partial\psi/\partial r = 0$ we have, from equation (6.4.4), $\partial\psi_s/\partial x = 0$ and using this result in equation (6.4.5) gives

$$v_{z1}\big|_{x=0} = \left[-A_1^2\frac{\partial^2\psi_1}{\partial x^2}\right]\Bigg|_{x=0} \tag{6.4.46}$$

where the coefficient A_1 is given by equation (6.4.8).

To evaluate $\partial^2\psi_1/\partial x^2$ on the boundary a quadratic function is fitted through the finite difference values $\psi_{s\ i,j}$ at the three meshpoints closest to the boundary (*i.e.* at $i = 0,1,2$). Using this quadratic function and noting that on this boundary $\psi_s = 0$ and $\partial\psi_s/\partial x = 0$, the secondary velocity $v_{z1\ 0,j}$ is given by

$$v_{z1\ 0,j} = a_1(0)\,\psi_{1\ 1,j} \tag{6.4.47}$$

for $j = 1$ to $n_1 - 1$, where the discrete function $a_1(i) = -2\,A_1^2$ can be calculated by making the substitution $x = i$ in the A_1 coefficient of equation (6.4.8).

Boundaries AB and CD

On these boundaries $\psi = 0$ and since $\partial v_{r1}/\partial z = 0$ we have, from equation

(6.3.25), the condition $\partial^2\psi/\partial z^2 = 0$ which implies that $\psi_{s\ i,n_s+1} = -\psi_{s\ i,n_s-1}$ (for $s = 1,3$).

Using this condition in equation (6.4.43) the secondary velocity $v_{rs\ i,n_s}$ is given by

$$v_{rs\ i,n_s} = -2\,a_s(i,n_s)\,\psi_{s\ i,n_s-1} \tag{6.4.48}$$

where $i = 1$ to $m_s - 1$ for $s = 1, 3$

In this equation the discrete function $a_s(i,j) = C_s\,D_s/2$ can be calculated at each meshpoint (i,j) by making the substitutions $x = i$ and $y = j$ in equations (6.4.8) to (6.4.11).

Interface between sub-domains 1 and 2

The secondary velocities $v_{r1\ m_1,j}$ and $v_{z1\ m_1,j}$ can be calculated at meshpoints on this interface using the formulae

$$v_{r1\ m_1,j} = \frac{\varepsilon_1^{2(j-1)}\,\psi_{1\ m_1,j+1} + (\varepsilon_1^{2j} - \varepsilon_1^{2(j-1)})\,\psi_{1\ m_1,j} - \varepsilon_1^2\,\psi_{1\ m_1,j-1}}{\varepsilon_1^j\,\varepsilon_1^{(j-1)}(\varepsilon_1^j + \varepsilon_1^{(j-1)})k_1} \tag{6.4.49}$$

$$v_{z1\ m_1,j} = \frac{\delta_1^{2(m_1-1)}\,\psi_{2\ 1,j} + (h_2^2 - \delta_1^{2(m_1-1)})\,\psi_{1\ m_1,j} - h_2^2\,\psi_{1\ m_1-1,j}}{\delta_1^{(m_1-1)}h_1\,h_2\,(\delta_1^{(m_1-1)}h_1 + h_2)} \tag{6.4.50}$$

for $j = 1$ to $n_1 - 1$

When the values of $v_{r1\ m_1,j}$ and $v_{z1\ m_1,j}$ have been calculated, using equations (6.4.49) and (6.5.50) respectively, we let $v_{r2\ 0,j} = v_{r1\ m_1,j}$ and $v_{z2\ 0,j} = v_{z1\ m_1,j}$ for $j = 1$ to $n_1 - 1$.

Interface between sub-domains 2 and 3

At meshpoints on this interface the secondary velocities $v_{r2\ i,n_2}$ and $v_{z2\ i,n_2}$ are calculated using the formulae

$$v_{r1\ i,n_2} = \frac{\varepsilon_2^{2(n_2-1)}\,k_2^2\,\psi_{3\ i,1} + (k_3^2 - \varepsilon_2^{2(n_2-1)}k_2^2)\,\psi_{2\ i,n_2} - k_3^2\,\psi_{2\ i,n_2-1}}{\varepsilon_2^{(n_2-1)}k_2\,k_3\,(\varepsilon_2^{(n_2-1)}k_2 + k_3)} \tag{6.4.51}$$

$$v_{z1\ i,n_2} = \frac{\delta_2^{2(i-1)}\psi_{2\ i+1,n_2} + (\delta_2^{2i} - \delta_2^{2(i-1)})\psi_{2\ i,n_2} - \delta_2^{2i}\psi_{2\ i-1,n_2}}{\delta_2^i \delta_2^{(i-1)} h_2 (\delta_2^{(i-1)} + \delta_2^i)} \tag{6.4.52}$$

for $i = 1$ to $m_2 - 1$

When the values of $v_{r1\ i,n_2}$ and $v_{z1\ i,n_2}$ have been calculated, using equations (6.4.51) and (6.5.52) respectively, we let $v_{r3\ i,0} = v_{r2\ i,n_2}$ and $v_{z3\ i,0} = v_{z2\ i,n_2}$ for $i = 1$ to $m_2 - 1$.

6.4.6 Finite difference equations for the second order component of the primary velocity function $v_{\theta 2}(r,z)$

Transforming from the physical plane (r,z) to the computational plane (x,y), we let the second order velocity function $v_{\theta 2}(r,z)$ be transformed to $v_{2s}(x,y)$ for $s = 1,2,3$. From equations (6.4.4) to (6.4.11), equation (6.3.22) can be transformed to the xy-plane to give a partial differential equation for $v_{2s}(x,y)$ as

$$A_s^2 \frac{\partial^2 v_{2s}}{\partial x^2} + (B_s - A_s C_s)\frac{\partial v_{2s}}{\partial x} - C_s^2 v_{2s} + D_s^2 \frac{\partial^2 v_{2s}}{\partial y^2} + E_s \frac{\partial v_{2s}}{\partial y}$$

$$= A_s v_{rs} \frac{\partial v_{0s}}{\partial x} + C_s v_{rs} v_{0s} + D_s v_{zs} \frac{\partial v_{0s}}{\partial y} \tag{6.4.53}$$

for $s = 1,2,3$, where the coefficients A_s, B_s, C_s, D_s and E_s are given in equations (6.4.8) to (6.4.11).

In equation (6.4.53) $v_{0s}(x,y)$ is known at each meshpoint from the finite difference solution of $v_{0s\ i,j}$. Also $v_{rs}(x,y)$ and $v_{zs}(x,y)$ can be determined at each meshpoint ($v_{rs\ i,j}$ and $v_{zs\ i,j}$) from the finite difference solution for $\psi_{s\ i,j}$. Therefore, on using central difference formulae for uniformly spaced meshpoints, the right hand side of equation (6.4.53) (denoted by the discrete function $f_s(i,j)$) can be calculated at each meshpoint using the formula

$$f_s(i,j) = ra_s(i)\, v_{rs\ i,j}\left[v_{0s\ i+1,j} - v_{0s\ i-1,j}\right] + rb_s(i)\, v_{rs\ i,j}\, v_{0s\ i,j}$$

$$+ rc_s(i)\, v_{zs\ i,j}\left[v_{0s\ i,j+1} - v_{0s\ i,j-1}\right] \qquad (6.4.54)$$

where $i = 1$ to $m_s - 1$ and $j = 1$ to $n_s - 1$ for $s = 1,2,3$.

In this equation the discrete functions $ra_s(i) = A_s/2$, $rb_s(i) = C_s$ and $rc_s(i) = D_s/2$ can be calculated at each meshpoint (i,j) by making the substitutions $x = i$ and $y = j$ in equations (6.4.8) to (6.4.11). Equation (6.4.54) is not applicable on the free surface boundaries ($j = n_1$ and $j = n_3$) as this would involve using the fictitious points ($j = n_1 + 1$ and $j = n_3 + 1$). However on these boundaries we have $v_{zs\ i,n_s} = 0$ (for $s = 1,3$) and therefore the right hand side of equation (6.4.53) for meshpoints on these free surface boundaries is given by

$$f_s(i,n_s) = ra_s(i)\, v_{rs\ i,n_s}\left[v_{0s\ i+1,n_s} - v_{0s\ i-1,n_s}\right] + rb_s(i)\, v_{rs\ i,n_s}\, v_{0s\ i,n_s} \qquad (6.4.55)$$

where $i = 1$ to $m_s - 1$ for $s = 1,3$.

The velocity $v_{2s}(x,y)$ over the xy-plane is denoted at each meshpoint (i,j) by $v_{2s\ i,j}$. It is noted that the left hand side of equation (6.4.53) for $v_{2s}(x,y)$ is of the same form as the left hand side of equation (6.4.12) for $v_{0s}(x,y)$. Therefore on modifying equation (6.4.13) to include the non-homogeneous term $f_s(i,j)$, the finite difference equations for $v_{2s\ i,j}$ are given by

$$v_{2s\ i,j} = \frac{1}{e_s(i,j)}\left[a_s(i)\, v_{2s\ i+1,j} + b_s(i)\, v_{2s\ i-1,j} + c_s(j)\, v_{2s\ i,j+1} + d_s(j)\, v_{2s\ i,j-1} - f_s(i,j)\right] \qquad (6.4.56)$$

where $i = 1$ to $m_s - 1$ and $j = 1$ to n_s for $s = 1,3$
$i = 1$ to $m_s - 1$ and $j = 1$ to $n_s - 1$ for $s = 2$

and the discrete functions $a_s(i)$, $b_s(i), c_s(j), d_s(j)$ and $e_s(i,j)$ are given in equation (6.4.14).

In sub-domains 1 and 3 equation (6.4.56) is to be applied on the free surface boundaries (for $j = n_1$ and $j = n_3$). We therefore introduce a row of 'fictitious points' (for $j = n_1 + 1$ and $j = n_3 + 1$) above these boundaries and the velocity $v_{2s\ i,j}$ will satisfy the condition

$$v_{2s\ i,n_s+1} = v_{2s\ i,n_s-1} \tag{6.4.57}$$

for $i = 1$ to $m_s - 1$ $(s = 1,3)$.

Equation (6.4.57) is used to update the values of $v_{2s\ i,n_s+1}$ at the 'fictitious points', which will be required when equation (6.4.56) is applied at $j = n_s$ in the next iteration of the SOR method.

The finite difference equations for meshpoints on the interfaces between sub-domains are considered in terms of irregularly spaced meshpoints in the physical plane (r,z).

Interface between sub-domains 1 and 2

The right hand side of equation (6.3.22) is calculated at each meshpoint on the interface between sub-domains 1 and 2 using the formula

$$f_{m_1}(j) = v_{r1\ m_1,j} \frac{\left[\delta_1^{2(m_1-1)} h_1^2\, v_{02\ 1,j} + (h_2^2 - \delta_1^{2(m_1-1)} h_1^2)\, v_{01\ m_1,j} - h_2^2\, v_{01\ m_1-1,j}\right]}{\delta_1^{(m_1-1)} h_1 h_2 (\delta_1^{(m_1-1)} h_1 + h_2)} + v_{r1\ m_1,j} v_{01\ m_1,j}$$

$$+ v_{z1\ m_1,j} \frac{\left[\varepsilon_1^{2(j-1)}\, v_{01\ m_1,j+1} + (\varepsilon_1^{2j} - \varepsilon_1^{2(j-1)})\, v_{01\ m_1,j} - \varepsilon_1^{2j}\, v_{01\ m_1,j-1}\right]}{\varepsilon_1^{(j-1)} \varepsilon_1^{j} (\varepsilon_1^{(j-1)} + \varepsilon_1^{j}) k_1} \tag{6.4.58}$$

for $j = 1$ to $n_1 - 1$.

The left hand side of equation (6.3.22) for $v_{\theta 2}(r,z)$ is of the same form as the left hand side of equation (6.3.19) for $v_{\theta 0}(r,z)$. Therefore on modifying equation (6.4.17) to include the

non-homogeneous term $f_{m_1}(j)$, the finite difference equations for meshpoints on the interface between sub-domains 1 and 2 are given by

$$v_{21\ m_1,j} = \frac{1}{e_{m_1}(j)}\left[a_{m_1} v_{22\ 1,j} + b_{m_1} v_{21\ m_1-1,j} + c_{m_1}(j) v_{21\ m_1,j+1} + d_{m_1}(j) v_{21\ m_1,j-1} - f_{m_1}(j)\right] \quad (6.4.59)$$

for $j = 1$ to $n_1 - 1$, where the discrete functions a_{m_1}, b_{m_1}, $c_{m_1}(j)$, $d_{m_1}(j)$ and $e_{m_1}(j)$ are given in equation (6.4.18).

It is noted that in order to match the finite difference equations across the interface between sub-domains 1 and 2 we let $v_{22\ 0,j} = v_{21\ m_1,j}$ for $j = 1$ to $n_1 - 1$ when the values of $v_{21\ m_1,j}$ have been obtained from equation (6.4.59).

Interface between sub-domains 2 and 3

At meshpoints on this interface the right hand side of equation (6.3.22) is given by

$$f_{n_2}(i) = v_{r2\ i,n_2} \frac{\left[\delta_2^{2(i-1)} v_{02\ i+1,n_2} + (\delta_2^{2i} - \delta_2^{2(i-1)}) v_{02\ i,n_2} - \delta_2^{2i} v_{02\ i-1,n_2}\right]}{\delta_2^{(i-1)}\delta_2^{i}(\delta_2^{(i-1)} + \delta_2^{i})h_2} + v_{r2\ i,n_2} v_{02\ i,n_2}$$

$$+ v_{z1\ i,n_2} \frac{\left[\varepsilon_2^{2(n_2-1)} k_2^2 v_{03\ i,1} + (k_3^2 - \varepsilon_2^{2(n_2-1)} k_2^2) v_{02\ i,n_2} - k_3^2 v_{02\ i,n_2-1}\right]}{\varepsilon_2^{(n_2-1)} k_2 k_3 (\varepsilon_2^{(n_2-1)} k_2 + k_3)} \quad (6.4.60)$$

On modifying equation (6.4.20) to include the non-homogeneous term $f_{n_2}(i)$, the finite difference equations for meshpoints on the interface between sub-domains 2 and 3 are given by

$$v_{22\ i,n_2} = \frac{1}{e_{n_2}(i)}\left[a_{n_2}(i) v_{22\ i+1,n_2} + b_{n_2}(i) v_{22\ i-1,n_2} + c_{n_2} v_{23\ i,1} + d_{n_2} v_{22\ i,n_2-1} - f_{n_2}(i)\right] \quad (6.4.61)$$

for $i = 1$ to $m_2 - 1$, where the discrete functions $a_{n_2}(i)$, $b_{n_2}(i)$, c_{n_2}, d_{n_2} and $e_{n_2}(i)$ are given in equation (6.4.21).

On making the substitution $x = i$ in equation (6.4.2) the value of r in the discrete functions

$a_{n_2}(i)$, $b_{n_2}(i)$ and $e_{n_2}(i)$ can be obtained using $r = 1 + h_2(1-\delta_2^i)/(1-\delta_2)$. In order to match the finite difference equations across the interface between sub-domains 2 and 3 we let $v_{23\ i,0} = v_{22\ i,n_2}$ for $i = 1$ to $m_2 - 1$ when the values of $v_{22\ i,n_2}$ have been obtained from equation (6.4.61).

The iterative procedure for solving the finite difference equations presented in this section is given in appendix 6.3

6.4.7 Calculation of the geometry dependent constants β_m from the finite difference solutions for $v_{\theta 0}(r,z)$ and $v_{\theta 2}(r,z)$.

In equation (6.3.34) the torque exerted on the inner cylinder due to the motion of the fluid is expressed in terms of the non-dimensional geometry dependent constants β_0 and β_2. These constants are to be determined from equation (6.3.35) using the velocity distributions obtained for $v_{\theta 0}(r,z)$ and $v_{\theta 2}(r,z)$ from the finite difference method. With reference to figure 6.4 the inner cylinder wall lies in sub-domain 3. On using equations (6.4.3) and (6.4.4) in equation (6.3.35) the geometry dependent constants β_m are given by

$$\beta_m = -\frac{k_3 \ln(\varepsilon_3)}{(1-\varepsilon_3)} \int_0^{n_3} \left[\frac{(1-\beta_3)}{h_3 \ln(\beta_3)} \frac{\partial v_{m3}}{\partial x} + v_{m3} \right]_{x=0} \varepsilon_3^{\,y}\, dy \qquad (6.4.62)$$

for $m = 0,2$

In the computational plane (x,y) all meshpoints are separated by a unit distance of 1 and therefore for the meshpoint node notation used we have $y = j$. The velocity distributions for $v_{m3}(x,y)$ $(m = 0,2)$ are known at a discrete number of meshpoints from the finite difference solutions for $v_{03\ i,j}$ and $v_{23\ i,j}$. Therefore on using these known velocities the continuous integral in equation (6.4.62) can be evaluated numerically, over the discrete

intervals $j=0$ to n_3, using the composite Simpsons rule (Burden and Faires [33]). In equation (6.4.62) $v_{m3}\big|_{x=0}$ is equivalent to $v_{m3\ 0,j}$ for $j=0$ to n_3. The derivative $\partial v_{m3}/\partial x\big|_{x=0}$ can be evaluated at each j by fitting a cubic function through the discrete values $v_{m3\ i,j}$ at the four meshpoints closest to the inner cylinder wall (*i.e.* $i=0,1,2,3$). Noting that all meshpoints in the xy-plane are separated by a unit distance of 1 we have

$$\left.\frac{\partial v_{m3}}{\partial x}\right|_{x=0} = \frac{18 v_{m3\ 1,j} - 11 v_{m3\ 0,j} - 9 v_{m3\ 2,j} + 2 v_{m3\ 3,j}}{6} \qquad (6.4.63)$$

for $m=0,2$.

Therefore on using equations (6.4.62) and (6.4.63) and the method described the non-dimensional geometry dependent constants β_0 and β_2 can be calculated from the finite difference solutions for $v_{\theta 0}(r,z)$ and $v_{\theta 2}(r,z)$.

6.4.8 Selection of the mesh constants in the finite difference equations

In order to give maximum choice and flexibility in the mesh used, the finite difference method has been formed to allow the steplengths to be varied by a different geometric progression ratio in each of the three sub-domains. However the accuracy and rate of convergence of the solution is maximised when derivative terms at a given meshpoint are approximated using meshpoints which are at an equal distance either side of it. If irregularly spaced meshpoints are used one order of accuracy is lost (Jones and Thompson [10]) from that given by a regular mesh. The greatest variation in velocity and streamfunction profiles, and hence the largest values of their derivatives, are expected near corner B in figure 6.2. Therefore we choose the steplengths h_s and k_s and the geometric progression ratios δ_s and ε_s in each sub-domain, such that the seven meshpoints which surround the meshpoint on corner B are all at an equal distance from it in the physical plane

(r,z). Moving away from corner B the distances between successive meshpoints will increase or decrease depending on the geometric progression ratios δ_s and ε_s used in each sub-domain.

With reference to figure 6.2 the gap between $z=0$ and $z=z_1$ below the inner cylinder is much smaller in comparison to any other dimension of the flow domain for the three CSR geometries. We choose regularly spaced meshpoints in this gap and therefore in sub-domains 1 and 2 we have the ratios $\varepsilon_1 = 1$ and $\varepsilon_2 = 1$ respectively, hence $k_1 = z_1/n_1 = k_2 = z_2/n_2$. The ratio ε_3 is chosen such that the meshpoints which lie on either side of the interface between sub-domains 2 and 3 are at an equal distance from it. In sub-domain 2 all meshpoints are separated by the steplength k_2 in the z-direction and we require that the steplength in region 3 between the interface and the first meshpoint above it is equal to k_2. Therefore using equation (6.4.3) and setting $k_3 = k_2$ we have

$$z_2 - z_1 = \frac{k_2(1-\varepsilon_3^{n_3})}{(1-\varepsilon_3)} \tag{6.4.64}$$

This equation can be solved numerically to determine the geometric progression ratio ε_3. In order to have the meshpoints surrounding corner B all at an equal distance from it in the physical plane (r,z) we must set $h_2 = k_2$. Therefore from equation (6.4.2) we can obtain the geometric progression ratio δ_2 by numerically solving the equation

$$r_2 - r_1 = \frac{h_2(1-\delta_2^{m_2})}{(1-\delta_2)} \tag{6.4.65}$$

To ensure that the finite difference equations can be matched across the interface between sub-domains 2 and 3 we must set $h_3 = h_2$ and $\delta_3 = \delta_2$. Considering the interface between sub-domains 1 and 2, we must set $h_1\delta_1^{(m_1-1)} = h_2$ to have meshpoints at an equal distance either side of it in the physical plane (r,z). On using this condition in equation (6.4.1) we have

$$r_1 = \frac{h_2}{\delta_1^{(m_1-1)}} \frac{(1-\delta_1^{m_1})}{(1-\delta_1)} \tag{6.4.66}$$

This equation can be solved numerically to determine the geometric progression ratio δ_1. The steplength h_1 can then be determined using $h_1 = h_2/\delta_1^{(m_1-1)}$. A final condition on the chosen finite difference mesh is that the same number of meshpoints are used in both the r-direction and z-direction in each sub-domain. Hence we have $m_1 = n_1 = m_2 = n_2 = m_3 = n_3$.

For the 1:2 ratio gap geometry we also wish to concentrate meshpoints around corner B in figure 6.2. The mesh constants in each sub-domain are chosen such that the largest distance between any two successive meshpoints is 10 times greater than the smallest distance between any two successive meshpoints in that sub-domain.

6.5 Steady shear results

Steady shear end effects and fluid inertia effects are considered for the three CSR geometries and the 1:2 ratio gap geometry previously described. The finite element mesh used in the Polyflow package has irregularly spaced meshpoints, where the steplength varies with a geometric progression ratio. The flow domain is separated into three rectangular sub-domains as shown in figure 6.4 and the ratios are chosen as described in section 6.4.8.

Using Polyflow the $\tau_{r\theta}$ shear stresses along the inner cylinder wall can be determined and used in equation (6.2.7) to calculate the torque C_F exerted on the inner cylinder due to the motion of the fluid. The convergence of the Polyflow solution is examined by considering the steady shear flow $(\Omega = 1\,\text{rad/sec})$ of a Newtonian fluid $(\eta_0 = 1\,\text{Pa.sec})$ in the medium gap CSR geometry where fluid inertia effects are ignored $(\rho = 0)$. The torque exerted on the inner cylinder due to the motion of the fluid has been calculated for various sizes of the finite element mesh. Due to the size of memory on the computer system available to run Polyflow the largest finite element mesh that can be used

has 36×36 divisions in each of the three sub-domains. However a mesh of this size provides a sufficiently accurate solution where the difference in the torque value obtained from a 24×24 mesh and a 36×36 mesh is only 0·211%.

We examine the convergence of the finite difference method by calculating the value of the non-dimensional geometry dependent constant β_0 for various mesh sizes. Values of β_0 have been calculated for the medium gap CSR geometry using meshes with up to 320×320 divisions in each sub-domain. There is a 0·234 % difference between the value of β_0 obtained with a 320×320 mesh and the value obtained with a 160×160 mesh. It should be noted that convergence of the finite difference scheme for a 320×320 mesh requires considerably more computational time than convergence with a 160×160 mesh. A sufficiently accurate solution is obtained with a 160×160 mesh and therefore this mesh size is used for the perturbation theory results presented in this section. The value of β_0 can also be obtained by ignoring fluid inertia effects in the Polyflow package. For the medium gap CSR geometry the difference between these values is only 0·204%. This gives a validation of the computer code used to generate the solution of the finite difference equations.

When fluid inertia effects are included in the theory of steady shear concentric cylinder flow there is a critical value of the Reynolds number beyond which the flow becomes unstable (Bird *et al* [2]). Referring to the Reynolds number defined in equation (6.3.8), for concentric cylinder flow in which the inner cylinder rotates with constant angular velocity and the outer cylinder is stationary, the critical value of the Reynolds number is given by Bird *et al* [2] as

$$R_{e_{crit}} = \frac{41.3\,(r_1/r_2)}{(1-r_1/r_2)^{3/2}} \tag{6.5.1}$$

Therefore in the analysis of fluid inertia effects on steady shear viscosity predictions we restrict our attention to concentric cylinder flows below this critical value, where the flow is

stable.

In figures 6.6(a) and 6.6(b) we present the primary velocity flow contours and secondary flow velocity streamlines respectively, in a wide gap geometry for a Newtonian fluid at $R_e = 1$ ($1 \cdot 008\,\%$ of the critical Reynolds number). These flow patterns have been obtained using the velocity distributions obtained from the finite difference method in equation (6.3.16). In figure 6.6 (a) it is seen that the primary velocity flow distribution deviates from the uniform distribution obtained when end effects are ignored. Therefore, from equation (6.2.8), end effects will produce a change in the $\tau_{r\theta}$ shear stresses used to calculate the torque C_F. Figure 6.6(b) shows a weak single Taylor like vortex cell (Taylor [28]) between the inner and outer cylinder walls. In figures 6.7(a) and 6.7(b) we present the corresponding primary velocity flow contours and secondary flow velocity streamlines at $R_e = 93 \cdot 75$ ($94 \cdot 47\,\%$ of the critical Reynolds number). The flow patterns in these figures have been obtained using the Polyflow package. Comparing figures 6.6(a) and 6.7(a) it is seen that at a higher Reynolds number there is a slight deviation in the primary velocity flow field near the base of the outer cylinder. This deviation is due to centrifugal forces which result in the fluid being forced outwards in the r-direction by the motion of the inner cylinder. The magnitude of the centrifugal forces increases with increasing Reynolds number and hence we have the distorted primary velocity flow field observed in figure 6.7(a). It is seen in figure 6.7(b) that there are six Taylor like vortex cells between the inner and outer cylinder walls. The strength of the lowest of these cells is much stronger than that of the single cell shown in figure 6.6(b) at only $1 \cdot 008\,\%$ of the critical Reynolds number. Moving upwards in the region between the inner and outer cylinders the vortex cells in figure 6.7(b) alternate in sign and decrease in strength. Similar secondary flow velocity streamlines have been produced for a range of Reynolds number flows and show that the number of vortex cells will increase with Reynolds number up to the critical Reynolds number where the flow

becomes unstable.

In figure 6.8 we present the normalised $\tau_{r\theta}$ shear stress distribution on the inner cylinder wall of a narrow gap, medium gap and wide gap geometry for a Newtonian fluid at zero Reynolds number. Each stress distribution is normalised with respect to the corresponding $\tau_{r\theta}$ shear stress value, obtained from equation (6.2.2), when end effects are ignored. It can be seen from this figure that for a given inner cylinder angular velocity the shear stresses near the base of the inner cylinder are greater than those predicted from the standard theory in which end effects are ignored. The normalised $\tau_{r\theta}$ shear stress distribution on the inner cylinder wall of a wide-gap geometry is presented for various power law fluids, at zero Reynolds number, in figure 6.9. Each stress distribution in this figure is normalised with respect to the corresponding $\tau_{r\theta}$ shear stress value, given by equation (6.2.9), when end effects are ignored. In figure 6.9 it is seen that, as for a Newtonian fluid, the shear stresses near the base of the inner cylinder are greater than those predicted from the standard theory. It is noted that in this figure the end effect error in the shear stress values decreases with decreasing power law index n. Since the shear stresses near the base of the inner cylinder are greater than those predicted from the standard theory, the fluid will exert a larger torque on the inner cylinder than that predicted from the standard theory. This is demonstrated in figure 6.10, where we present the torque exerted on the inner cylinder of all three CSR geometries for various power law fluids at zero Reynolds number. In this figure the torque is expressed as a percentage error of the value predicted from the standard theory in equation (6.2.10). The expected zero percentage error in torque for a fluid with constant stress ($n = 0$) is also included in figure 6.10. These results show that end effects can lead to errors of up to 10%, for the CSR geometries, in the steady shear viscosity prediction of fluids. This error decreases with decreasing geometry gap and decreasing power law index n.

The CSR computer software calculates the steady shear viscosity of a fluid, from the applied torque C_0 and the measured inner cylinder angular velocity Ω, using the standard theory in which end effects are ignored (equation (6.2.3)). When end effects are included the fluid directly above the base of the outer cylinder creates an extra drag on the motion of the inner cylinder, causing it to rotate at a slower angular velocity than expected from the standard theory. Therefore if the standard theory is used to calculate the shear viscosity of a fluid the slower angular velocity will be interpreted as being due to a more viscous fluid. Hence when end effects are ignored the shear viscosity of a fluid will be overestimated.

Figure 6.11 shows the percentage error in torque for a Newtonian fluid for non-zero Reynolds number flows below the critical Reynolds number. In this figure we compare the torque obtained from the perturbation theory (equation (6.3.34)) with the value obtained from Polyflow which includes full fluid inertia effects. It can be seen from this figure that for the three CSR geometries the percentage error in torque shows a negligible dependence on Reynolds number. Therefore for these geometries fluid inertia effects can be ignored and only end effects need to be included in the theory. However fluid inertia effects can be important in larger gap geometries. This is demonstrated in figure 6.11 for a 1:2 ratio gap geometry in which the perturbation theory percentage error in torque varies from 22% to 29% over the range of Reynolds numbers considered. For this geometry the perturbation theory gives good agreement with the Polyflow results up to 50% of the critical Reynolds number. Polyflow results have also shown that fluid inertia effects are negligible for power law fluids in the three CSR geometries and therefore the results presented in figure 6.10 are also valid for non zero Reynolds number flows.

We now consider the results for the perturbation theory. On using the non-dimensional geometry dependent constants β_0 and β_2 the geometry dependent factors f_0 and f_2 in equation (6.3.37) can be calculated. These factors are presented in table 6.1 for

the three CSR geometries and the 1:2 ratio gap geometry.

	With End Effects		Without End Effects	
	f_0	f_2	f_0	f_2
Narrow Gap	0·973	$-4{\cdot}919 \times 10^{-10}$	1	0
Medium Gap	0·927	$4{\cdot}588 \times 10^{-8}$	1	0
Wide Gap	0·908	$3{\cdot}646 \times 10^{-7}$	1	0
1:2 ratio Gap	0.820	$1{\cdot}745 \times 10^{-5}$	1	0

Table 6.1: Steady shear factors.

The f_0 factors in table 6.1 show that when end effects are included in the theory the shear viscosity prediction will be less than that predicted from the standard theory. The reduction being 2·7%, 7·3% and 9·2% for the narrow gap, medium gap and wide gap geometries respectively. For the three CSR geometries, the end effect f_2 factors in table 6.1 confirm the results of figure 6.11 that fluid inertia effects are negligible for flows below the critical Reynolds number. It is noted that in table 6.1 the f_2 factor for the narrow gap geometry is negative. On inspection of the narrow gap data which includes full fluid inertia effects, presented in figure 6.11, it is found that in comparison to the percentage error in torque at zero Reynolds number there is a very small reduction in the percentage error for flows below approximately 50% of the critical Reynolds number. For flows above 50% of the critical value the percentage error in torque is greater in comparison to that at zero Reynolds number. This is consistent with the negative f_2 factor obtained for the narrow gap geometry from the fluid inertia perturbation theory which is valid for small Reynolds number flows.

6.6 Flow simulation of a Newtonian fluid in a 1:2 ratio gap geometry

To determine the limitations of the second order fluid inertia perturbation theory for

larger gap geometries we simulate the steady shear flow behaviour of a Newtonian fluid in a 1:2 ratio gap geometry. On taking into account full fluid inertia effects the torque required to rotate the inner cylinder at a prescribed angular velocity Ω is determined using Polyflow. These torque values can then be used in equation (6.3.37), together with the steady shear factors of table 6.1, to establish the influence of concentric cylinder end effects and fluid inertia effects on the steady shear viscosity prediction of fluids. On using the torque values in the standard formula (equation (6.3.37) with $f_0 = 1$ and $f_2 = 0$) the percentage error in shear viscosity prediction is presented as the uncorrected data in figure 6.12. In this figure we also present the error in shear viscosity prediction when end effects are taken into account (equation (6.3.37) with $f_0 = 0 \cdot 820$ and $f_2 = 0$) and good agreement is obtained with the exact viscosity up to 25% of the critical Reynolds number. When corrected for end effects and second order fluid inertia effects (equation (6.3.37) with $f_0 = 0 \cdot 820$ and $f_2 = 1.745 \times 10^{-5}$) agreement to within 1% of the exact value is obtained for Reynolds numbers up to 60% of the critical value.

6.7 Conclusions

Using a Newtonian fluid inertia perturbation analysis it has been shown that existing shear viscosity formulae can be modified to include end effects and second order fluid inertia effects. Results show that end effects produce errors of 2·7%, 7·3% and 9·2% in Newtonian shear viscosity predictions for the narrow, medium and wide gap CSR geometries respectively. For power law shear thinning fluids these errors decrease with decreasing power law index n. When end effects are included in the steady shear theory fluid inertia effects can no longer be ignored. However it is shown that for flows below the critical Reynolds number fluid inertia effects are negligible in the three CSR geometries. Using simulated Newtonian steady shear data it is shown that correcting for both end effects and

second order fluid inertia effects gives improved shear viscosity predictions in wider gap geometries where fluid inertia effects are important.

Some of the work presented in this chapter is included in a paper which has been accepted for publication in the Journal of Non-Newtonian Fluid Mechanics.

CHAPTER 7

CONCENTRIC CYLINDER END EFFECTS AND FLUID INERTIA EFFECTS ON STEADY SHEAR VISCOSITY PREDICTIONS OBTAINED FROM A WEISSENBERG RHEOGONIOMETER

7.1 Introduction

In steady shear concentric cylinder flow on a controlled strain Weissenberg rheogoniometer, the outer cylinder rotates with constant angular velocity and the inner cylinder remains stationary at its equilibrium position. This is in contrast to the steady shear flow conditions on a CSR controlled stress rheometer in which the inner cylinder is the rotating member. An advantage of the Weissenberg concentric cylinder set up is that the flow is significantly more stable than that for the corresponding set up on the CSR instrument, particularly for mobile fluids. Therefore for a given fluid and concentric cylinder geometry higher Reynolds number flows can be considered on a Weissenberg rheogoniometer. Hence shear viscosity measurements of mobile fluids can be obtained at high shear rates on this instrument. For the higher Reynolds number flows fluid inertia effects may be important in the standard CSR geometries. Therefore in this chapter we consider concentric cylinder end effects and fluid inertia effects on shear viscosity predictions obtained from a Weissenberg rheogoniometer.

On a commercially available Weissenberg rheogoniometer the calculation of the steady shear viscosity of a fluid, in a concentric cylinder geometry, is based on a theory in which end effects and fluid inertia effects are ignored (T.A. Instruments [34]). In this chapter we consider the same recessed concentric cylinder geometries as those used in chapter 6 for the CSR controlled stress rheometer, as shown in figure 6.1.

The analysis will follow a similar approach to that presented in chapter 6 for a CSR

controlled stress rheometer, using a low Reynolds number fluid inertia perturbation analysis and Polyflow to solve the relevant equations. From the fluid inertia perturbation theory the existing steady shear formulae are modified to include end effects and second order fluid inertia effects. These modified formulae can be used as an on line correction for Newtonian shear viscosity data obtained from a Weissenberg rheogoniometer. Simulated steady shear data will be generated for a Newtonian fluid to establish the limitations of the second order fluid inertia perturbation theory. For comparison with the results presented in chapter 6 we consider the wide, medium and narrow gap CSR geometries described in section 6.4. Attachments have been manufactured at the University of Plymouth to allow the use of the CSR concentric cylinder geometries on the Weissenberg rheogoniometer.

7.2 Steady shear theory

On a Weissenberg rheogoniometer the outer cylinder is forced to rotate at a constant angular velocity Ω. The resulting motion of the fluid causes a constant angular displacement of the inner cylinder, which is constrained by a torsion bar of stiffness K. We denote the torque acting on the inner cylinder, due to the deflection of the torsion bar, by C_0 which is equal in magnitude to the torque C_F exerted on the inner cylinder due to the motion of the fluid. As for the CSR controlled stress rheometer, the present formula for calculating the shear viscosity of a fluid on a Weissenberg rheogoniometer is determined from a theory in which end effects and fluid inertia effects are ignored. This formula is given in equation (6.2.3) where the value of C_0 is now obtained by multiplying the inner cylinder displacement by the torsion bar stiffness K. For Newtonian fluids a low Reynolds number fluid inertia perturbation analysis is used to determine a formula for predicting the shear viscosity of a fluid which includes end effects and second order fluid inertia effects.

7.2.1 Governing equations and boundary conditions

When the outer cylinder rotates at a constant angular velocity the resulting motion of the fluid produces a constant angular displacement of the inner cylinder. Therefore the analysis will consider the inner cylinder to remain stationary while the outer cylinder rotates at a prescribed angular velocity Ω.

The physical dimensions of the flow domain are identical to those shown in figure 6.2 for the concentric cylinder geometry on a CSR controlled stress rheometer. We shall again assume that the 'free surface' boundaries AB and CD remain in their horizontal positions and therefore the boundary conditions on all six boundaries of the flow domain are identical to those described in section 6.2.2. However it is noted that boundaries OE and DE are now moving surfaces and boundary BC is the stationary surface.

For steady shear concentric cylinder flow on a Weissenberg rheogoniometer the governing equations are identical to those presented in section 6.2.2 for a CSR controlled stress rheometer. These equations ((6.2.4) to (6.2.6)) are solved using the numerical techniques discussed in chapter 6 and the torque exerted on the inner cylinder due to the motion of the fluid can then be calculated using equation (6.2.7) with a sign change. This torque is then compared with the value obtained from the theory in which end effects and fluid inertia effects are ignored.

7.2.2 Stability of concentric cylinder flow

The critical Reynolds number at which steady shear concentric cylinder flow on a Weissenberg rheogoniometer becomes unstable is much greater than the corresponding value for a CSR controlled stress rheometer (Bird *et al* [2]). This is due to the flow situation where the outer cylinder rotates being significantly more stable than the case where the inner cylinder rotates. An explanation for this increase in stability now follows.

With reference to figure 6.2 the centrifugal force on a fluid particle will act outwards in the positive r-direction. When the outer cylinder rotates the centrifugal force acting on a fluid particle increases in the radial direction. Therefore a fluid particle near the rotating outer surface will not move inwards since it has a greater centrifugal force acting on it than particles nearer the stationary inner surface. The motion of a fluid particle in the outwards direction will also be resisted, since particles nearer the moving outer surface have a greater centrifugal force. Therefore the centrifugal forces strongly stabilise the flow and the transition to turbulent flow, when the outer cylinder rotates, will occur at a much greater Reynolds number than in the system in which the inner cylinder rotates. It is noted that when the inner cylinder rotates centrifugal forces will introduce an instability into the flow.

7.3 Fluid inertia perturbation theory for a Newtonian fluid

In this analysis we consider a Newtonian fluid in a concentric cylinder geometry where the outer cylinder rotates at a constant angular velocity Ω and the inner cylinder remains stationary. The fluid inertia perturbation analysis is carried out in exactly the same manner as described in section 6.3 for the steady shear flow of Newtonian fluids on a CSR controlled stress rheometer. From the perturbation theory we will obtain equations (6.3.19) to (6.3.22) which must be solved subject to the relevant boundary conditions. The Weissenberg rheogoniometer boundary conditions for the perturbation theory variables are identical to those used in section 6.3 except for the zero order velocity component $v_{\theta 0}(r,z)$ which is given by

$$\left.\begin{aligned} v_{\theta 0} &= 0 \quad \text{on boundaries OA and BC.} \\ \partial v_{\theta 0}/\partial z &= 0 \quad \text{on free surface boundaries AB and CD.} \\ v_{\theta 0} &= r \quad \text{on the moving boundaries DE and OE} \end{aligned}\right\} \qquad (7.3.1)$$

For a Weissenberg rheogoniometer the Newtonian shear viscosity of a fluid can be calculated using equation (6.3.37) where C_0 is now obtained by multiplying the inner

cylinder displacement by the torsion bar stiffness K. It is noted that for a Weissenberg rheogoniometer the relationship between f_0 and β_0 in equation (6.3.37) is now given by $f_0 = -2hr_2^2/[\beta_0 r_1(r_2^2 - r_1^2)]$, where the geometry dependent constant β_0 is defined in equation (6.3.35). The perturbation theory equations are solved using the finite difference method described in section 6.4. Using the finite difference solution the geometry dependent factors f_0 and f_2 in equation (6.3.37) can be evaluated for the steady shear concentric cylinder flow of Newtonian fluids on a Weissenberg rheogoniometer.

7.4 Relationship between concentric cylinder end effects on a Weissenberg rheogoniometer and a CSR controlled stress rheometer

When fluid inertia effects are included in the theory there is no direct relationship between the velocity distributions on the Weissenberg and CSR instruments. However we shall now show that there is a direct relationship between these instruments when fluid inertia effects are ignored.

We denote the velocity distribution for steady shear concentric cylinder flow on the CSR controlled stress rheometer and the Weissenberg rheogoniometer by v_c and v_w respectively. When fluid inertia effects are ignored both v_c and v_w must satisfy $L[v] = 0$ over the same flow domains as shown in figures 7.1(a) and 7.1(b) respectively.

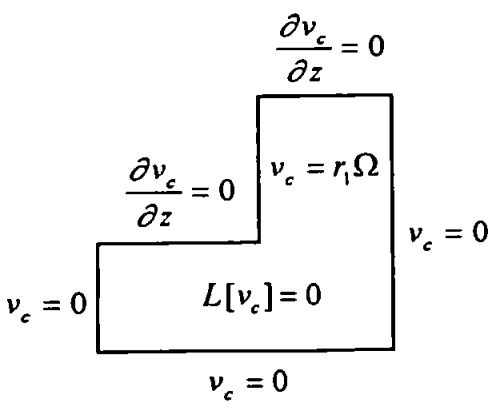

Figure 7.1(a):-
Boundary conditions for v_c

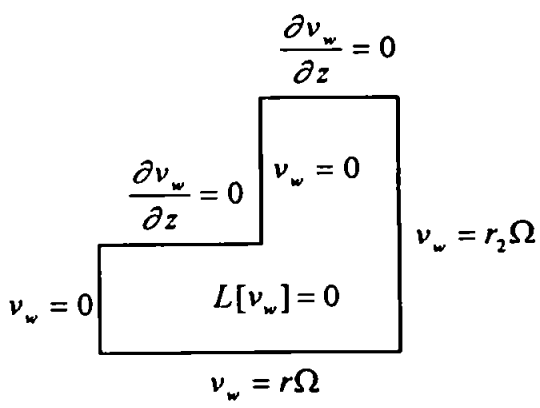

Figure 7.1(b):-
Boundary conditions for v_w

In these figures we also include the boundary conditions that must be satisfied by v_c and v_w. It can be seen that a direct relationship between the boundary conditions for v_c and v_w is given by $v_w = r\Omega - v_c$. This relationship implies that if $L[v_c] = 0$ then it follows that $L[v_w] = 0$ in which case $v_w = r\Omega - v_c$ is valid over the whole flow domain. It then follows from equation (6.2.8) that the $\tau_{r\theta}$ shear stresses are related by $\tau_{r\theta c} = -\tau_{r\theta w}$, which implies that when fluid inertia effects are ignored the end effect errors on viscosity prediction will be identical on both instruments.

7.5 Steady shear results

Steady shear concentric cylinder end effects and fluid inertia effects on a Weissenberg rheogoniometer are considered for the three CSR geometries described in section 6.4. The meshes used in the finite difference method and the Polyflow package are identical to those used to generate the results presented in section 6.5 for a CSR controlled stress rheometer.

When fluid inertia effects are included in the theory of steady shear concentric cylinder flow there is a critical value of the Reynolds number above which the flow will be unstable (Bird *et al* [2]). In the fluid inertia perturbation theory the Reynolds number R_e was defined by equation (6.3.8). Bird *et al* [2] define a Newtonian Reynolds number for concentric cylinder flow where the outer cylinder rotates with constant angular velocity and the inner cylinder is stationary as

$$R_e = \frac{\rho r_2^2 \Omega}{\eta_0} \tag{7.5.1}$$

For convenience, in this chapter we shall present the results in terms of this Reynolds number. Bird *et al* [2] presented a graph of the critical value of the Reynolds number, at

which the flow becomes unstable, as a function of r_1/r_2. This graph shows that for the three CSR geometries the flow will be stable for Reynolds numbers up to approximately 50000. However for these geometries the Polyflow numerical scheme is only convergent up to a Reynolds numbers of approximately 3500 and therefore we shall only present results for Reynolds numbers below this value.

In figures 7.2(a) and 7.2(b) we present the primary velocity flow contours and secondary flow velocity streamlines respectively in a wide gap geometry for a Newtonian fluid at a low Reynolds number ($R_e = 1$). These flow patterns have been produced using the velocity distributions obtained from the finite difference method in equation (6.3.16). It is seen in figure 7.2 (a) that the primary velocity flow distribution deviates from the uniform distribution obtained when end effects are ignored which, from equation (6.2.8), will result in a change in the $\tau_{r\theta}$ shear stresses used to calculate the torque C_F. Figure 7.2(b) shows a weak single Taylor like vortex cell (Taylor [28]) between the inner and outer cylinder walls. The streamlines in this figure are opposite in sign to those of the single vortex cell presented in figure 6.6(b) for concentric cylinder flow on a CSR controlled stress rheometer. In figures 7.3(a) and 7.3(b) we present the corresponding primary velocity flow contours and secondary flow velocity streamlines at a higher Reynolds number ($R_e = 3445$). The flow patterns in these figures have been obtained using the Polyflow package. Comparing figures 7.2(a) and 7.3(a) it is seen that at a higher Reynolds number there is a deviation in the primary velocity flow field near the base of the outer cylinder. In figure 7.3(b) it is seen that, as for low Reynolds numbers, there is a single Taylor like vortex cell between the inner and outer cylinder walls. It is noted that at a higher Reynolds number the strength of the vortex cell has increased and become more triangular in shape. Similar secondary flow velocity streamlines have been produced for a range of Reynolds numbers up to $R_e = 3445$ and all show a single Taylor like vortex cell which increases in strength and becomes more

triangular in shape with increasing Reynolds number.

The Weissenberg computer software calculates the steady shear viscosity of a fluid from the measured outer cylinder angular velocity Ω and torque C_0 using the standard theory in which end effects are ignored. When including end effects, the rotating base of the outer cylinder member will result in the fluid exerting a greater torque on the inner cylinder than that predicted from the standard theory. Therefore when concentric cylinder end effects are ignored on a Weissenberg rheogoniometer the steady shear viscosity of a fluid will be overestimated.

In section 7.4 it was shown that when fluid inertia effects are ignored the end effect errors for a Weissenberg rheogoniometer are identical to those for the CSR instrument. Therefore, when fluid inertia effects are ignored, the normalised $\tau_{r\theta}$ shear stress distributions on the inner cylinder wall for a Weissenberg rheogoniometer are identical to those presented for the CSR instrument in figures 6.8 and 6.9.

In figure 7.4 we present the percentage error in torque for a Newtonian fluid for non-zero Reynolds number flows in the three CSR geometries. It can be seen from this figure that for the wide gap geometry the percentage error in torque varies from 10% to 39% over the range of Reynolds numbers considered. The corresponding variation in torque for the medium gap geometry is 8% to 27% and for the narrow gap geometry it is 2·7% to 6·7%. Therefore at high Reynolds numbers fluid inertia effects cannot be ignored when end effects are included in the theory.

We now consider the effect of fluid inertia on the steady shear viscosity prediction of power law fluids in the three CSR geometries. A Reynolds number for power law fluids, which is consistent with the Newtonian value when $n = 1$, can be defined as

$$R_e = \frac{\rho r_2^2 \Omega}{k \dot{\gamma}^{n-1}} \tag{7.5.2}$$

where $\dot{\gamma}$ is a typical shear rate of the steady shear concentric cylinder flow.

A typical shear rate for steady shear concentric cylinder flow is given by $\dot{\gamma} = r_2\Omega/(r_2 - r_1)$ and the Reynolds number can then be expressed as

$$R_e = \frac{\rho\, r_2^{(3-n)}\Omega^{(2-n)}}{k\,(r_2 - r_1)^{(1-n)}} \tag{7.5.3}$$

It is noted that on setting $n = 1$ in equation (7.5.3) we obtain the Reynolds number for Newtonian fluids as defined in equation (7.5.1).

In figure 7.5 we present the percentage error in torque for non-zero Reynolds number flows of various power law fluids in the wide gap geometry. It is seen in this figure that for all the power law fluids considered, the percentage error in torque has a similar rate of increase with Reynolds number. The percentage error in torque for non-zero Reynolds number flows in the medium gap and narrow gap geometries is presented in figures 7.6 and 7.7 respectively. In both of these figures we see that the percentage error in torque increases at a similar rate with Reynolds number for all values of the power law index n. These results indicate that at high Reynolds numbers fluid inertia effects are important in concentric cylinder shear viscosity predictions of power law fluids on a Weissenberg rheogoniometer. It is noted that end effects are less important for highly shear thinning fluids.

We now consider the results for the perturbation theory. The velocity distributions obtained from the solution to the finite difference equations in section 6.4 are used to calculate the geometry dependent factors f_0 and f_2 required in equation (6.3.37). These factors for steady shear concentric cylinder flow on a Weissenberg rheogoniometer are presented in table 7.1.

	With End Effects		Without End Effects	
	f_0	f_2	f_0	f_2
Narrow Gap	0·973	$3{\cdot}745 \times 10^{-9}$	1	0
Medium Gap	0·927	$1{\cdot}663 \times 10^{-7}$	1	0
Wide Gap	0·908	$1{\cdot}041 \times 10^{-6}$	1	0

Table 7.1: Steady shear factors.

It is noted that as expected the f_0 factors in table 7.1 are identical to those presented, for the three CSR geometries, in table 6.1 for a CSR controlled stress rheometer. Comparing the f_2 factors of tables 6.1 and 7.1, in which end effects are included, it is seen that concentric cylinder second order fluid inertia effects on a Weissenberg rheogoniometer are an order of magnitude higher than those for a CSR controlled stress rheometer. It should be noted that the f_0 and f_2 factors in table 7.1 can be used in equation (6.3.37) to calculate the shear viscosity of a fluid. Although this equation is expressed in terms of the Reynolds number defined by equation (6.3.8), the f_2 factor can easily be modified so that equation (6.3.37) is valid for the Reynolds number defined in equation (7.5.1).

7.6 Flow simulation of a Newtonian fluid in the three CSR geometries

In order to determine the limitations of the second order fluid inertia perturbation theory we simulate the steady shear flow behaviour of a Newtonian fluid in the three CSR geometries. On taking into account full fluid inertia effects, the torque exerted on the inner cylinder due to the motion of the fluid for a prescribed outer cylinder angular velocity Ω is determined using Polyflow. This torque is then used as the C_0 value in equation (6.3.37), together with the steady shear factors of table 7.1, to establish the magnitude of end effects

and fluid inertia effects on the steady shear viscosity prediction of Newtonian fluids.

On using the torque values for the wide gap geometry in the standard formula (equation (6.3.37) with $f_0 = 1$ and $f_2 = 0$) the percentage error in shear viscosity prediction is presented as the uncorrected data in figure 7.8. In this figure we also present the percentage error in shear viscosity prediction when end effects are taken into account (equation (6.3.37) with $f_0 = 0 \cdot 908$ and $f_2 = 0$) and agreement is obtained to within 1% of the exact value for Reynolds numbers below 150. Correcting for end effects and second order fluid inertia effects (equation (6.3.37) with $f_0 = 0 \cdot 908$ and $f_2 = 1 \cdot 041 \times 10^{-6}$) gives agreement to within 1% of the exact viscosity data up to a Reynolds number of 270.

The torque values obtained for a Newtonian fluid in the medium gap geometry are used in the standard formula (equation (6.3.37) with $f_0 = 1$ and $f_2 = 0$) and the percentage error in shear viscosity prediction is presented as the uncorrected data in figure 7.9. On correcting for end effects (equation (6.3.37) with $f_0 = 0 \cdot 927$ and $f_2 = 0$) agreement is obtained to within 1% of the exact viscosity data up to Reynolds numbers of 300. Correcting for end effects and second order fluid inertia effects (equation (6.3.37) with $f_0 = 0 \cdot 927$ and $f_2 = 1 \cdot 663 \times 10^{-7}$) gives agreement to within 1% of the exact value up to a Reynolds number of 600.

Using the torque values obtained for the narrow gap geometry in the standard formula (equation (6.3.37) with $f_0 = 1$ and $f_2 = 0$) the percentage error in shear viscosity prediction is presented as the uncorrected data in figure 7.10. In this figure we also present data corrected for end effects (equation (6.3.37) with $f_0 = 0 \cdot 973$ and $f_2 = 0$) and data corrected for both end effects and second order fluid inertia effects (equation (6.3.37) with $f_0 = 0 \cdot 973$ and $f_2 = 3 \cdot 745 \times 10^{-9}$). In figure 7.10 it is seen that when corrected for end effects and second order fluid inertia effects agreement to within 0·5% of the exact value is

obtained for the full range of Reynolds numbers considered.

7.7 Conclusions

For a Weissenberg rheogoniometer it is shown that when fluid inertia effects are ignored, the concentric cylinder end effect produces errors of 2·7%, 7·3% and 9·2% in Newtonian shear viscosity predictions for the narrow, medium and wide gap CSR geometries respectively. These errors increase with increasing Reynolds number. For power law shear thinning fluids the error in shear viscosity prediction decreases with decreasing power law index n. However, for a given power law fluid, it is seen that the error in shear viscosity prediction increases with increasing Reynolds number. Using a perturbation analysis the existing formulae for calculating the shear viscosity of a fluid on a Weissenberg rheogoniometer can be modified to include end effects and second order fluid inertia effects. Numerically simulated steady shear data for Newtonian fluids has shown that shear viscosity predictions in the three CSR geometries are significantly improved when end effects and second order fluid inertia effects are taken into account. It is seen that the modified shear viscosity formulae give agreement to within 1% of the exact Newtonian viscosity data up to Reynolds numbers of 270, 600 and 3500 for the wide, medium and narrow gap CSR geometries respectively.

CHAPTER 8

CONCENTRIC CYLINDER END EFFECTS AND FLUID INERTIA EFFECTS ON COMPLEX VISCOSITY PREDICTIONS IN CONTROLLED STRESS RHEOMETRY

8.1 Introduction

An oscillatory shear theory for predicting the complex viscosity of a fluid using a controlled stress rheometer was first developed by Holder [35]. Formulae which included first order fluid inertia effects were produced for both the cone and plate and the parallel plate geometries. Using this theory Jones *et al* [36] showed that the controlled stress rheometer could be used to produce meaningful complex viscosity data. Jones *et al* [37] extended the oscillatory shear theory to the concentric cylinder geometry, producing formulae for predicting the complex viscosity of a fluid which included first order fluid inertia effects. These workers carried out experiments on viscoelastic fluids and compared the complex viscosity data obtained using a concentric cylinder geometry with that obtained using the cone and plate and the parallel plate geometries. It was concluded that fluid inertia effects must be taken into account in the concentric cylinder geometry especially for high-density mobile fluids. The theory for the three geometries previously discussed was extended to include both first order and second order fluid inertia effects by Golden [21]. It is shown by this worker that second order fluid inertia effects in CSR concentric cylinder geometries can be important in oscillatory shear experiments. Golden [21] obtained experimental complex viscosity data using the parallel plate geometry, the cone and plate geometry and various concentric cylinder geometries. Some discrepancies were observed between the concentric cylinder data and the data obtained from the parallel plate and cone and plate geometries. These discrepancies varied with the concentric cylinder gap and

Golden [21] suggested that they could be due to end effects.

In this chapter we consider concentric cylinder end effects and fluid inertia effects on complex viscosity predictions obtained using a CSR controlled stress rheometer. The concentric cylinder geometries employed in oscillatory shear experiments on the CSR controlled stress rheometer are identical to those used for steady shear. On a CSR controlled stress rheometer the complex viscosity prediction of a fluid is based on infinite cylinder theory in which end effects are ignored (Golden [21]). Using a perturbation analysis which is valid for small fluid inertia effects, this worker has produced formulae for determining the complex viscosity of a fluid which include first order and second order fluid inertia effects. In this chapter a similar approach to Golden [21] is used to develop new concentric cylinder formulae, for predicting the complex viscosity of a fluid on a CSR controlled stress rheometer, which include both end effects and second order fluid inertia effects. The equations obtained from the perturbation theory are solved using a finite difference method with an irregular mesh, as described in section 6.4.

A numerical simulation of the oscillatory shear flow behaviour of a Newtonian fluid and a single element Maxwell fluid in a concentric cylinder geometry will be performed. From the simulation we will produce complex viscosity data which has not been corrected for end effects and fluid inertia effects. Using this data a comparison in complex viscosity predictions can be made between the standard formulae (Golden [21]) and the formulae modified to include end effects. We shall also consider the frequency range of applicability of the second order fluid inertia correction formulae which include end effects.

8.2 Oscillatory shear theory

A generalised linear viscoelastic theory which takes into account end effects is developed for the concentric cylinder geometry on a CSR controlled stress rheometer. An

oscillatory torque of amplitude C_0 and frequency f (cycles/sec) is applied to the inner cylinder forcing it to make small amplitude oscillations of amplitude X_0 with a phase lag c behind the applied torque. The outer cylinder remains stationary. The amplitude X_0 and phase lag c are measured by the rheometer and together with the applied amplitude C_0 and frequency f can be used to calculate the complex viscosity of a fluid. At present this viscosity prediction is determined from infinite cylinder theory in which end effects are ignored (Golden [21]).

In the analysis we shall consider the inner cylinder to oscillate with amplitude X_0 at a prescribed frequency f. It is assumed that the amplitude of oscillation of the inner cylinder is sufficiently small to ensure that the flow is in the linear viscoelastic region and hence non-linear fluid inertia terms can be ignored in the equations of motion. Referring to a set of cylindrical polar coordinates (r,θ,z) we may assume a velocity distribution for the axisymmetric flow of the form (Jones *et al* [37])

$$v_r = 0 \quad , \quad v_\theta = v(r,z)\, e^{i\omega t} \quad , \quad v_z = 0 \tag{8.2.1}$$

where $\omega = 2\pi f$ (radians/sec) is the angular frequency of oscillation and the real part of these quantities is implied.

The velocity distribution of equation (8.2.1) gives two non-zero components of the shear stress tensor as

$$\tau_{r\theta} = \eta^* r \frac{\partial}{\partial r}\left(\frac{v}{r}\right) e^{i\omega t} \qquad \tau_{\theta z} = \eta^* \frac{\partial v}{\partial z} e^{i\omega t} \tag{8.2.2}$$

where η^* is the complex viscosity of the fluid.

Throughout the analysis the following non-dimensional variables will be used

$$r^+ = \frac{r}{r_1} \quad , \quad z^+ = \frac{z}{r_1} \quad , \quad z_1^+ = \frac{z_1}{r_1} \quad , \quad z_2^+ = \frac{z_2}{r_1} \quad , \quad v^+ = \frac{v}{r_1 i\omega X_0} \tag{8.2.3}$$

Substituting equations (8.2.1) and (8.2.2) into the relevant stress equations of motion (Bird *et al* [1]) and using the non-dimensional variables of equation (8.2.3) we have

$$\left(L+(\alpha r_1)^2\right)[v]=0 \tag{8.2.4}$$

where the complex parameter α is defined in equation (4.2.4) and the operator L is the θ component of the Laplacian operator of a vector field which is defined as

$$L=\frac{\partial^2}{\partial r^2}+\frac{1}{r}\frac{\partial}{\partial r}-\frac{1}{r^2}+\frac{\partial^2}{\partial z^2}=\nabla^2-\frac{1}{r^2} \tag{8.2.5}$$

In equations (8.2.4) and (8.2.5) the non-dimensional $^+$ notation is implied but has been omitted for convenience.

With reference to figure 6.2 and using equation (8.2.1) we consider the boundary conditions for the velocity function $v(r,z)$. On the stationary boundaries OE and DE and the moving boundary BC the no slip condition is imposed. Therefore $v=0$ on boundaries OE and DE and on boundary BC we have $v=1$. For the CSR geometries considered in this chapter it has been observed experimentally, that the 'free surface' boundaries AB and CD remain in a horizontal position for small amplitude oscillatory shear flow. Therefore, as for the analysis of steady shear concentric cylinder flow, we shall impose the condition that the 'free surface' boundaries remain in their horizontal positions. On the 'free surface' the shear stress is zero and hence $\tau_{\theta z}=0$. Therefore from equation (8.2.2) the condition $\partial v/\partial z=0$ is applied on boundaries AB and CD. There is no θ-direction fluid motion on the line of symmetry and therefore on boundary OA we have $v=0$. In summary the boundary conditions are given by

$$\left.\begin{aligned} v &= 0 \quad \text{on boundaries OA, OE and DE.} \\ \partial v/\partial z &= 0 \quad \text{on free surface boundaries AB and CD.} \\ v &= 1 \quad \text{on the moving boundary BC.} \end{aligned}\right\} \tag{8.2.6}$$

The equation of motion of the inner cylinder can be written as (Golden [21])

$$C_0 e^{i(\alpha t+c)} + I\omega^2 X_0 e^{i\alpha t} = C_F \tag{8.2.7}$$

where I is the moment of inertia of the oscillating member and C_F is the torque exerted on the inner cylinder due to the motion of the fluid, given by equation (6.2.7). Using equations (8.2.1), (8.2.2) and (8.2.3) the torque C_F, for a generalised linear viscoelastic fluid, can be expressed as

$$C_F = -2\pi i\omega X_0 r_1^3 \eta^* e^{i\alpha t} \int_{z_1}^{z_2} \left(\frac{\partial v}{\partial r} - \frac{v}{r} \right)\Bigg|_{r=1} dz \tag{8.2.8}$$

On substituting equation (8.2.8) into equation (8.2.7) we have

$$\frac{C_0 e^{ic}}{X_0} + I\omega^2 = -2\pi i\omega r_1^3 \eta^* \int_{z_1}^{z_2} \left(\frac{\partial v}{\partial r} - \frac{v}{r} \right)\Bigg|_{r=1} dz \tag{8.2.9}$$

The complex viscosity η^* of the fluid can be obtained from the solution to the coupled equations (8.2.4) and (8.2.9) subject to the boundary conditions in equation (8.2.6). These equations would have to be solved using a suitable numerical iterative technique. However this is not a simple task and therefore in the following section we shall use a perturbation analysis to solve these equations, which will be valid for the case when fluid inertia effects are small.

8.3 Fluid inertia perturbation theory for a generalised linear viscoelastic fluid

The perturbation analysis will follow a similar procedure to Golden [21] except that end effects will now be included in the theory. We consider a second order power series expansion of the function $v(r,z)$ in terms of the non-dimensional parameter $(\alpha r_1)^2$ as

$$v(r,z) = v_0(r,z) + (\alpha r_1)^2 v_1(r,z) + (\alpha r_1)^4 v_2(r,z) \tag{8.3.1}$$

Substituting the expansion of equation (8.3.1) into equation (8.2.4) and comparing

coefficients of the $(\alpha r_1)^2$ terms gives

Zero order: $$L[v_0] = 0 \tag{8.3.2}$$

First order: $$L[v_1] = -v_0 \tag{8.3.3}$$

Second order: $$L[v_2] = -v_1 \tag{8.3.4}$$

On considering the boundary conditions in equation (8.2.6) and the series expansion in equation (8.3.1) the boundary conditions for the functions $v_0(r,z)$, $v_1(r,z)$ and $v_2(r,z)$ can be determined. For $v_0(r,z)$ we have

$$\left.\begin{aligned} v_0 &= 0 \quad \text{on boundaries OA, OE and DE.} \\ \partial v_0/\partial z &= 0 \quad \text{on free surface boundaries AB and CD.} \\ v_0 &= 1 \quad \text{on the moving boundary BC.} \end{aligned}\right\} \tag{8.3.5}$$

The boundary conditions for $v_1(r,z)$ and $v_2(r,z)$ are given by

$$\left.\begin{aligned} v_1 = v_2 &= 0 \quad \text{on boundaries OA, OE, DE and BC.} \\ \partial v_1/\partial z = \partial v_2/\partial z &= 0 \quad \text{on free surface boundaries AB and CD.} \end{aligned}\right\} \tag{8.3.6}$$

The values of the boundary conditions for the functions $v_0(r,z)$, $v_1(r,z)$ and $v_2(r,z)$ are all real quantities. It then follows that the solutions to equations (8.3.2) to (8.3.4) will also be real quantities. These equations are to be solved using a finite difference method with an irregular mesh, which will be described in section 8.4.

On substitution of the series expansion for the function $v(r,z)$ in equation (8.3.1) into the equation of motion of the inner cylinder, equation (8.2.9), we have

$$\frac{C_0 e^{ic}}{X_0} + I\omega^2 = 2\pi i\omega r_1^3 \eta^* \left[\beta_0 + (\alpha r_1)^2 \beta_1 + (\alpha r_1)^4 \beta_2\right] \tag{8.3.7}$$

where $$\beta_m = -\int_{z_1}^{z_2} \left(\frac{\partial v_m}{\partial r} - \frac{v_m}{r} \right)\Bigg|_{r=1} dz \qquad m = 0, 1, 2 \tag{8.3.8}$$

are non-dimensional geometry dependent constants.

We define η_0^* to be the complex viscosity of the fluid when fluid inertia effects are ignored.

η_0^* can then be obtained from equation (8.3.7) by setting $\alpha = 0$ and replacing η^* by η_0^* to give

$$\eta_0^* = \frac{1}{2\pi i\omega r_1^3 \beta_0}\left(\frac{C_0 e^{ic}}{X_0} + I\omega^2\right) \tag{8.3.9}$$

It is convenient to express this formula in the form

$$\eta_0^* = \frac{f_0(r_2^2 - r_1^2)}{4\pi i\omega h r_1^2 r_2^2}\left(\frac{C_0 e^{ic}}{X_0} + I\omega^2\right) \tag{8.3.10}$$

where h is the height of the inner cylinder and f_0 $(=2hr_2^2/[\beta_0 r_1(r_2^2 - r_1^2)])$ is a geometry dependent end effect correction factor. It should be noted that in this form the factor f_0 has a value of 1 when end effects are ignored. In this case equation (8.3.10) then becomes the standard concentric cylinder geometry formula for calculating the complex viscosity of the fluid (Golden [21]). We define the complex parameter α_0^2 as

$$\alpha_0^2 = \frac{-i\omega\rho}{\eta_0^*} \tag{8.3.11}$$

On using equations (8.3.7), (8.3.10) and (8.3.11) a relationship between η_0^* and η^* is given by

$$\eta_0^* = \eta^*\left[1 + \frac{\beta_1}{\beta_0}(\alpha_0 r_1)^2 \frac{\eta_0^*}{\eta^*} + \frac{\beta_2}{\beta_0}(\alpha_0 r_1)^4 \frac{\eta_0^{*2}}{\eta^{*2}}\right] \tag{8.3.12}$$

In order to determine an expression for η^* in terms of η_0^* from this equation we expand η^* as a second order power series in the non-dimensional parameter $(\alpha_0 r_1)^2$ given by

$$\eta^* = \eta_0^* + (\alpha_0 r_1)^2 \eta_1^* + (\alpha_0 r_1)^4 \eta_2^* \tag{8.3.13}$$

On substituting equation (8.3.13) into equation (8.3.12) we obtain

$$\eta_0^* = \eta_0^* + (\alpha_0 r_1)^2\left[\eta_1^* + \eta_0^* \frac{\beta_1}{\beta_0}\right] + (\alpha_0 r_1)^4\left[\eta_2^* + \eta_0^* \frac{\beta_2}{\beta_0}\right] \tag{8.3.14}$$

where terms of order $(\alpha_0 r_1)^6$ and higher have been neglected.

Comparing coefficients of the $(\alpha_0 r_1)^2$ terms in equation (8.3.14) we can obtain η_1^* and η_2^* which on substitution into equation (8.3.13) give

$$\eta^* = \eta_0^*\left[1 - \frac{\beta_1}{\beta_0}(\alpha_0 r_1)^2 - \frac{\beta_2}{\beta_0}(\alpha_0 r_1)^4\right] \tag{8.3.15}$$

On using equation (8.3.11) we can write

$$\eta^* = \eta_0^* - f_1 i\omega\rho r_1^2 - f_2\frac{\omega^2\rho^2 r_1^4}{\eta_0^*} \tag{8.3.16}$$

where $f_1 = -\beta_1/\beta_0$ and $f_2 = -\beta_2/\beta_0$ are non dimensional geometry dependent factors. Using the numerical solutions to equations (8.3.2) to (8.3.4) the non-dimensional geometry dependent constants β_0, β_1 and β_2 can be determined from equation (8.3.8). The geometry dependent factors f_0, f_1 and f_2 can then be calculated.

Equation (8.3.16) is the modified formula for calculating the complex viscosity of a fluid which corrects for both end effects and second order fluid inertia effects. This equation takes a similar form to the second order fluid inertia correction determined by Golden [21] in which end effects are ignored. It is noted that η_0^* in equation (8.3.16) is known from equation (8.3.10). The f_1 and f_2 factors in equation (8.3.16) can be evaluated for the case when end effects are ignored from the analytical expressions of Golden [21]. In order to establish the limitations of the second order fluid inertia perturbation theory, we shall simulate the oscillatory shear flow behaviour of a Newtonian fluid and a single element Maxwell fluid on a controlled stress rheometer for the three CSR geometries.

8.4 Finite difference method of solution for the perturbation theory equations

Equations (8.3.2) to (8.3.4) obtained from the fluid inertia perturbation theory are to be solved using a finite difference method. With reference to figure 6.1 we wish to use a finer mesh near the recessed end (corner B) where the greatest shear stress variation occurs.

Therefore an irregular mesh in which the steplength varies with a geometric progression ratio is used, as described in section 6.4. The whole flow domain is separated into three sub-domains, as shown in figure 6.4, and the physical domain (r,z) is transformed to a computational plane (x,y) using equations (6.4.1) to (6.4.3). We let the functions $v_0(r,z)$, $v_1(r,z)$ and $v_2(r,z)$ be transformed to $v_{0_s}(x,y)$, $v_{1_s}(x,y)$ and $v_{2_s}(x,y)$ respectively for $s=1,2,3$. The finite difference method of solution for each of these velocity functions is now described.

8.4.1 Finite difference equations for the velocity function $v_0(r,z)$

The transformed velocity function $v_{0_s}(x,y)$ over the xy-plane is denoted at each meshpoint (i,j) by $v_{0_s\,i,j}$. It is noted that equation (8.3.2) is of the same form as equation (6.3.19) with identical boundary conditions. We can therefore use the finite difference equations presented in section 6.4 (equations (6.4.13), (6.4.17) and (6.4.20)) to obtain the solution of equation (8.3.2). As before we impose equation (6.4.15) on the free surface boundaries AB and CD and use equations (6.4.19) and (6.4.22) to match the finite difference equations across the interfaces between each sub-domain. The iterative procedure presented in appendix 6.1 can be used to solve the finite difference equations discussed in this section.

8.4.2 Finite difference equations for the velocity function $v_1(r,z)$

We denote the transformed velocity function $v_{1_s}(x,y)$ over the xy-plane at each meshpoint (i,j) by $v_{1_s\,i,j}$. The left hand side of equation (8.3.3) has the same operator as the left hand side of equation (6.3.19). It is noted that the right hand side of equation (8.3.3) is known at every meshpoint from the finite difference solution of $v_0(r,z)$. Therefore on

modifying equation (6.4.13) to include the non-homogeneous term $v_{0s\ i,j}$ the finite difference equations for $v_{1s\ i,j}$ are given by

$$v_{1s\ i,j} = \frac{1}{e_s(i,j)}\left[a_s(i)\, v_{1s\ i+1,j} + b_s(i)\, v_{1s\ i-1,j} + c_s(j)\, v_{1s\ i,j+1} + d_s(j)\, v_{1s\ i,j-1} + v_{0s\ i,j}\right] \quad (8.4.1)$$

where $i = 1$ to $m_s - 1$ and $j = 1$ to n_s for $s = 1,3$
$i = 1$ to $m_s - 1$ and $j = 1$ to $n_s - 1$ for $s = 2$

and the discrete functions $a_s(i)$, $b_s(i)$, $c_s(j)$, $d_s(j)$ and $e_s(i,j)$ are given in equation (6.4.14).

The condition $\partial v_1/\partial z = 0$ is to be applied on the free surface boundaries AB and CD. As described in section 6.4.3 the velocity $v_{1s\ i,j}$ on these boundaries will satisfy the condition

$$v_{1s\ i,n_s+1} = v_{1s\ i,n_s-1} \quad (8.4.2)$$

for $i = 1$ to $m_s - 1$ $(s = 1,3)$.

Modifying equation (6.4.17) to include the non-homogeneous term $v_{01\ m_1,j}$ gives the finite difference equations for $v_{11\ m_1,j}$, on the interface between sub-domains 1 and 2, as

$$v_{11\ m_1,j} = \frac{1}{e_{m_1}(j)}\left[a_{m_1}\, v_{12\ 1,j} + b_{m_1}\, v_{11\ m_1-1,j} + c_{m_1}(j)\, v_{11\ m_1,j+1} + d_{m_1}(j)\, v_{11\ m_1,j-1} + v_{01\ m_1,j}\right] \quad (8.4.3)$$

for $j = 1$ to $n_1 - 1$, where the discrete functions a_{m_1}, b_{m_1}, $c_{m_1}(j)$, $d_{m_1}(j)$ and $e_{m_1}(j)$ are given in equation (6.4.18). In order to match the finite difference equations across the interface between sub-domains 1 and 2 we let $v_{12\ 0,j} = v_{11\ m_1,j}$ for $j = 1$ to $n_1 - 1$ when the values of $v_{11\ m_1,j}$ have been obtained from equation (8.4.3).

On modifying equation (6.4.20) to include the non-homogeneous term $v_{02\ i,n_2}$ we obtain the finite difference equations for $v_{12\ i,n_2}$, on the interface between sub-domains 2

and 3, as

$$v_{12\ i,n_2} = \frac{1}{e_{n_2}(i)}\left[a_{n_2}(i)\, v_{12\ i+1,n_2} + b_{n_2}(i)\, v_{12\ i-1,n_2} + c_{n_2}\, v_{13\ i,1} + d_{n_2}\, v_{12\ i,n_2-1} + v_{02\ i,n_2}\right] \qquad (8.4.4)$$

for $i = 1$ to $m_2 - 1$, where the discrete functions $a_{n_2}(i)$, $b_{n_2}(i)$, c_{n_2}, d_{n_2} and $e_{n_2}(i)$ are given in equation (6.4.21). We match the finite difference equations across the interface between sub-domains 2 and 3 by letting $v_{13\ i,0} = v_{12\ i,n_2}$ for $i = 1$ to $m_2 - 1$ when the values of $v_{12\ i,n_2}$ have been obtained from equation (8.4.4).

The iterative procedure for solving the finite difference equations presented in this section is given in appendix 8.1.

8.4.3 Finite difference equations for the velocity function $v_2(r,z)$

The transformed velocity function $v_{2_s}(x,y)$ over the xy-plane is denoted at each meshpoint (i,j) by $v_{2_s\ i,j}$. From equations (8.3.3) and (8.3.4) it is seen that the relationship between $v_0(r,z)$ and $v_1(r,z)$ is identical to the relationship between $v_1(r,z)$ and $v_2(r,z)$. It is noted that that $v_1(r,z)$ and $v_2(r,z)$ are subject to the same boundary conditions. Therefore the finite difference equations for $v_{2_s\ i,j}$ will take the same form as those for $v_{1_s\ i,j}$ in equation (8.4.1) and are given by

$$v_{2_s\ i,j} = \frac{1}{e_s(i,j)}\left[a_s(i)\, v_{2_s\ i+1,j} + b_s(i)\, v_{2_s\ i-1,j} + c_s(j)\, v_{2_s\ i,j+1} + d_s(j)\, v_{2_s\ i,j-1} + v_{1_s\ i,j}\right] \qquad (8.4.5)$$

where $i = 1$ to $m_s - 1$ and $j = 1$ to n_s for $s = 1,3$
$i = 1$ to $m_s - 1$ and $j = 1$ to $n_s - 1$ for $s = 2$

and the discrete functions $a_s(i)$, $b_s(i)$, $c_s(j)$, $d_s(j)$ and $e_s(i,j)$ are given in equation (6.4.14). In equation (8.4.5) the velocity $v_{2_s\ i,j}$ must satisfy the condition

$$v_{2s\ i,n_s+1} = v_{2s\ i,n_s-1} \tag{8.4.6}$$

for $i = 1$ to $m_s - 1$ $(s = 1,3)$.

For meshpoints on the interface between sub-domains 1 and 2, the finite difference equations for $v_{21\ m_1,j}$ will take the same form as those for $v_{11\ m_1,j}$ in equation (8.4.3) and are given by

$$v_{21\ m_1,j} = \frac{1}{e_{m_1}(j)}\left[a_{m_1}\, v_{22\ 1,j} + b_{m_1}\, v_{21\ m_1-1,j} + c_{m_1}(j)\, v_{21\ m_1,j+1} + d_{m_1}(j)\, v_{21\ m_1,j-1} + v_{11\ m_1,j}\right] \tag{8.4.7}$$

for $j = 1$ to $n_1 - 1$, where the discrete functions a_{m_1}, b_{m_1}, $c_{m_1}(j)$, $d_{m_1}(j)$ and $e_{m_1}(j)$ are given in equation (6.4.18). The finite difference equations are matched across the interface between sub-domains 1 and 2 by letting $v_{22\ 0,j} = v_{21\ m_1,j}$ for $j = 1$ to $n_1 - 1$ when the values of $v_{21\ m_1,j}$ have been obtained from equation (8.4.7).

The finite difference equations for $v_{22\ i,n_2}$, on the interface between sub-domains 2 and 3, will take the same form as those for $v_{12\ i,n_2}$ in equation (8.4.4) and are given by

$$v_{22\ i,n_2} = \frac{1}{e_{n_2}(i)}\left[a_{n_2}(i)\, v_{22\ i+1,n_2} + b_{n_2}(i)\, v_{22\ i-1,n_2} + c_{n_2}\, v_{23\ i,1} + d_{n_2}\, v_{22\ i,n_2-1} + v_{12\ i,n_2}\right] \tag{8.4.8}$$

for $i = 1$ to $m_2 - 1$, where the discrete functions $a_{n_2}(i)$, $b_{n_2}(i)$, c_{n_2}, d_{n_2} and $e_{n_2}(i)$ are given in equation (6.4.21). In order to match the finite difference equations across the interface between sub-domains 2 and 3 we let $v_{23\ i,0} = v_{22\ i,n_2}$ for $i = 1$ to $m_2 - 1$ when the values of $v_{22\ i,n_2}$ have been obtained from equation (8.4.8).

The iterative procedure for solving the finite difference equations presented in this section is given in appendix 8.2.

8.4.4 Calculation of the geometry dependent constants β_m from the finite difference solutions for $v_0(r,z)$, $v_1(r,z)$ and $v_2(r,z)$

In equation (8.3.7) the motion of the inner cylinder is expressed in terms of the non-dimensional geometry dependent constants β_0, β_1 and β_2. These constants can be determined from the finite difference solutions for the velocity distributions $v_0(r,z)$, $v_1(r,z)$ and $v_2(r,z)$ using equations (6.4.62) and (6.4.63) for $m = 0,1,2$ and the method described in section 6.4.7.

8.5 Results for the fluid inertia perturbation theory

End effects and fluid inertia effects in concentric cylinder oscillatory shear flows are considered for the same three CSR geometries as for steady shear flow in chapter 6. Therefore the finite difference equations presented in section 8.4 are solved using 160×160 meshes as described in section 6.4.8. It is noted that equation (8.3.2) for $v_0(r,z)$ in the oscillatory shear perturbation analysis is of the same form as equation (6.3.19) for $v_{\theta 0}(r,z)$ in the steady shear perturbation analysis. The velocity functions $v_0(r,z)$ and $v_{\theta 0}(r,z)$ must also satisfy the same boundary conditions. Therefore, for a given concentric cylinder geometry, steady shear and oscillatory shear end effects will be identical when fluid inertia effects are ignored.

From the numerical solution of the equations obtained from the perturbation theory, the non-dimensional geometry dependent constants β_0, β_1 and β_2 are determined and the geometry dependent factors f_0, f_1 and f_2 required in equation (8.3.16) are then known. These geometry dependent factors are presented in table 8.1 for the three CSR geometries.

	With End Effects			Without End Effects		
	f_0	f_1	f_2	f_0	f_1	f_2
Narrow Gap	0·973	$4{\cdot}021 \times 10^{-3}$	$3{\cdot}937 \times 10^{-6}$	1	$4{\cdot}152 \times 10^{-3}$	$4{\cdot}088 \times 10^{-6}$
Medium Gap	0·927	$2{\cdot}725 \times 10^{-2}$	$2{\cdot}576 \times 10^{-4}$	1	$3{\cdot}016 \times 10^{-2}$	$2{\cdot}918 \times 10^{-4}$
Wide Gap	0·908	$5{\cdot}932 \times 10^{-2}$	$1{\cdot}612 \times 10^{-3}$	1	$6{\cdot}811 \times 10^{-2}$	$1{\cdot}919 \times 10^{-3}$

Table 8.1:- Oscillatory shear factors.

In this table we also present the geometry dependent factors when end effects are ignored, which have been evaluated from the analytical expressions of Golden [21]. It should be noted that as expected the oscillatory shear f_0 factors in table 8.1 are identical to the steady shear f_0 factors in table 6.1. In order to establish the limitations of the second order fluid inertia perturbation theory, we shall simulate the oscillatory shear flow behaviour of Newtonian fluids and single element Maxwell fluids in the three CSR geometries.

8.6 Flow simulation of a Newtonian fluid and a single element Maxwell fluid

For a Newtonian fluid and a single element Maxwell fluid the complex viscosity of the fluid is given by $\eta^* = \eta_0$ and $\eta^* = \eta_0/(1+i\lambda\omega)$ respectively, where η_0 is the Newtonian viscosity and λ is the relaxation time. The complex viscosity of these theoretical model fluids is known and will be referred to as the exact viscosity data throughout this section. At a prescribed inner cylinder frequency of oscillation the velocity distribution for the theoretical model fluids can be determined from the numerical solution of equation (8.2.4). Using this velocity distribution in equation (8.2.9) the expression $C_0 e^{ic}/X_0 + I\omega^2$ can be evaluated numerically. Hence on using this value in equation (8.3.9) the complex viscosity η_0^*, when fluid inertia effects are ignored, can be determined where the f_0 values are given in table 8.1. This value of η_0^* can then be used in equation (8.3.16) to determine

the first order and second order fluid inertia corrections, both with and without end effects, where the f_1 and f_2 values are given in table 8.1. Since the exact complex viscosity of the theoretical model fluids is known we can establish the limitations of the second order fluid inertia perturbation theory. The numerical finite difference method used to solve equation (8.2.4) for a known fluid at a prescribed frequency of oscillation is now described .

8.6.1 Finite difference equations for the velocity function $v(r,z)$

For a known fluid at a prescribed frequency of oscillation the non-dimensional complex parameter $(\alpha r_1)^2$ can be evaluated for a given concentric cylinder geometry. When the value of $(\alpha r_1)^2$ is known equation (8.2.4) can be solved numerically, subject to the boundary conditions of equation (8.2.6), to determine the complex velocity function $v(r,z)$. This equation is to be solved using a finite difference method with an irregular mesh, as described in section 6.4. The whole flow domain is separated into three sub-domains as shown in figure 6.4 and the physical domain (r,z) is transformed to a computational plane (x,y) using equations (6.4.1) to (6.4.3). We let the complex velocity function $v(r,z)$ be transformed to $v_s(x,y)$ for $s=1,2,3$.

The velocity function $v_s(x,y)$ over the xy-plane is denoted at each meshpoint (i,j) by $v_{s\ i,j}$. It is noted that equations (6.3.19) and (8.2.4) are of the same form where equation (6.3.19) has the operator L and equation (8.2.4) has the operator $L+(\alpha r_1)^2$. Therefore on modifying equation (6.4.13) to take account of the $(\alpha r_1)^2$ operator term the finite difference equations for $v_{s\ i,j}$ are given by

$$v_{s\ i,j} = \frac{1}{\left[e_s(i,j)-(\alpha r_1)^2\right]}\left[a_s(i)v_{s\ i+1,j} + b_s(i)v_{s\ i-1,j} + c_s(j)v_{s\ i,j+1} + d_s(j)v_{s\ i,j-1}\right] \qquad (8.6.1)$$

where $i=1$ to m_s-1 and $j=1$ to n_s for $s=1,3$
$i=1$ to m_s-1 and $j=1$ to n_s-1 for $s=2$

and the discrete functions $a_s(i)$, $b_s(i)$, $c_s(j)$, $d_s(j)$ and $e_s(i,j)$ are given in equation (6.4.14).

From equation (8.2.6) the condition $\partial v/\partial z = 0$ is to be applied on the free surface boundaries AB and CD. As described in section 6.4.3 the velocity $v_{s\ i,j}$ on these boundaries will satisfy the condition

$$v_{s\ i,n_s+1} = v_{s\ i,n_s-1} \tag{8.6.2}$$

for $i = 1$ to $m_s - 1$ $(s = 1,3)$

Modifying equation (6.4.17) to take account of the $(\alpha r_1)^2$ operator term gives the finite difference equations for $v_{1\ m_1,j}$, on the interface between sub-domains 1 and 2, as

$$v_{1\ m_1,j} = \frac{1}{\left[e_{m_1}(j) - (\alpha r_1)^2\right]}\left[a_{m_1} v_{2\ 1,j} + b_{m_1} v_{1\ m_1-1,j} + c_{m_1}(j) v_{1\ m_1,j+1} + d_{m_1}(j) v_{1\ m_1,j-1}\right] \tag{8.6.3}$$

for $j = 1$ to $n_1 - 1$, where the discrete functions a_{m_1}, b_{m_1}, $c_{m_1}(j)$, $d_{m_1}(j)$ and $e_{m_1}(j)$ are given in equation (6.4.18). In order to match the finite difference equations across the interface between sub-domains 1 and 2 we let $v_{2\ 0,j} = v_{1\ m_1,j}$ for $j = 1$ to $n_1 - 1$ when the values of $v_{1\ m_1,j}$ have been obtained from equation (8.6.3).

On modifying equation (6.4.20) to take into account the $(\alpha r_1)^2$ operator term we obtain finite difference equations for $v_{2\ i,n_2}$, on the interface between sub-domains 2 and 3, as

$$v_{2\ i,n_2} = \frac{1}{\left[e_{n_2}(i) - (\alpha r_1)^2\right]}\left[a_{n_2}(i) v_{2\ i+1,n_2} + b_{n_2}(i) v_{2\ i-1,n_2} + c_{n_2} v_{3\ i,1} + d_{n_2} v_{2\ i,n_2-1}\right] \tag{8.6.4}$$

for $i = 1$ to $m_2 - 1$, where the discrete functions $a_{n_2}(i)$, $b_{n_2}(i)$, c_{n_2}, d_{n_2} and $e_{n_2}(i)$ are given in equation (6.4.21). The finite difference equations are matched across the interface between sub-domains 2 and 3 by letting $v_{3\ i,0} = v_{2\ i,n_2}$ for $i = 1$ to $m_2 - 1$ when the values

of $v_{2\ i,n_2}$ have been obtained from equation (8.6.4).

The iterative procedure to solve the finite difference equations presented in this section is given in appendix 8.3.

The numerically obtained velocity distribution for $v(r,z)$ can be used in equation (8.2.9) to evaluate the expression $C_0 e^{ic}/X_0 + I\omega^2$ numerically. It is noted that the integral in equation (8.2.9) is evaluated from the finite difference velocity distribution using the method presented in section 6.4.7.

8.6.2 Results for the oscillatory shear flow simulation

It can be shown that the normalised complex viscosity (η^*/η_0) of a Newtonian fluid, in a given concentric cylinder geometry, can be represented as a function of the non-dimensional normalised frequency $(=\rho r_1^2\omega/\eta_0)$. In figures 8.1 and 8.2 we present end effect corrections and fluid inertia corrections for the simulated dynamic viscosity and dynamic rigidity data respectively of a Newtonian fluid in a wide gap geometry. The uncorrected data in these figures is obtained from the standard formula (equation (8.3.10) with $f_0 = 1$) in which end effects and fluid inertia effects are ignored. In figures 8.1 and 8.2 we also present complex viscosity data corrected for end effects only, corrected for second order fluid inertia effects only and corrected for both end effects and second order fluid inertia effects. In these figures it should be noted that the uncorrected data and the data corrected for end effects differ by a scaling factor of $f_0 = 0\cdot908$ for all frequencies of oscillation. Equation (8.3.16) shows that dynamic viscosity data is not influenced by first order fluid inertia effects. Therefore first order fluid inertia corrections with and without end effects are only presented for the dynamic rigidity data in figure 8.2. This figure shows an apparent negative dynamic rigidity when fluid inertia effects are ignored and an apparent

positive dynamic rigidity when fluid inertia effects are included in the theory. It is seen in figures 8.1 and 8.2 that when both end effects and second order fluid inertia effects are taken into account good agreement is obtained with the exact data up to a normalised frequency of 10.

In figures 8.3 and 8.4 we present end effect corrections and fluid inertia effect corrections for the simulated dynamic viscosity and dynamic rigidity data respectively of a Newtonian fluid in a medium gap geometry. These figures include the uncorrected data, data corrected for end effects only, data corrected for second order fluid inertia effects only and data corrected for both end effects and second order fluid inertia effects. In figure 8.4 we also present first order fluid inertia corrections with and without end effects. It is seen in figures 8.3 and 8.4 that data corrected for both end effects and second order fluid inertia effects gives good agreement with the exact complex viscosity data up to a normalised frequency of 15.

The simulated dynamic viscosity data and dynamic rigidity data of a Newtonian fluid in a narrow gap geometry is presented in figures 8.5 and 8.6 respectively. In these figures it is seen that when both end effects and second order fluid inertia effects are taken into account good agreement with the exact data is obtained for normalised frequencies below 50.

For a single element Maxwell fluid in which $\eta^* = \eta_0/(1+i\lambda\omega)$, it can be shown that for a given concentric cylinder geometry the normalised complex viscosity (η^*/η_0) can be represented as a function of the two non-dimensional quantities R $(=\rho r_1^2/(\lambda\omega))$ and the Deborah number $De\,(=\lambda\omega)$. In figures 8.7 and 8.8 we present end effect corrections and second order fluid inertia corrections for simulated dynamic viscosity and dynamic rigidity data respectively of a single element Maxwell fluid in a wide gap geometry when $R = 5$. When both end effects and second order fluid inertia effects are taken into account it

is seen that good agreement is obtained with the exact data up to a Deborah number of 0·8.

We now consider the Deborah number range of applicability of the complex viscosity corrections which include both end effects and second order fluid inertia effects for various values of R. The dynamic viscosity and dynamic rigidity corrections for a wide gap geometry are presented in figures 8.9 and 8.10 respectively. It can be seen in these figures that when R has a value below 15, good agreement is obtained with the exact data up to a Deborah number of 0·4. However if R has a value below 2 then good agreement with the exact data is obtained up to a Deborah number of 1·6. The dynamic viscosity and dynamic rigidity corrections are presented for both the medium gap geometry (figures 8.11 and 8.12 respectively) and the narrow gap geometry (figures 8.13 and 8.14 respectively). In the case of the medium gap geometry, R values below 30 give good agreement with the exact data up to Deborah numbers of 0·4, whereas for R values below 4 good agreement with the exact data is obtained up to a Deborah number of 1·6. For the narrow gap geometry, R values below 180 give good agreement with the exact data up to Deborah numbers of 0·5, whereas for R values below 30 good agreement with the exact data is obtained up to a Deborah number of 1·6.

8.7 Conclusions

It has been shown that the standard formulae for complex viscosity prediction on a CSR controlled stress rheometer can be modified to include both end effects and second order fluid inertia effects. These modified formulae are expressed in terms of geometry dependent factors and can be incorporated into the CSR software to correct the complex viscosity prediction for these effects. Numerically simulated oscillatory shear data has been generated for Newtonian fluids and single element Maxwell fluids on a CSR controlled stress rheometer. Results for Newtonian fluids show the validity of the modified complex

viscosity formulae up to normalised frequencies of 10, 15 and 50 for the wide, medium and narrow gap geometries respectively. For Deborah numbers below 1·6, oscillatory shear flow simulations of single element Maxwell fluids show the validity of the modified complex viscosity formulae for R values below 2, 4 and 30 for the wide, medium and narrow gap geometries respectively.

Some of the work presented in this chapter is included in a paper which has been accepted for publication in the Journal of Non-Newtonian Fluid Mechanics.

CHAPTER 9

CONCENTRIC CYLINDER END EFFECTS AND FLUID INERTIA EFFECTS ON COMPLEX VISCOSITY PREDICTIONS OBTAINED FROM A WEISSENBERG RHEOGONIOMETER

9.1 Introduction

A concentric cylinder oscillatory shear theory for predicting the complex viscosity of a fluid on the controlled strain Weissenberg rheogoniometer, which included second order fluid inertia effects, was presented in chapter 4. This theory was based on infinite cylinder theory in which end effects are ignored. It is seen in chapter 8 that concentric cylinder end effects can be important in oscillatory shear flows on a CSR controlled stress rheometer.

In this chapter we develop a concentric cylinder oscillatory shear theory for the Weissenberg rheogoniometer which includes both end effects and second order fluid inertia effects. The analysis will follow a similar approach to the fluid inertia perturbation theory for the CSR rheometer in chapter 8 and modified formulae will be produced for predicting the complex viscosity. The equations obtained from the perturbation theory are solved using a finite difference method with an irregular mesh, as described in section 6.4. End effects and fluid inertia effects are considered for the three CSR concentric cylinder geometries previously described in this thesis.

A numerical simulation of the oscillatory shear flow behaviour of a Newtonian fluid and a single element Maxwell fluid in a concentric cylinder geometry on the Weissenberg rheogoniometer will be performed. As in chapter 4 we shall consider the case where the inner cylinder is constrained by a torsion bar and the case where the inner cylinder is connected to a strain gauge torsion head. Using the simulated data, a comparison of complex viscosity predictions is made between the formulae which ignore end effects (see

chapter 4) and the formulae produced in this chapter which include end effects. The numerically simulated data will also be used to establish the frequency range of applicability of the modified second order fluid inertia correction formulae. A comparison will also be made, for a given concentric cylinder geometry, between the complex viscosity data obtained from the Weissenberg rheogoniometer fitted with a strain gauge torsion head and the corresponding data obtained from a CSR controlled stress rheometer.

9.2 Oscillatory shear theory

A generalised linear viscoelastic theory which takes into account end effects is developed for the concentric cylinder geometry on a Weissenberg rheogoniometer. In the oscillatory shear mode the outer cylinder is forced to perform small amplitude oscillations of amplitude θ_2 and frequency f (cycles/sec) about the z-axis. The resulting motion of the fluid causes the inner cylinder, which is constrained by a torsion bar of stiffness K, to perform oscillations about the z-axis of amplitude θ_1 with a phase lag c behind the motion of the outer cylinder. The amplitude θ_1 and phase lag c are measured by the rheogoniometer and together with the applied amplitude θ_2 and frequency f can be used to predict the complex viscosity of a fluid.

In the analysis we consider the outer cylinder to oscillate with amplitude θ_2 at a prescribed frequency f and the inner cylinder to oscillate with amplitude θ_1 at this frequency. It is assumed that the amplitude of oscillation of the driven outer cylinder is sufficiently small to ensure that the flow is in the linear viscoelastic region and hence non-linear fluid inertia terms can be ignored in the equations of motion. Referring to a set of cylindrical polar coordinates (r,θ,z) we may assume a velocity distribution for the axisymmetric flow of the form

$$v_r = 0 \quad , \quad v_\theta = v(r,z)e^{i\alpha t} \quad , \quad v_z = 0 \tag{9.2.1}$$

where $\omega = 2\pi f$ (radians/sec) is the angular frequency of oscillation and the real part of these quantities is implied.

The velocity distribution of equation (9.2.1) gives two non-zero components of the shear stress tensor as

$$\tau_{r\theta} = \eta^{*} r \frac{\partial}{\partial r}\left(\frac{v}{r}\right) e^{i\omega t} \qquad \tau_{\theta z} = \eta^{*} \frac{\partial v}{\partial z} e^{i\omega t} \tag{9.2.2}$$

where η^{*} is the complex viscosity of the fluid.

On substituting equations (9.2.1) and (9.2.2) into the relevant stress equations of motion (Bird *et al* [1]) we have

$$\left(L + \alpha^{2}\right)[v] = 0 \tag{9.2.3}$$

where the fluid inertia parameter α is defined in equation (4.2.4) and the operator L is defined in equation (8.2.5).

With reference to figure 6.2 and using equation (9.2.1) we consider the boundary conditions for the complex velocity function $v(r,z)$. On the moving boundaries the no slip condition is imposed, hence $v = r i w \theta_2 e^{ic}$ on boundaries OE and DE and $v = r_1 i w \theta_1$ on boundary BC. As for the analysis of oscillatory shear flow on a CSR controlled stress rheometer, in chapter 8, we shall impose the condition that the 'free surface' boundaries AB and CD remain in their horizontal positions. On these 'free surface' boundaries we have $\tau_{\theta z} = 0$ and therefore from equation (9.2.2) we have the condition $\partial v/\partial z = 0$. On the line of symmetry boundary OA we have $v = 0$. In summary the boundary conditions for the function $v(r,z)$ are given by

$$\left.\begin{aligned} v &= 0 && \text{on boundary OA.} \\ \partial v/\partial z &= 0 && \text{on free surface boundaries AB and CD.} \\ v &= r_1 i\omega\theta_1 && \text{on the moving boundary BC.} \\ v &= r i\omega\theta_2 e^{ic} && \text{on the moving boundaries DE and OE.} \end{aligned}\right\} \tag{9.2.4}$$

In order to solve equation (9.2.3) numerically it is convenient to express the velocity function $v(r,z)$ as a linear superposition of two velocity functions $v_M(r,z)$ and $v_T(r,z)$ in the form

$$v(r,z) = v_M(r,z) + v_T(r,z) \tag{9.2.5}$$

In this equation we choose $v_M(r,z)$ to be the velocity function which satisfies the oscillatory shear flow situation where $v_M = r\,i\omega\,\theta_2\,e^{ic}$ on the outer cylinder and $v_M = 0$ on the inner cylinder. $v_T(r,z)$ is chosen to be the velocity function which satisfies the oscillatory shear flow situation where $v_T = r_1\,i\omega\,\theta_1$ on the inner cylinder and $v_T = 0$ on the outer cylinder. It can be shown that the expression for $v(r,z)$ in equation (9.2.5) satisfies equation (9.2.3) subject to the boundary conditions in equation (9.2.4).

Throughout the analysis the following non-dimensional variables will be used

$$r^* = \frac{r}{r_1}\,,\quad z^* = \frac{z}{r_1}\,,\quad z_1^+ = \frac{z_1}{r_1}\,,\quad z_2^+ = \frac{z_2}{r_1}\,,\quad v_M^+ = \frac{v_M}{r_1\,i\omega\,\theta_2\,e^{ic}}\,,\quad v_T^+ = \frac{v_T}{r_1\,i\omega\,\theta_1} \tag{9.2.6}$$

Substituting equation (9.2.5) into equation (9.2.3) and using equation (9.2.6) gives the two equations

$$\left(L + (\alpha r_1)^2\right)\left[v_M\right] = 0 \tag{9.2.7}$$

$$\left(L + (\alpha r_1)^2\right)\left[v_T\right] = 0 \tag{9.2.8}$$

where the non-dimensional * notation is implied but has been omitted for convenience.

The non-dimensional function $v_M(r,z)$ in equation (9.2.7) is subject to the boundary conditions

$$\left.\begin{aligned} v_M &= 0 \quad \text{on boundaries OA and BC.} \\ \partial v_M/\partial z &= 0 \quad \text{on free surface boundaries AB and CD.} \\ v_M &= r \quad \text{on the moving boundaries OE and DE.} \end{aligned}\right\} \tag{9.2.9}$$

For the non-dimensional function $v_T(r,z)$ in equation (9.2.9) the boundary conditions are given by

$$\left.\begin{aligned} v_T &= 0 \quad \text{on boundaries OA, OE and DE.} \\ \partial v_T/\partial z &= 0 \quad \text{on free surface boundaries AB and CD.} \\ v_T &= 1 \quad \text{on the moving boundary BC.} \end{aligned}\right\} \tag{9.2.10}$$

It should be noted that the boundary conditions for the non-dimensional velocity functions $v_M(r,z)$ and $v_T(r,z)$ are independent of the amplitude ratios θ_1, θ_2 and the phase lag c.

The equation of motion of the inner cylinder can be written as

$$C_F = (K - I\omega^2)\theta_1 e^{i\alpha t} \tag{9.2.11}$$

where C_F is the torque exerted on the inner cylinder due to the motion of the fluid and I is the moment of inertia of the member constrained by the torsion bar.

The torque C_F exerted on the inner cylinder due to the motion of the inner cylinder is given by equation (6.2.7) with a sign change. Using equations (9.2.2), (9.2.5) and (9.2.6) the torque C_F, for a generalised linear viscoelastic fluid, can be expressed as

$$C_F = -2\pi i\omega r_1^3 \eta^* e^{i\alpha t}\left\{\theta_1 \int_{z_1}^{z_2}\left(\frac{\partial v_T}{\partial r} - \frac{v_T}{r}\right)\bigg|_{r=1} dz + \theta_2 e^{ic}\int_{z_1}^{z_2}\left(\frac{\partial v_M}{\partial r} - \frac{v_M}{r}\right)\bigg|_{r=1} dz\right\} \tag{9.2.12}$$

On substituting equation (9.2.12) into equation (9.2.11) we have

$$\frac{e^{ic}}{\vartheta} = \frac{1}{\beta_M}\left[\frac{i\left(K - I\omega^2\right)}{2\pi r_1^3 \omega \eta^*} - \beta_T\right] \tag{9.2.13}$$

where ϑ $(= \theta_1/\theta_2)$ is the amplitude ratio and

$$\beta_m = -\int_{z_1}^{z_2}\left(\frac{\partial v_m}{\partial r} - \frac{v_m}{r}\right)\bigg|_{r=1} dz \qquad m = M, T \tag{9.2.14}$$

are non-dimensional constants which are dependent on the geometry dimensions and the fluid inertia parameter α.

In principle the complex viscosity η^* of a fluid can be obtained from the solution to the coupled equations (9.2.7), (9.2.8) and (9.2.13) subject to the boundary conditions in equations (9.2.9) and (9.2.10). However a solution to these equations can only be obtained

using a suitable numerical iterative technique. This is not a simple task and therefore we shall solve these equations using a perturbation analysis which will be valid when fluid inertia effects are small.

9.3 Fluid inertia perturbation theory for a generalised linear viscoelastic fluid

The perturbation analysis will follow a similar procedure to the perturbation analysis in section 8.3 for concentric cylinder oscillatory shear flow on a CSR controlled stress rheometer. We consider a second order power series expansion of the functions $v_M(r,z)$ and $v_T(r,z)$ in terms of the non-dimensional parameter $(\alpha r_1)^2$ as

$$v_m(r,z) = v_{m0}(r,z) + (\alpha r_1)^2 v_{m1}(r,z) + (\alpha r_1)^4 v_{m2}(r,z) \qquad m = M,T \tag{9.3.1}$$

Substituting the expansion of equation (9.3.1) into equations (9.2.7) and (9.2.8) and comparing coefficients of the non-dimensional $(\alpha r_1)^2$ terms gives

Zero order: $\quad L[v_{m0}] = 0 \qquad m = M,T \qquad (9.3.2)$

First order: $\quad L[v_{m1}] = -v_{m0} \qquad m = M,T \qquad (9.3.3)$

Second order: $\quad L[v_{m2}] = -v_{m1} \qquad m = M,T \qquad (9.3.4)$

On considering equations (9.2.9) and (9.2.10) and the series expansion in equation (9.3.1), the boundary conditions for the non-dimensional functions $v_{M0}(r,z), v_{M1}(r,z), v_{M2}(r,z)$, $v_{T0}(r,z), v_{T1}(r,z)$ and $v_{T2}(r,z)$ can be determined. For $v_{M0}(r,z)$ we have

$$\left.\begin{aligned} v_{M0} &= 0 \quad \text{on boundaries OA and BC.} \\ \partial v_{M0}/\partial z &= 0 \quad \text{on free surface boundaries AB and CD.} \\ v_{M0} &= r \quad \text{on the moving boundaries OE and DE.} \end{aligned}\right\} \tag{9.3.5}$$

The boundary conditions for $v_{T0}(r,z)$ are given by

$$\left.\begin{aligned} v_{T0} &= 0 \quad \text{on boundaries OA, OE and DE.} \\ \partial v_{T0}/\partial z &= 0 \quad \text{on free surface boundaries AB and CD.} \\ v_{T0} &= 1 \quad \text{on the moving boundary BC.} \end{aligned}\right\} \tag{9.3.6}$$

For $v_{M1}(r,z)$, $v_{M2}(r,z)$, $v_{T1}(r,z)$ and $v_{T2}(r,z)$ we have the conditions

$$\left.\begin{aligned} v_{m1} = v_{m2} &= 0 \quad \text{on boundaries OA, OE, DE and BC.} \\ \partial v_{m1}/\partial z = \partial v_{m2}/\partial z &= 0 \quad \text{on free surface boundaries AB and CD.} \end{aligned}\right\} \tag{9.3.7}$$

where $m = M, T$

The values of the boundary conditions for the velocity functions $v_{m0}(r,z)$, $v_{m1}(r,z)$ and $v_{m2}(r,z)$ for $m = M, T$ are all real quantities. It then follows that the solutions to equations (9.3.2) to (9.3.4) will also be real quantities. These equations are to be solved using a finite difference method with an irregular mesh, which will be described in section 9.4.

On substitution of the series expansions for $v_M(r,z)$ and $v_T(r,z)$, from equation (9.3.1), into equation (9.2.12) the torque C_F exerted on the inner cylinder due to the motion of the fluid can be expressed as

$$C_F = -2\pi i\omega r_1^3 \eta^* e^{i\alpha t}\Big\{\theta_1\left[\beta_{T0} + (\alpha r_1)^2\beta_{T1} + (\alpha r_1)^4\beta_{T2}\right]$$

$$+\theta_2 e^{ic}\left[\beta_{M0} + (\alpha r_1)^2\beta_{M1} + (\alpha r_1)^4\beta_{M2}\right]\Big\} \tag{9.3.8}$$

where $$\beta_m = -\int_{z_1}^{z_2}\left(\frac{\partial v_m}{\partial r} - \frac{v_m}{r}\right)\Bigg|_{r=1} dz \quad m = T0, T1, T2, M0, M1, M2 \tag{9.3.9}$$

are non-dimensional geometry dependent constants.

We define η_0^* to be the complex viscosity of the fluid when fluid inertia effects are ignored. The torque C_F exerted on the inner cylinder due to the motion of the fluid when fluid inertia effects are ignored can then be obtained from equation (9.3.8) by setting $\alpha = 0$ and replacing η^* by η_0^* to give

$$C_F = -2\pi i\omega r_1^3 \eta_0^* e^{i\alpha t}\left\{\theta_1\beta_{T0} + \theta_2 e^{ic}\beta_{M0}\right\} \tag{9.3.10}$$

Using equations (9.2.11) and (9.3.10) we have

$$\frac{e^{ic}}{\vartheta} = \frac{1}{\beta_{M0}}\left[\frac{i\left(K - I\omega^2\right)}{2\pi r_1^3\omega\eta_0^*} - \beta_{T0}\right] \tag{9.3.11}$$

Following a similar analysis to that presented in section 7.4 it can be shown that $\beta_{T0} = -\beta_{M0}$ and it is then convenient to express equation (9.3.11) in the form

$$\eta_0^* = f_0 \frac{iS}{\left(1 - e^{ic}/\vartheta\right)} \tag{9.3.12}$$

where S is the geometrical parameter defined in equation (4.3.15) and $f_0 (= -2hr_2^2 / [\beta_{M0} r_1 (r_2^2 - r_1^2)]$ is a geometry dependent end effect correction factor in which h is the height of the inner cylinder. It should be noted that in this form the factor f_0 has a value of 1 when end effects are ignored. In this case equation (9.3.12) reduces to the formula given in equation (4.2.17) for determining the complex viscosity η_0^* of a fluid.

We define the complex parameter α_0^2 as

$$\alpha_0^2 = \frac{-i\omega\rho}{\eta_0^*} \tag{9.3.13}$$

On using equations (9.3.8), (9.3.10) and (9.3.13) we obtain a relationship between η_0^* and η^* given by

$$\eta_0^* \left\{ \beta_{T0} + \frac{e^{ic}}{\vartheta} \beta_{M0} \right\} = \eta^* \left\{ \left[\beta_{T0} + \beta_{M0} \frac{e^{ic}}{\vartheta} \right] + \left[\beta_{T1} + \beta_{M1} \frac{e^{ic}}{\vartheta} \right] (\alpha_0 r_1)^2 \frac{\eta_0^*}{\eta^*} \right.$$

$$\left. + \left[\beta_{T2} + \beta_{M2} \frac{e^{ic}}{\vartheta} \right] (\alpha_0 r_1)^4 \frac{\eta_0^{*2}}{\eta^{*2}} \right\} \tag{9.3.14}$$

In order to determine an expression for η^* in terms of η_0^*, from this equation, we expand η^* as a second order power series in the non-dimensional parameter $(\alpha_0 r_1)^2$ given by

$$\eta^* = \eta_0^* + (\alpha_0 r_1)^2 \eta_1^* + (\alpha_0 r_1)^4 \eta_2^* \tag{9.3.15}$$

On substituting equation (9.3.15) into equation (9.3.14) we obtain

$$\eta_0^*\left\{\beta_{T0}+\frac{e^{ic}}{\vartheta}\beta_{M0}\right\}=\eta_0^*\left\{\beta_{T0}+\frac{e^{ic}}{\vartheta}\beta_{M0}\right\}+\left\{\left[\beta_{T1}\eta_0^*+\beta_{T0}\eta_1^*\right]+\frac{e^{ic}}{\vartheta}\left[\beta_{M1}\eta_0^*+\beta_{M0}\eta_1^*\right]\right\}(\alpha_0 r_1)^2$$

$$+\left\{\left[\beta_{T2}\eta_0^*+\beta_{T0}\eta_2^*\right]+\frac{e^{ic}}{\vartheta}\left[\beta_{M2}\eta_0^*+\beta_{M0}\eta_2^*\right]\right\}(\alpha_0 r_1)^4 \qquad (9.3.16)$$

where terms of order $(\alpha_0 r_1)^6$ and higher have been neglected.

Comparing coefficients of the $(\alpha_0 r_1)^2$ terms in equation (9.3.16) and using equation (9.3.11) and the result that $\beta_{T0}=-\beta_{M0}$ we have

$$\eta_1^*=\left[\frac{2\pi i\omega r_1^3\eta_0^*}{\left(K-I\omega^2\right)}(\beta_{M1}+\beta_{T1})-\frac{\beta_{M1}}{\beta_{M0}}\right]\eta_0^* \qquad (9.3.17)$$

$$\eta_2^*=\left[\frac{2\pi i\omega r_1^3\eta_0^*}{\left(K-I\omega^2\right)}(\beta_{M2}+\beta_{T2})-\frac{\beta_{M2}}{\beta_{M0}}\right]\eta_0^* \qquad (9.3.18)$$

Substituting these expressions for η_1^* and η_2^* into equation (9.3.15) gives

$$\eta^*=\eta_0^*\left[1-\left\{f_1+\frac{i\eta_0^*}{S}f_2\right\}(\alpha_0 r_1)^2-\left\{f_3+\frac{i\eta_0^*}{S}f_4\right\}(\alpha_0 r_1)^4\right] \qquad (9.3.19)$$

where f_1, f_2, f_3 and f_4 are non-dimensional geometry dependent factors given by

$$f_1=\frac{\beta_{M1}}{\beta_{M0}} \qquad f_2=\frac{r_1\left(r_2^2-r_1^2\right)}{2hr_2^2}(\beta_{M1}+\beta_{T1})$$

$$f_3=\frac{\beta_{M2}}{\beta_{M0}} \qquad f_4=\frac{r_1\left(r_2^2-r_1^2\right)}{2hr_2^2}(\beta_{M2}+\beta_{T2}) \qquad (9.3.20)$$

On using equation (9.3.13) we can express the correction for second order fluid inertia effects as

$$\eta^*=\eta_0^*+i\omega\rho r_1^2\left\{f_1+\frac{i\eta_0^*}{S}f_2\right\}+\frac{\omega^2\rho^2 r_1^4}{\eta_0^*}\left\{f_3+\frac{i\eta_0^*}{S}f_4\right\} \qquad (9.3.21)$$

Using the numerical solution to equations (9.3.2) to (9.3.4), the non-dimensional geometry dependent constants β_{m0}, β_{m1} and β_{m2} for $m=M,T$ can be determined from equation

(9.3.9). The geometry dependent factors f_0, f_1, f_2, f_3 and f_4 required in equations (9.3.12) and (9.3.21) can then be calculated. A finite difference method for the solution of equations (9.3.2) to (9.3.4) will be presented in section 9.4.

Equation (9.3.21) is the modified formula for calculating the complex viscosity of a fluid which corrects for both end effects and second order fluid inertia effects. This equation takes a similar form to the second order fluid inertia correction, given in equation (4.3.27), where end effects were ignored. The f_1, f_2, f_3 and f_4 factors in equation (9.3.21) are known for the case when end effects are ignored from equations (4.3.26) and (4.3.27). It is noted that η_0^* in equation (9.3.26) is known from equation (9.3.17). In order to establish the limitations of the second order fluid inertia perturbation theory, we shall simulate the oscillatory shear flow behaviour of a Newtonian fluid and a single element Maxwell fluid in the medium gap CSR geometry on a Weissenberg rheogoniometer. From the simulation we can generate complex viscosity data which is equivalent to the data obtained from the rheogoniometer software when end effects and fluid inertia effects are ignored. The simulated data will be used to establish how the complex viscosity prediction of a fluid in a concentric cylinder geometry is influenced by end effects and fluid inertia effects.

9.3.1 Complex viscosity prediction for a strain gauge torsion head system on the Weissenberg rheogoniometer

On a Weissenberg rheogoniometer, instead of constraining the inner cylinder with a torsion bar it is possible to connect the inner cylinder to a strain gauge torsion head. As discussed in chapter 4 we can assume that when a strain gauge is used the inner cylinder will remain stationary. Therefore we consider the strain gauge to be infinitely stiff and a relationship η_0^* and η^* for this type of oscillatory shear flow is then obtained by combining equations (9.2.13) and (9.3.11) and setting $K = \infty$ to give

$$\eta_0^* = f_0 \frac{r_1(r_1^2 - r_2^2)}{2hr_2^2} \beta_M \eta^* \tag{9.3.22}$$

where f_0 is the geometry dependent end effect correction factor defined in equation (9.3.12).

It is noted that if $K = \infty$ then it follows that the geometrical parameter S defined in equation (4.3.15) is also infinite. On setting $S = \infty$ in equation (9.3.19) we obtain the second order fluid inertia correction for complex viscosity data obtained using a strain gauge torsion head as

$$\eta^* = \eta_0^* \left[1 - f_1 (\alpha_0 r_1)^2 - f_3 (\alpha_0 r_1)^4 \right] \tag{9.3.23}$$

where f_1 and f_3 are defined in equation (9.3.20)

9.4 Finite difference method of solution for the perturbation theory equations

Equations (9.3.2) to (9.3.4), obtained from the fluid inertia perturbation theory, are to be solved using a finite difference method with a finer mesh near the recessed end (corner B). Therefore, as described in section 6.4, the whole flow domain is separated into three sub-domains as shown in figure 6.4 and the physical domain (r,z) is transformed to a computational plane (x,y) using equations (6.4.1) to (6.4.3). We let the non-dimensional functions $v_{M0}(r,z)$, $v_{M1}(r,z)$ and $v_{M2}(r,z)$ be transformed to $v_{M0_s}(x,y)$, $v_{M1_s}(x,y)$ and $v_{M2_s}(x,y)$ respectively for $s = 1,2,3$. The non-dimensional functions $v_{T0}(r,z)$, $v_{T1}(r,z)$ and $v_{T2}(r,z)$ are transformed to $v_{T0_s}(x,y)$, $v_{T1_s}(x,y)$ and $v_{T2_s}(x,y)$ respectively for $s = 1,2,3$. The finite difference method of solution for each of the transformed velocity functions is now described.

9.4.1 Finite difference equations for the velocity functions $v_{M0}(r,z)$ and $v_{T0}(r,z)$

The velocity functions $v_{M0_s}(x,y)$ and $v_{T0_s}(x,y)$ over the xy-plane are denoted at each meshpoint (i,j) by $v_{M0_s\ i,j}$ and $v_{T0_s\ i,j}$ respectively. It is noted that equation (9.3.2) is of the same form as equation (6.3.19), but the boundary conditions are now given by equations (9.3.5) and (9.3.6). Therefore on making the substitutions $v_{0_s} = v_{M0_s}$ and $v_{0_s} = v_{T0_s}$ in the equations presented in section 6.4.3 (equations (6.4.13), (6.4.17) and (6.4.20)) we obtain the respective finite difference equations for $v_{M0_s\ i,j}$ and $v_{T0_s\ i,j}$. As before the velocities $v_{M0_s\ i,j}$ and $v_{T0_s\ i,j}$ on the 'free surface' boundaries' will satisfy the condition in equation (6.4.15). Equations (6.4.19) and (6.4.22) are used to match the finite difference equations across the interfaces between sub-domains. The iterative procedure presented in appendix 6.1 can be followed to solve the finite difference equations for $v_{M0_s\ i,j}$ and $v_{T0_s\ i,j}$.

9.4.2 Finite difference equations for the velocity functions $v_{M1}(r,z)$ and $v_{T1}(r,z)$

The velocity functions $v_{M1_s}(x,y)$ and $v_{T1_s}(x,y)$ over the xy-plane are denoted at each meshpoint (i,j) by $v_{M1_s\ i,j}$ and $v_{T1_s\ i,j}$ respectively. It is noted that equation (9.3.3) is of the same form as equation (8.3.3) and the velocity boundary conditions are also the same. Therefore on making the substitutions $v_{0_s} = v_{M0_s}$ and $v_{1_s} = v_{M1_s}$ in the equations presented in section 8.4.2 (equations (8.4.1) to (8.4.4)) we obtain the finite difference equations for $v_{M1_s\ i,j}$. Making the substitutions $v_{0_s} = v_{T0_s}$ and $v_{1_s} = v_{T1_s}$ in equations (8.4.1) to (8.4.4) gives the finite difference equations for $v_{T1_s\ i,j}$. The iterative procedure presented in appendix 8.1 can be followed to solve the finite difference equations for $v_{M1_s\ i,j}$ and

$v_{T1_s}{}_{i,j}$ discussed in this section.

9.4.3 Finite difference equations for the velocity functions $v_{M2}(r,z)$ and $v_{T2}(r,z)$

The velocity functions $v_{M2_s}(x,y)$ and $v_{T2_s}(x,y)$ over the xy-plane are denoted at each meshpoint (i,j) by $v_{M2_s}{}_{i,j}$ and $v_{T2_s}{}_{i,j}$ respectively. It is noted that equation (9.3.4) is of the same form as equation (8.3.4) with the same velocity boundary conditions. Therefore the finite difference equations for $v_{M2_s}{}_{i,j}$ are obtained by making the substitutions $v_{1_s} = v_{M1_s}$ and $v_{2_s} = v_{M2_s}$ in the equations presented in section 8.4.3 (equations (8.4.5) to (8.4.8)). Substituting $v_{1_s} = v_{T1_s}$ and $v_{2_s} = v_{T2_s}$ into the equations presented in section 8.4.3 (equations (8.4.5) to (8.4.8)) gives the finite difference equations for $v_{M2_s}{}_{i,j}$. The iterative procedure presented in appendix 8.2 can be followed to solve the finite difference equations for $v_{M2_s}{}_{i,j}$ and $v_{T2_s}{}_{i,j}$ discussed in this section.

9.4.4 Calculation of the geometry dependent constants β_m from the finite difference solutions for the perturbation theory equations

In equation (9.3.8) the torque C_F exerted on the inner cylinder due to the motion of the fluid is expressed in terms of the non-dimensional constants β_{M0}, β_{M1}, β_{M2}, β_{T0}, β_{T1} and β_{T2}. These constants can be determined from the finite difference solutions for the velocity distributions $v_{M0}(r,z)$, $v_{M1}(r,z)$, $v_{M2}(r,z)$, $v_{T0}(r,z)$, $v_{T1}(r,z)$ and $v_{T2}(r,z)$ using equations (6.4.62) and (6.4.63) for $m = M0, M1, M2, T0, T1, T2$ and the method described in section 6.4.7.

9.5 Results for the fluid inertia perturbation theory

Oscillatory shear end effects and fluid inertia effects are considered for the same

three CSR geometries as for steady shear flow on a CSR controlled stress rheometer. Therefore the finite difference equations given in section 9.4 are solved using 160×160 meshes as described in section 6.4.8.

Using the numerical solution to equations (9.3.2) to (9.3.4) for the three CSR geometries, the non-dimensional geometry dependent constants β_{M0}, β_{M1}, β_{M2}, β_{T0}, β_{T1} and β_{T2} are determined. The geometry dependent factors f_0, f_1, f_2, f_3, f_4 required in equations (9.3.17) and (9.3.26) are therefore known and presented in table 9.1(a).

	With End Effects				
	f_0	f_1	f_2	f_3	f_4
Narrow Gap	0·973	$2{\cdot}429 \times 10^{-3}$	$6{\cdot}627 \times 10^{-3}$	$4{\cdot}156 \times 10^{-6}$	$8{\cdot}314 \times 10^{-6}$
Medium Gap	0·927	$2{\cdot}248 \times 10^{-2}$	$5{\cdot}364 \times 10^{-2}$	$3{\cdot}739 \times 10^{-4}$	$6{\cdot}812 \times 10^{-4}$
Wide Gap	0·908	$6{\cdot}378 \times 10^{-2}$	$1{\cdot}355 \times 10^{-1}$	$3{\cdot}091 \times 10^{-3}$	$5{\cdot}179 \times 10^{-3}$

Table 9.1(a):- Oscillatory shear factors with end effects.

	Without End Effects				
	f_0	f_1	f_2	f_3	f_4
Narrow Gap	1	$2{\cdot}464 \times 10^{-3}$	$6{\cdot}616 \times 10^{-3}$	$4{\cdot}248 \times 10^{-6}$	$8{\cdot}336 \times 10^{-6}$
Medium Gap	1	$2{\cdot}437 \times 10^{-2}$	$5{\cdot}452 \times 10^{-2}$	$4{\cdot}150 \times 10^{-4}$	$7{\cdot}068 \times 10^{-4}$
Wide Gap	1	$7{\cdot}170 \times 10^{-2}$	$1{\cdot}398 \times 10^{-1}$	$3{\cdot}587 \times 10^{-3}$	$5{\cdot}507 \times 10^{-3}$

Table 9.1(b):- Oscillatory shear factors without end effects.

For comparison we present the geometry dependent factors when end effects are ignored in table 9.1(b). The factors in this table have been evaluated using equations (4.3.26) and (4.3.27). It should be noted that the oscillatory shear f_0 factors in table 9.1(a) are identical to both the steady shear f_0 factors presented in tables 6.1 and 7.1 and the oscillatory shear

f_0 factors for the CSR controlled stress rheometer presented in table 8.1. In order to establish the limitations of the second order fluid inertia perturbation theory, we simulate the oscillatory shear flow behaviour of a Newtonian fluid and a single element Maxwell fluid in the medium gap CSR geometry. The simulation is considered for the case where the inner cylinder is constrained by a torsion bar of finite stiffness K and the case where the inner cylinder is connected to a strain gauge torsion head, which we consider to have infinite stiffness.

9.6 Flow simulation of a Newtonian fluid and a single element Maxwell fluid

For a Newtonian fluid and a single element Maxwell fluid the complex viscosity is given by $\eta^* = \eta_0$ and $\eta^* = \eta_0/(1+i\lambda\omega)$ respectively, where η_0 is the Newtonian viscosity and λ is the relaxation time. The complex viscosity of these theoretical model fluids is known and will be referred to as the exact viscosity data throughout this section. At a prescribed outer cylinder frequency of oscillation f the velocity distribution $v_M(r,z)$, for the theoretical model fluids, can be determined from the numerical solution of equation (9.2.7) subject to the boundary equations in equation (9.2.9). Similarly equation (9.2.8) can be solved numerically, subject to the boundary conditions in equation (9.2.10), for the frequency f to give the velocity distribution $v_T(r,z)$ for the theoretical model fluids. Using these velocity distributions in equation (9.2.13) the expression e^{ic}/ϑ can be evaluated numerically. Hence on using this value in equation (9.3.12) the complex viscosity η_0^*, when fluid inertia effects are ignored, can be determined where the f_0 values are given in tables 9.1(a) and 9.1(b). This value of η_0^* can then be used in equation (9.3.21) to determine the first order and second order fluid inertia corrections, both with and without end effects, where the f_1, f_2, f_3 and f_4 values are given in tables 9.1(a) and 9.1(b). Since the exact

complex viscosity data of the theoretical model fluids is known, the limitations of the second order fluid inertia perturbation theory can be established.

Simulations will also be performed for the case where the inner cylinder is constrained by a strain gauge torsion head. The complex viscosity data obtained from these simulations will be compared with the corresponding data obtained from a CSR controlled stress rheometer.

The numerical finite difference method used to solve equations (9.2.7) and (9.2.8) for a known fluid at a prescribed frequency of oscillation is now described.

9.6.1 Finite difference equations for the velocity functions $v_M(r,z)$ and $v_T(r,z)$

For a known fluid at a prescribed frequency of oscillation the non-dimensional complex parameter $(\alpha r_1)^2$ can be evaluated for a given concentric cylinder geometry. When the value of $(\alpha r_1)^2$ is known equations (9.2.7) and (9.2.8) can be solved numerically, subject to the boundary conditions of equations (9.2.9) and (9.2.10) respectively, to determine the complex velocity functions $v_M(r,z)$ and $v_T(r,z)$. Equations (9.2.7) and (9.2.8) are to be solved using a finite difference method with an irregular mesh, as described in section 6.4. Therefore the whole flow domain is separated into three sub-domains, as shown in figure 6.4, and the physical domain (r,z) is transformed to a computational plane (x,y) using equations (6.4.1) to (6.4.3). We let the complex velocity functions $v_M(r,z)$ and $v_T(r,z)$ be transformed to $v_{M_s}(x,y)$ and $v_{T_s}(x,y)$ respectively for $s = 1,2,3$.

The velocity functions $v_{M_s}(x,y)$ and $v_{T_s}(x,y)$ over the xy-plane are denoted at each meshpoint (i,j) by $v_{M_s\,i,j}$ and $v_{T_s\,i,j}$ respectively. It is noted that both equations (9.2.7) and (9.2.8) are of the same form as equation (8.2.4), where the velocity boundary conditions are now given by equations (9.2.9) and (9.2.10). Therefore on making the

substitutions $v_s = v_{Ms}$ and $v_s = v_{Ts}$ in the equations presented in section 8.6.1 (equations (8.6.1) to (8.6.4)) we obtain the respective finite difference equations for $v_{Ms\ i,j}$ and $v_{Ts\ i,j}$.

The iterative procedure presented in appendix 8.3 can be followed to solve the finite difference equations for $v_{Ms\ i,j}$ and $v_{Ts\ i,j}$ discussed in this section.

In equation (9.2.13) the motion of the inner cylinder is expressed in terms of the non-dimensional constants β_M and β_T. These constants can be determined from the finite difference solutions for $v_M(r,z)$ and $v_M(r,z)$ using equations (6.4.62) and (6.4.63) for $m = M, T$ and the method described in section 6.4.7.

9.6.2 Results for the oscillatory shear flow simulations with a torsion bar system

The numerical simulations are performed for a medium gap CSR geometry, where the inner cylinder is constrained by a torsion bar of stiffness $K = 5 \cdot 005\,\mathrm{Nm/rad}$ and the member constrained by the torsion bar has moment of inertia $I = 164\,\mu\mathrm{Ns}^2$. For these values of K and I the member constrained by the torsion bar will have a natural frequency of $\omega_0 = 174 \cdot 695\,\mathrm{rad/s}$.

For a given concentric cylinder geometry and torsion bar (*i.e.* r_1, r_2, I, K known), it can be shown that the normalised complex viscosity (η^*/η_0) of a Newtonian fluid can be represented as a function of the two non-dimensional quantities $R\,(=\rho r_1^2\omega_0/\eta_0)$ and the normalised frequency (ω/ω_0). As for the numerical simulations presented in section 5.3, where end effects were ignored, we consider the oscillatory shear flow behaviour of Newtonian fluids over the frequency range $0 < \omega < 2\omega_0$. In figures 9.1 and 9.2 we present end effect corrections and fluid inertia corrections for the simulated dynamic viscosity and dynamic rigidity data respectively of a Newtonian fluid in a medium gap geometry when $R = 10$. The uncorrected data in these figures is obtained from the standard formula

(equation (9.3.12) with $f_0 = 1$) in which end effects and fluid inertia effects are ignored. In figures 9.1 and 9.2 we also present complex viscosity data corrected for end effects only, corrected for second order fluid inertia effects only and corrected for both end effects and second order fluid inertia effects. In these figures it should be noted that the uncorrected data and the data corrected for end effects differ by a scaling factor of $f_0 = 0{\cdot}927$ for all frequencies of oscillation. Figure 9.2 shows an apparent positive dynamic rigidity when fluid inertia effects are ignored and an apparent negative dynamic rigidity when second order fluid inertia effects are included in the theory. It is seen in figure 9.1 that when both end effects and second order fluid inertia effects are taken into account good agreement is obtained with the exact dynamic viscosity data over the full normalised frequency range considered. However in figure 9.2 it is seen that when both end effects and second order fluid inertia effects are taken into account good agreement with the exact dynamic rigidity data is only obtained up to a normalised frequency of 0·8.

For a given concentric cylinder geometry and torsion bar (*i.e.* r_1, r_2, I, K known), the normalised complex viscosity (η^*/η_0) of a single element Maxwell fluid, with a specific relaxation time λ, can be written as a function of the two non-dimensional quantities $R\,(=\rho r_1^2\omega_0/\eta_0)$ and the normalised frequency (ω/ω_0). The oscillatory shear flow behaviour of single element Maxwell fluids is simulated over the frequency range $0 < \omega < 2\omega_0$ and the relaxation time λ is chosen such that $\lambda\omega_0 = 1$. Figures 9.3 and 9.4 show end effect corrections and fluid inertia effect corrections for the simulated dynamic viscosity and dynamic rigidity data respectively of a single element Maxwell fluid in the medium gap geometry when $R = 5$. These figures include uncorrected data, data corrected for end effects only, data corrected for second order fluid inertia effects only and data corrected for both end effects and second order fluid inertia effects. It is seen in figure 9.3 that dynamic viscosity data corrected for both end effects and second order fluid inertia

effects gives good agreement with the exact data for Deborah numbers below 0·8. However the corresponding dynamic rigidity data, presented in figure 9.4, corrected for both end effects and second order fluid inertia effects gives good agreement with the exact data up to a higher Deborah number of 1·2.

9.6.3 Results for the oscillatory shear flow simulations with a strain gauge torsion head system

The numerical simulations are performed for a medium gap CSR geometry where the inner cylinder is connected to a strain gauge torsion head and is therefore assumed to remain stationary. As before we consider the oscillatory shear flow behaviour of Newtonian fluids and single element Maxwell fluids. On using the non-dimensional constant β_M in equation (9.3.22) the complex viscosity η_0^*, when fluid inertia effects are ignored, can be determined where the f_0 values are given in tables 9.1(a) and 9.1(b). This value of η_0^* can then be used in equation (9.3.23) to determine the first and second order fluid inertia corrections, both with and without end effects, where the f_1 and f_2 values are given in tables 9.1(a) and 9.1(b). For comparison purposes, the concentric cylinder oscillatory shear flow behaviour of Newtonian fluids and single element Maxwell fluids is also simulated for a CSR controlled stress rheometer. This simulation is carried out as described in section 8.6.

For a Newtonian fluid in a given concentric cylinder geometry it can be shown that, on both the Weissenberg rheogoniometer fitted with a strain gauge and the CSR controlled stress rheometer, the normalised complex viscosity (η^*/η_0) can be represented as a function of the non-dimensional normalised frequency ($= \rho\, r_1^2\, \omega/\eta_0$). In figures 9.5 and 9.6 we present end effect and fluid inertia corrections for the simulated dynamic viscosity and dynamic rigidity data of a Newtonian fluid in the medium gap geometry. These figures include uncorrected data, data corrected for end effects and data corrected for both end

effects and second order fluid inertia effects obtained from both the Weissenberg and CSR instruments. It is noted that for both instruments in figures 9.5 and 9.6, the uncorrected data and the data corrected for end effects differ by a scaling factor of $f_0 = 0 \cdot 927$ for all frequencies of oscillation. It is seen in figure 9.5 that, for both instruments, the dynamic viscosity data corrected for both end effects and second order fluid inertia effects gives good agreement with the exact data for normalised frequencies below 20. However the dynamic rigidity data in figure 9.6 shows that the CSR correction for end effects and second order fluid inertia effects gives good agreement with the exact data up to a normalised frequency of 40, whereas the corresponding data for the Weissenberg instrument is only in agreement for normalised frequencies below 10.

For a single element Maxwell fluid in a given concentric cylinder geometry it can be shown that, on both the Weissenberg rheogoniometer fitted with a strain gauge and the CSR controlled stress rheometer, the normalised complex viscosity (η^*/η_0) can be represented as a function of the two non dimensional quantities $R\,(=\rho r_1^2/(\lambda\eta_0))$ and the Deborah number $De\,(=\lambda\omega)$. Figures 9.7 and 9.8 show end effect and fluid inertia corrections for the simulated dynamic viscosity and dynamic rigidity data respectively of a single element Maxwell fluid when $R = 10$. In these figures we present uncorrected data, data corrected for end effects and data corrected for both end effects and second order fluid inertia effects from both the Weissenberg and CSR instruments. It is seen in figures 5.7 and 5.8 that when correcting for end effects and second order fluid inertia effects, both instruments give good agreement with the exact complex viscosity data up to a normalised frequency of 0·8.

9.7 Conclusions

Using a perturbation analysis we have produced an analytical formula which can be

used to correct Weissenberg rheogoniometer complex viscosity data for concentric cylinder end effects and second order fluid inertia effects. This formula is expressed in terms of geometry dependent factors and can be incorporated into the Weissenberg rheogoniometer software to correct complex viscosity predictions for these effects. Simulated oscillatory shear data on a Weissenberg rheogoniometer has shown that correcting for end effects and second order fluid inertia effects gives more accurate complex viscosity predictions. As in chapter 5, the inclusion of second order fluid inertia effects gives a significant improvement in the complex viscosity prediction at frequencies of oscillation near the natural frequency of the inner cylinder constrained by the torsion bar.

APPENDICES

Appendix 4.1

The properties of Bessel functions used to determine equation (4.3.14) are given by

$$J_{p+1}(x) = -J_{p-1}(x) + \frac{2p}{x} J_p(x) \tag{A4.3.1}$$

$$-(x)^{-1} J_2(x) = \frac{d}{dx}[x^{-1} J_1(x)] \tag{A4.3.2}$$

$$J_1(x) Y_1'(x) - J_1'(x) Y_1(x) = \frac{2}{\pi x} \tag{A4.3.3}$$

Appendix 6.1 Iterative procedure used to solve the finite difference equations for $v_{\theta 0}(r,z)$ presented in section 6.4.3

The steps for solving the finite difference equations presented in section 6.4.3 are as follows.

1. Set initial values for $v_{0_s\ i,j}$ at all internal meshpoints, boundary meshpoints and the 'fictitious meshpoints' above the free surface boundaries.
2. Calculate the discrete functions given in equations (6.4.14), (6.4.18) and (6.4.21) at all relevant meshpoints.
3. Apply equation (6.4.13) in sub-domain 1 ($s=1$) for $i=1$ to m_1-1 and $j=1$ to n_1. Use equation (6.4.15) (for $s=1$) to update the values at the 'fictitious meshpoints' ($j=n_1+1$) for $i=1$ to m_1-1.
4. Apply equation (6.4.17) for $j=1$ to n_1-1 at meshpoints on the interface between sub-domains 1 and 2. Let $v_{02\ 0,j}=v_{01\ m_1,j}$ for $j=1$ to n_1-1 in order to match the finite difference equations across the interface between sub-domains 1 and 2.
5. Apply equation (6.4.13) in sub-domain 2 ($s=2$) for $i=1$ to m_2-1 and $j=1$ to n_2-1.
6. Apply equation (6.4.20) for $i=1$ to m_2-1 at meshpoints on the interface between sub-domains 2 and 3. Let $v_{03\ i,0}=v_{02\ i,n_2}$ for $i=1$ to m_2-1 in order to match the finite difference equations across the interface between sub-domains 2 and 3.
7. Apply equation (6.4.13) in sub-domain 3 ($s=3$) for $i=1$ to m_3-1 and $j=1$ to n_3. Use equation (6.4.15) (for $s=3$) to update the values at the 'fictitious meshpoints' ($j=n_3+1$) for $i=1$ to m_3-1.
8. If convergence is achieved go to step 9 if not return to step 3 to start another iteration of the SOR method.
9. Store the discrete velocities $v_{0_s\ i,j}$ at every meshpoint in each sub-domain as an array.

Appendix 6.2 Iterative procedure used to solve the finite difference equations for $\psi(r,z)$ and $\phi(r,z)$ presented in section 6.4.4

The steps for solving the finite difference equations presented in section 6.4.4 are as follows.

1. Set initial values for $\phi_{s\ i,j}$ and $\psi_{s\ i,j}$ at all internal meshpoints and boundary meshpoints.
2. Calculate the discrete functions given in equations (6.4.28), (6.4.31) and (6.4.34) at all relevant meshpoints.
3. Using the previously determined finite difference solution $v_{0s\ i,j}$ to calculate the discrete function $f_s(i,j)$ given in equations (6.4.25), (6.4.31) and (6.4.34) at all relevant meshpoints.
4. Apply equation (6.4.26) in sub-domain 1 ($s=1$) for $i=1$ to m_1-1 and $j=1$ to n_1-1.
5. Apply equation (6.4.29) for $j=1$ to n_1-1 at meshpoints on the interface between sub-domains 1 and 2. Let $\phi_{2\ 0,j}=\phi_{1\ m_1,j}$ for $j=1$ to n_1-1 in order to match the finite difference equations across the interface between sub-domains 1 and 2.
6. Apply equation (6.4.26) in sub-domain 2 ($s=2$) for $i=1$ to m_2-1 and $j=1$ to n_2-1.
7. Apply equation (6.4.32) for $i=1$ to m_2-1 at meshpoints on the interface between sub-domains 2 and 3. Let $\phi_{3\ i,0}=\phi_{2\ i,n_2}$ for $i=1$ to m_2-1 in order to match the finite difference equations across the interface between sub-domains 2 and 3.
8. Apply equation (6.4.26) in sub-domain 3 ($s=3$) for $i=1$ to m_3-1 and $j=1$ to n_3-1.
9. Apply equation (6.4.27) in sub-domain 1 ($s=1$) for $i=1$ to m_1-1 and $j=1$ to n_1-1.
10. Apply equation (6.4.30) for $j=1$ to n_1-1 at meshpoints on the interface between sub-domains 1 and 2. Let $\psi_{2\ 0,j}=\psi_{1\ m_1,j}$ for $j=1$ to n_1-1 in order to match the finite difference equations across the interface between sub-domains 1 and 2.
11. Apply equation (6.4.27) in sub-domain 2 ($s=2$) for $i=1$ to m_2-1 and $j=1$ to n_2-1.
12. Apply equation (6.4.33) for $i=1$ to m_2-1 at meshpoints on the interface between sub-domains 2 and 3. Let $\psi_{3\ i,0}=\psi_{2\ i,n_2}$ for $i=1$ to m_2-1 in order to match the finite difference equations across the interface between sub-domains 2 and 3.

13. Apply equation (6.4.27) in sub-domain 3 $(s=3)$ for $i=1$ to m_3-1 and $j=1$ to n_3-1.
14. If convergence is achieved go to step 16 if not proceed to step 15.
15. Update the boundary conditions for $\phi_{s\ i,j}$ using equations (6.4.36), (6.4.38), (6.4.39) and (6.4.41) and then return to step 3 to start another iteration of the SOR method.
16. Store the discrete streamfunction values $\psi_{s\ i,j}$ at every meshpoint in each sub-domain as an array.

Appendix 6.3 Iterative procedure used to solve the finite difference equations for $v_{\theta 2}(r,z)$ presented in section 6.4.6

The steps for solving the finite difference equations presented in section 6.4.6 are as follows.

1. Set initial values at all internal meshpoints, boundary meshpoints and 'fictitious meshpoints' above the free surface boundaries.
2. Calculate the discrete functions given in equations (6.4.14), (6.4.18) and (6.4.21) at all relevant meshpoints.
3. Calculate the discrete functions $f_s(i,j)$ given in equations (6.4.54), (6.4.55), (6.4.58) and (6.4.60) at all relevant meshpoints.
4. Apply equation (6.4.56) in sub-domain 1 ($s=1$) for $i=1$ to m_1-1 and $j=1$ to n_1. Use equation (6.4.57) (for $s=1$) to update the values at the fictitious points ($j=n_1+1$) for $i=1$ to m_1-1.
5. Apply equation (6.4.59) for $j=1$ to n_1-1 at meshpoints on the interface between sub-domains 1 and 2. Let $v_{22\ 0,j}=v_{21\ m_1,j}$ for $j=1$ to n_1-1 in order to match the finite difference equations across the interface between sub-domains 1 and 2.
6. Apply equation (6.4.56) in sub-domain 2 ($s=2$) for $i=1$ to m_2-1 and $j=1$ to n_2-1.
7. Apply equation (6.4.61) for $i=1$ to m_2-1 at meshpoints on the interface between sub-domains 2 and 3. Let $v_{23\ i,0}=v_{22\ i,n_2}$ for $i=1$ to m_2-1 in order to match the finite difference equations across the interface between sub-domains 2 and 3.
8. Apply equation (6.4.56) in sub-domain 3 ($s=3$) for $i=1$ to m_3-1 and $j=1$ to n_3. Use equation (6.4.57) (for $s=3$) to update the values at the fictitious points ($j=n_3+1$) for $i=1$ to m_3-1.
9. If convergence is achieved go to step 10 if not return to step 4 to start another iteration of the SOR method.
10. Store the discrete velocities $v_{2s\ i,j}$ at every meshpoint in each sub-domain as an array.

Appendix 8.1 Iterative procedure used to solve the finite difference equations for $v_1(r,z)$ presented in section 8.4.2

The steps for solving the finite difference equations presented in section 8.4.2 are as follows.

1. Set initial values for $v_{1_s}{}_{i,j}$ at all internal meshpoints, boundary meshpoints and the 'fictitious meshpoints' above the free surface boundaries.
2. Calculate the discrete functions given in equations (6.4.14), (6.4.18) and (6.4.21) at all relevant meshpoints.
3. Apply equation (8.4.1) in sub-domain 1 ($s=1$) for $i=1$ to m_1-1 and $j=1$ to n_1. Use equation (8.4.2) (for $s=1$) to update the values at the 'fictitious meshpoints' ($j=n_1+1$) for $i=1$ to m_1-1.
4. Apply equation (8.4.3) for $j=1$ to n_1-1 at meshpoints on the interface between sub-domains 1 and 2. Let $v_{12}{}_{0,j}=v_{11}{}_{m_1,j}$ for $j=1$ to n_1-1 in order to match the finite difference equations across the interface between sub-domains 1 and 2.
5. Apply equation (8.4.1) in sub-domain 2 ($s=2$) for $i=1$ to m_2-1 and $j=1$ to n_2-1.
6. Apply equation (8.4.4) for $i=1$ to m_2-1 at meshpoints on the interface between sub-domains 2 and 3. Let $v_{13}{}_{i,0}=v_{12}{}_{i,n_2}$ for $i=1$ to m_2-1 in order to match the finite difference equations across the interface between sub-domains 2 and 3.
7. Apply equation (8.4.1) in sub-domain 3 ($s=3$) for $i=1$ to m_3-1 and $j=1$ to n_3. Use equation (8.4.2) (for $s=3$) to update the values at the 'fictitious meshpoints' ($j=n_3+1$) for $i=1$ to m_3-1.
8. If convergence is achieved go to step 9 if not return to step 3 to start another iteration of the SOR method.
9. Store the discrete velocities $v_{1_s}{}_{i,j}$ at every meshpoint in each sub-domain as an array.

Appendix 8.2 Iterative procedure used to solve the finite difference equations for $v_2(r,z)$ presented in section 8.4.3

The steps for solving the finite difference equations presented in section 8.4.3 are as follows.

1. Set initial values for $v_{2_{s\ i,j}}$ at all internal meshpoints, boundary meshpoints and the 'fictitious meshpoints' above the free surface boundaries.
2. Calculate the discrete functions given in equations (6.4.14), (6.4.18) and (6.4.21) at all relevant meshpoints.
3. Apply equation (8.4.5) in sub-domain 1 ($s=1$) for $i=1$ to m_1-1 and $j=1$ to n_1. Use equation (8.4.6) (for $s=1$) to update the values at the 'fictitious meshpoints' ($j=n_1+1$) for $i=1$ to m_1-1.
4. Apply equation (8.4.7) for $j=1$ to n_1-1 at meshpoints on the interface between sub-domains 1 and 2. Let $v_{22_{0,j}}=v_{21_{m_1,j}}$ for $j=1$ to n_1-1 in order to match the finite difference equations across the interface between sub-domains 1 and 2.
5. Apply equation (8.4.5) in sub-domain 2 ($s=2$) for $i=1$ to m_2-1 and $j=1$ to n_2-1.
6. Apply equation (8.4.8) for $i=1$ to m_2-1 at meshpoints on the interface between sub-domains 2 and 3. Let $v_{23_{i,0}}=v_{22_{i,n_2}}$ for $i=1$ to m_2-1 in order to match the finite difference equations across the interface between sub-domains 2 and 3.
7. Apply equation (8.4.5) in sub-domain 3 ($s=3$) for $i=1$ to m_3-1 and $j=1$ to n_3. Use equation (8.4.6) (for $s=3$) to update the values at the 'fictitious meshpoints' ($j=n_3+1$) for $i=1$ to m_3-1.
8. If convergence is achieved go to step 9 if not return to step 3 to start another iteration of the SOR method.
9. Store the discrete velocities $v_{2_{s\ i,j}}$ at every meshpoint in each sub-domain as an array.

Appendix 8.3 Iterative procedure used to solve the finite difference equations for $v(r,z)$ presented in section 8.6.1

The steps for solving the finite difference equations presented in section 8.6.1 are as follows.

1. Set initial values for $v_{s\ i,j}$ at all internal meshpoints, boundary meshpoints and the 'fictitious meshpoints' above the free surface boundaries.
2. Evaluate the quantity $(\alpha r_1)^2$ for the known fluid and geometry parameters at the prescribed frequency of oscillation.
3. Calculate the discrete functions given in equations (6.4.14), (6.4.18) and (6.4.21) at all relevant meshpoints.
4. Apply equation (8.6.1) in sub-domain 1 ($s=1$) for $i=1$ to m_1-1 and $j=1$ to n_1. Use equation (8.6.2) (for $s=1$) to update the values at the 'fictitious meshpoints' ($j=n_1+1$) for $i=1$ to m_1-1.
5. Apply equation (8.6.3) for $j=1$ to n_1-1 at meshpoints on the interface between sub-domains 1 and 2. Let $v_{2\ 0,j}=v_{1\ m_1,j}$ for $j=1$ to n_1-1 in order to match the finite difference equations across the interface between sub-domains 1 and 2.
6. Apply equation (8.6.1) in sub-domain 2 ($s=2$) for $i=1$ to m_2-1 and $j=1$ to n_2-1.
7. Apply equation (8.6.4) for $i=1$ to m_2-1 at meshpoints on the interface between sub-domains 2 and 3. Let $v_{3\ i,0}=v_{2\ i,n_2}$ for $i=1$ to m_2-1 in order to match the finite difference equations across the interface between sub-domains 2 and 3.
8. Apply equation (8.6.1) in sub-domain 3 ($s=3$) for $i=1$ to m_3-1 and $j=1$ to n_3. Use equation (8.6.2) (for $s=3$) to update the values at the 'fictitious meshpoints' ($j=n_3+1$) for $i=1$ to m_3-1.
9. If convergence is achieved go to step 10 if not return to step 4 to start another iteration of the SOR method.
10. Store the discrete velocities $v_{s\ i,j}$ at every meshpoint in each sub-domain as an array.

REFERENCES

1. R.B. Bird, R.C. Armstrong and O. Hassager, Dynamics of Polymeric Liquids (Vol.1), Wiley, New York, 1987.

2. R.B. Bird, W.E. Stewart and E.N. Lightfoot, Transport Phenomena, Wiley, New York, 1960.

3. K.Walters, Rheometry, Chapman and Hall, London, 1975.

4. J.C. Maxwell, Phil. Trans. Roy. Soc. Lon., A157, 49 (1867)

5. J.F. Wendt, Computational Fluid Dynamics: An introduction (2nd Ed), Springer, Berlin, 1996.

6. M.J. Crochet, A.R. Davies and K. Walters, Numerical Simulation of Non-Newtonian Flow, Elsevier, Amsterdam, 1984.

7. G.D. Smith, Numerical Solution of Partial Differential Equations: Finite difference methods (3rd Ed), OUP, Belfast, 1993.

8. K.H. Huebner and E.A. Thornton, The Finite Element Method For Engineers (2nd Ed), Wiley, New York, 1982.

9. Polyflow s.a., Polyflow Users Manual, Louvain-la-Neuve, Belgium, 1995.

10. I.P. Jones and C.P. Thompson, On the use of non-uniform grids in finite difference calculations, Harwell Report AERE-R 9765, H.M.S.O, 1980.

11. J.D. Anderson, Jr., Computational Fluid Dynamics: The basics with applications, McGraw-Hill, Singapore, 1995.

12. J.G. Oldroyd, The motion of an elastico-viscous liquid contained between coaxial cylinders (I), Quart. J. Mech. Appl. Math., 4 (1951) 271.

13. H. Markovitz, A property of Bessel functions and its application to the theory of two rheometers, J. Appl. Phys., 23 (1952) 1070.

14. K. Walters, The motion of an elastico-viscous liquid contained between coaxial cylinders (II), Quart. J. Mech. Appl. Math., 13 (1960) 444.

15. K. Walters, The motion of an elastico-viscous liquid contained between coaxial cylinders (III), Quart. J. Mech. Appl. Math., 14 (1961) 431.

16. K. Weissenberg, The testing of materials by means of the rheogoniometer, Sangamo Controls Ltd.

17. A.D. Maude and K. Walters, Approximate theory for oscillatory experiments with a cone and plate viscometer, Nature, 201 (1964) 913.

18. M.C. Nally, The oscillatory motion of an elastico-viscous liquid in a cone and plate viscometer, Brit. J. Appl. Phys., 16 (1965) 1023.

19. K. Walters and R.A. Kemp, On the use of a rheogoniometer Part II- Oscillatory shear, Polymer Systems: Deformation and Flow, ed. R.E. Wetton and R.W. Whorlow, MacMillan, London, 1968.

20. K. Walters and R.A. Kemp, On the use of a rheogoniometer Part III- Oscillatory shear between parallel plates, Rheol. Acta., 7 (1968) 1.

21. K. Golden, Ph.D. Thesis, University of Plymouth, U K, 1990.

22. G.N. Watson, A Treatise on the Theory of Bessel Functions (2nd Ed), Camb. Univ. Press, London, 1966.

23. M. Abramowitz and I. Stegun, Handbook of Mathematical Functions, Dover Publications, New York, 1968.

24. CSR Instruction Manual for the Controlled Stress Rheometer, TA Instruments Ltd, 1984.

25. D.F. Griffiths and K. Walters, On edge effects in rheometry, J. Fluid Mech., 42 (1970) 379-390.

26. D. O. Olagunju, Effect of free surface and inertia on viscoelastic parallel plate flow, J. Rheol., 38 (1994) 151-168.

27. M. Short, Ph.D. Thesis, University of Plymouth, U K, 1977.

28. G.I. Taylor, Stability of a viscous fluid contained between two rotating cylinders, Phil. Trans. R. Soc. Lond. A, 233 (1923), 289-343.

29. K. Kataoka, Taylor vortices and instabilities in circular couette flows, Encyclopaedia of Fluid Mechanics (Vol.1), ed. N.P. Cheremisinoff, Gulf, Houston, 1986.

30. T.J. Lockett, S.M. Richardson and W.J. Worraker, The stability of inelastic non-Newtonian fluids in Couette flow between concentric cylinders: a finite-element study, J. Non-Newtonian fluid Mech., 43 (1992) 165-177.

31. J.P. Hughes, T.E.R Jones, J.M. Davies, 'End effects in concentric cylinder rheometry', Proc. 12th Int. Congress on Rheology, (1996) 391.

32. J.D. Anderson, Jr., Discretisation of partial differential equations, Computational Fluid Dynamics, ed. J.F. Wendt, Springer, Berlin, 1996.

33. R.L. Burden and J.D. Faires, Numerical Analysis (6th Ed.), Brookes/Cole, California, 1997.

34. Instruction Manual for the Weissenberg Rheogoniometer, T.A. Instruments Ltd, date.

35. E.F. Holder, M.Sc Thesis, U.C.W Aberystwyth, U K, 1982.

36. T.E.R Jones, J.M. Davies and H.A. Barnes, Proc. 8th Int. Congress on Rheology, 4 (1984) 45.

37. T.E.R Jones, J.M. Davies and A. Thomas, 'Fluid inertia effects on a Controlled Stress Rheometer in its oscillatory mode', Rheol. Acta, 26 (1987) 14-19.

NOMENCLATURE

(x,y,z)	: cartesian coordinates
(r,θ,z)	: cylindrical polar coordinates
(r,θ,φ)	: spherical polar coordinates
a	: parallel plate radius, cone base radius
a_n	: coefficients in cone and plate oscillatory shear theory
c	: phase lag
C_0	: applied torque (steady shear theory), applied torque amplitude (oscillatory shear theory for CSR rheometer)
C_F	: torque exerted on upper platen due to fluid motion
De	: Deborah number
$\frac{d}{dt}$	: total derivative
$\frac{\partial}{\partial t}$	: partial derivative
$\frac{D}{Dt}$	: substantial derivative
E^4	: bi-harmonic operator
f	: frequency (cycles/sec)
f_0, f_1, f_2, f_3, f_4	: non-dimensional geometry dependent factors
f_s	: tangential force (Polyflow boundary conditions)
f_θ	: θ-direction force (Polyflow boundary conditions)
g	: gravitational acceleration
G	: rigidity modulus of a Maxwell element spring
G'	: dynamic rigidity
G_0'	: zero order dynamic rigidity (fluid inertia effects ignored)
$G(t-t')$	: relaxation modulus
h	: parallel plate gap, concentric cylinder immersed height
I	: moment of inertia of oscillating upper platen member
I_2	: second invariant of the rate of strain tensor
J_n	: n^{th} order Bessel function of the first kind
k	: power law fluid consistency index

K	: torsion bar stiffness
L	: θ component of the Laplacian operator of a vector field
ln	: natural logarithm
n	: power law index
N	: non-dimensional fluid inertia parameter (oscillatory shear theory)
p	: pressure
P_n^m	: associated Legendre function of the first kind (degree n and order m)
Q_n^m	: associated Legendre function of the second kind (degree n and order m)
r_i, r_o, r_1, r_2	: concentric cylinder radii
R	: non-dimensional fluid inertia parameter (oscillatory shear theory)
R_e	: Reynolds number
S	: geometrical parameter
t	: time
t'	: past time for linear viscoelastic fluids
v	: velocity vector
(v_r, v_θ, v_z)	: velocity components in cylindrical polar coordinates
$(v_r, v_\theta, v_\varphi)$	: velocity components in spherical polar coordinates
$v_{\theta 0}, v_{r1}, v_{z1}, v_{\theta 2}$	: velocity components for steady shear perturbation theory (zero, first and second order)
v, v_0, v_1, v_2	: velocity functions for CSR oscillatory shear perturbation theory (full inertia, zero, first and second order)
v_M, v_T, v_{M0}, v_{T0}, $v_{M1}, v_{T1}, v_{M2}, v_{T2}$	: velocity functions for Weissenberg oscillatory shear perturbation theory (full inertia, zero, first and second order)
v_n, v_s	: normal, tangential velocity (Polyflow boundary conditions)
X_0	: amplitude of oscillation of inner cylinder (CSR rheometer)
Y_n	: n^{th} order Bessel function of the second kind
z_1, z_2	: concentric cylinder geometry dimensions in z-direction
α	: fluid inertia parameter (oscillatory shear theory)
α_0	: zero order fluid inertia parameter (oscillatory shear theory)
β_m	: non-dimensional geometry dependent constant
β_n	: fluid inertia parameter (cone and plate oscillatory shear theory)

ϕ	: variable for streamfunction equations
γ	: strain tensor
$\dot{\gamma}$	: shear rate tensor
$\dot{\gamma}$	: magnitude of the shear rate tensor
$\dot{\gamma}_0$	: shear rate amplitude
η	: shear viscosity
η_0	: Newtonian viscosity
η_k	: constant viscosity (generalised Maxwell model)
η'	: dynamic viscosity
η_0	: zero order dynamic viscosity (fluid inertia effects ignored)
η^*	: complex viscosity
$\eta_0^*, \eta_1^*, \eta_2^*$	: complex viscosity from oscillatory shear perturbation theory (zero, first and second order)
ϑ	: amplitude ratio (upper platen amplitude / lower platen amplitude)
λ_k	: relaxation time (generalised Maxwell model)
θ_c	: semi-vertical cone angle
θ_0	: small cone angle
θ_1	: upper platen amplitude of oscillation (parallel plate and concentric cylinder geometry)
θ_2	: lower platen amplitude of oscillation (parallel plate and concentric cylinder geometry)
ρ	: fluid density
τ	: stress tensor
τ_k	: stress tensor (generalised Maxwell model)
$\sum_{i=1}^{n}$	: summation sign
ω	: angular frequency of oscillation (radians/sec)
Ω	: angular velocity
ψ	: streamfunction
ψ_1	: upper platen amplitude of oscillation (cone and plate geometry)
ψ_2	: lower platen amplitude of oscillation (cone and plate geometry)

∇	: gradient operator
$\nabla\cdot$	: divergence operator
∇^2	: Laplacian operator
$^+$	: non-dimensional variable

Figure 4.1

The parallel plate geometry for the Weissenberg rheogoniometer.

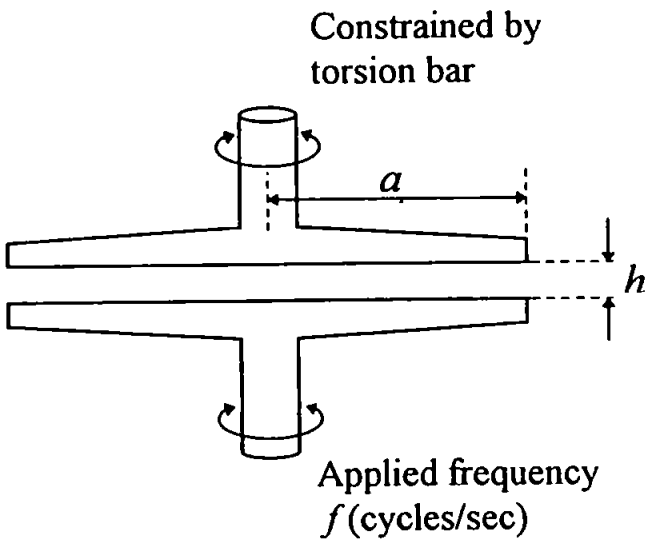
Constrained by
torsion bar
a
h
Applied frequency
f (cycles/sec)

Figure 4.2

The concentric cylinder geometry for the Weissenberg rheogoniometer.

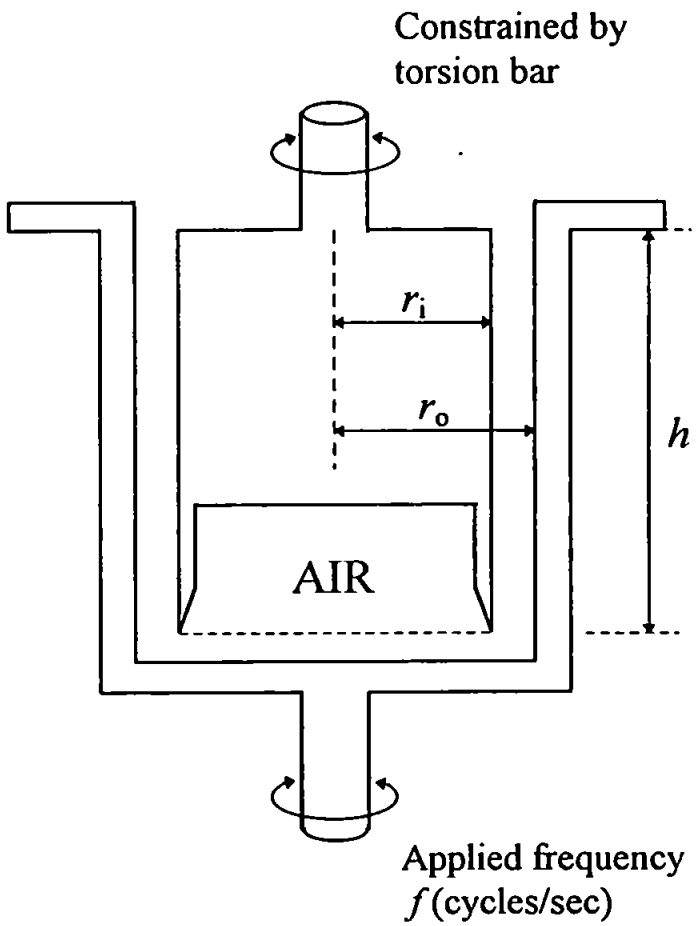
Constrained by
torsion bar
r_i
r_o
h
AIR
Applied frequency
f (cycles/sec)

Figure 4.3

Cone and plate geometry for the Weissenberg rheogoniometer

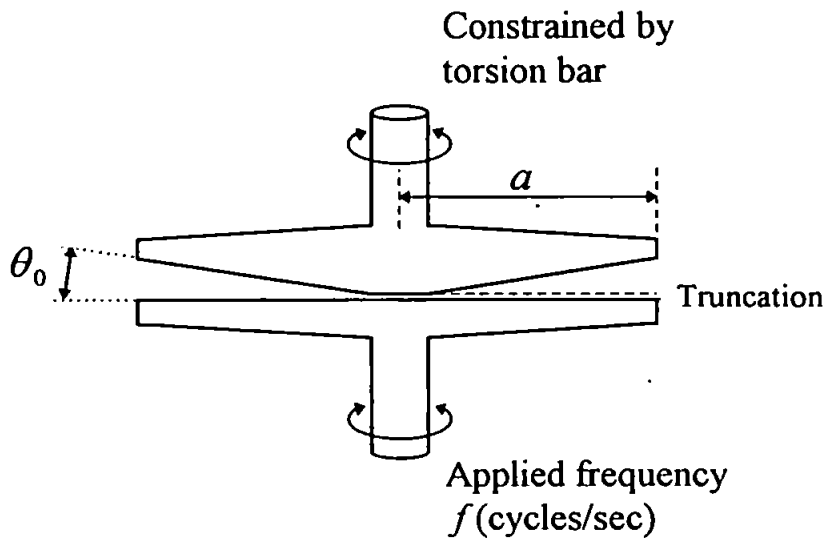
Constrained by
torsion bar
a
θ_0
Truncation
Applied frequency
f (cycles/sec)

Figures 5.1 and 5.2

Oscillatory shear flow simulations for a Weissenberg rheogoniometer with a torsion bar system.

Normalised dynamic viscosity and dynamic rigidity vs. normalised frequency for a Newtonian fluid in the parallel plate geometry $(a = 0{\cdot}0375\,\mathrm{m}, h = 500\,\mu\mathrm{m})$ when $R = 2$.

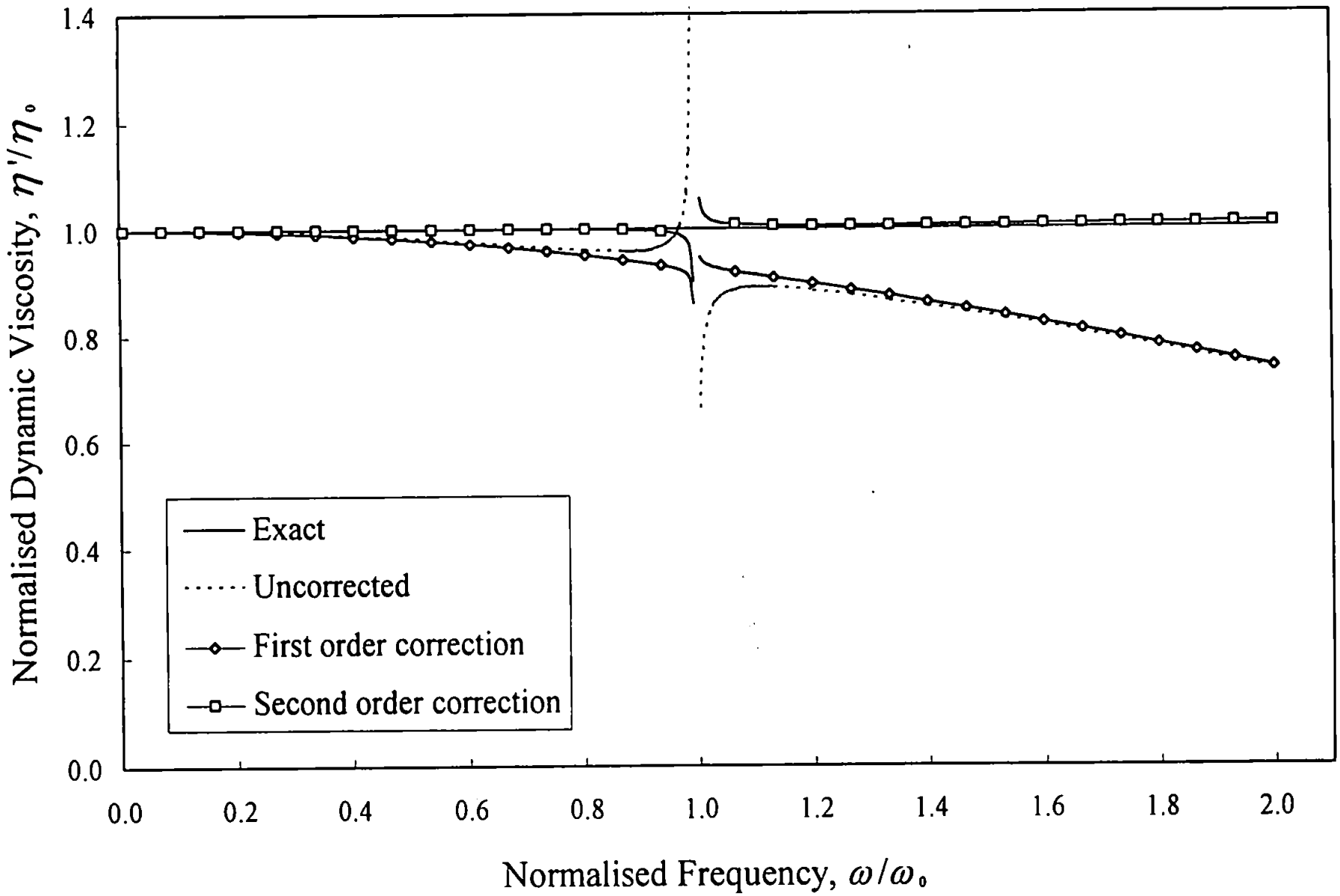
Normalised Dynamic Viscosity, η'/η_0
1.4
1.2
1.0
0.8
0.6
0.4
0.2
0.0
0.0
0.2
0.4
0.6
0.8
1.0
1.2
1.4
1.6
1.8
2.0
Normalised Frequency, ω/ω_0
Exact
Uncorrected
First order correction
Second order correction

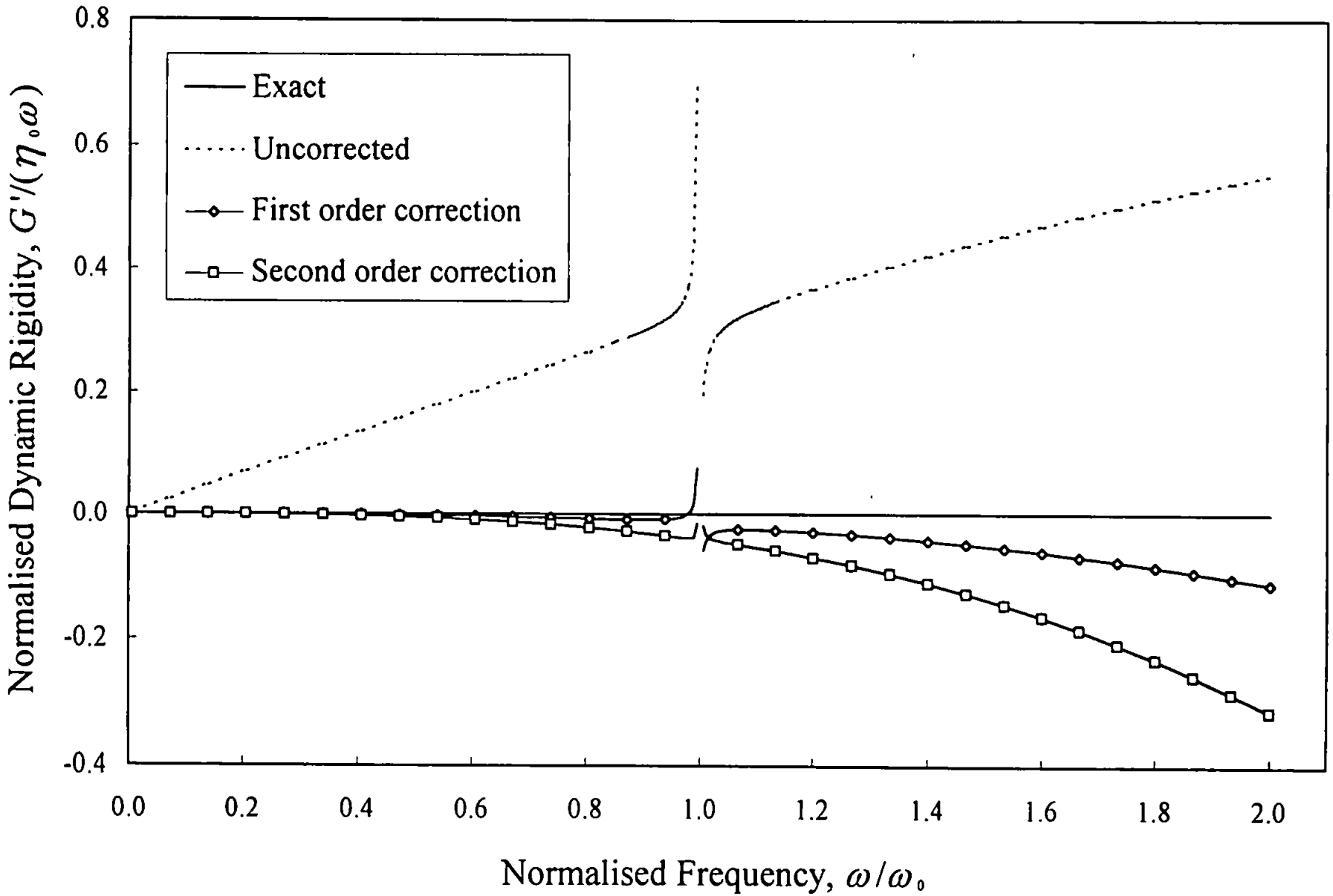
Exact
Uncorrected
First order correction
Second order correction
Normalised Dynamic Rigidity, $G'/(\eta_0\omega)$
Normalised Frequency, ω/ω_0
0.8
0.6
0.4
0.2
0.0
-0.2
-0.4
0.0
0.2
0.4
0.6
0.8
1.0
1.2
1.4
1.6
1.8
2.0

Figures 5.3 and 5.4

Oscillatory shear flow simulations for a Weissenberg rheogoniometer with a torsion bar system.

Normalised dynamic viscosity and dynamic rigidity data corrected for second order fluid inertia effects vs. normalised frequency for Newtonian fluids over a range of R values in the parallel plate geometry $(a = 0{\cdot}0375\,\mathrm{m}, h = 500\,\mu\mathrm{m})$.

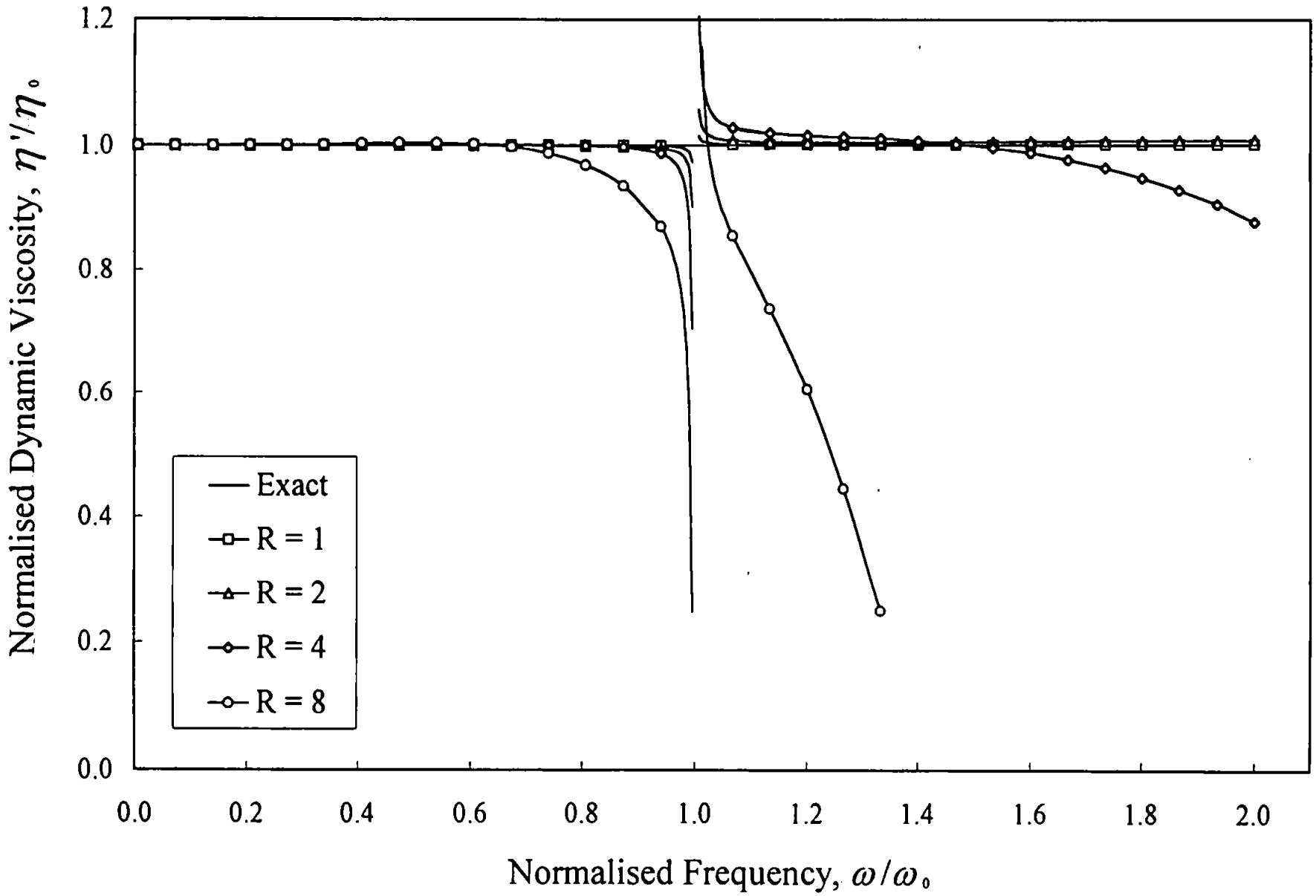
Normalised Dynamic Viscosity, η'/η_0
1.2
1.0
0.8
0.6
0.4
0.2
0.0
0.0
0.2
0.4
0.6
0.8
1.0
1.2
1.4
1.6
1.8
2.0
Normalised Frequency, ω/ω_0
Exact
R = 1
R = 2
R = 4
R = 8

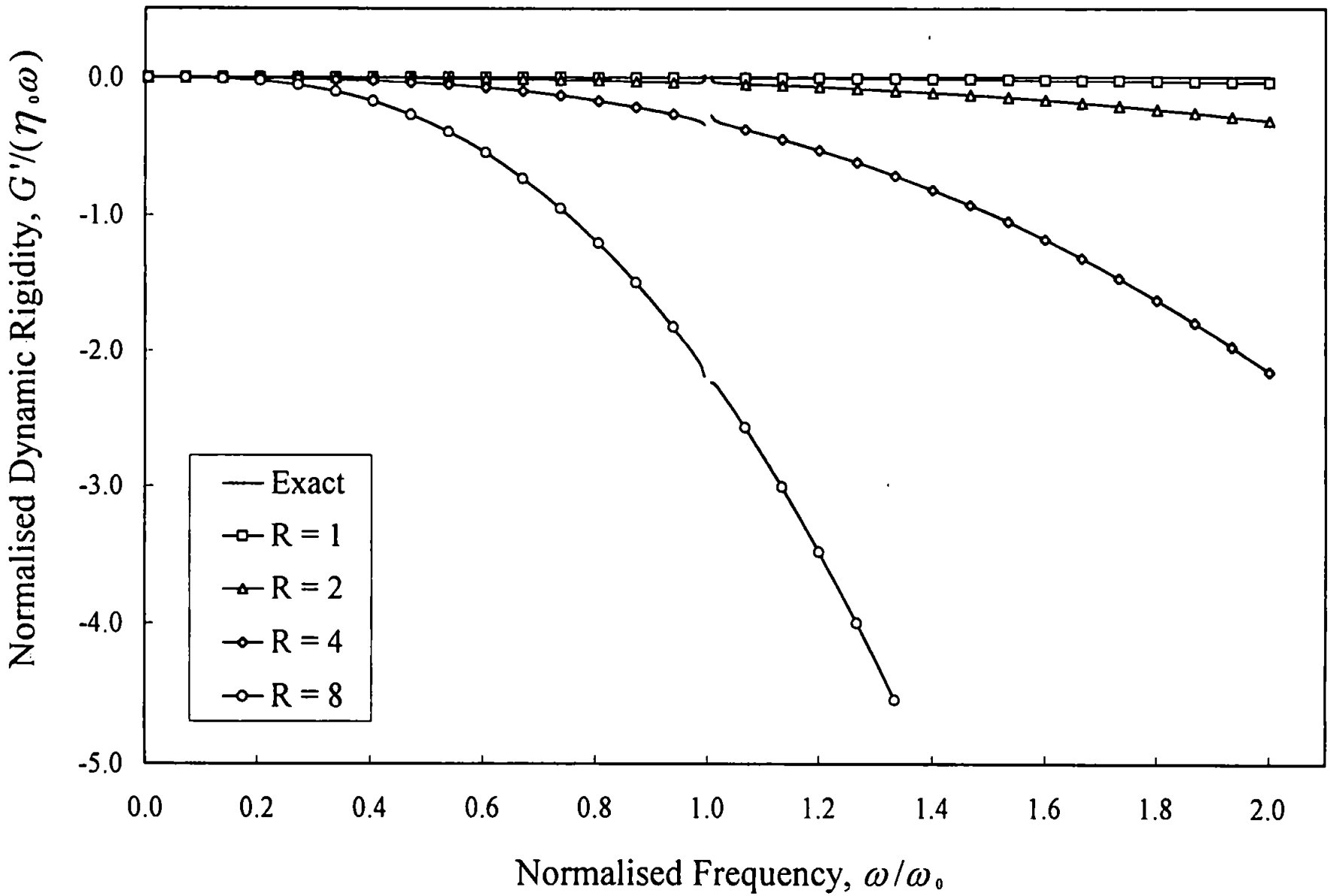
Normalised Dynamic Rigidity, $G'/(\eta_0\omega)$
0.0
-1.0
-2.0
-3.0
-4.0
-5.0
0.0
0.2
0.4
0.6
0.8
1.0
1.2
1.4
1.6
1.8
2.0
Normalised Frequency, ω/ω_0
Exact
R = 1
R = 2
R = 4
R = 8

Figure 5.5 and 5.6

Oscillatory shear flow simulations for a Weissenberg rheogoniometer with a torsion bar system.

Normalised dynamic viscosity and dynamic rigidity vs. normalised frequency for a single element Maxwell fluid in the parallel plate geometry $(a = 0{\cdot}0375\,\mathrm{m}, h = 500\,\mu\mathrm{m})$ when $R = 1$.

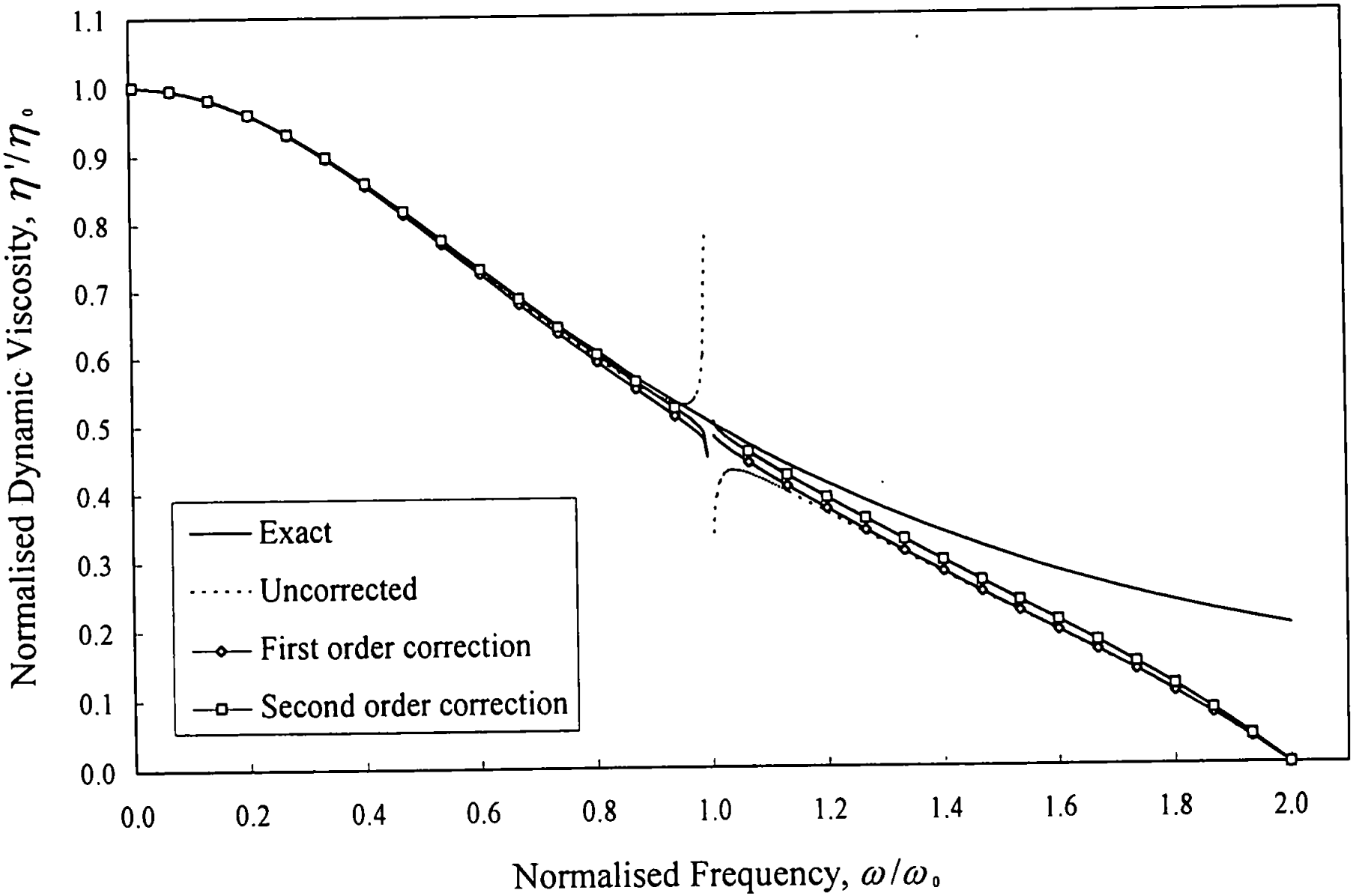
Normalised Dynamic Viscosity, η'/η_0
1.1
1.0
0.9
0.8
0.7
0.6
0.5
0.4
0.3
0.2
0.1
0.0
0.0
0.2
0.4
0.6
0.8
1.0
1.2
1.4
1.6
1.8
2.0
Normalised Frequency, ω/ω_0
Exact
Uncorrected
First order correction
Second order correction

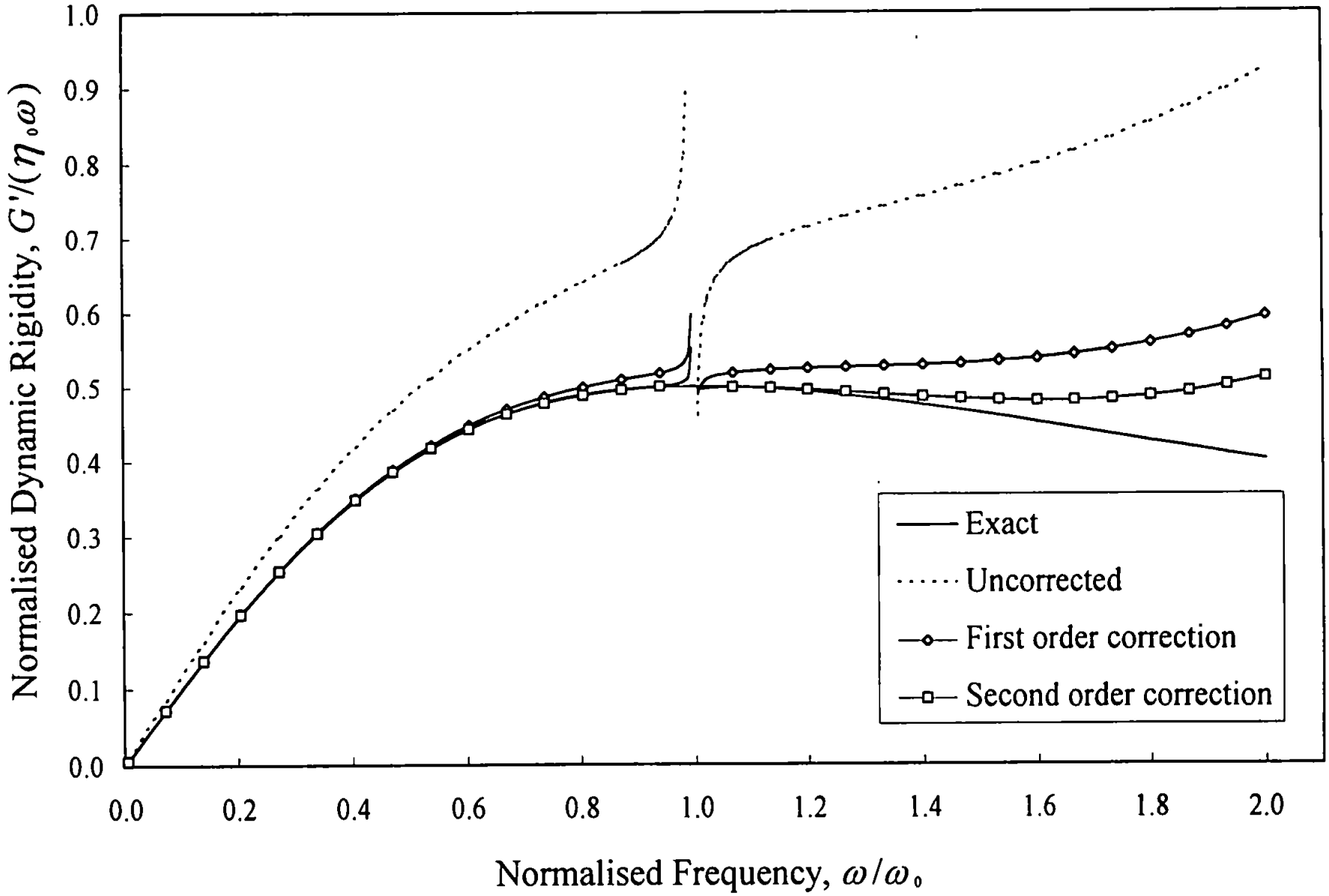
1.0
0.9
0.8
0.7
0.6
0.5
0.4
0.3
0.2
0.1
0.0
Normalised Dynamic Rigidity, $G'/(\eta_0\omega)$
0.0
0.2
0.4
0.6
0.8
1.0
1.2
1.4
1.6
1.8
2.0
Normalised Frequency, ω/ω_0
Exact
Uncorrected
First order correction
Second order correction

Figures 5.7 and 5.8

Oscillatory shear flow simulations for a Weissenberg rheogoniometer with a torsion bar system.

Normalised dynamic viscosity and dynamic rigidity data corrected for second order fluid inertia effects vs. normalised frequency for single element Maxwell fluids over a range of R values in the parallel plate geometry $(a = 0{\cdot}0375\,\mathrm{m}, h = 500\,\mu\mathrm{m})$.

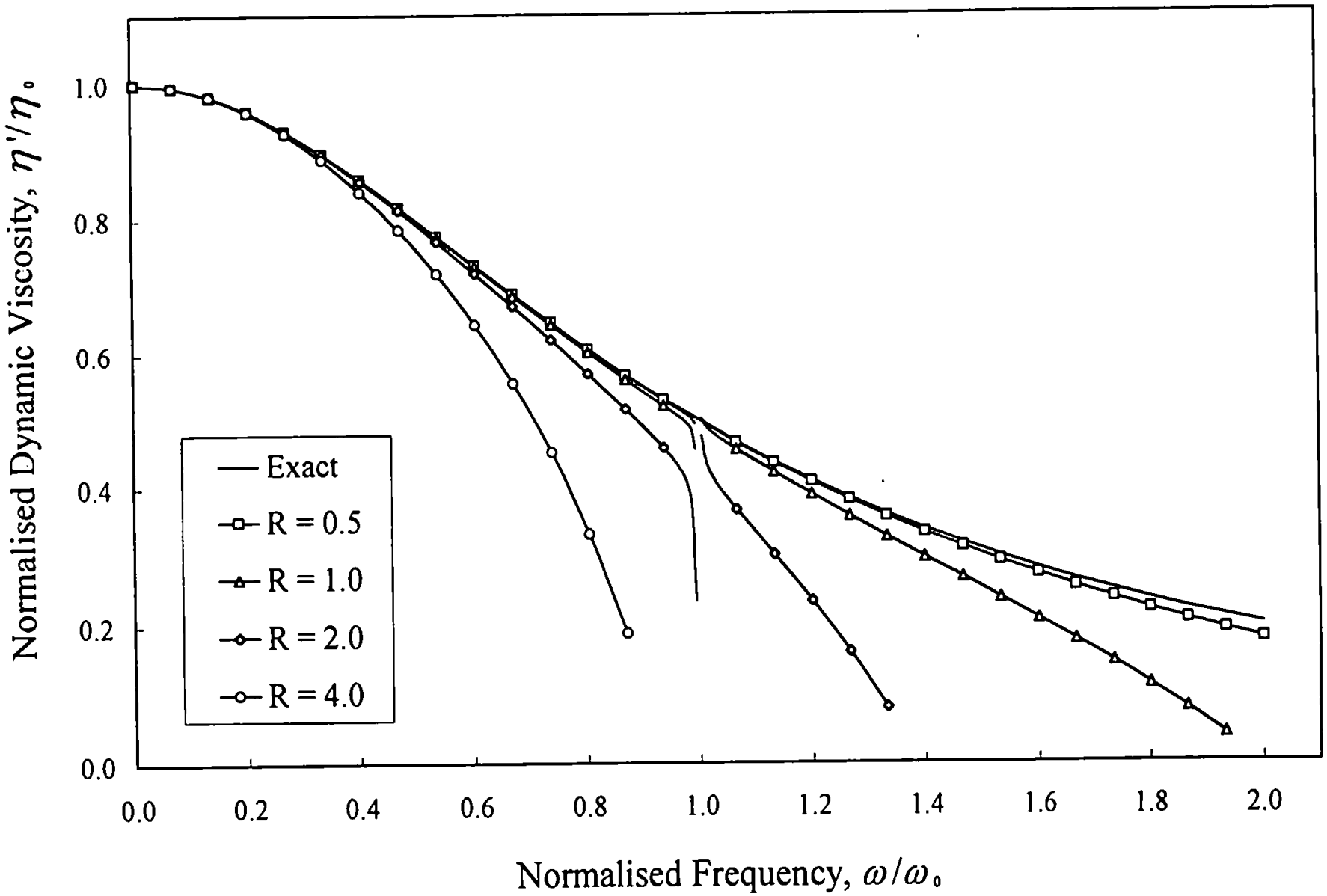
Normalised Dynamic Viscosity, η'/η_0
1.0
0.8
0.6
0.4
0.2
0.0
0.0
0.2
0.4
0.6
0.8
1.0
1.2
1.4
1.6
1.8
2.0
Normalised Frequency, ω/ω_0
Exact
R = 0.5
R = 1.0
R = 2.0
R = 4.0

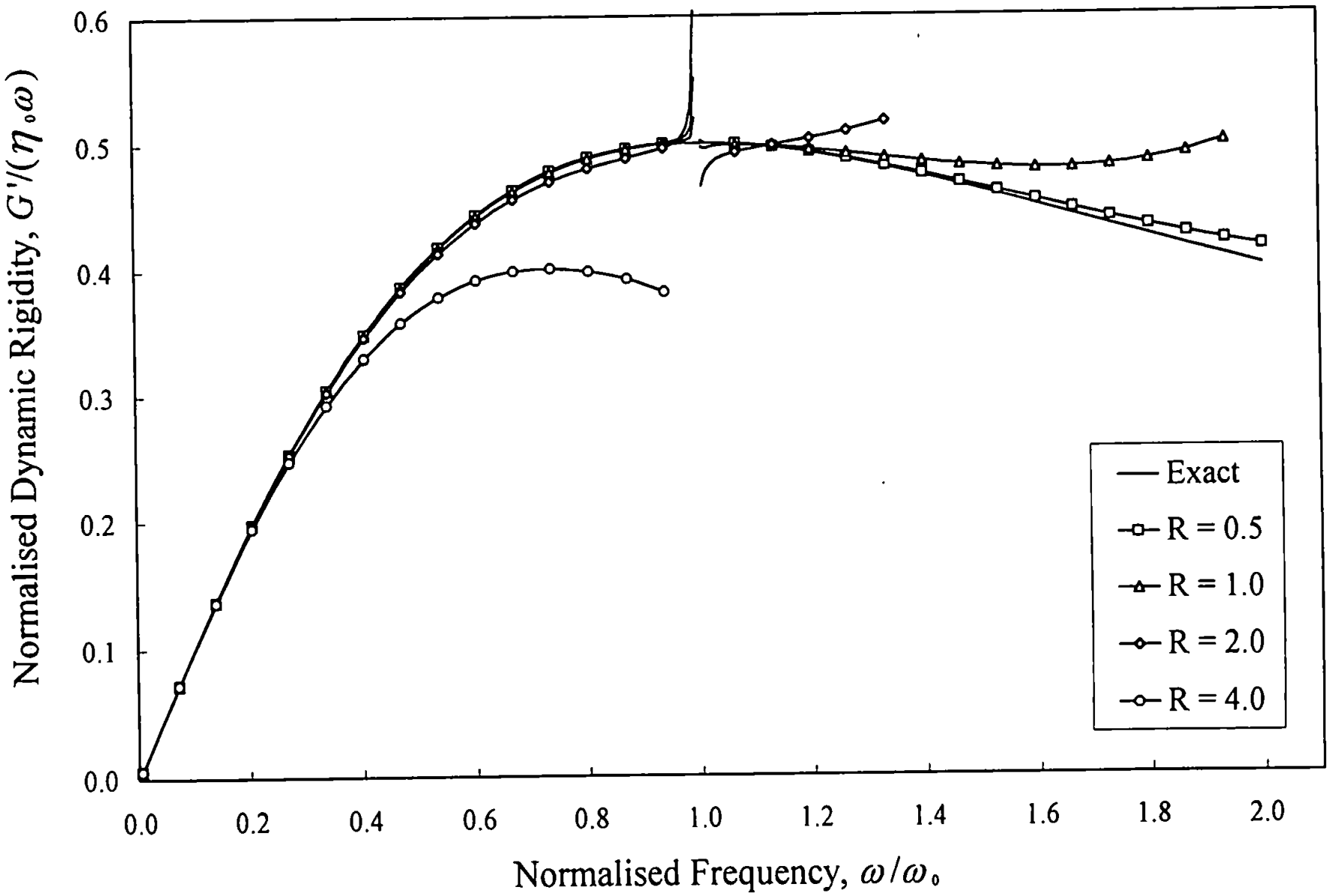
Normalised Dynamic Rigidity, $G'/(\eta_o\omega)$
0.0
0.1
0.2
0.3
0.4
0.5
0.6
0.0
0.2
0.4
0.6
0.8
1.0
1.2
1.4
1.6
1.8
2.0
Normalised Frequency, ω/ω_o
Exact
R = 0.5
R = 1.0
R = 2.0
R = 4.0

Figures 5.9 and 5.10

Oscillatory shear flow simulations for a Weissenberg rheogoniometer with a strain gauge torsion head system (W) and a CSR controlled stress rheometer (C).

Normalised dynamic viscosity and dynamic rigidity vs. normalised frequency for a Newtonian fluid in the parallel plate geometry $(a = 0{\cdot}0375\,\mathrm{m}, h = 500\,\mu\mathrm{m})$.

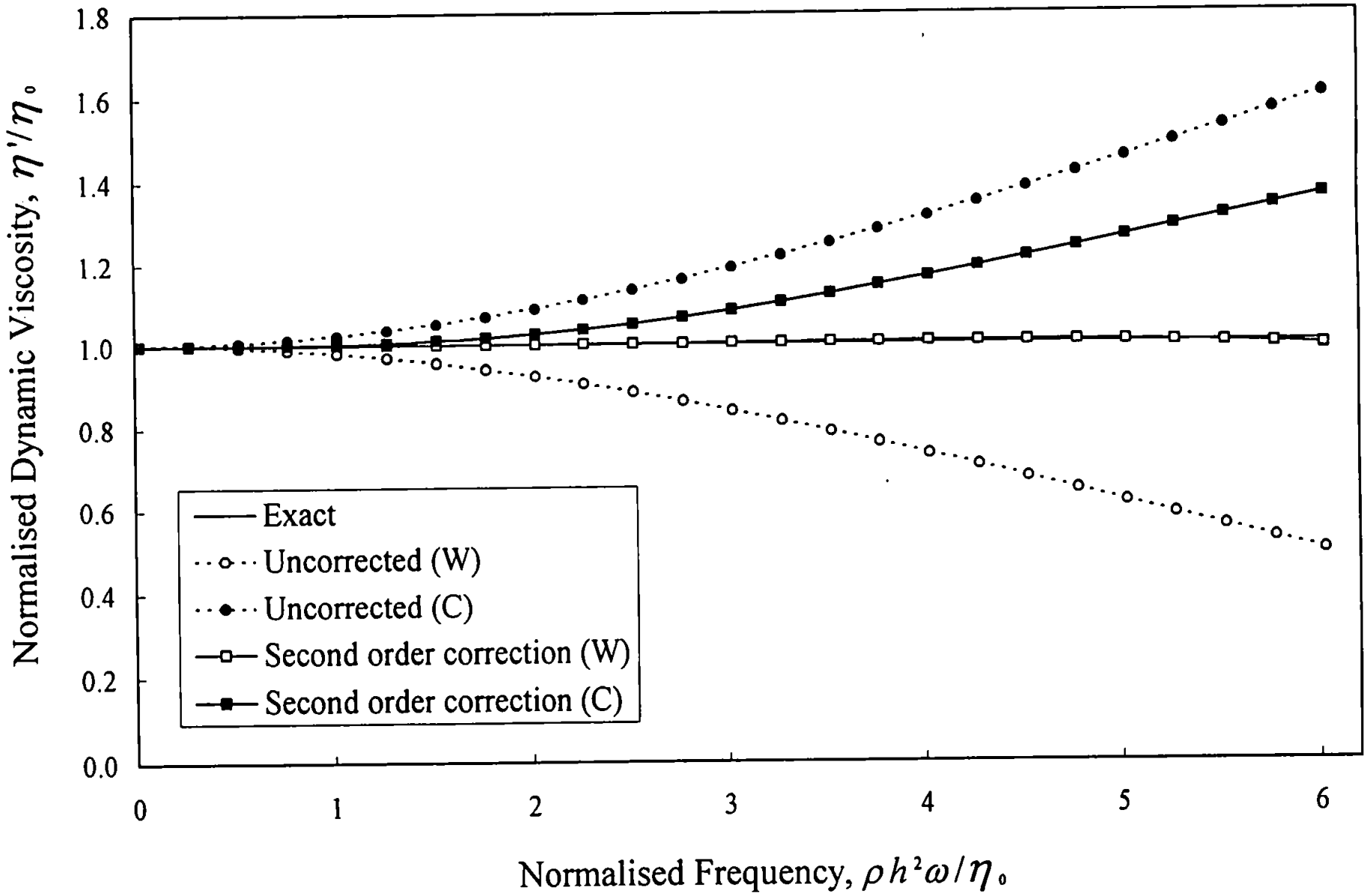
1.8
1.6
1.4
1.2
1.0
0.8
0.6
0.4
0.2
0.0
0
1
2
3
4
5
6
Normalised Dynamic Viscosity, η'/η_0
Normalised Frequency, $\rho h^2\omega/\eta_0$
Exact
Uncorrected (W)
Uncorrected (C)
Second order correction (W)
Second order correction (C)

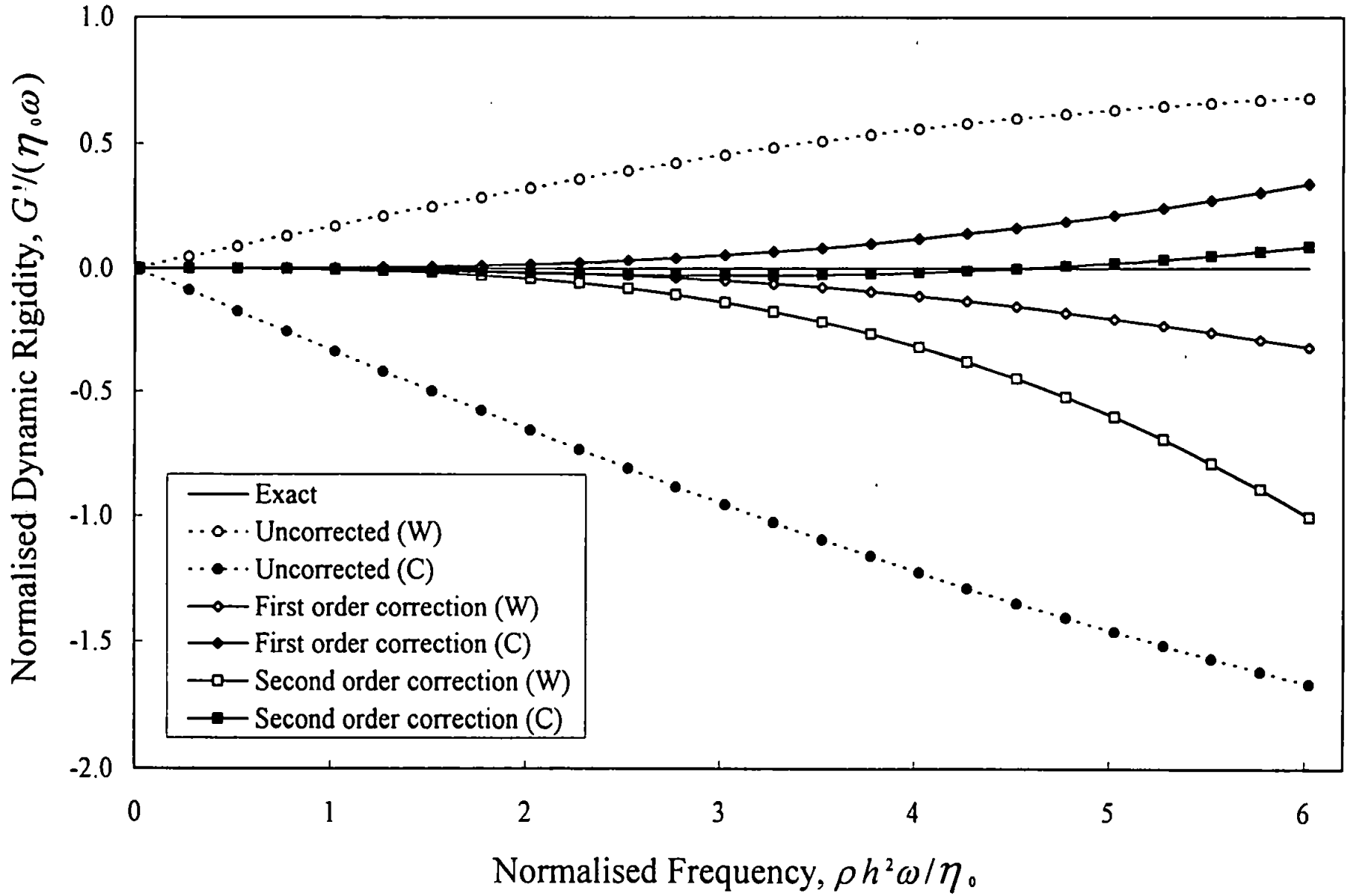
1.0
0.5
0.0
-0.5
-1.0
-1.5
-2.0
0
1
2
3
4
5
6
Normalised Dynamic Rigidity, $G'/(\eta_0\omega)$
Normalised Frequency, $\rho h^2\omega/\eta_0$
Exact
Uncorrected (W)
Uncorrected (C)
First order correction (W)
First order correction (C)
Second order correction (W)
Second order correction (C)

Figures 5.11 and 5.12

Oscillatory shear flow simulations for a Weissenberg rheogoniometer with a strain gauge torsion head system (W) and a CSR controlled stress rheometer (C).

Normalised dynamic viscosity and dynamic rigidity vs. normalised frequency for a single element Maxwell fluid in the parallel plate geometry $(a = 0{\cdot}0375\,\mathrm{m}, h = 500\,\mu\mathrm{m})$ when $R = 0{\cdot}5$.

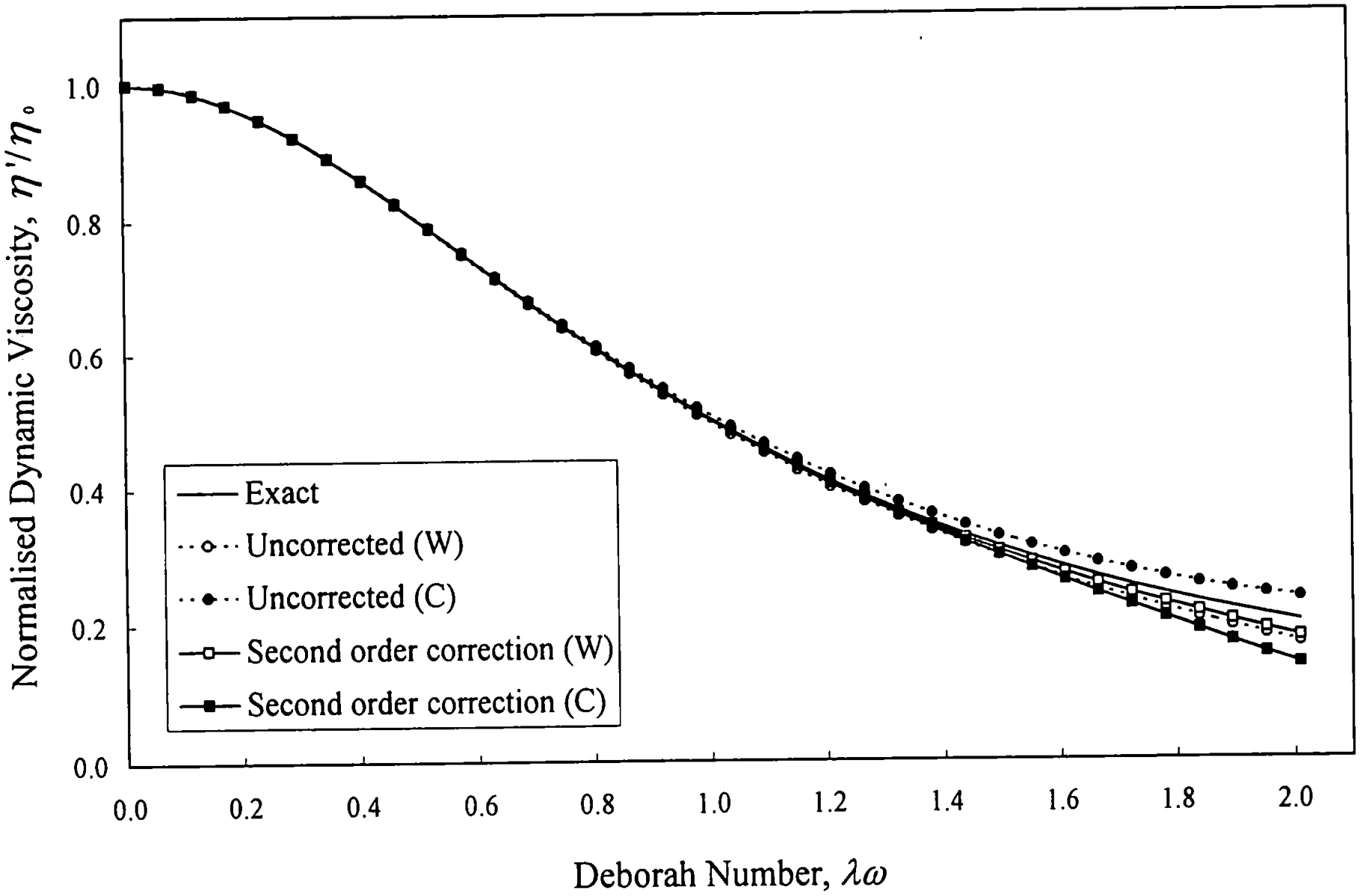
Normalised Dynamic Viscosity, η'/η_o
1.0
0.8
0.6
0.4
0.2
0.0
0.0
0.2
0.4
0.6
0.8
1.0
1.2
1.4
1.6
1.8
2.0
Deborah Number, $\lambda\omega$
Exact
Uncorrected (W)
Uncorrected (C)
Second order correction (W)
Second order correction (C)

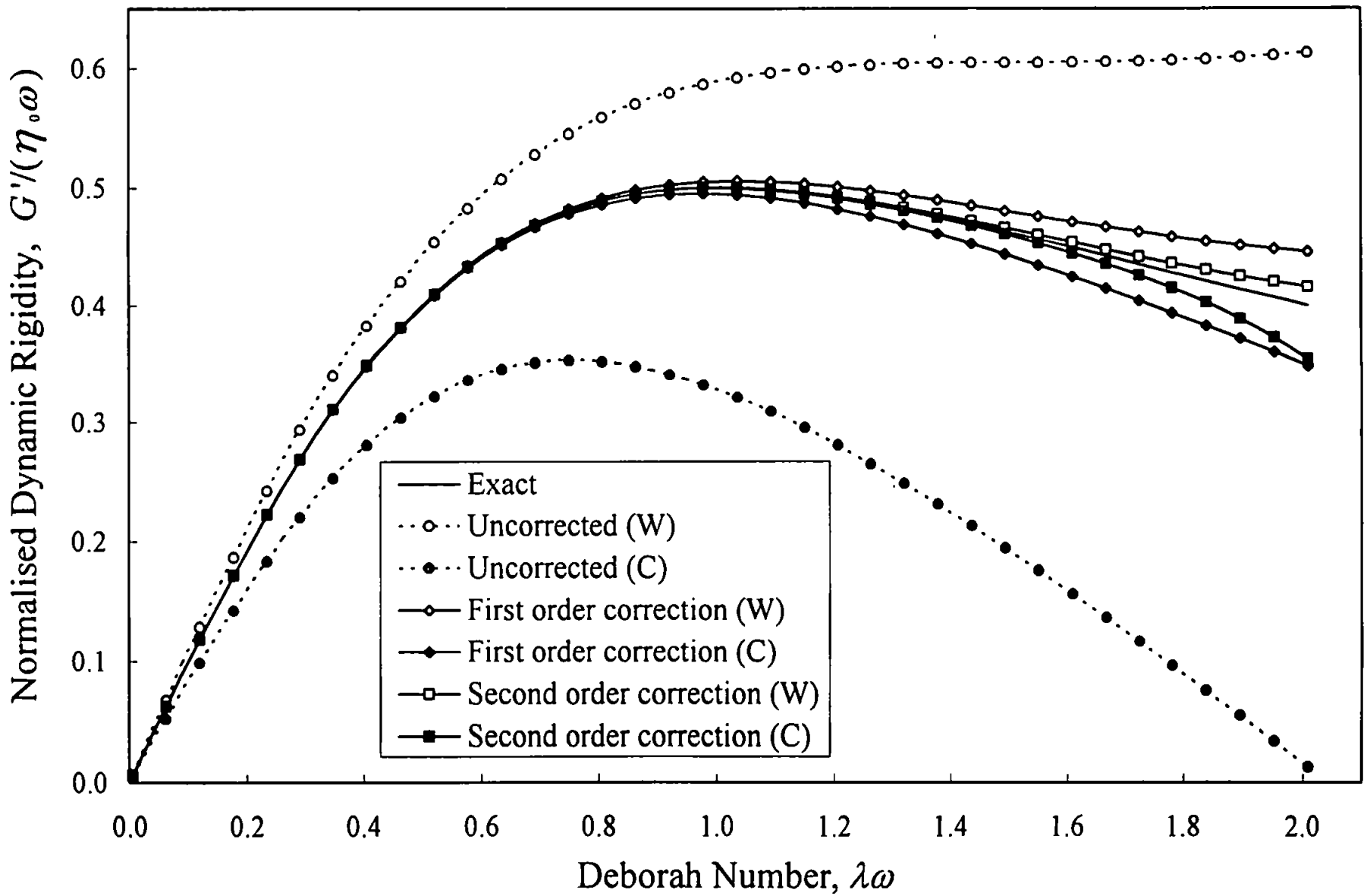
Normalised Dynamic Rigidity, $G'/(\eta_o\omega)$
0.0
0.1
0.2
0.3
0.4
0.5
0.6
0.0
0.2
0.4
0.6
0.8
1.0
1.2
1.4
1.6
1.8
2.0
Deborah Number, $\lambda\omega$
Exact
Uncorrected (W)
Uncorrected (C)
First order correction (W)
First order correction (C)
Second order correction (W)
Second order correction (C)

Figures 5.13 and 5.14

Oscillatory shear flow simulations for a Weissenberg rheogoniometer with a strain gauge torsion head system (W) and a CSR controlled stress rheometer (C).

Normalised dynamic viscosity and dynamic rigidity data corrected for second order fluid inertia effects vs. normalised frequency for single element Maxwell fluids over a range of R values in the parallel plate geometry $(a = 0{\cdot}0375\,\mathrm{m}, h = 500\,\mu\mathrm{m})$.

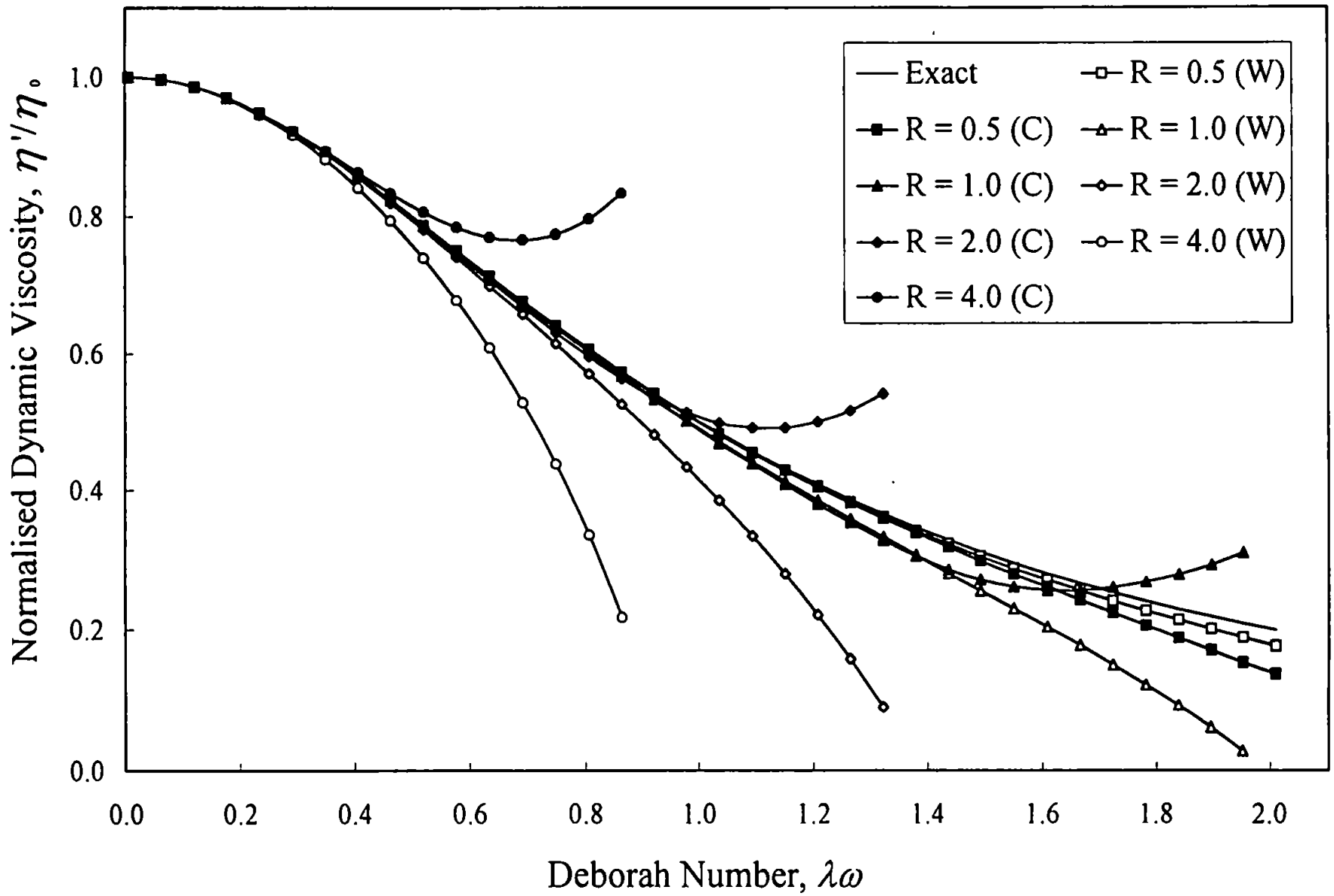
Exact
R = 0.5 (C)
R = 1.0 (C)
R = 2.0 (C)
R = 4.0 (C)
R = 0.5 (W)
R = 1.0 (W)
R = 2.0 (W)
R = 4.0 (W)
Normalised Dynamic Viscosity, η'/η_o
Deborah Number, $\lambda\omega$
0.0
0.2
0.4
0.6
0.8
1.0
1.2
1.4
1.6
1.8
2.0

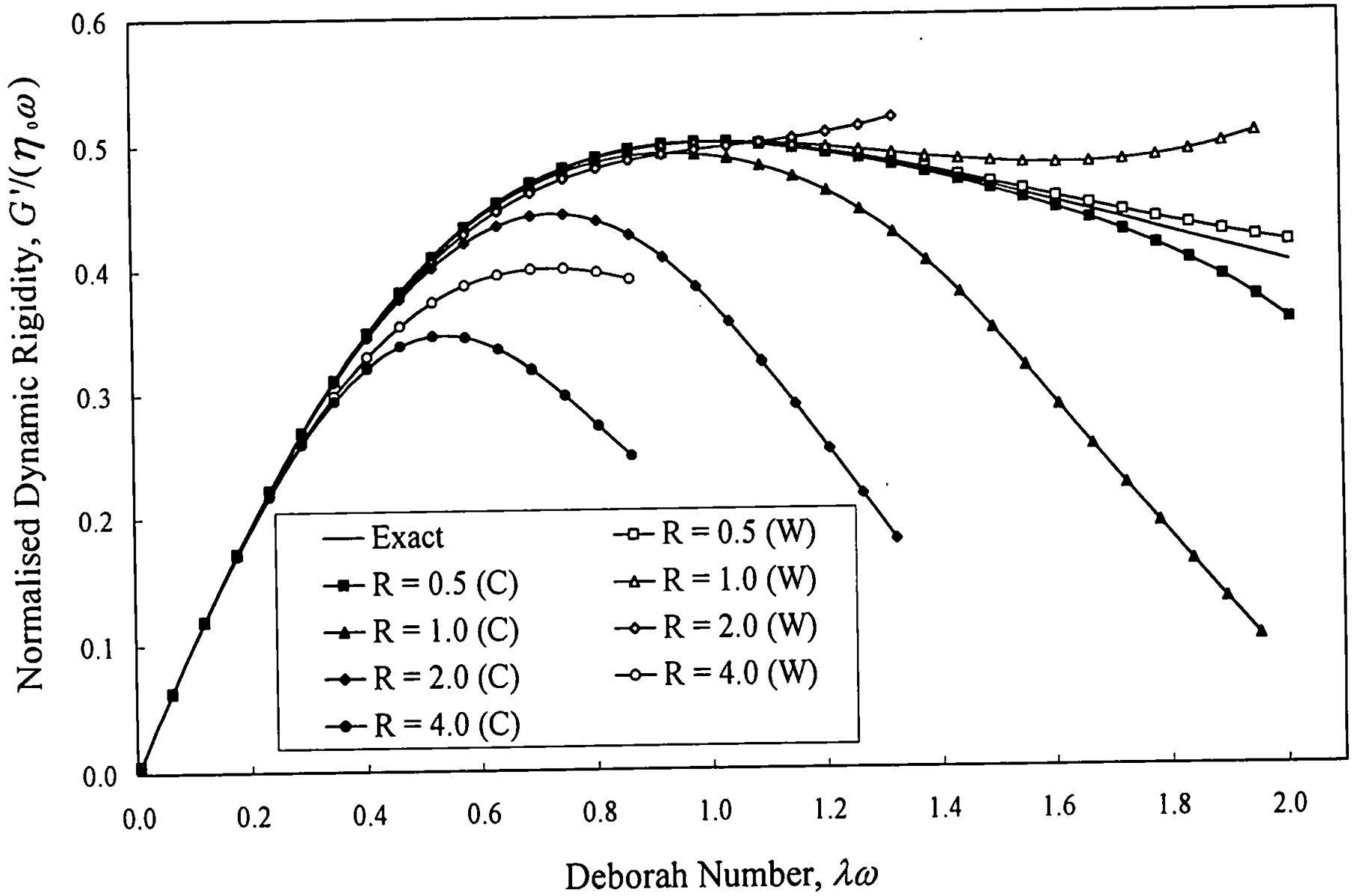
Normalised Dynamic Rigidity, $G'/(\eta_o\omega)$
Deborah Number, $\lambda\omega$
0.0
0.1
0.2
0.3
0.4
0.5
0.6
0.0
0.2
0.4
0.6
0.8
1.0
1.2
1.4
1.6
1.8
2.0
Exact
R = 0.5 (C)
R = 1.0 (C)
R = 2.0 (C)
R = 4.0 (C)
R = 0.5 (W)
R = 1.0 (W)
R = 2.0 (W)
R = 4.0 (W)

Figures 5.15 and 5.16

Oscillatory shear flow simulations for a Weissenberg rheogoniometer with a torsion bar system

Normalised dynamic viscosity and dynamic rigidity vs. normalised frequency for a Newtonian fluid in the concentric cylinder geometry $(r_i = 15\,\text{mm}, r_o = 20\cdot 75\,\text{mm})$ when $R = 10$.

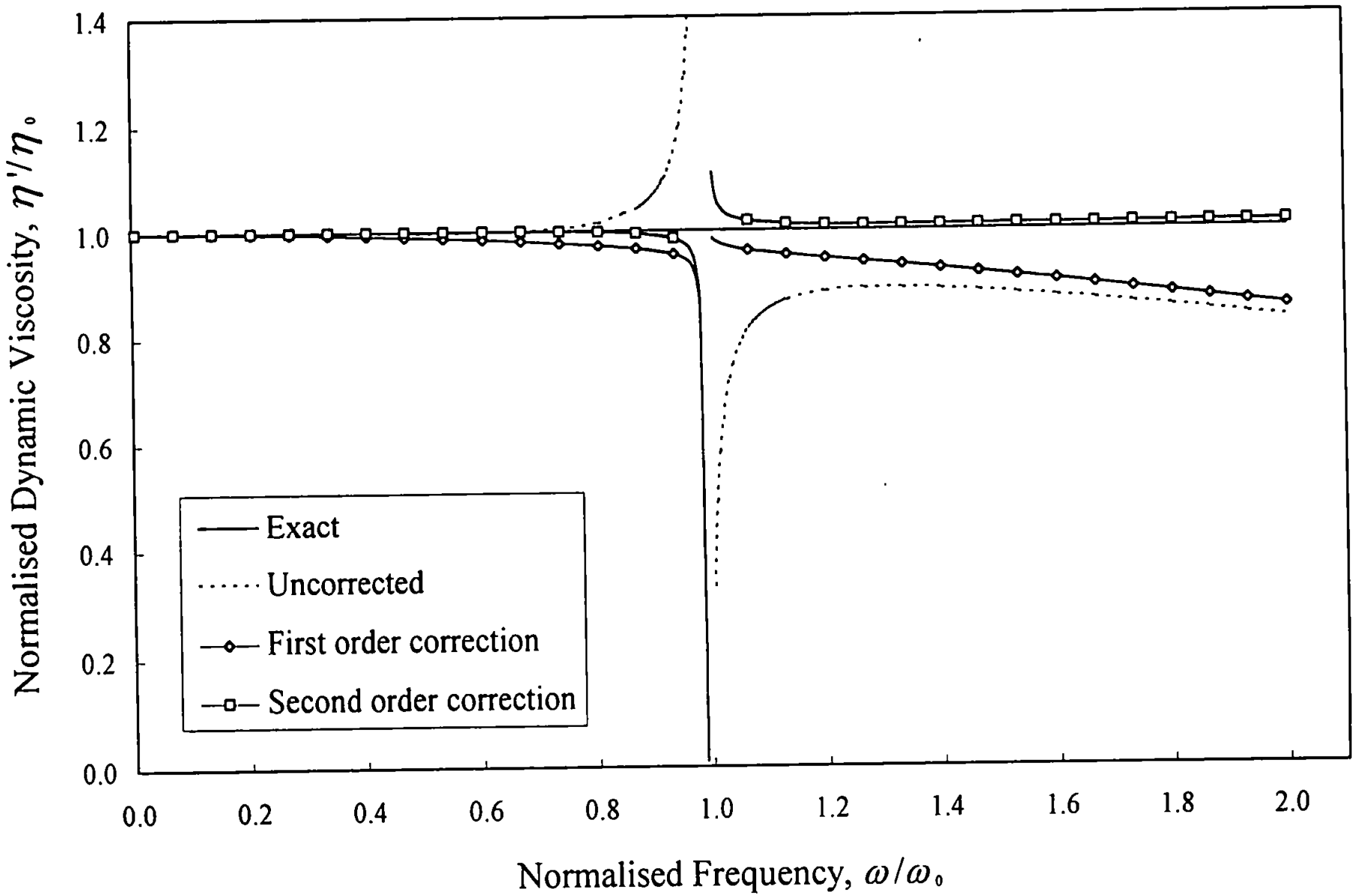
Normalised Dynamic Viscosity, η'/η_0
1.4
1.2
1.0
0.8
0.6
0.4
0.2
0.0
0.0
0.2
0.4
0.6
0.8
1.0
1.2
1.4
1.6
1.8
2.0
Normalised Frequency, ω/ω_0
Exact
Uncorrected
First order correction
Second order correction

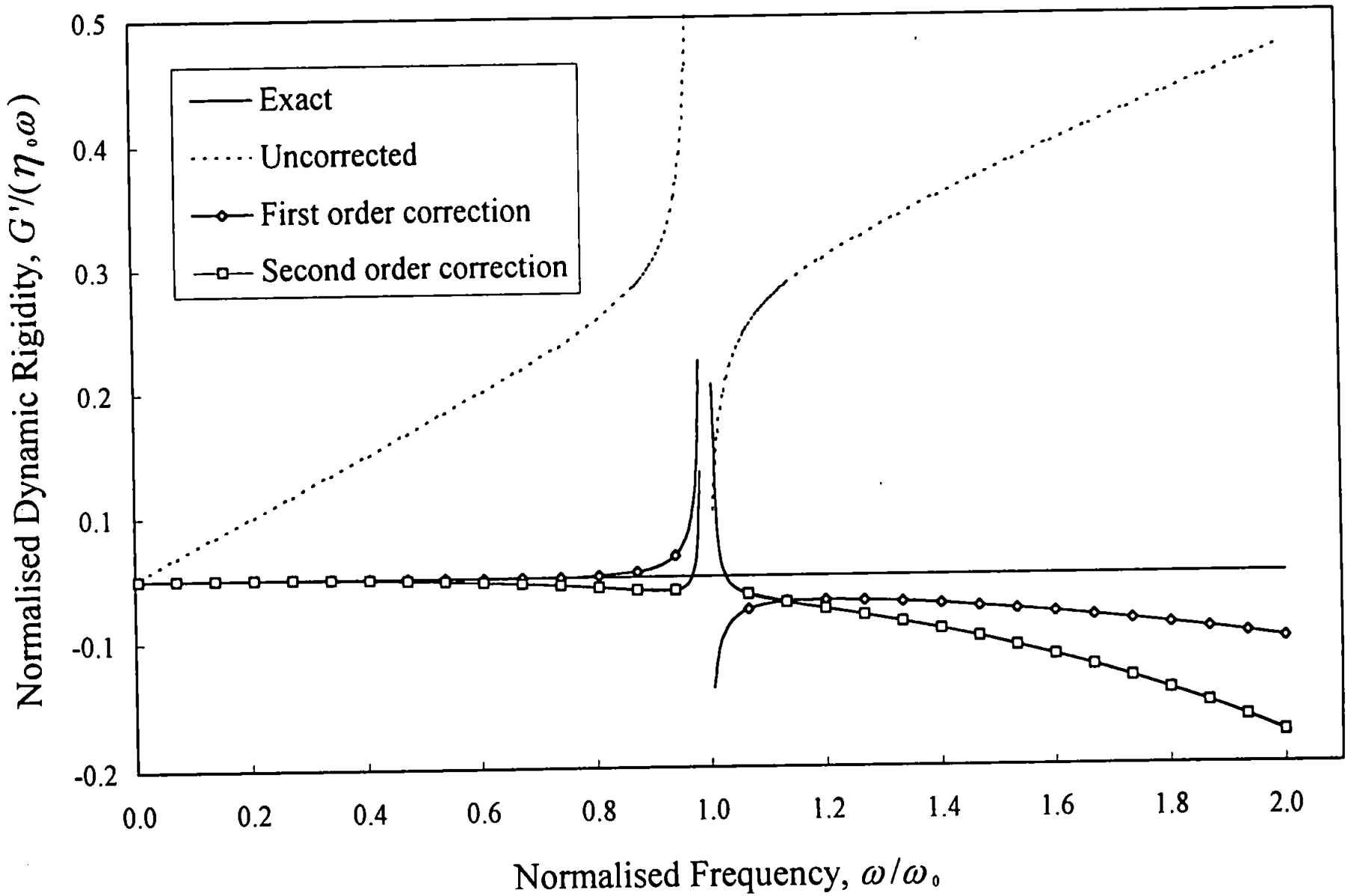
Exact
Uncorrected
First order correction
Second order correction
Normalised Dynamic Rigidity, $G'/(\eta_0\omega)$
Normalised Frequency, ω/ω_0
0.5
0.4
0.3
0.2
0.1
-0.1
-0.2
0.0
0.2
0.4
0.6
0.8
1.0
1.2
1.4
1.6
1.8
2.0

Figures 5.17 and 5.18

Oscillatory shear flow simulations for a Weissenberg rheogoniometer with a torsion bar system

Normalised dynamic viscosity and dynamic rigidity data corrected for second order fluid inertia effects vs. normalised frequency for Newtonian fluids over a range of R values in the concentric cylinder geometry $(r_i = 15\,\text{mm}, r_o = 20\cdot 75\,\text{mm})$.

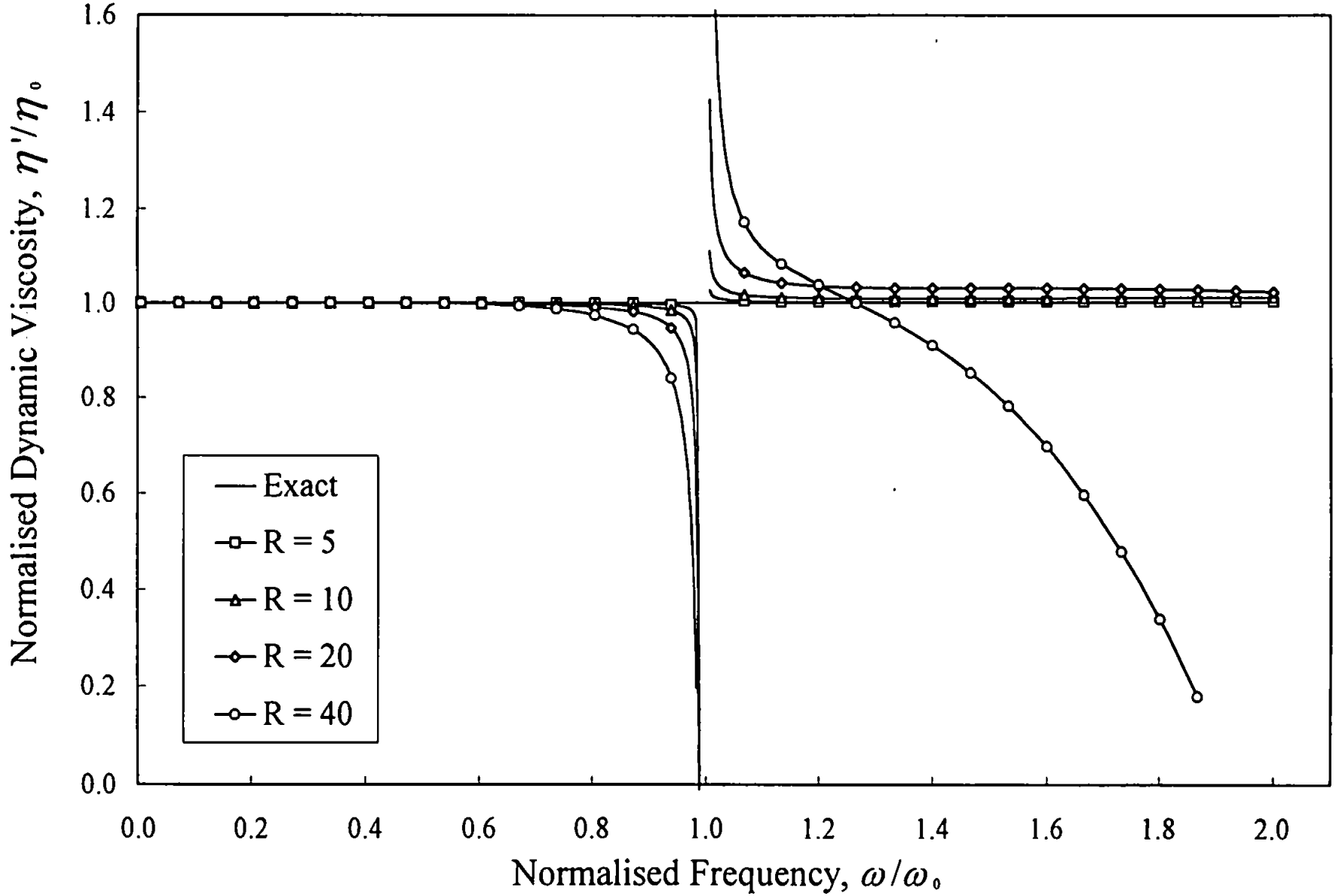
Normalised Dynamic Viscosity, η'/η_0
1.6
1.4
1.2
1.0
0.8
0.6
0.4
0.2
0.0
0.0
0.2
0.4
0.6
0.8
1.0
1.2
1.4
1.6
1.8
2.0
Normalised Frequency, ω/ω_0
Exact
R = 5
R = 10
R = 20
R = 40

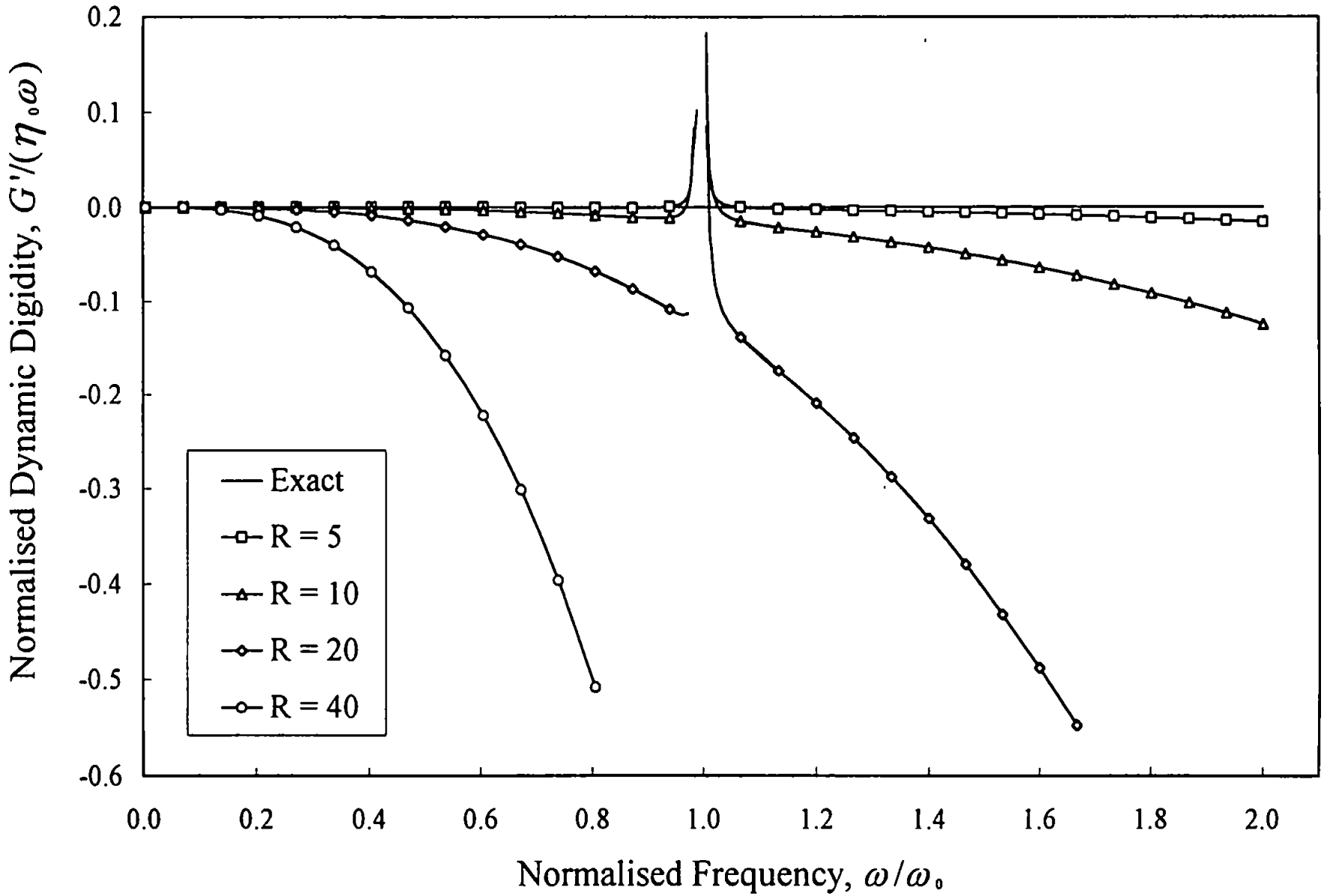
0.2
0.1
0.0
-0.1
-0.2
-0.3
-0.4
-0.5
-0.6
Normalised Dynamic Digidity, $G'/(\eta_0\omega)$
0.0
0.2
0.4
0.6
0.8
1.0
1.2
1.4
1.6
1.8
2.0
Normalised Frequency, ω/ω_0
Exact
R = 5
R = 10
R = 20
R = 40

Figures 5.19 and 5.20

Oscillatory shear flow simulations for a Weissenberg rheogoniometer with a torsion bar system

Normalised dynamic viscosity and dynamic rigidity vs. normalised frequency for a single element Maxwell fluid in the concentric cylinder geometry ($r_i = 15\,\text{mm}, r_o = 20\cdot 75\,\text{mm}$) when $R = 5$.

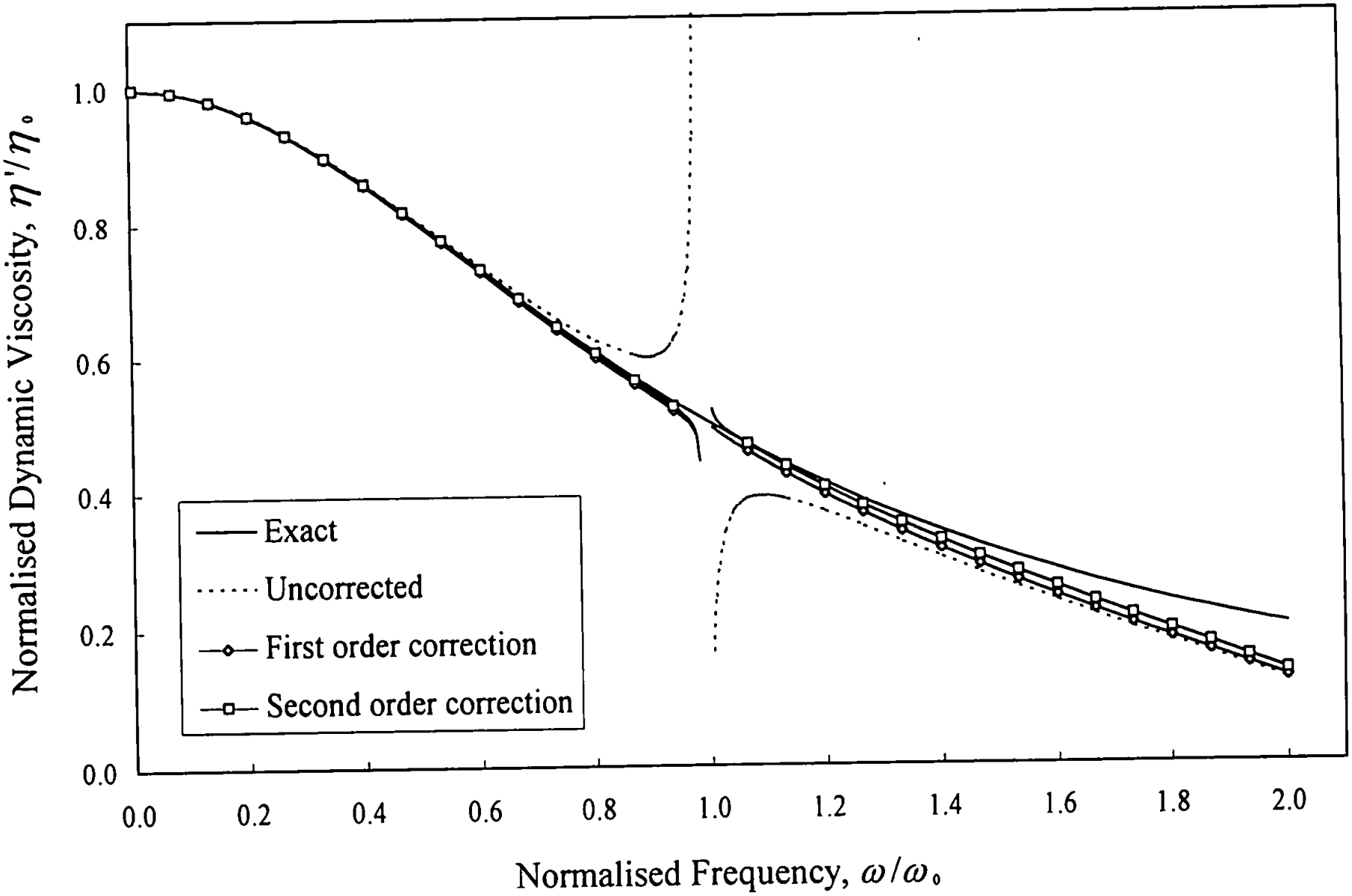
Normalised Dynamic Viscosity, η'/η_0
1.0
0.8
0.6
0.4
0.2
0.0
0.0
0.2
0.4
0.6
0.8
1.0
1.2
1.4
1.6
1.8
2.0
Normalised Frequency, ω/ω_0
Exact
Uncorrected
First order correction
Second order correction

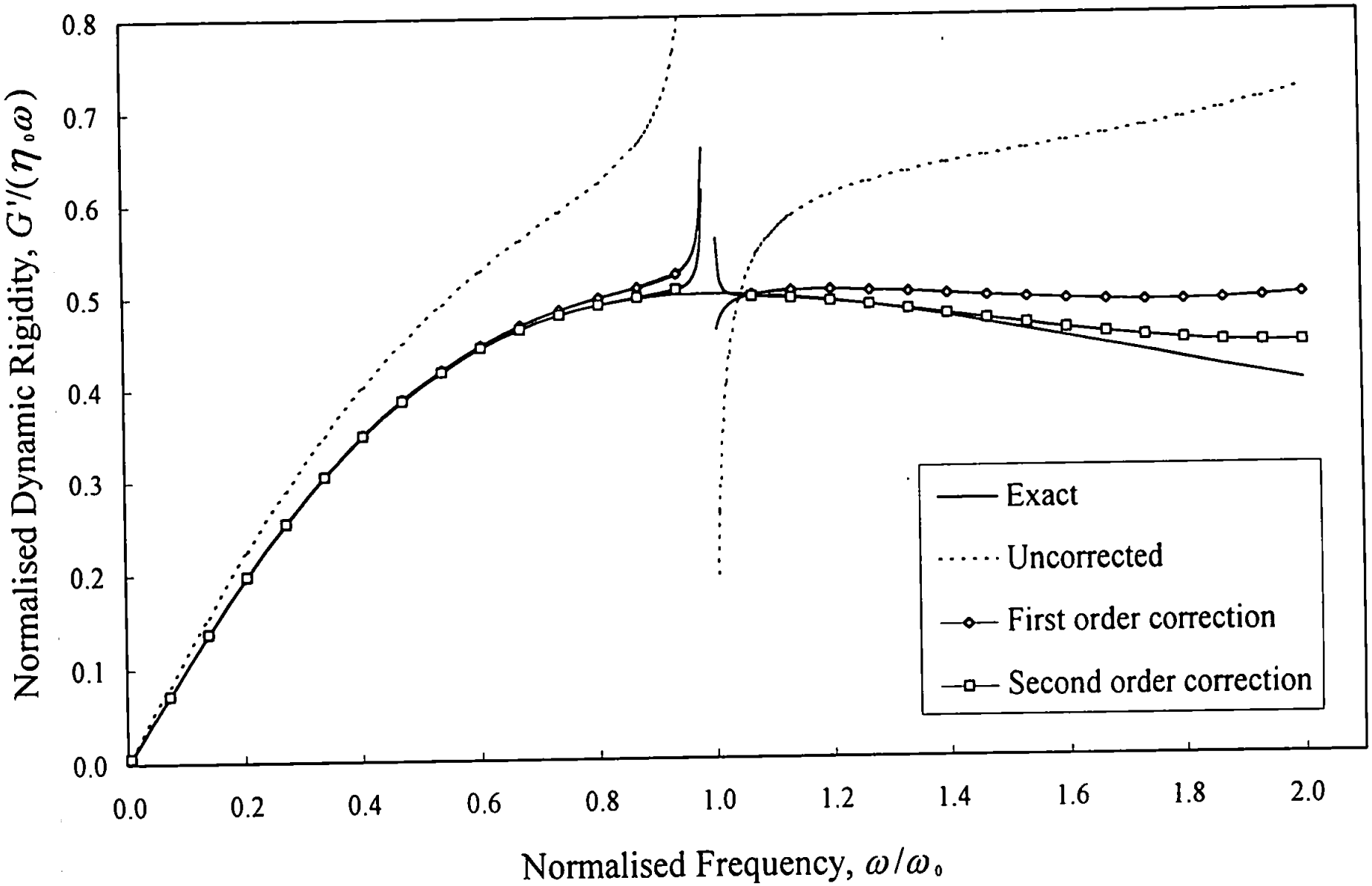
Normalised Dynamic Rigidity, $G'/(\eta_0\omega)$
0.0
0.1
0.2
0.3
0.4
0.5
0.6
0.7
0.8
0.0
0.2
0.4
0.6
0.8
1.0
1.2
1.4
1.6
1.8
2.0
Normalised Frequency, ω/ω_0
Exact
Uncorrected
First order correction
Second order correction

Figures 5.21 and 5.22

Oscillatory shear flow simulations for a Weissenberg rheogoniometer with a torsion bar system

Normalised dynamic viscosity and dynamic rigidity data corrected for second order fluid inertia effects vs. normalised frequency for single element Maxwell fluids over a range of R values in the concentric cylinder geometry ($r_i = 15\,\text{mm}, r_o = 20\cdot 75\,\text{mm}$).

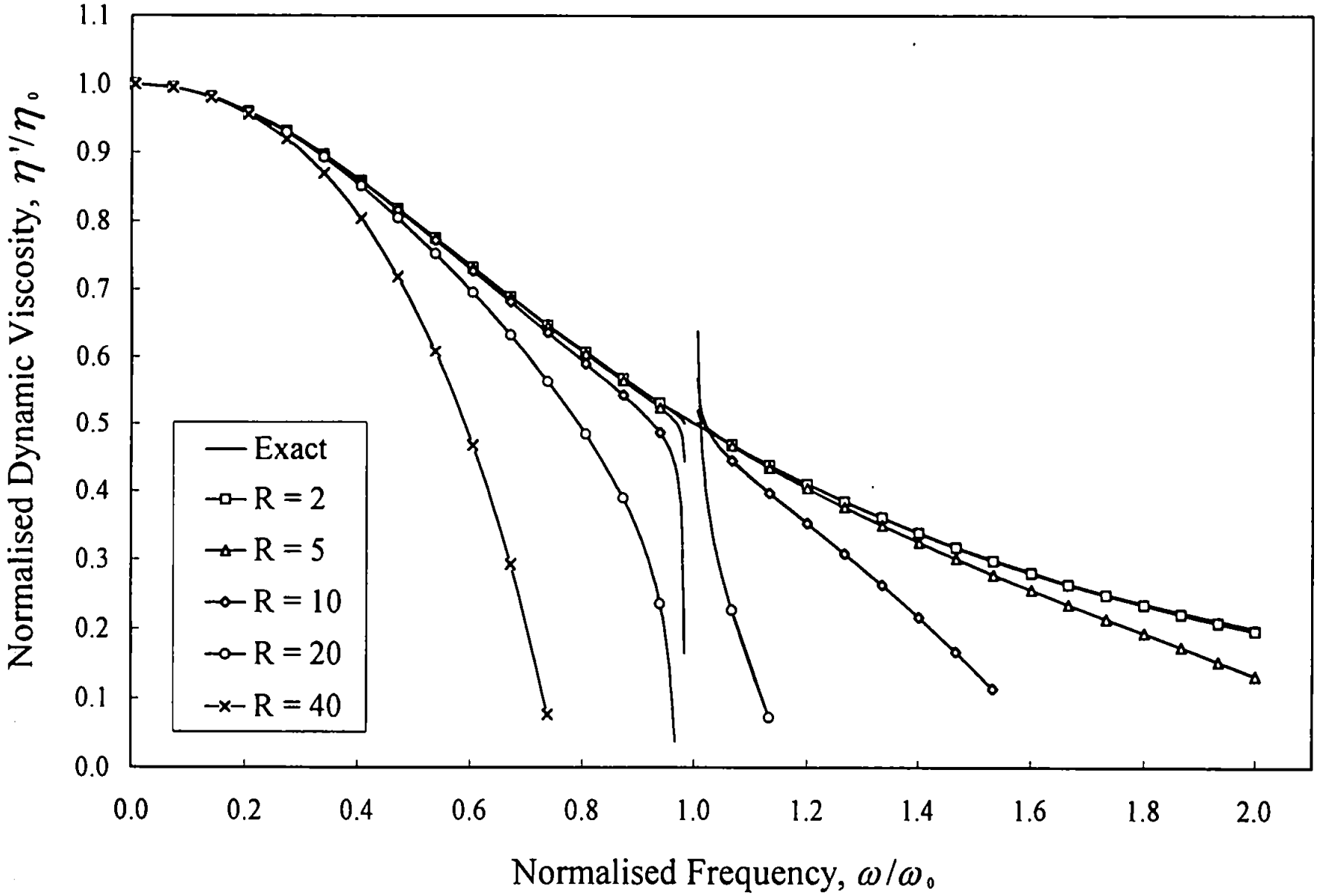
Normalised Dynamic Viscosity, η'/η_0
Normalised Frequency, ω/ω_0
Exact
R = 2
R = 5
R = 10
R = 20
R = 40
0.0
0.1
0.2
0.3
0.4
0.5
0.6
0.7
0.8
0.9
1.0
1.1
0.0
0.2
0.4
0.6
0.8
1.0
1.2
1.4
1.6
1.8
2.0

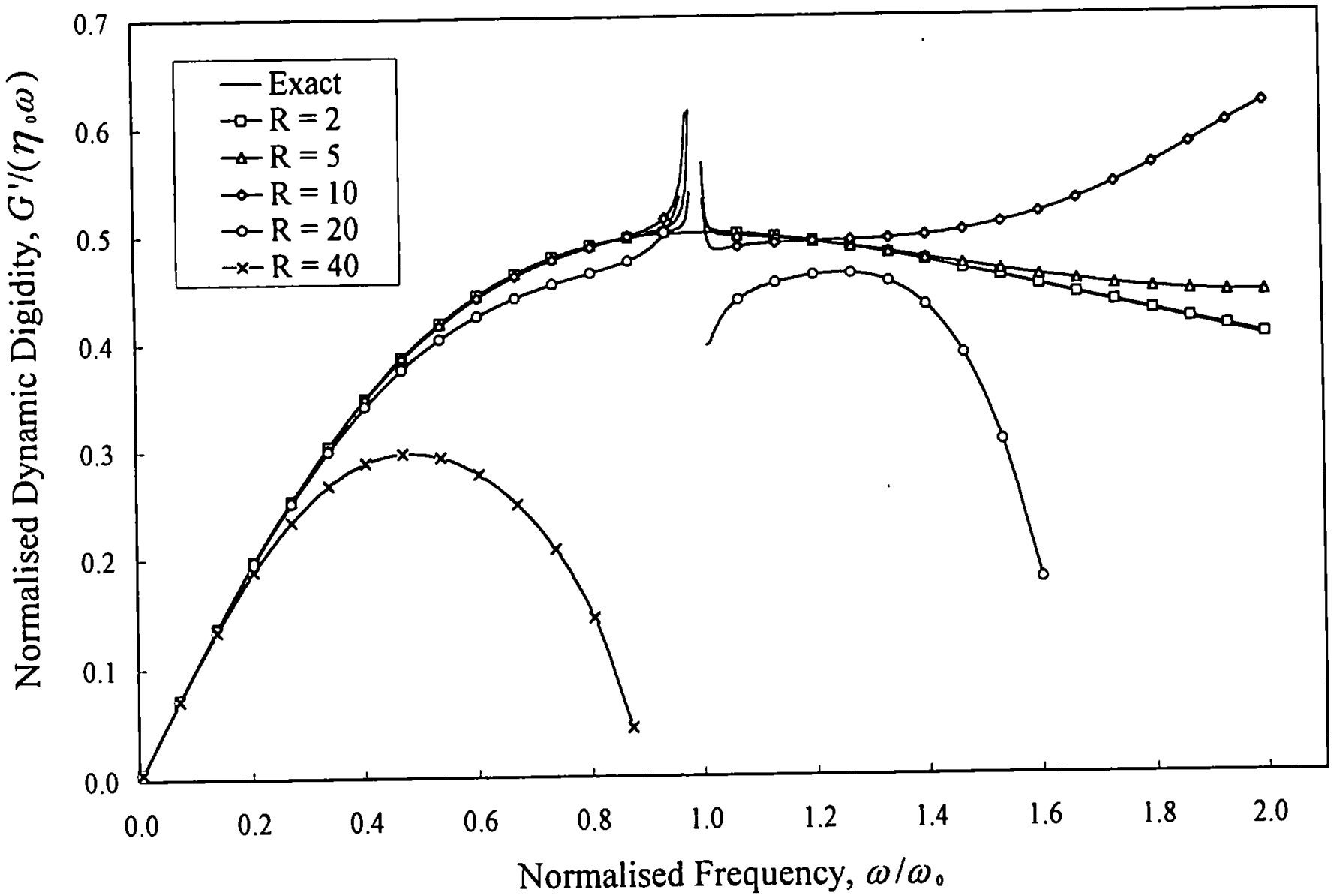
Exact
R = 2
R = 5
R = 10
R = 20
R = 40
Normalised Dynamic Digidity, $G'/(\eta_o\omega)$
Normalised Frequency, ω/ω_o
0.0
0.1
0.2
0.3
0.4
0.5
0.6
0.7
0.0
0.2
0.4
0.6
0.8
1.0
1.2
1.4
1.6
1.8
2.0

Figures 5.23 and 5.24

Oscillatory shear flow simulations for a Weissenberg rheogoniometer with a strain gauge torsion head system (W) and a CSR controlled stress rheometer (C).

Normalised dynamic viscosity and dynamic rigidity vs. normalised frequency for a Newtonian fluid in the concentric cylinder geometry $(r_i = 15\,\text{mm}, r_o = 20\cdot 75\,\text{mm})$.

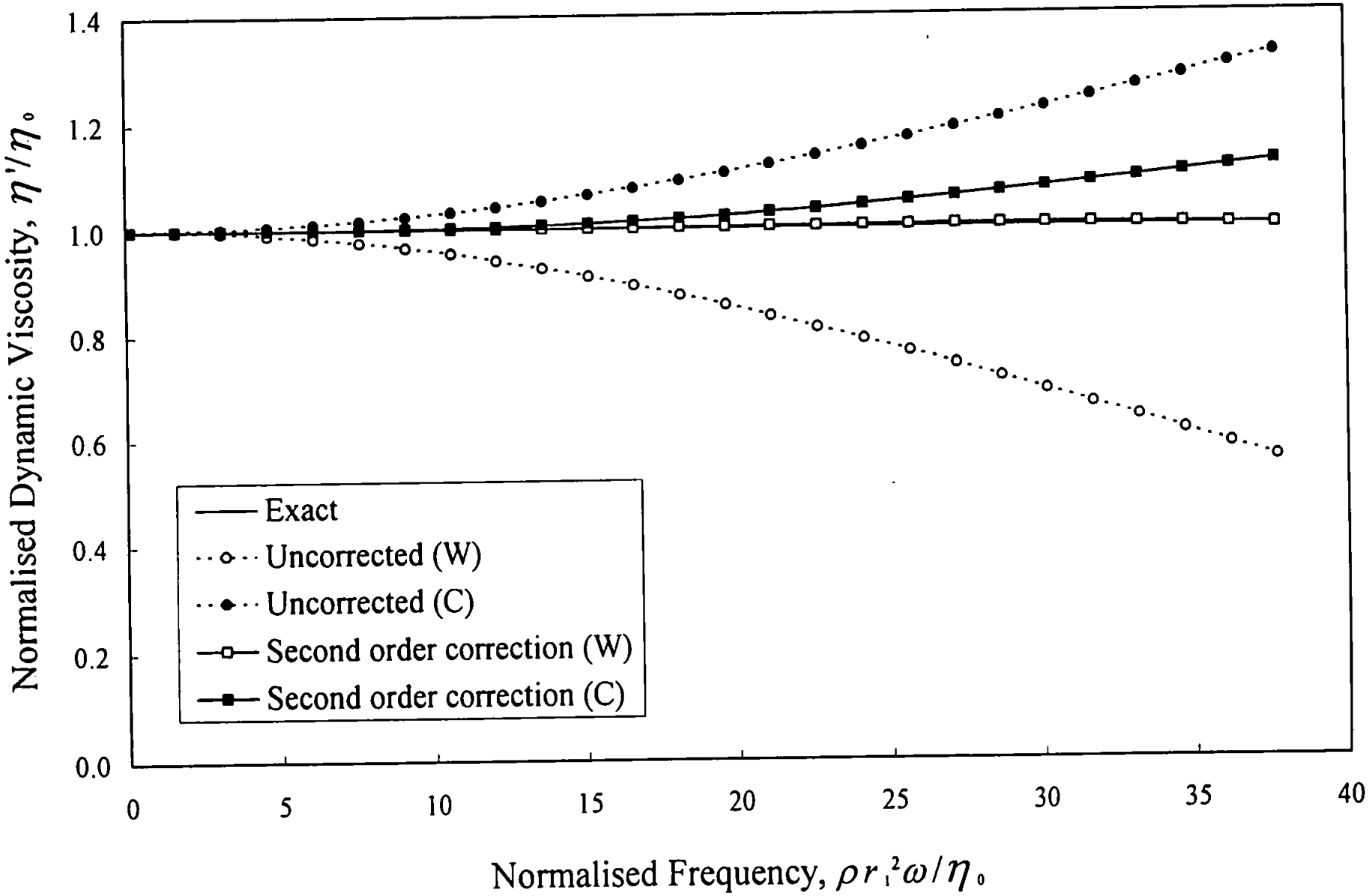
1.4
1.2
1.0
0.8
0.6
0.4
0.2
0.0
0
5
10
15
20
25
30
35
40
Normalised Dynamic Viscosity, η'/η_0
Normalised Frequency, $\rho r_1^2\omega/\eta_0$
Exact
Uncorrected (W)
Uncorrected (C)
Second order correction (W)
Second order correction (C)

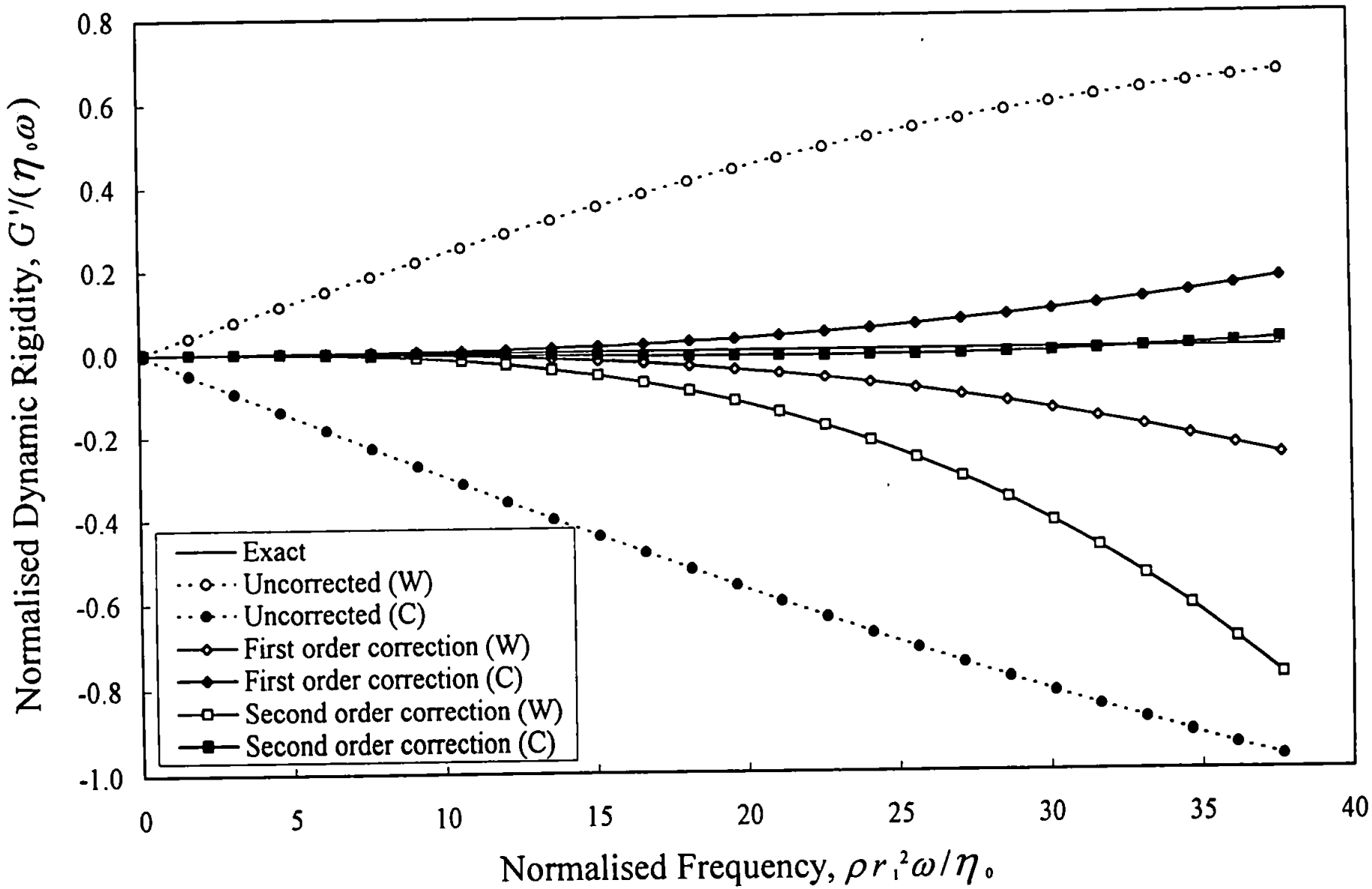
0.8
0.6
0.4
0.2
0.0
-0.2
-0.4
-0.6
-0.8
-1.0
0
5
10
15
20
25
30
35
40
Normalised Dynamic Rigidity, $G'/(\eta_0\omega)$
Normalised Frequency, $\rho r_1^2\omega/\eta_0$
Exact
Uncorrected (W)
Uncorrected (C)
First order correction (W)
First order correction (C)
Second order correction (W)
Second order correction (C)

Figures 5.25 and 5.26

Oscillatory shear flow simulations for a Weissenberg rheogoniometer with a strain gauge torsion head system (W) and a CSR controlled stress rheometer (C).

Normalised dynamic viscosity and dynamic rigidity vs. normalised frequency for a single element Maxwell fluid in the concentric cylinder geometry ($r_i = 15\,\text{mm}, r_o = 20\cdot 75\,\text{mm}$) when $R = 5$.

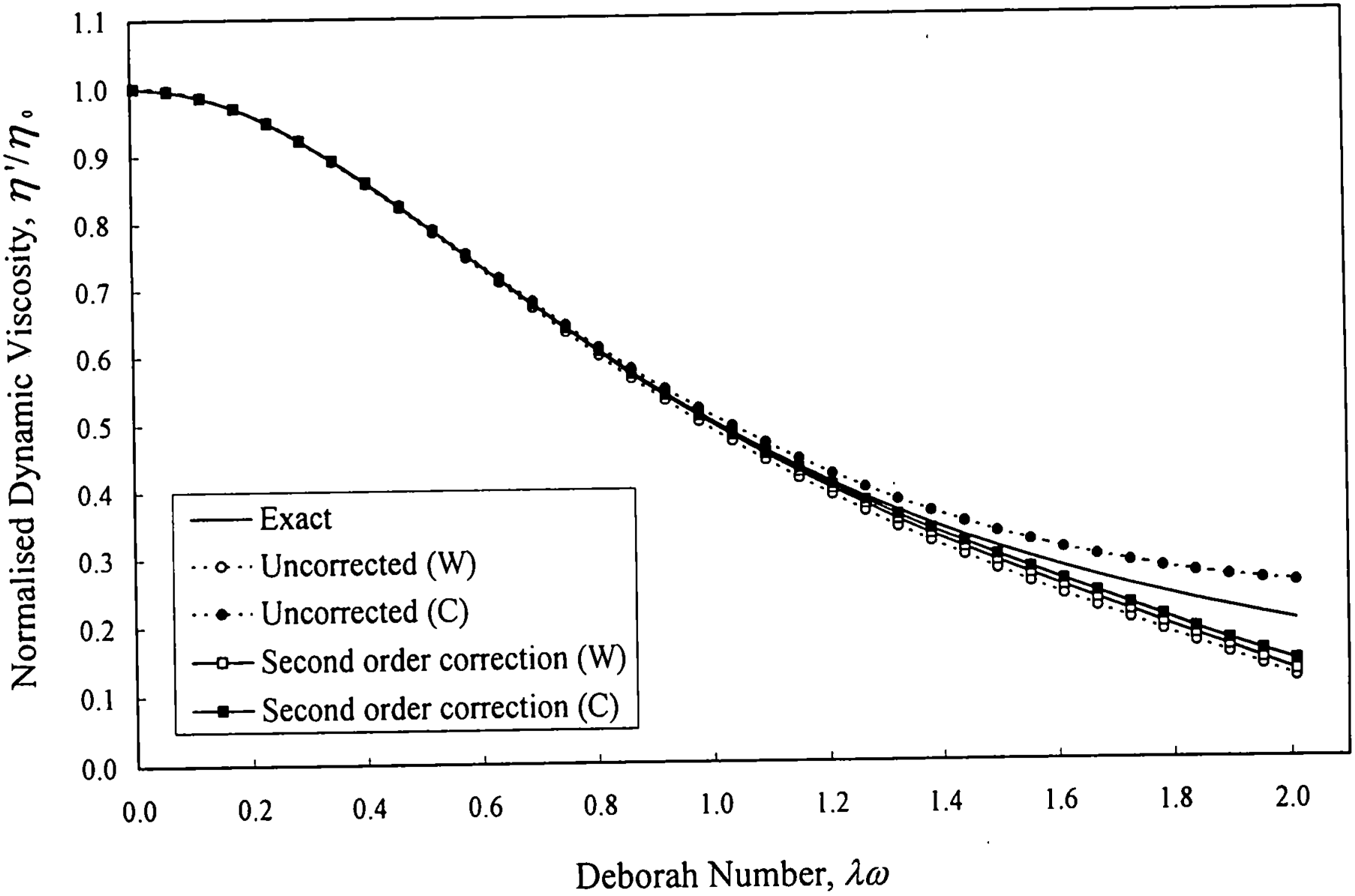
Normalised Dynamic Viscosity, η'/η_o
1.1
1.0
0.9
0.8
0.7
0.6
0.5
0.4
0.3
0.2
0.1
0.0
0.0
0.2
0.4
0.6
0.8
1.0
1.2
1.4
1.6
1.8
2.0
Deborah Number, $\lambda\omega$
Exact
Uncorrected (W)
Uncorrected (C)
Second order correction (W)
Second order correction (C)

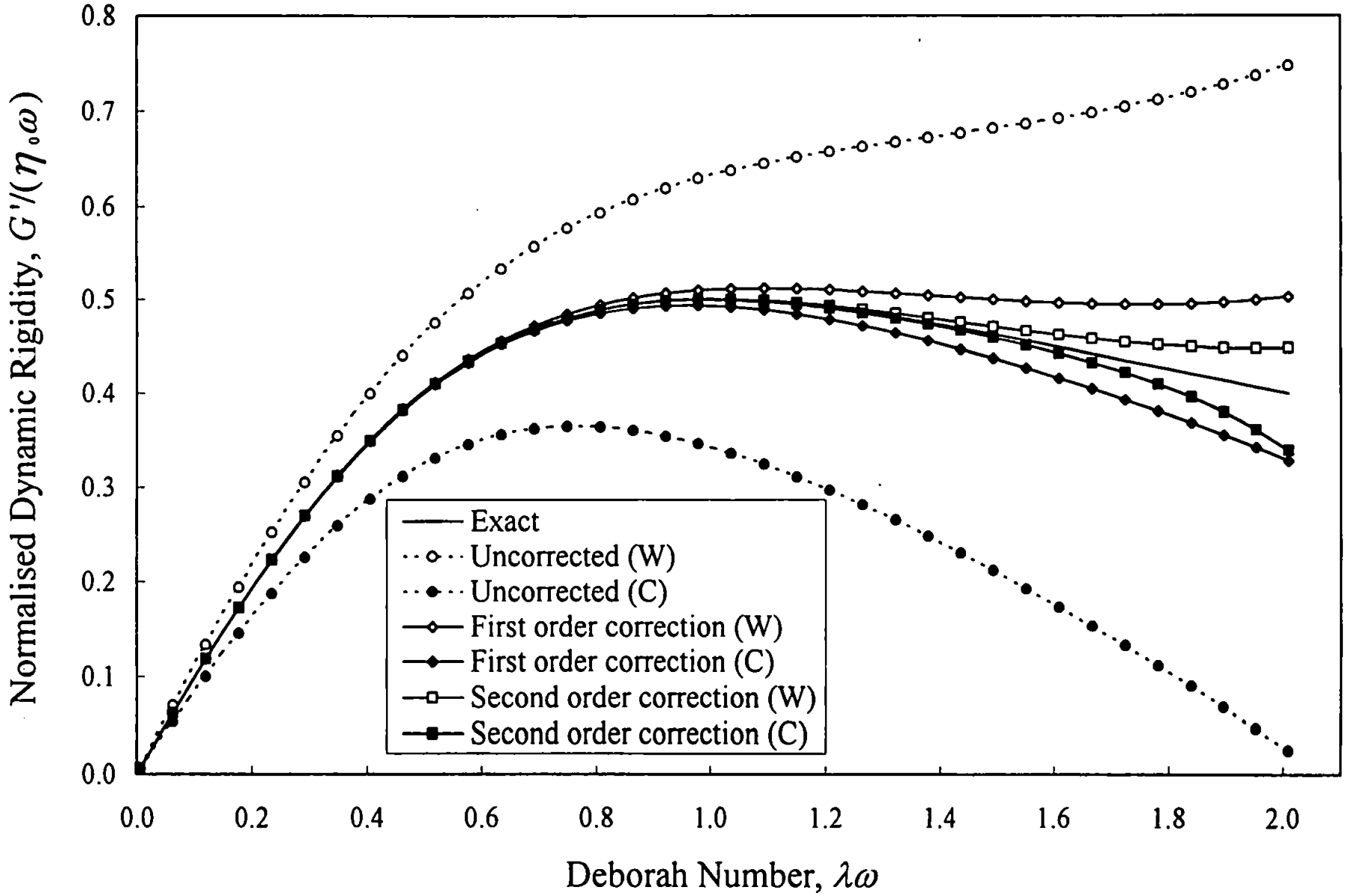
Normalised Dynamic Rigidity, $G'/(\eta_o\omega)$
Deborah Number, $\lambda\omega$
0.0
0.1
0.2
0.3
0.4
0.5
0.6
0.7
0.8
0.0
0.2
0.4
0.6
0.8
1.0
1.2
1.4
1.6
1.8
2.0
Exact
Uncorrected (W)
Uncorrected (C)
First order correction (W)
First order correction (C)
Second order correction (W)
Second order correction (C)

Figures 5.27 and 5.28

Oscillatory shear flow simulations for a Weissenberg rheogoniometer with a strain gauge torsion head system (W) and a CSR controlled stress rheometer (C).

Normalised dynamic viscosity and dynamic rigidity data corrected for second order fluid inertia effects vs. normalised frequency for single element Maxwell fluids over a range of R values in the concentric cylinder geometry $(r_i = 15\,\text{mm}, r_o = 20\cdot 75\,\text{mm})$.

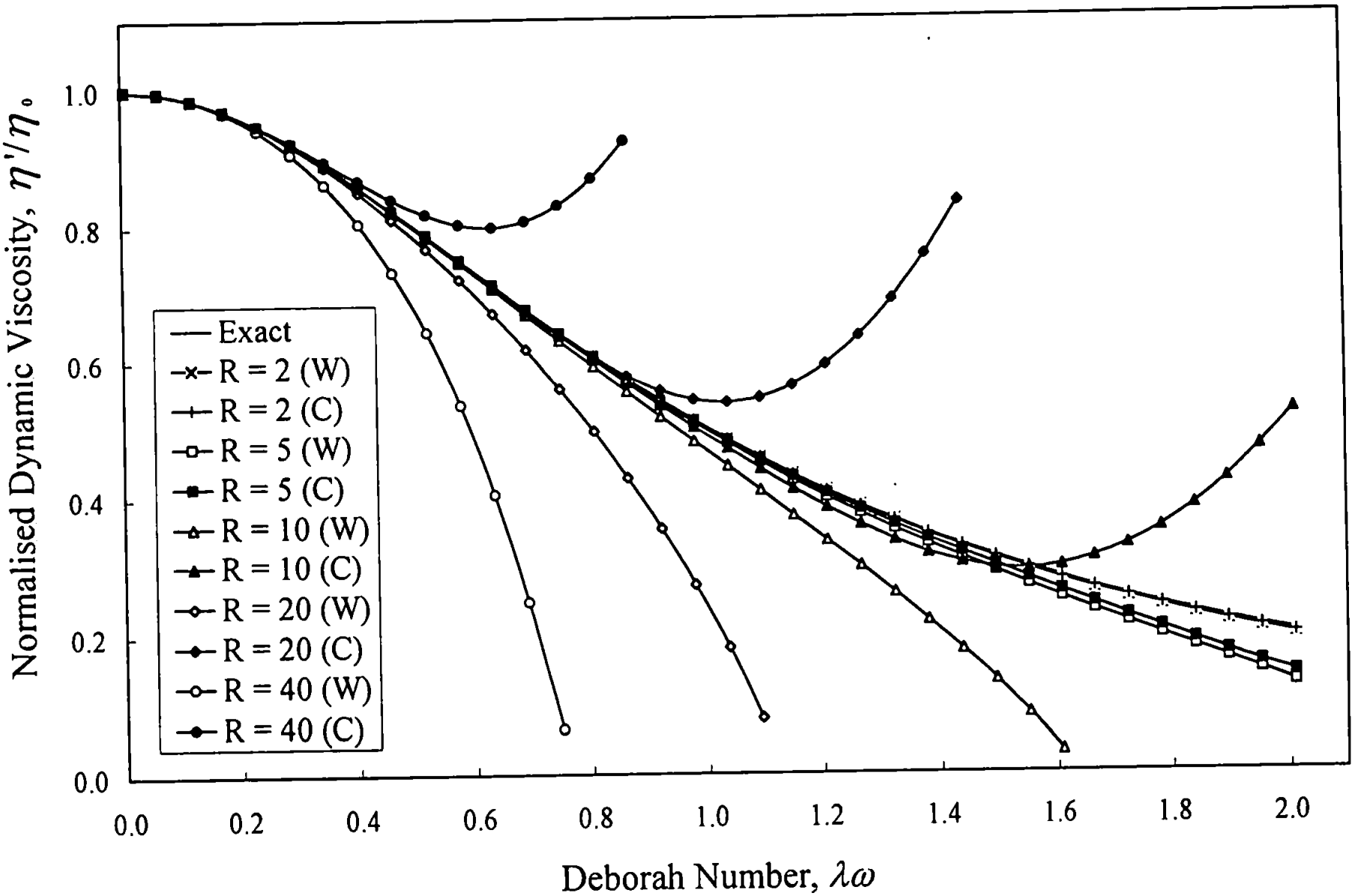
Normalised Dynamic Viscosity, η'/η_o
1.0
0.8
0.6
0.4
0.2
0.0
0.0
0.2
0.4
0.6
0.8
1.0
1.2
1.4
1.6
1.8
2.0
Deborah Number, $\lambda\omega$
Exact
R = 2 (W)
R = 2 (C)
R = 5 (W)
R = 5 (C)
R = 10 (W)
R = 10 (C)
R = 20 (W)
R = 20 (C)
R = 40 (W)
R = 40 (C)

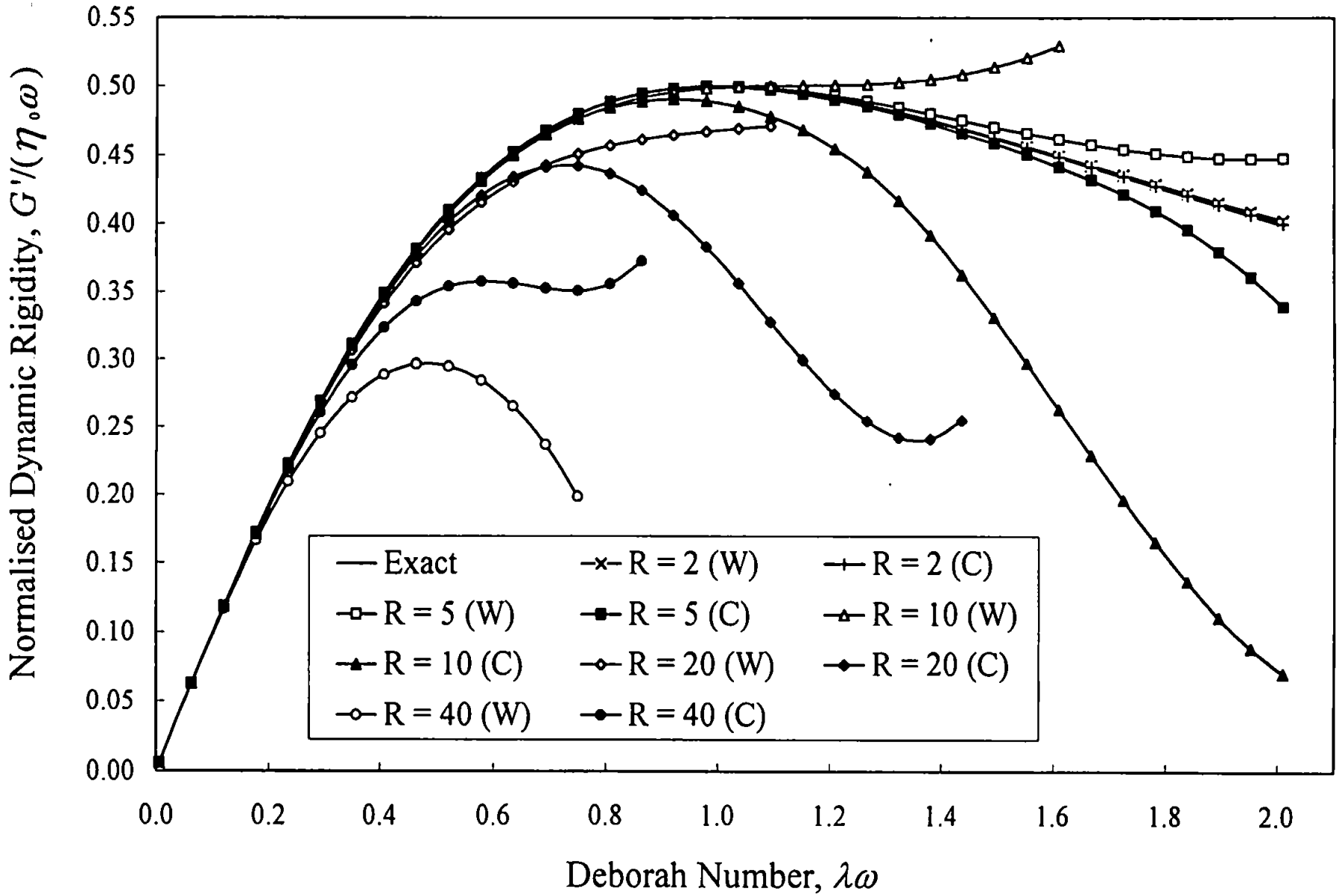
Normalised Dynamic Rigidity, $G'/(\eta_o\omega)$
0.55
0.50
0.45
0.40
0.35
0.30
0.25
0.20
0.15
0.10
0.05
0.00
0.0
0.2
0.4
0.6
0.8
1.0
1.2
1.4
1.6
1.8
2.0
Deborah Number, $\lambda\omega$
Exact
R = 2 (W)
R = 2 (C)
R = 5 (W)
R = 5 (C)
R = 10 (W)
R = 10 (C)
R = 20 (W)
R = 20 (C)
R = 40 (W)
R = 40 (C)

Figures 5.29 and 5.30

Oscillatory shear flow simulations for a Weissenberg rheogoniometer with a torsion bar system

Normalised dynamic viscosity and dynamic rigidity vs. normalised frequency for a Newtonian fluid in the cone and plate geometry $(a = 0 \cdot 0375\,\mathrm{m}, \theta_0 = 2^\circ)$ when $R = 1000$.

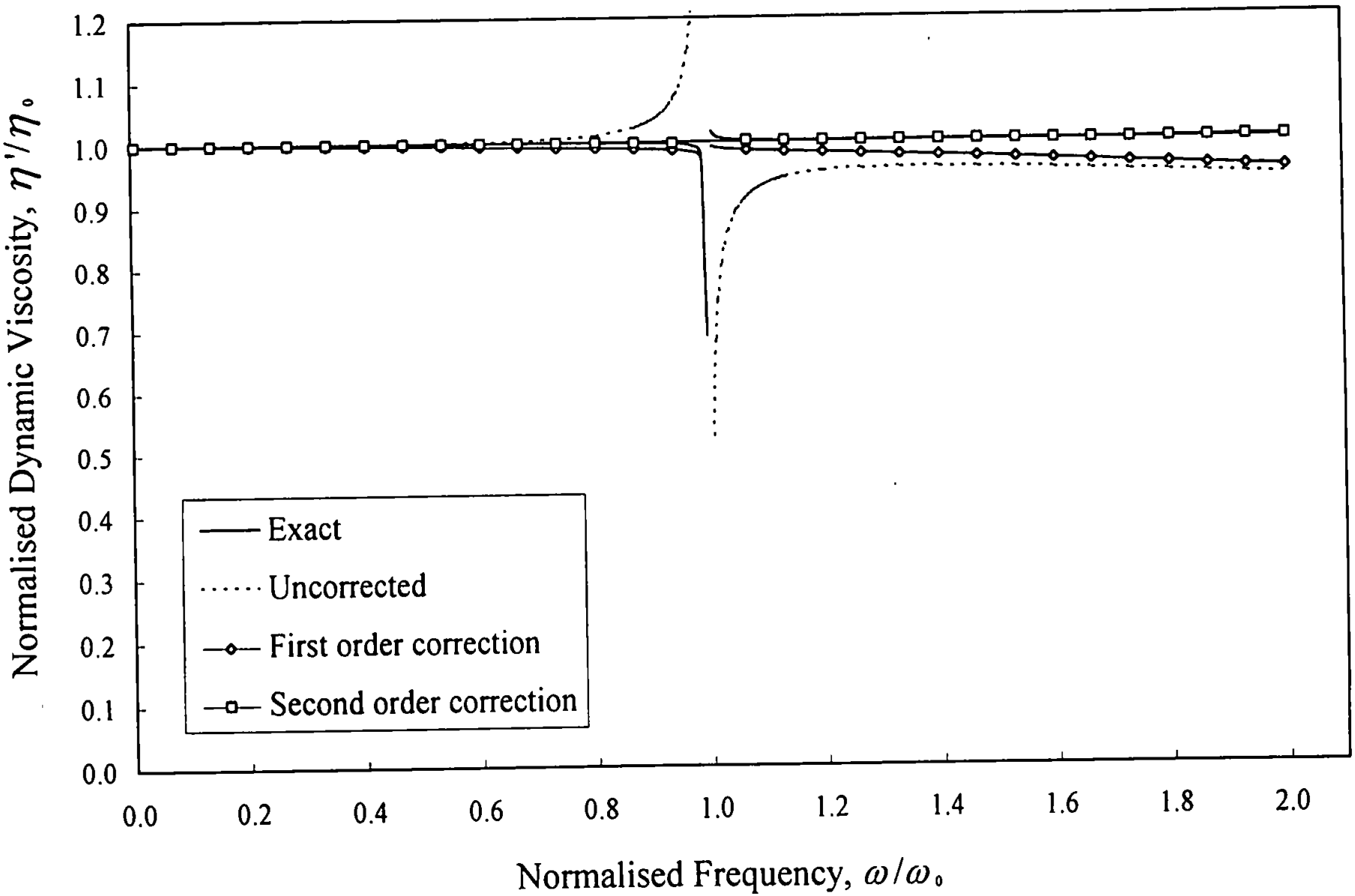
Normalised Dynamic Viscosity, η'/η_0
1.2
1.1
1.0
0.9
0.8
0.7
0.6
0.5
0.4
0.3
0.2
0.1
0.0
0.0
0.2
0.4
0.6
0.8
1.0
1.2
1.4
1.6
1.8
2.0
Normalised Frequency, ω/ω_0
Exact
Uncorrected
First order correction
Second order correction

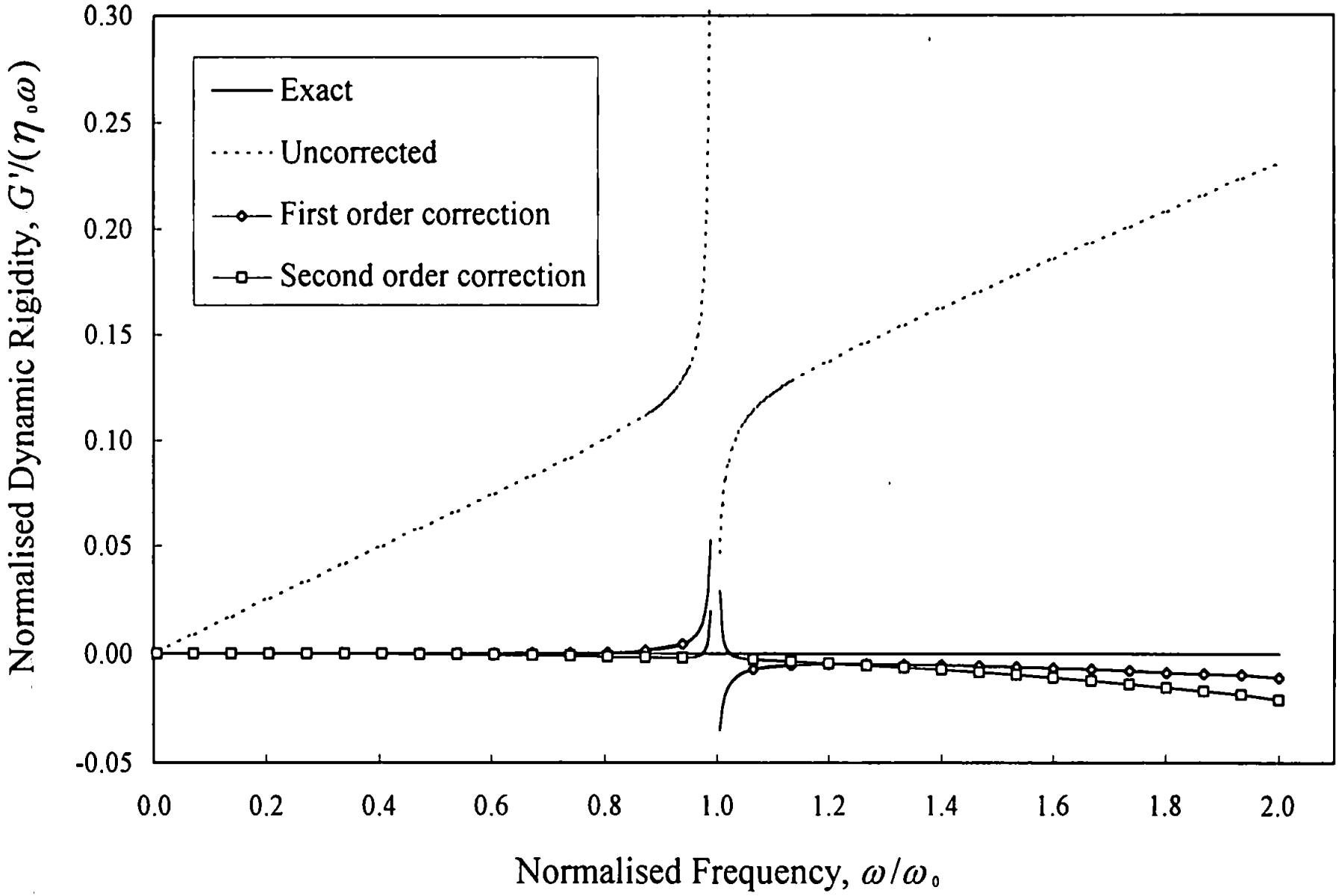
Exact
Uncorrected
First order correction
Second order correction
Normalised Dynamic Rigidity, $G'/(\eta_0\omega)$
Normalised Frequency, ω/ω_0
0.30
0.25
0.20
0.15
0.10
0.05
0.00
-0.05
0.0
0.2
0.4
0.6
0.8
1.0
1.2
1.4
1.6
1.8
2.0

Figures 5.31 and 5.32

Oscillatory shear flow simulations for a Weissenberg rheogoniometer with a torsion bar system.

Normalised dynamic viscosity and dynamic rigidity vs. normalised frequency for a single element Maxwell fluid in the cone and plate geometry $(a = 0{\cdot}0375\,\mathrm{m}, \theta_0 = 2^\circ)$ when $R = 1000$.

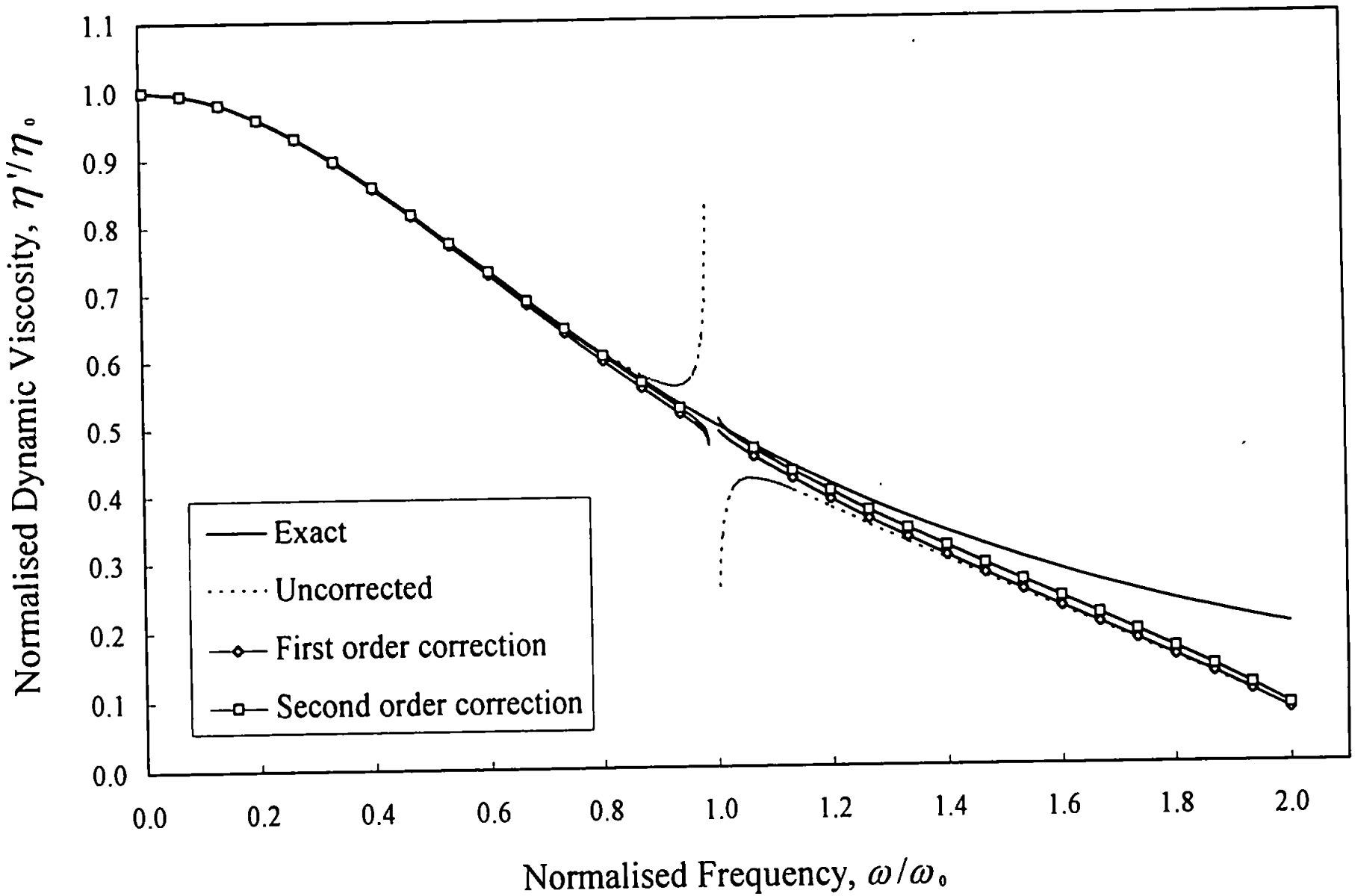
Normalised Dynamic Viscosity, η'/η_0
1.1
1.0
0.9
0.8
0.7
0.6
0.5
0.4
0.3
0.2
0.1
0.0
0.0
0.2
0.4
0.6
0.8
1.0
1.2
1.4
1.6
1.8
2.0
Normalised Frequency, ω/ω_0
Exact
Uncorrected
First order correction
Second order correction

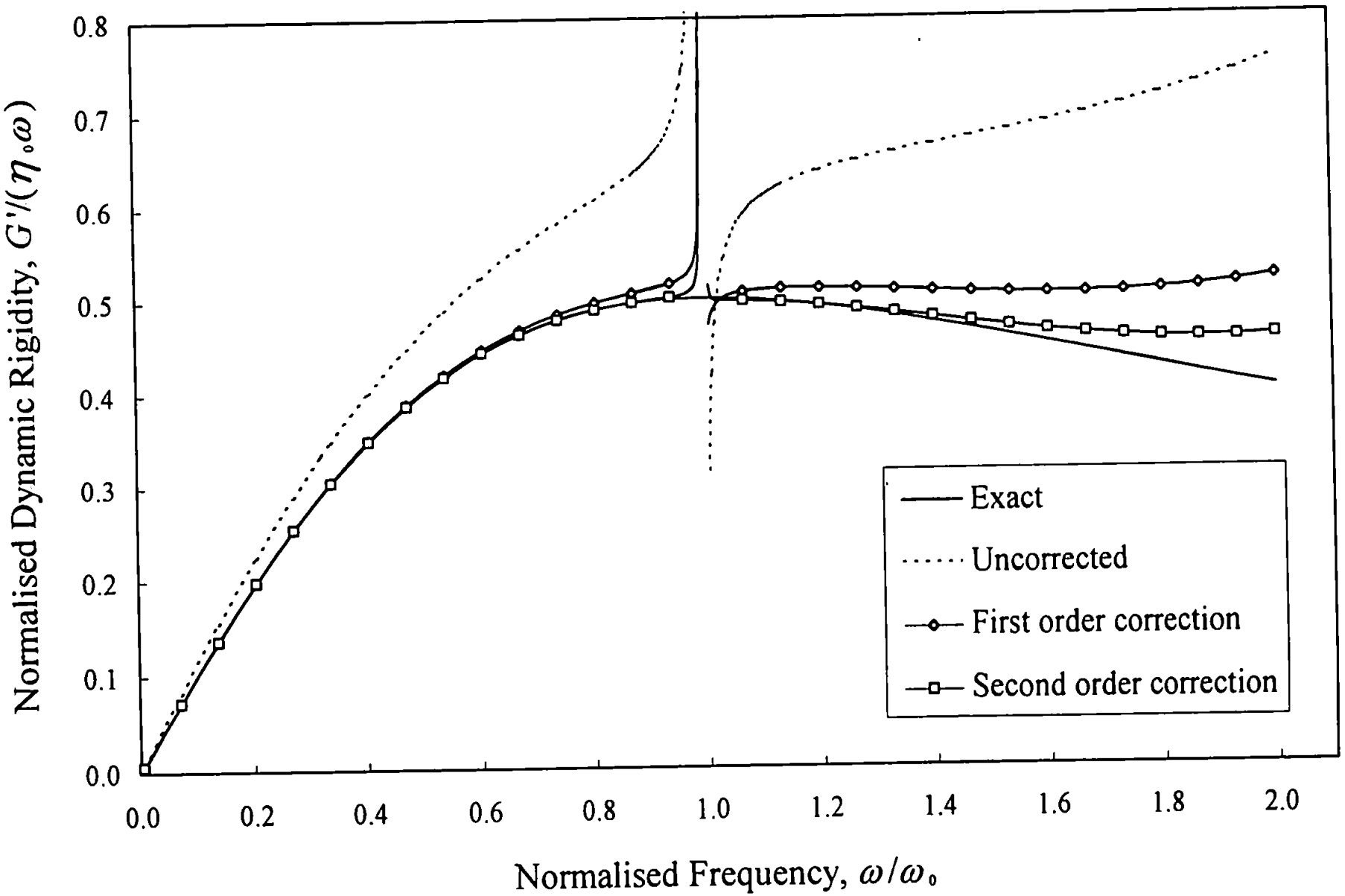
Normalised Dynamic Rigidity, $G'/(\eta_0\omega)$
0.0
0.1
0.2
0.3
0.4
0.5
0.6
0.7
0.8
0.0
0.2
0.4
0.6
0.8
1.0
1.2
1.4
1.6
1.8
2.0
Normalised Frequency, ω/ω_0
Exact
Uncorrected
First order correction
Second order correction

Figures 5.33 and 5.34

Oscillatory shear flow simulations for a Weissenberg rheogoniometer with a strain gauge torsion head system (W) and a CSR controlled stress rheometer (C).

Normalised dynamic viscosity and dynamic rigidity vs. normalised frequency for a Newtonian fluid in the cone and plate geometry $(a = 0{\cdot}0375\,\mathrm{m}, \theta_0 = 2^\circ)$.

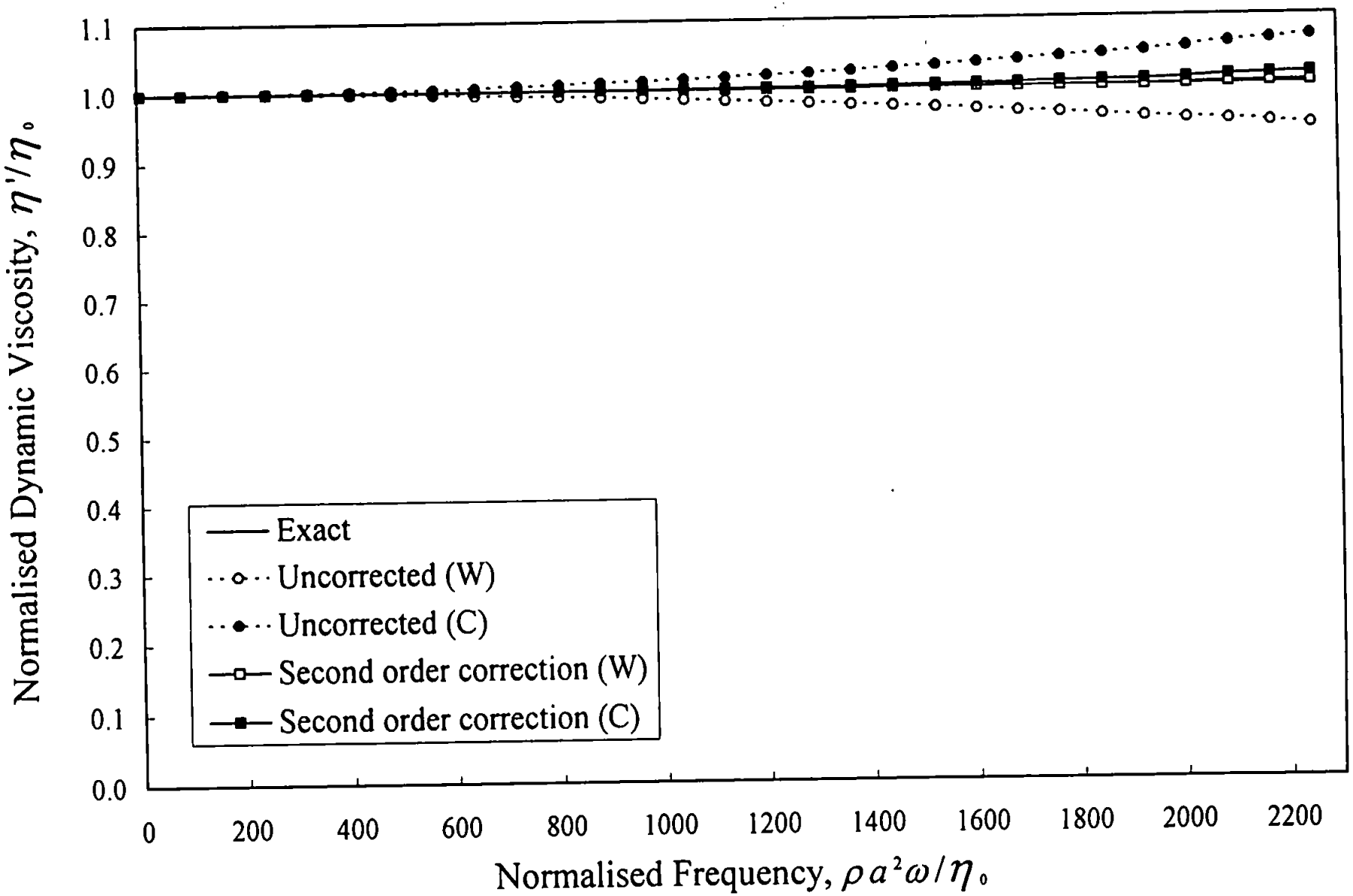
Normalised Dynamic Viscosity, η'/η_0
1.1
1.0
0.9
0.8
0.7
0.6
0.5
0.4
0.3
0.2
0.1
0.0
0
200
400
600
800
1000
1200
1400
1600
1800
2000
2200
Normalised Frequency, $\rho a^2\omega/\eta_0$
Exact
Uncorrected (W)
Uncorrected (C)
Second order correction (W)
Second order correction (C)

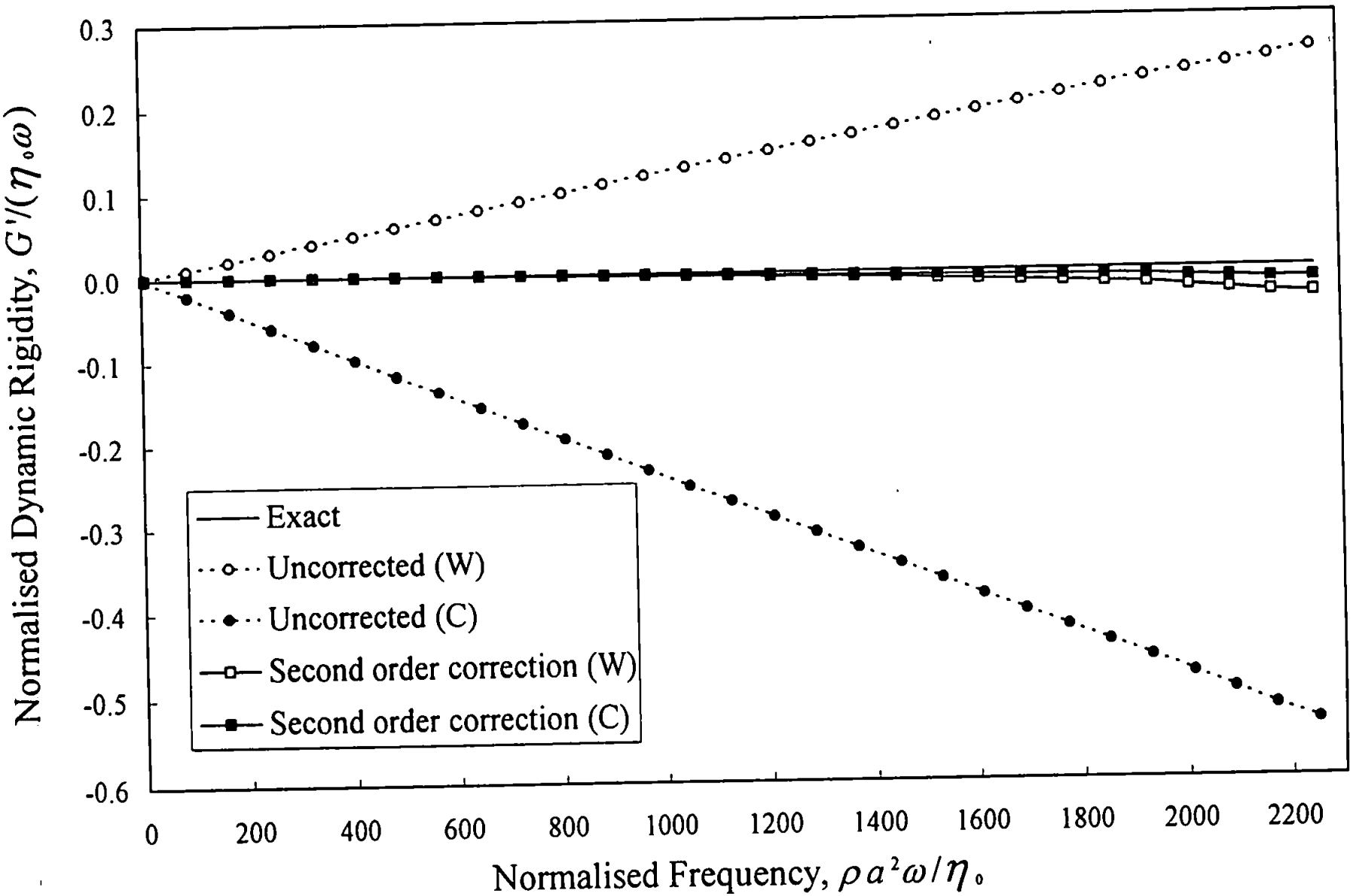
0.3
0.2
0.1
0.0
-0.1
-0.2
-0.3
-0.4
-0.5
-0.6
Normalised Dynamic Rigidity, $G'/(\eta_o\omega)$
0
200
400
600
800
1000
1200
1400
1600
1800
2000
2200
Normalised Frequency, $\rho a^2\omega/\eta_o$
Exact
Uncorrected (W)
Uncorrected (C)
Second order correction (W)
Second order correction (C)

Figures 5.35 and 5.36

Oscillatory shear flow simulations for a Weissenberg rheogoniometer with a strain gauge torsion head system (W) and a CSR controlled stress rheometer (C).

Normalised dynamic viscosity and dynamic rigidity vs. normalised frequency for a single element Maxwell fluid in the cone and plate geometry $(a = 0{\cdot}0375\,\mathrm{m}, \theta_0 = 2^\circ)$ when $R = 1000$.

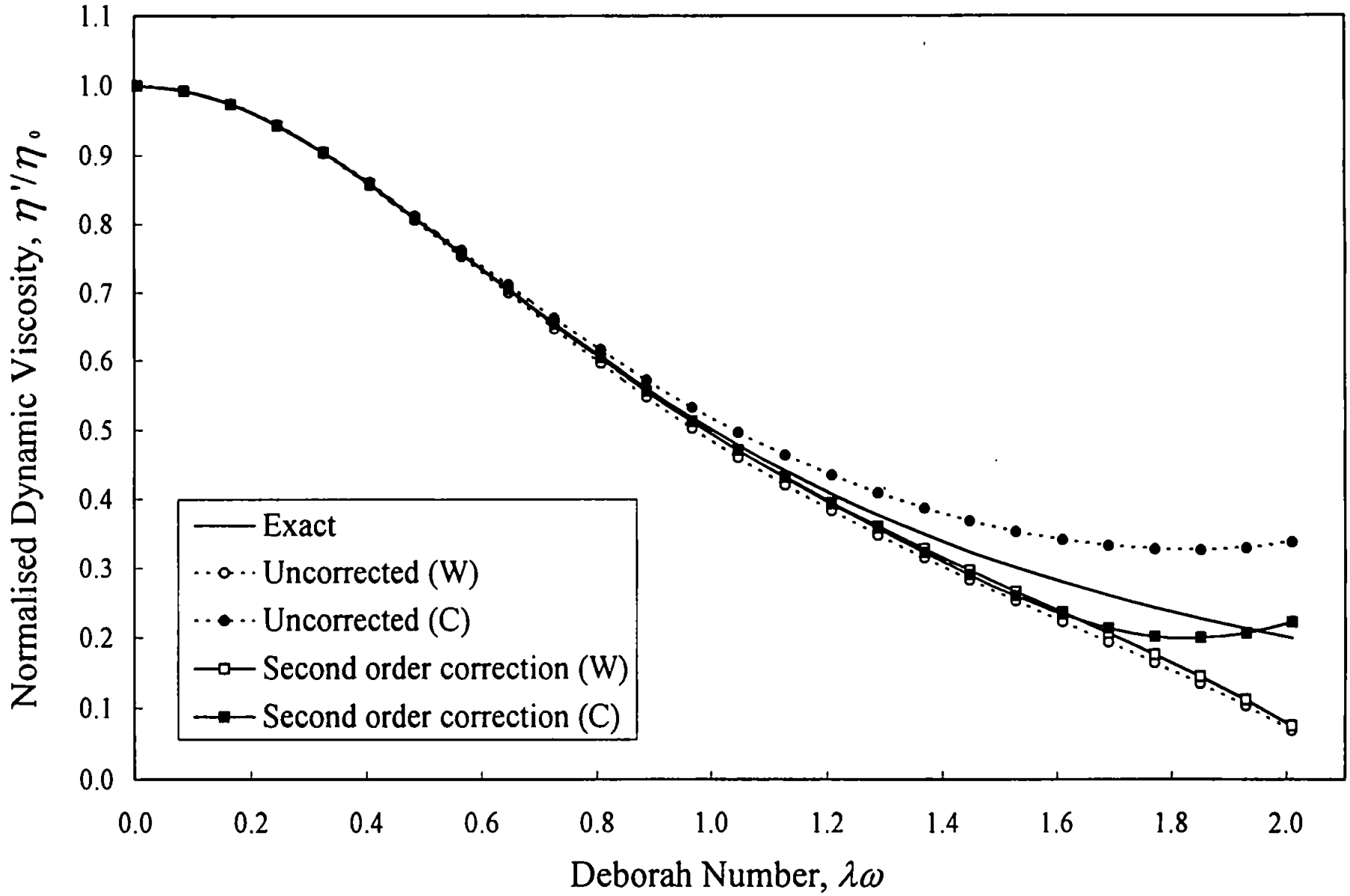
Normalised Dynamic Viscosity, η'/η_o
1.1
1.0
0.9
0.8
0.7
0.6
0.5
0.4
0.3
0.2
0.1
0.0
0.0
0.2
0.4
0.6
0.8
1.0
1.2
1.4
1.6
1.8
2.0
Deborah Number, $\lambda\omega$
Exact
Uncorrected (W)
Uncorrected (C)
Second order correction (W)
Second order correction (C)

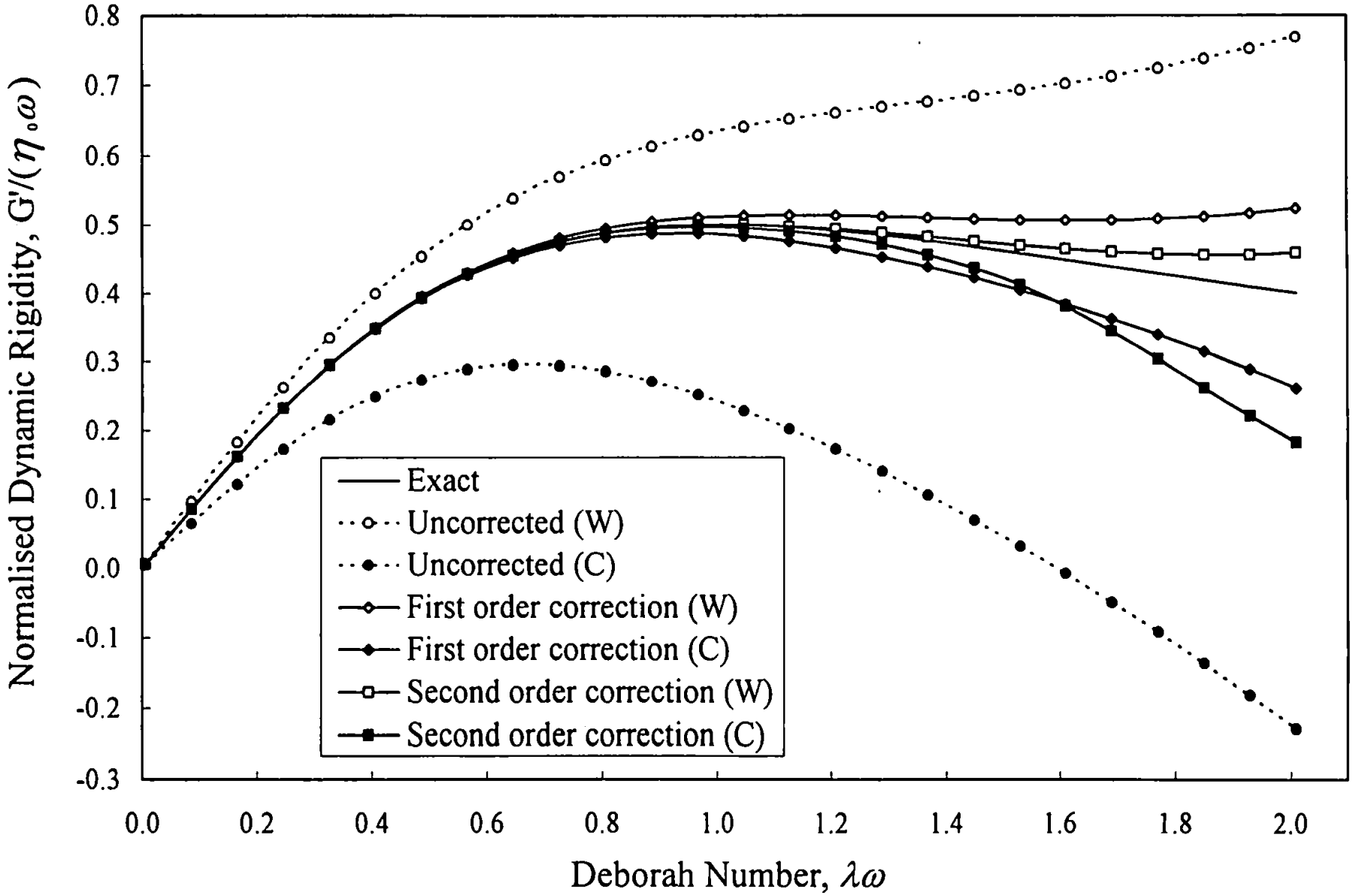
Normalised Dynamic Rigidity, $G'/(\eta_o\omega)$
0.8
0.7
0.6
0.5
0.4
0.3
0.2
0.1
0.0
-0.1
-0.2
-0.3
0.0
0.2
0.4
0.6
0.8
1.0
1.2
1.4
1.6
1.8
2.0
Deborah Number, $\lambda\omega$
Exact
Uncorrected (W)
Uncorrected (C)
First order correction (W)
First order correction (C)
Second order correction (W)
Second order correction (C)

Figure 6.1

The recessed concentric cylinder geometry for the CSR controlled stress rheometer.

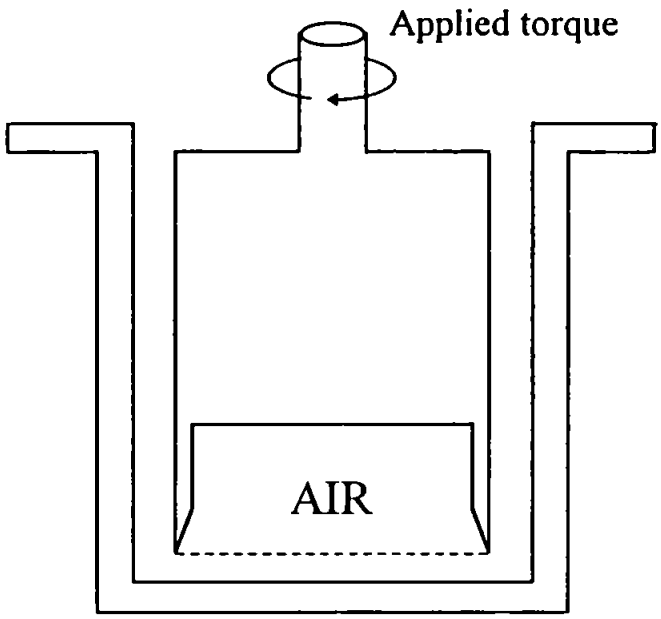
Applied torque
AIR

Figure 6.2

Schematic diagram of a recessed concentric cylinder geometry.

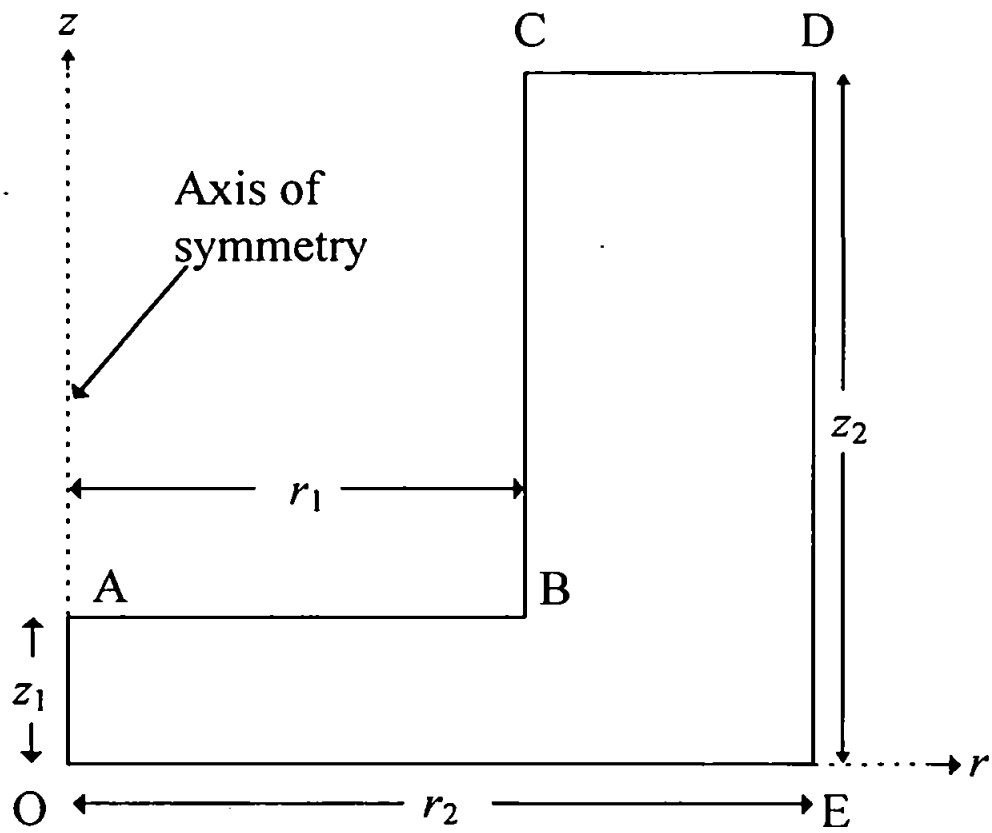
z
C
D
Axis of
symmetry
z_2
r_1
A
B
z_1
r
O
r_2
E

Figures 6.6(a) and 6.6(b)

Primary flow velocity contours and secondary flow streamlines for a Newtonian fluid in a wide gap geometry at $R_e = 1$ (1·008% of the critical Reynolds number).

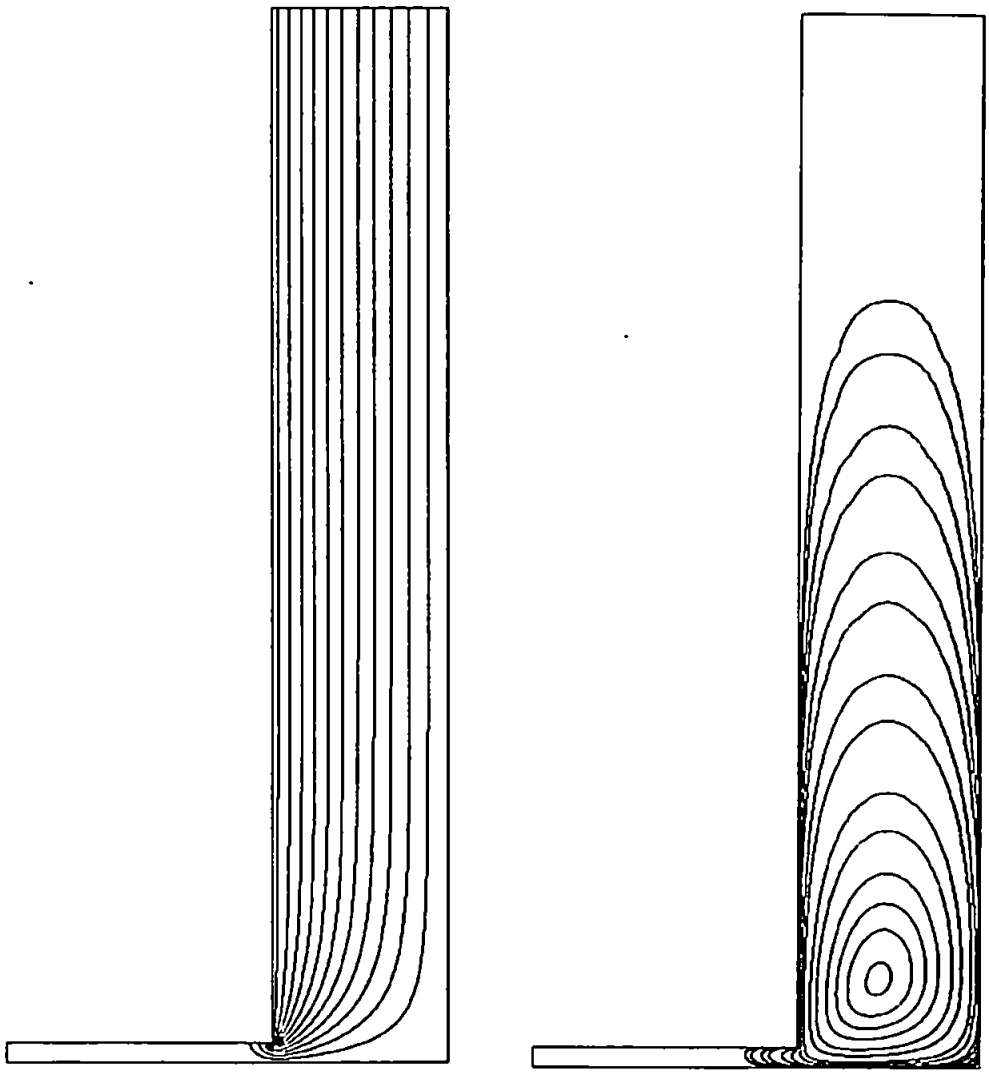

Figures 6.7(a) and 6.7(b)

Primary flow velocity contours and secondary flow streamlines for a Newtonian fluid in a wide gap geometry at $R_e = 93 \cdot 75$ (94·47% of the critical Reynolds number).

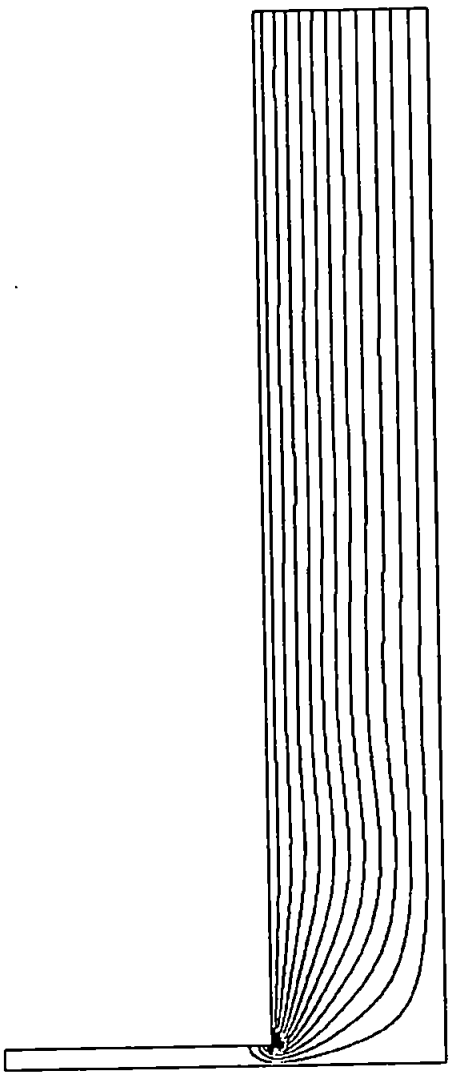

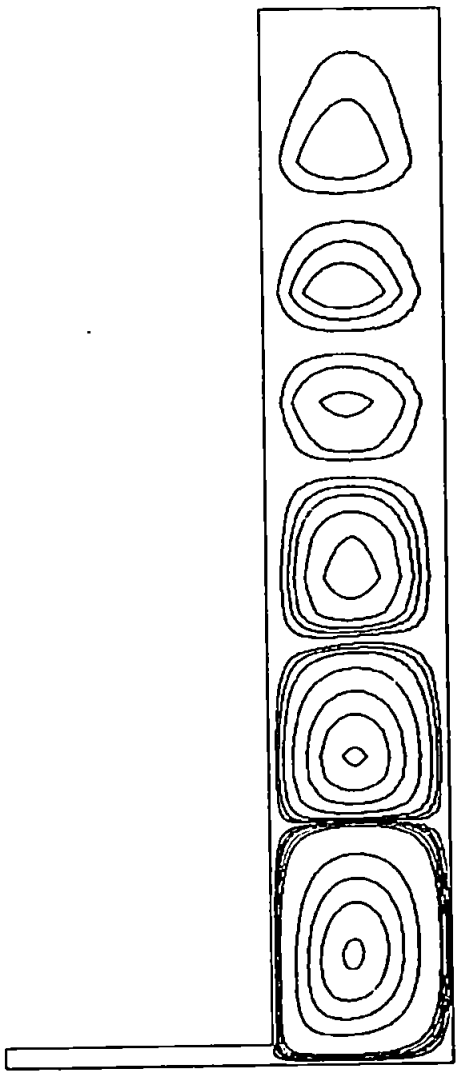

Figure 6.8

Normalised shear stress distribution on inner cylinder wall for a Newtonian fluid in the CSR geometries at zero Reynolds number.

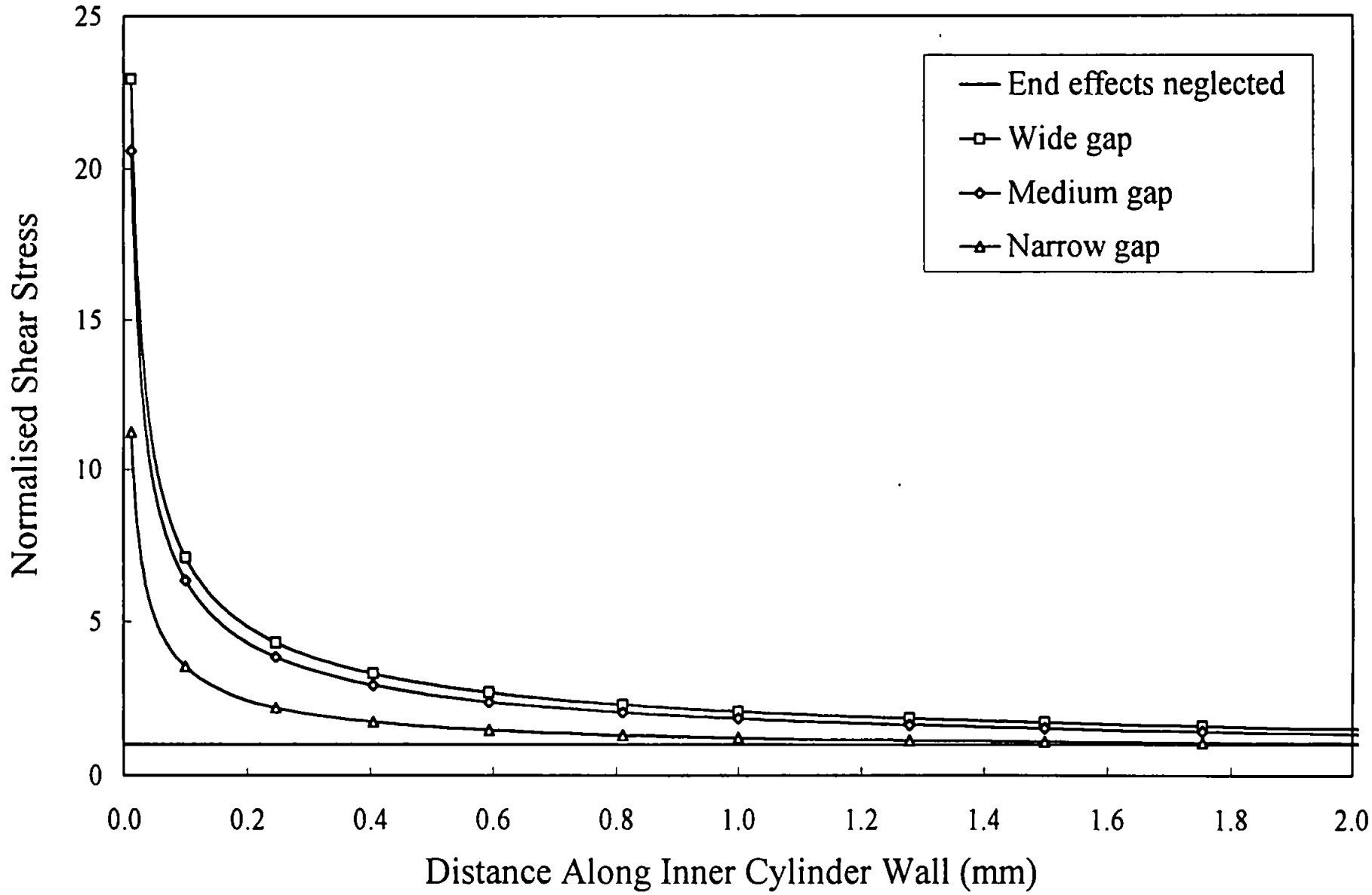
End effects neglected
Wide gap
Medium gap
Narrow gap
Normalised Shear Stress
Distance Along Inner Cylinder Wall (mm)
0
5
10
15
20
25
0.0
0.2
0.4
0.6
0.8
1.0
1.2
1.4
1.6
1.8
2.0

Figure 6.9

Normalised shear stress distribution on inner cylinder wall for various power law fluids in the wide gap geometry at zero Reynolds number.

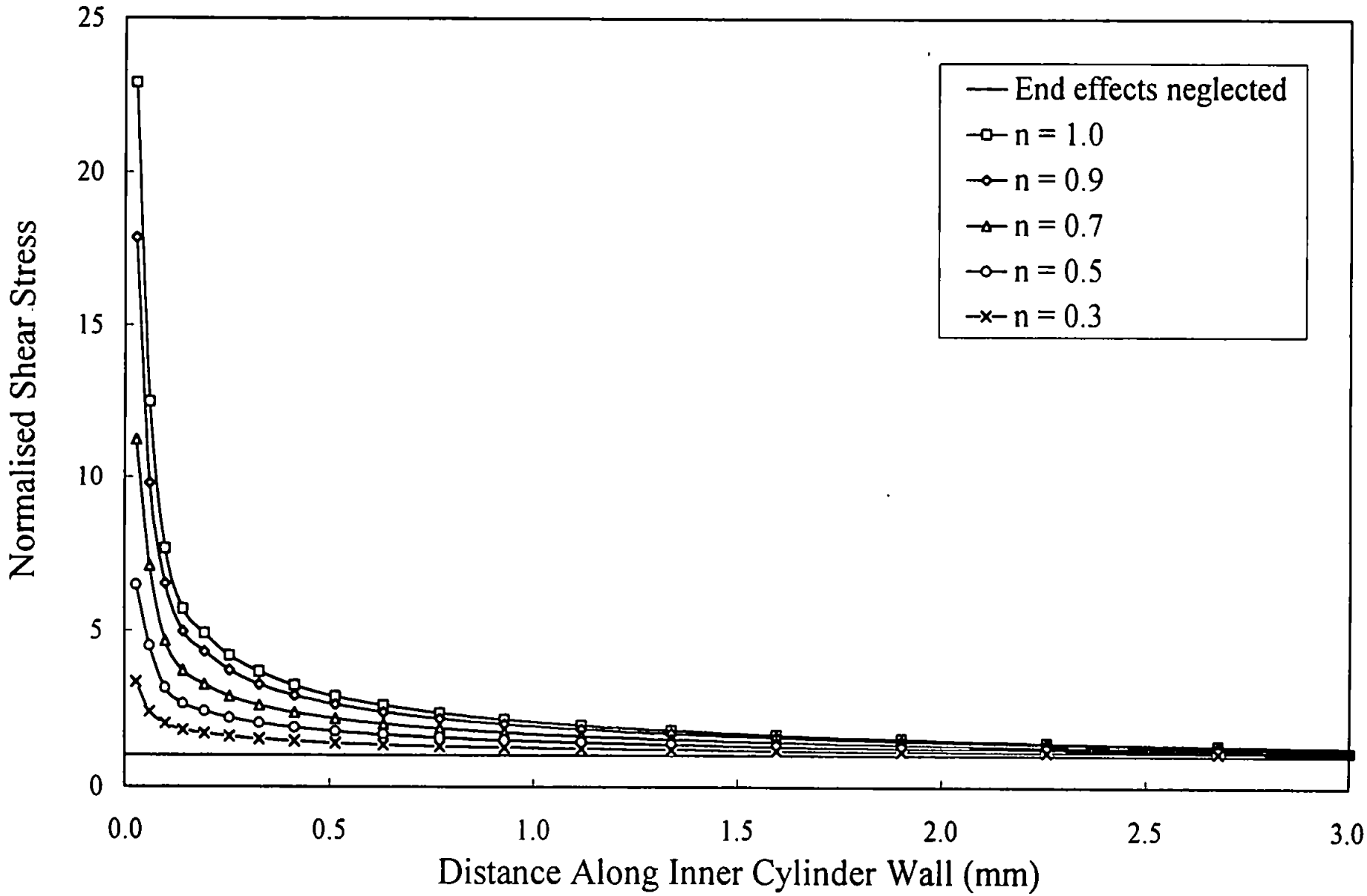
End effects neglected
n = 1.0
n = 0.9
n = 0.7
n = 0.5
n = 0.3
Normalised Shear Stress
Distance Along Inner Cylinder Wall (mm)
0
5
10
15
20
25
0.0
0.5
1.0
1.5
2.0
2.5
3.0

Figure 6.10

Percentage error in torque vs. $(1-n)$ for the CSR geometries at zero Reynolds number.

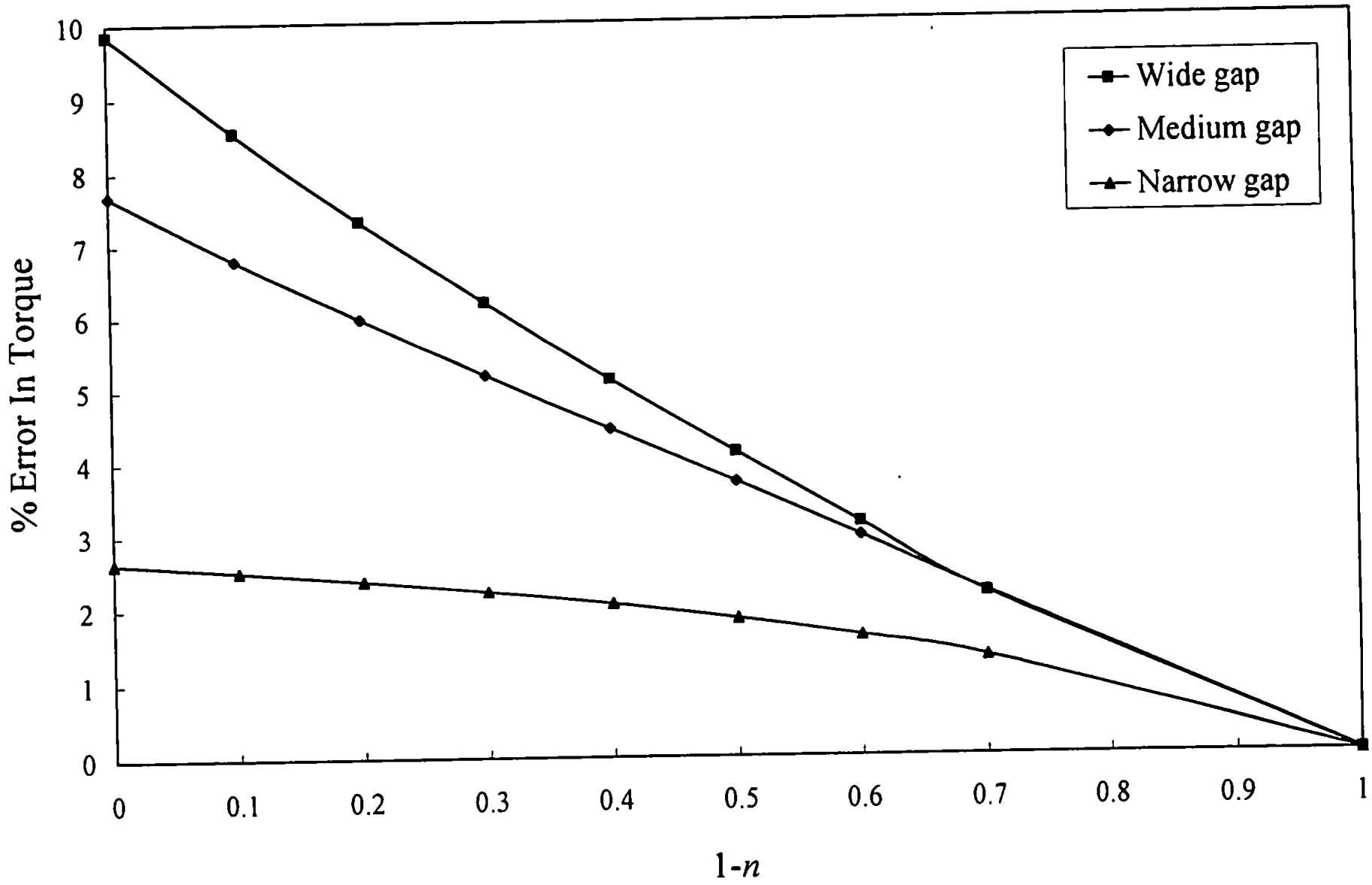
% Error In Torque
10
9
8
7
6
5
4
3
2
1
0
0
0.1
0.2
0.3
0.4
0.5
0.6
0.7
0.8
0.9
1
1-n
Wide gap
Medium gap
Narrow gap

Figure 6.11

Percentage error in torque for a Newtonian fluid vs. % critical Reynolds number, for the second order perturbation theory and Polyflow with full fluid inertia effects.

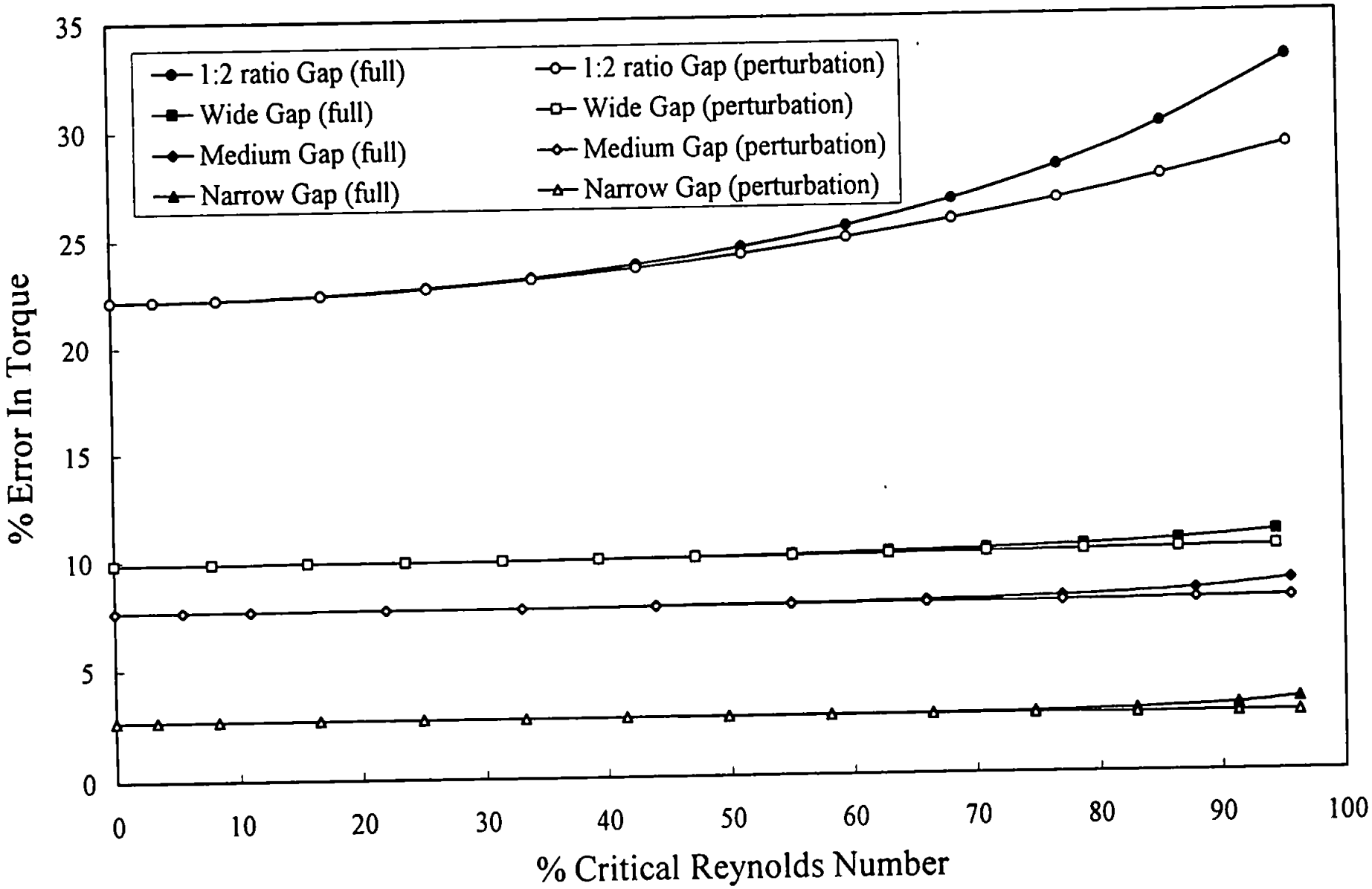
1:2 ratio Gap (full)
Wide Gap (full)
Medium Gap (full)
Narrow Gap (full)
1:2 ratio Gap (perturbation)
Wide Gap (perturbation)
Medium Gap (perturbation)
Narrow Gap (perturbation)
% Error In Torque
% Critical Reynolds Number
0
5
10
15
20
25
30
35
0
10
20
30
40
50
60
70
80
90
100

Figure 6.12

Percentage error in Newtonian shear viscosity prediction vs. % critical Reynolds number for the 1:2 ratio gap geometry.

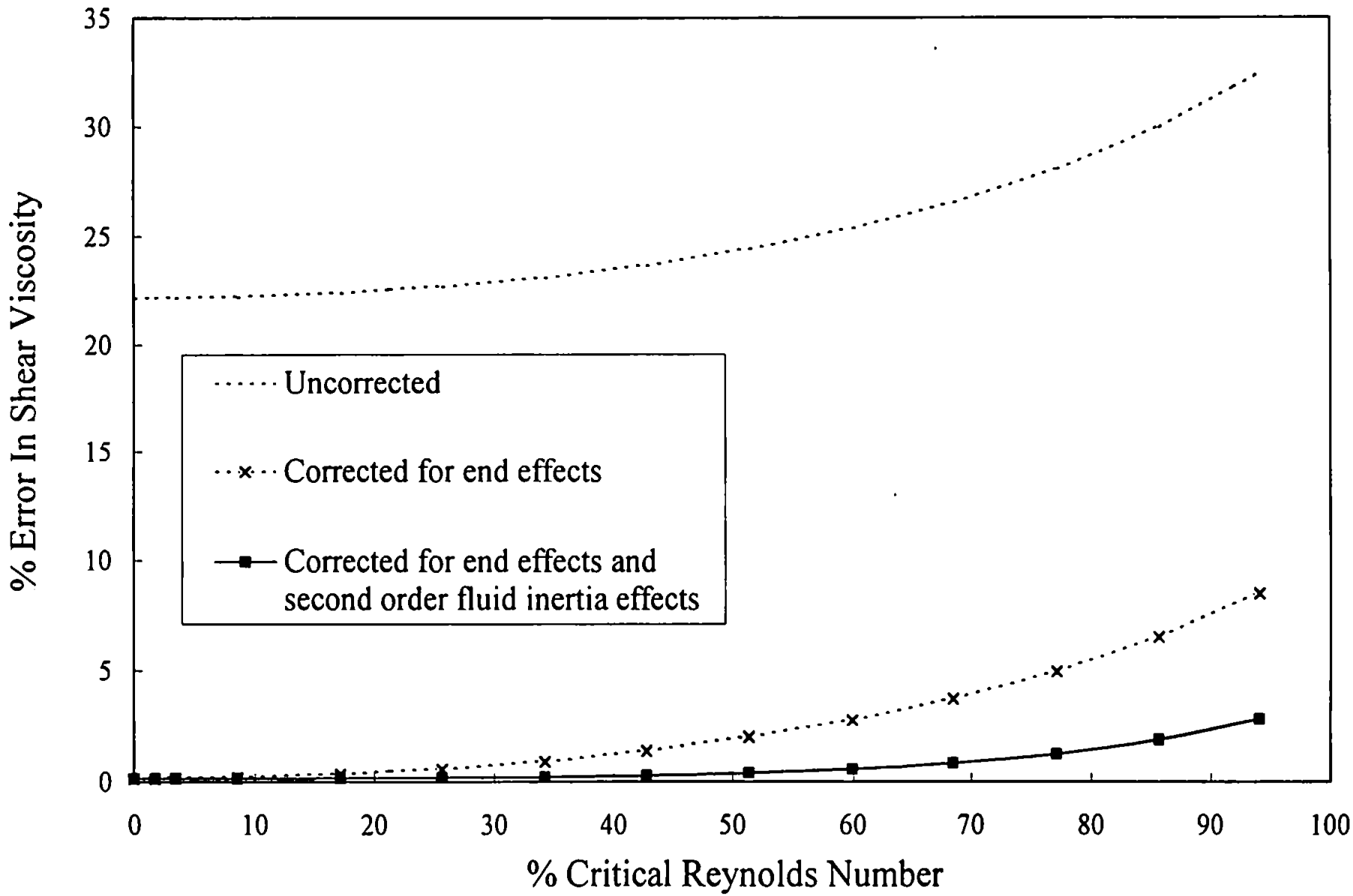
35
30
25
20
15
10
5
0
% Error In Shear Viscosity
Uncorrected
Corrected for end effects
Corrected for end effects and second order fluid inertia effects
0
10
20
30
40
50
60
70
80
90
100
% Critical Reynolds Number

Figures 7.2(a) and 7.2(b)

Primary flow velocity contours and secondary flow streamlines for a Newtonian fluid in a wide gap geometry on the Weissenberg rheogoniometer when $R_e = 1$.

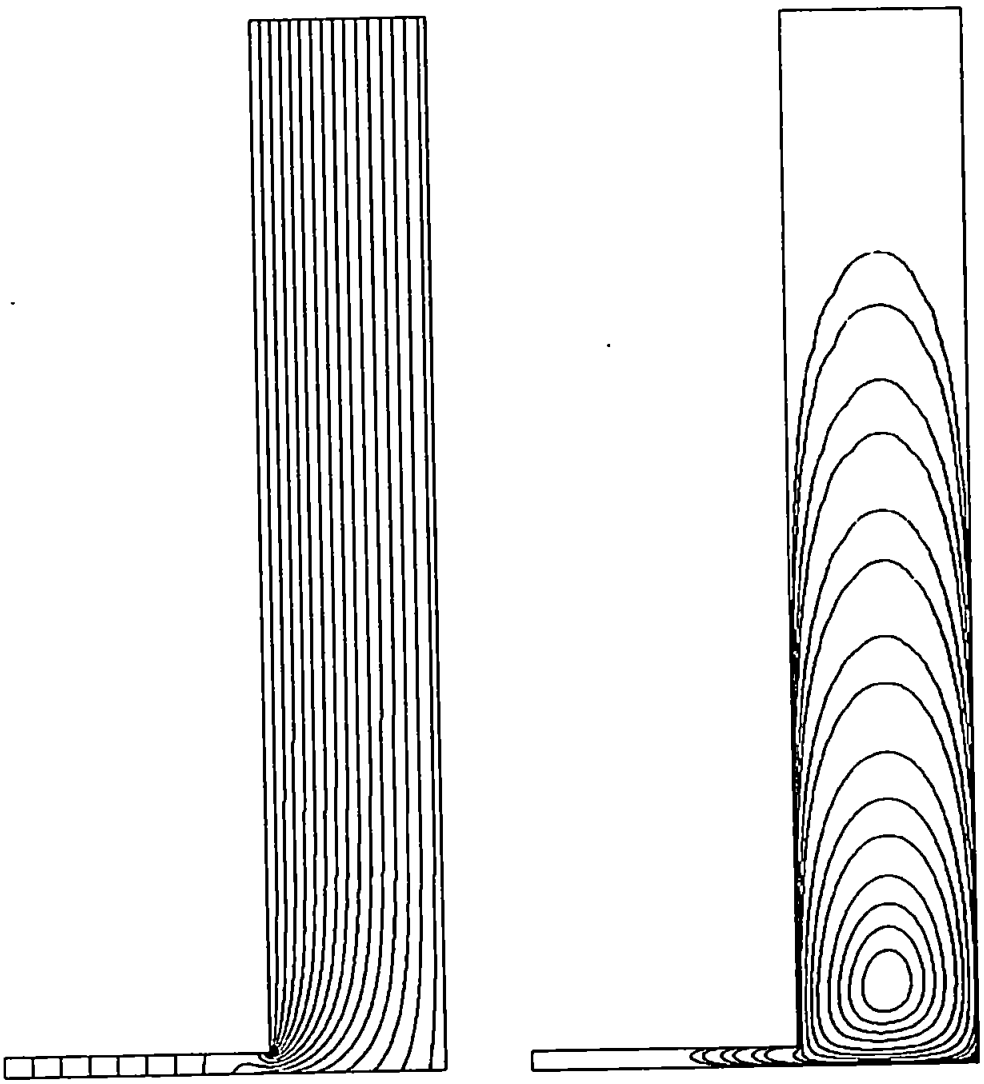

Figures 7.3(a) and 7.3(b)

Primary flow velocity contours and secondary flow streamlines for a Newtonian fluid in a wide gap geometry on the Weissenberg rheogoniometer when $R_e = 3445$.

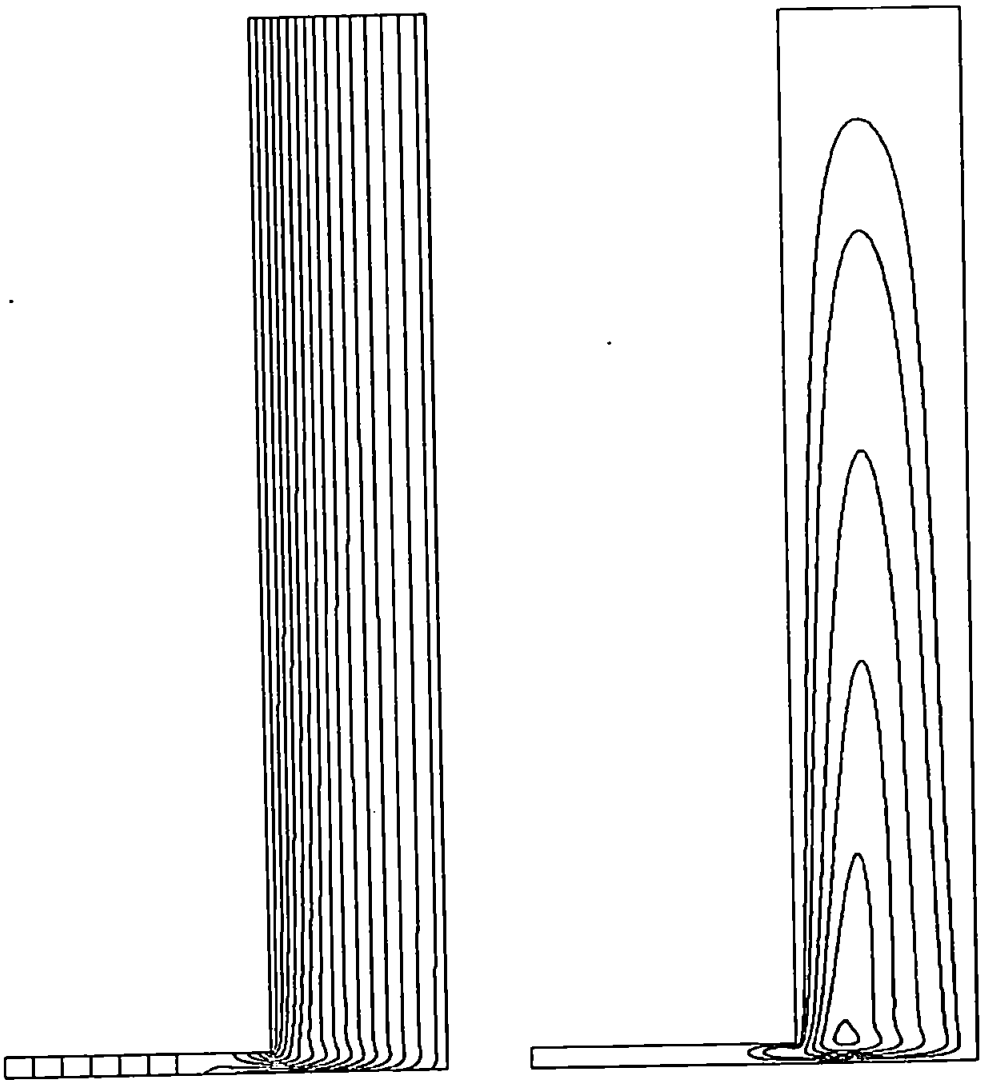

Figure 7.4

Percentage error in torque vs. Reynolds number for Newtonian fluids in the CSR geometries on the Weissenberg rheogoniometer.

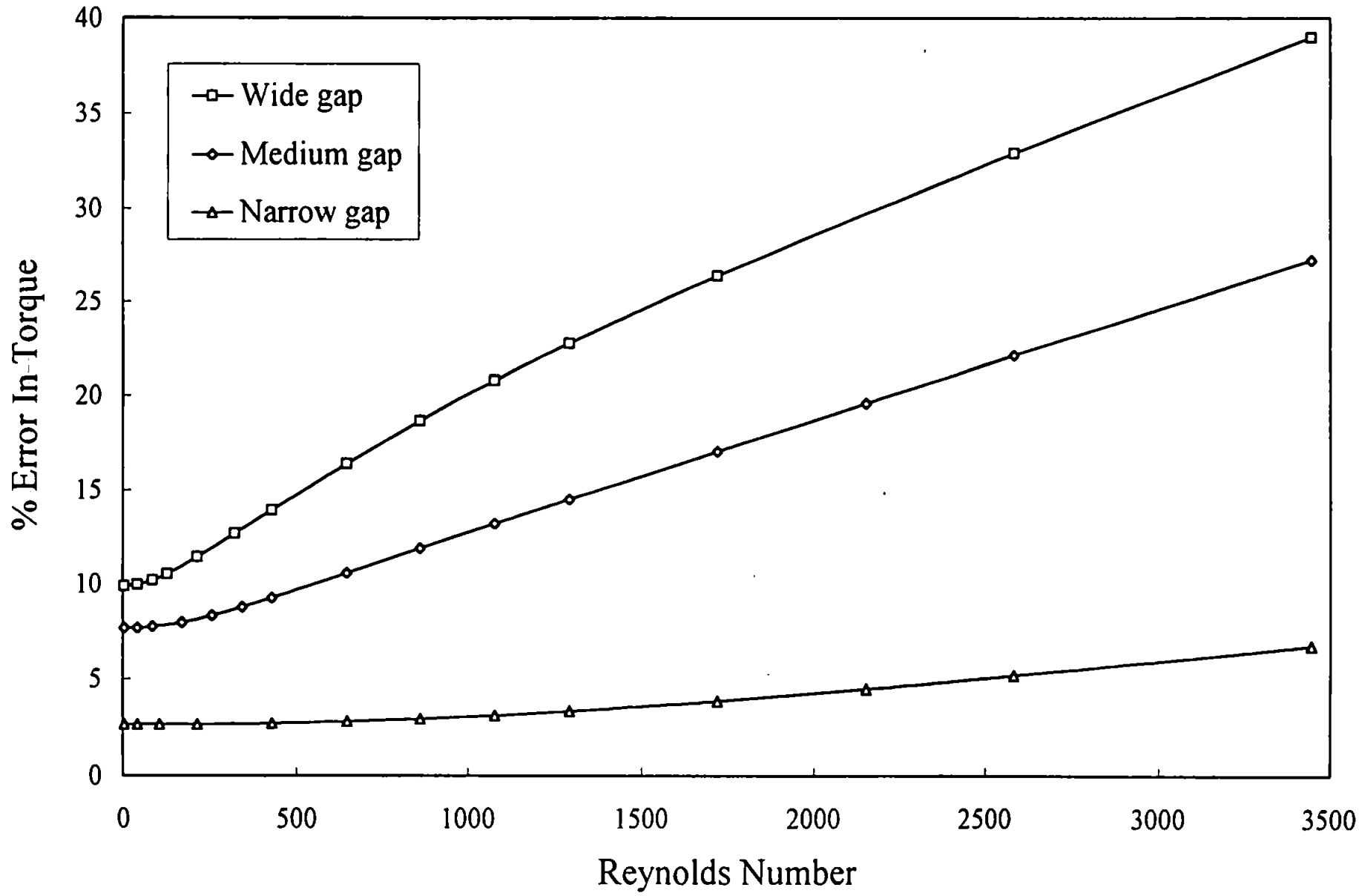
Wide gap
Medium gap
Narrow gap
% Error In Torque
Reynolds Number
0
5
10
15
20
25
30
35
40
0
500
1000
1500
2000
2500
3000
3500

Figure 7.5

Percentage error in torque vs. Reynolds number for various power law fluids in the wide gap geometry on a Weissenberg rheogoniometer.

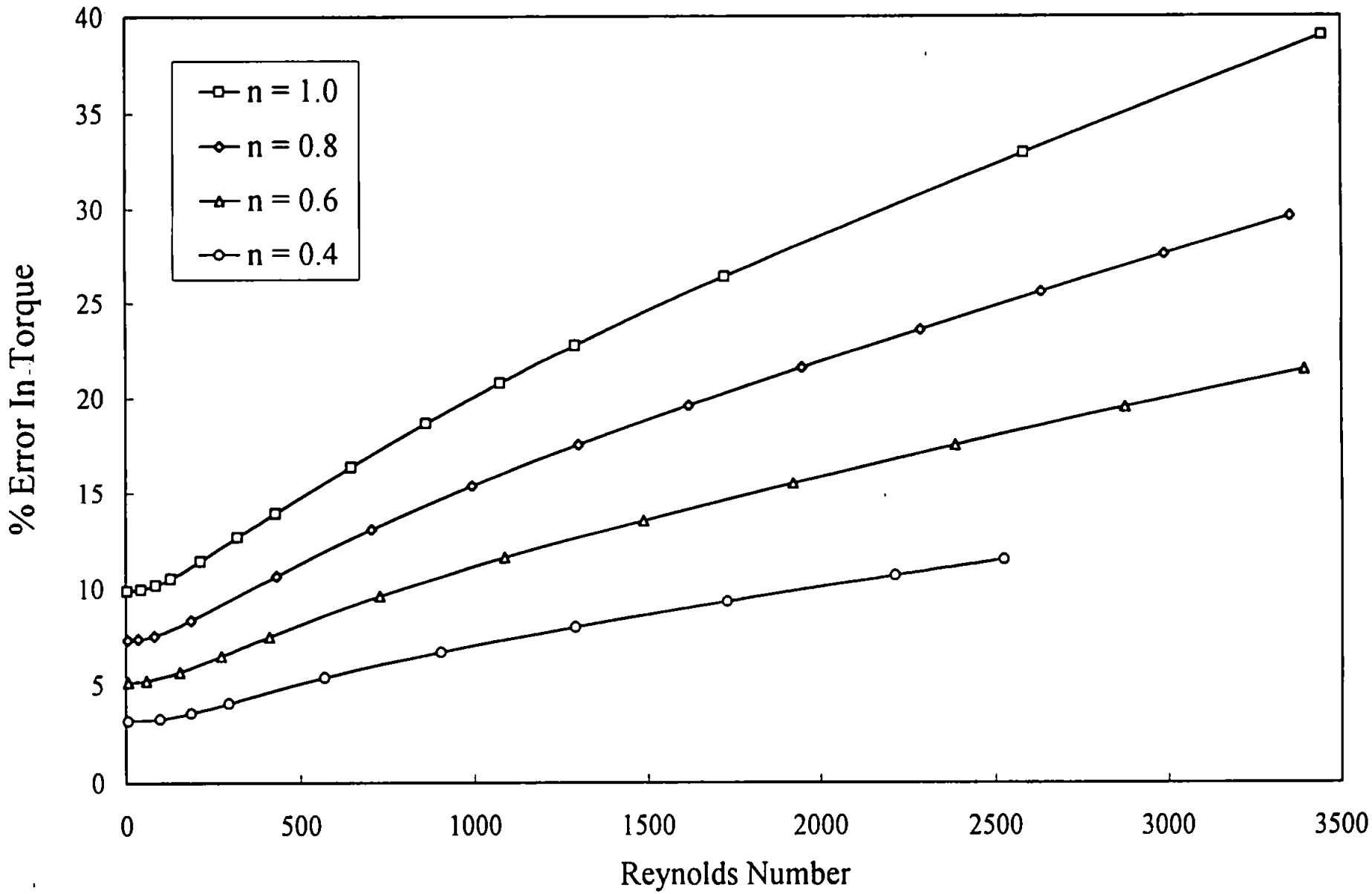
n = 1.0
n = 0.8
n = 0.6
n = 0.4
% Error In Torque
Reynolds Number
0
5
10
15
20
25
30
35
40
0
500
1000
1500
2000
2500
3000
3500

Figure 7.6

Percentage error in torque vs. Reynolds number for various power law fluids in the medium gap geometry on a Weissenberg rheogoniometer.

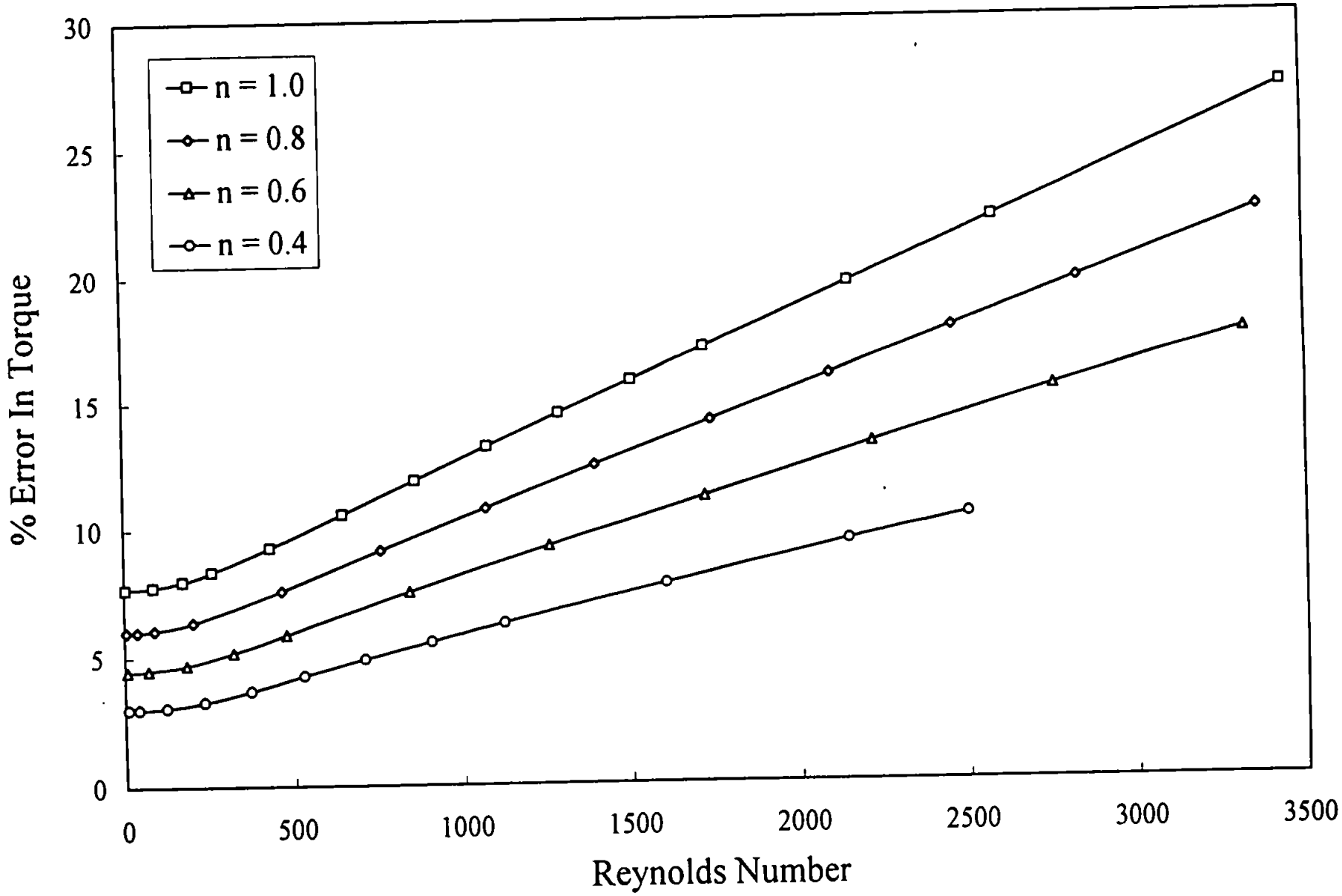
n = 1.0
n = 0.8
n = 0.6
n = 0.4
% Error In Torque
Reynolds Number
0
5
10
15
20
25
30
0
500
1000
1500
2000
2500
3000
3500

Figure 7.7

Percentage error in torque vs. Reynolds number for various power law fluids in the narrow gap geometry on a Weissenberg rheogoniometer.

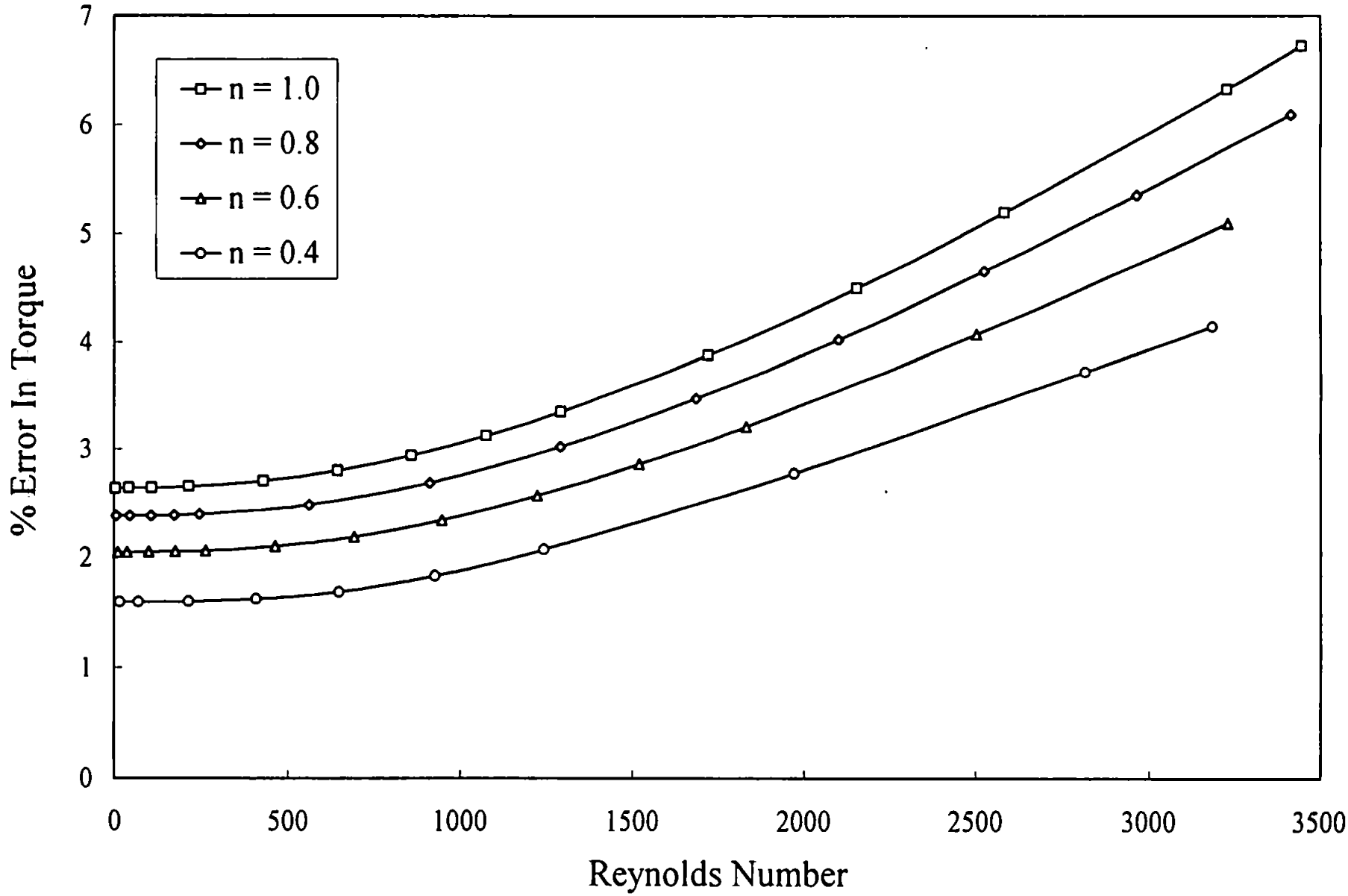
n = 1.0
n = 0.8
n = 0.6
n = 0.4
% Error In Torque
Reynolds Number
0
1
2
3
4
5
6
7
0
500
1000
1500
2000
2500
3000
3500

Figure 7.8

Percentage error in Newtonian shear viscosity prediction vs. Reynolds number for the wide gap geometry on a Weissenberg rheogoniometer.

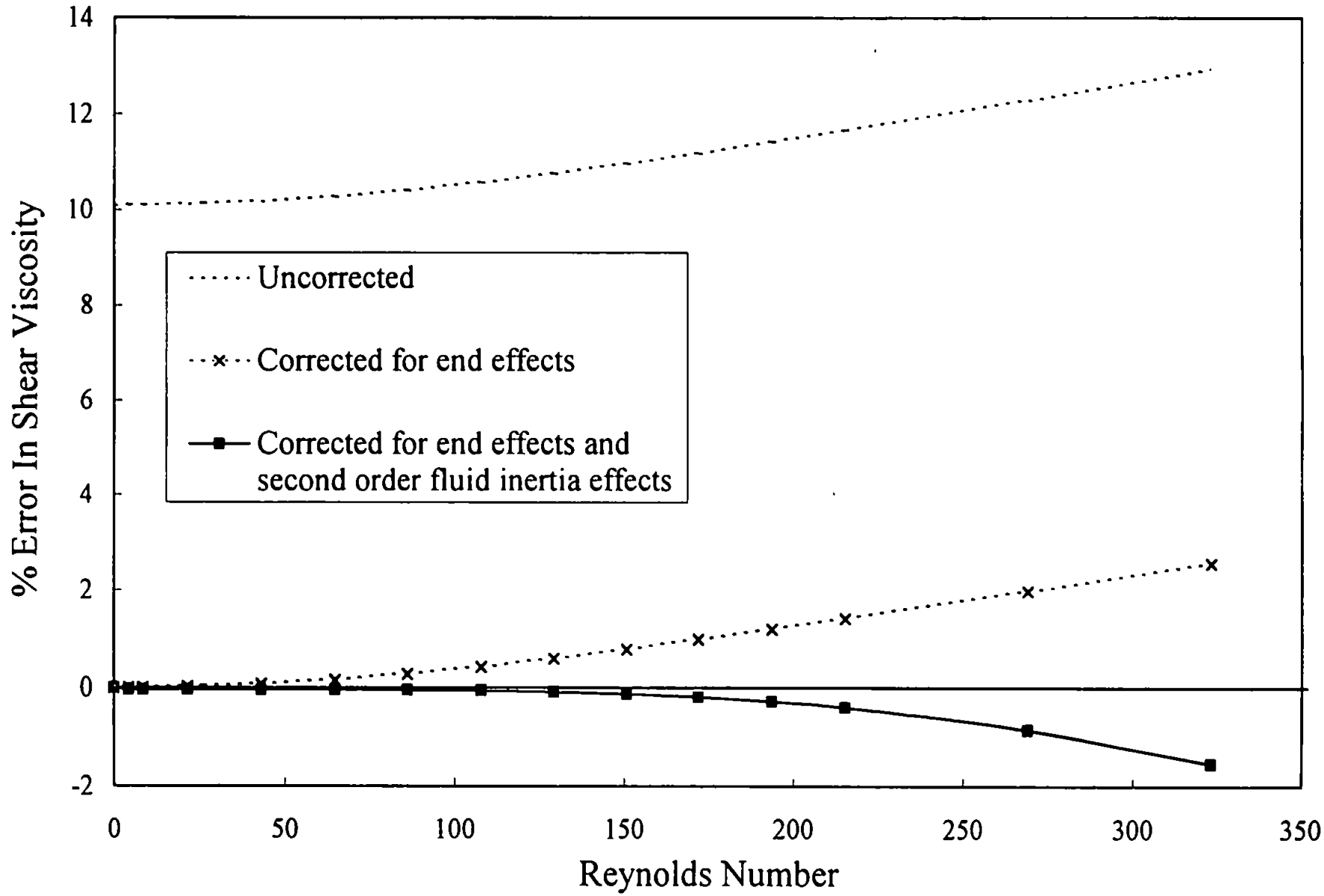
14
12
10
8
6
4
2
0
-2
% Error In Shear Viscosity
Uncorrected
Corrected for end effects
Corrected for end effects and second order fluid inertia effects
0
50
100
150
200
250
300
350
Reynolds Number

Figure 7.9

Percentage error in Newtonian shear viscosity prediction vs. Reynolds number for the medium gap geometry on a Weissenberg rheogoniometer.

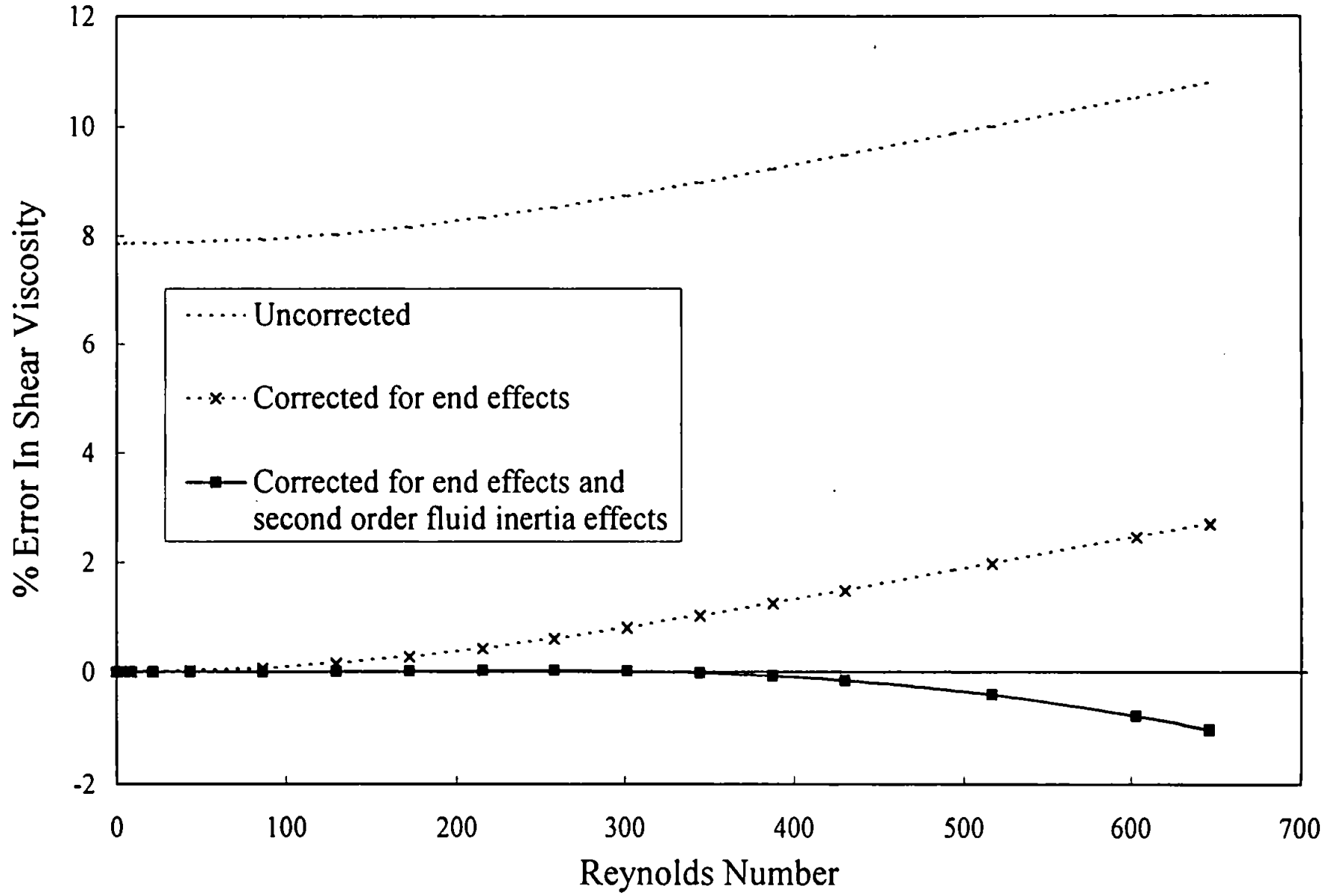
12
10
8
6
4
2
0
-2
% Error In Shear Viscosity
Uncorrected
Corrected for end effects
Corrected for end effects and second order fluid inertia effects
0
100
200
300
400
500
600
700
Reynolds Number

Figure 7.10

Percentage error in Newtonian shear viscosity prediction vs. Reynolds number for the narrow gap geometry on a Weissenberg rheogoniometer.

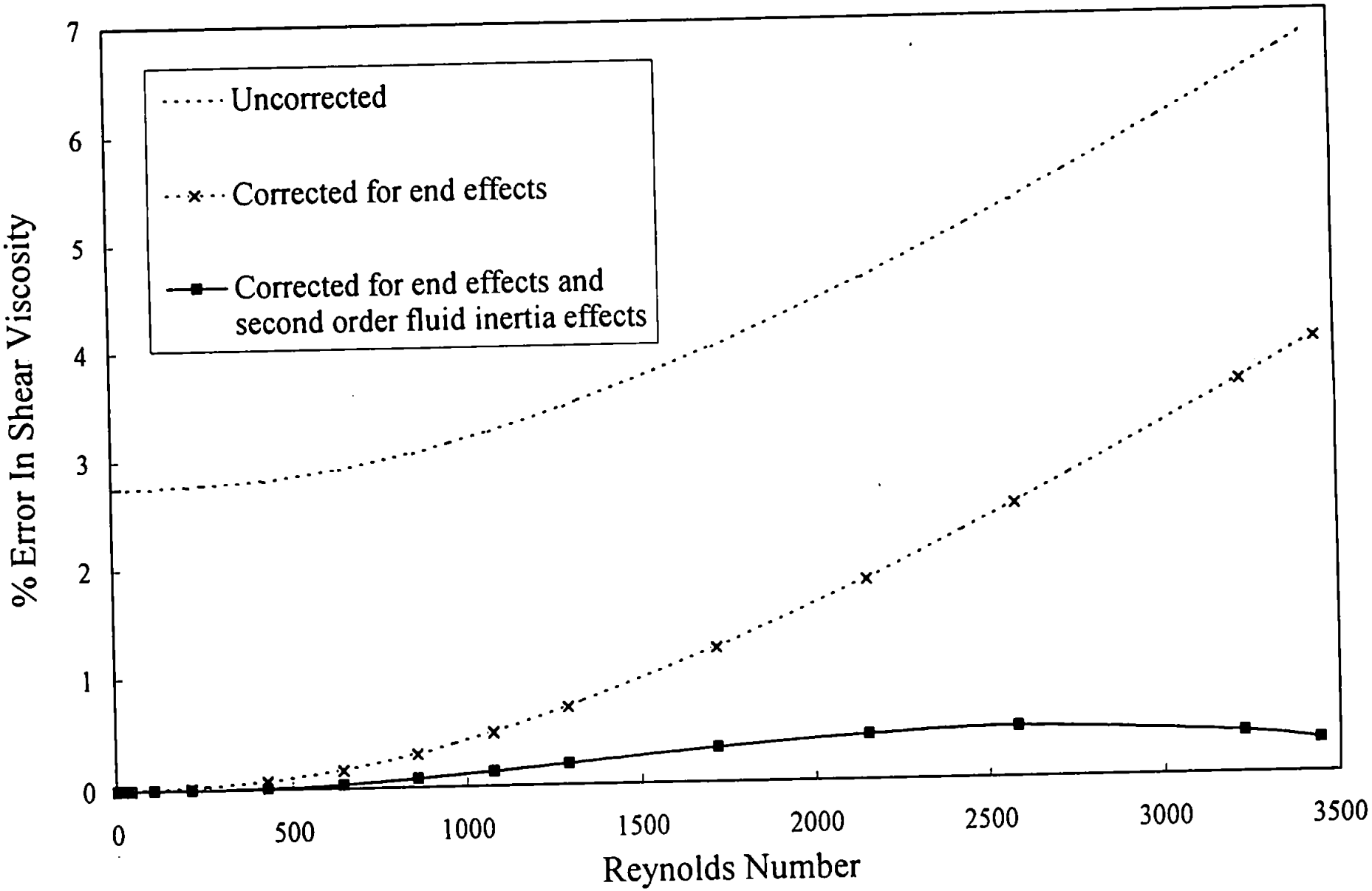
Uncorrected
Corrected for end effects
Corrected for end effects and second order fluid inertia effects
% Error In Shear Viscosity
Reynolds Number
0
1
2
3
4
5
6
7
0
500
1000
1500
2000
2500
3000
3500

Figures 8.1 and 8.2

Oscillatory shear flow simulations for a CSR controlled stress rheometer.

Normalised dynamic viscosity and dynamic rigidity vs. normalised frequency for a Newtonian fluid in the wide gap geometry.

——— Exact , ····· Uncorrected (f_0=1, f_1=0, f_2=0),
····×···· Corrected for end effects (f_0=0·908, f_1=0, f_2=0),
—◇— Corrected for first order fluid inertia effects (f_0=1, f_1=6·811×10^{-2}, f_2=0),
—◆— Corrected for end effects and first order fluid inertia effects (f_0=0·908, f_1=5·932×10^{-2}, f_2=0),
—□— Corrected for second order fluid inertia effects (f_0=1, f_1=6·811×10^{-2}, f_2=1·919×10^{-3}),
—■— Corrected for end effects and second order fluid inertia effects (f_0=0·908, f_1=5·932×10^{-2}, f_2=1·612×10^{-3}).

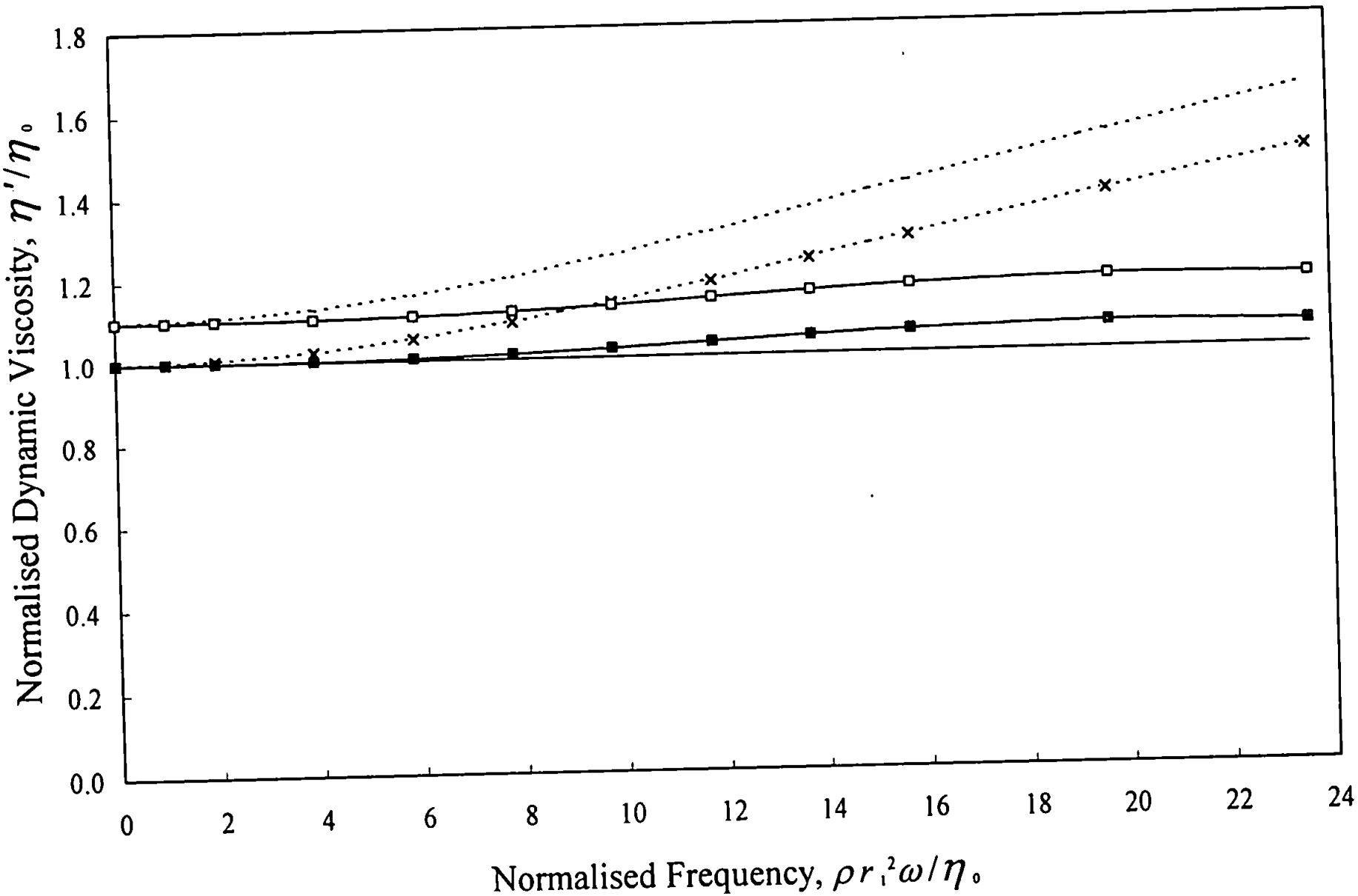
1.8
1.6
1.4
1.2
1.0
0.8
0.6
0.4
0.2
0.0
Normalised Dynamic Viscosity, η'/η_0
0
2
4
6
8
10
12
14
16
18
20
22
24
Normalised Frequency, $\rho r_1^2\omega/\eta_0$

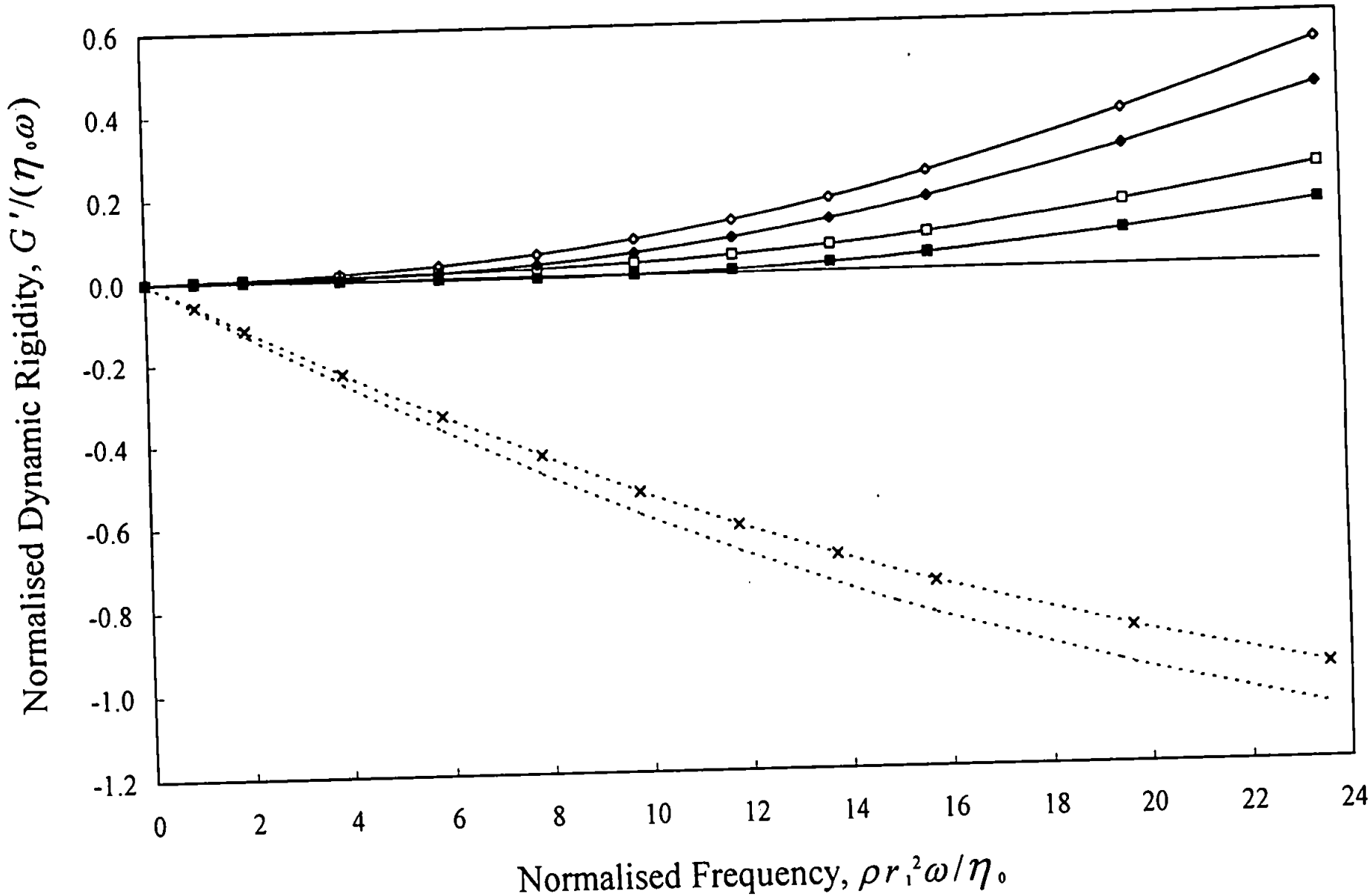
0.6
0.4
0.2
0.0
-0.2
-0.4
-0.6
-0.8
-1.0
-1.2
0
2
4
6
8
10
12
14
16
18
20
22
24
Normalised Dynamic Rigidity, $G'/(\eta_o\omega)$
Normalised Frequency, $\rho r_1^2\omega/\eta_o$

Figures 8.3 and 8.4

Oscillatory shear flow simulations for a CSR controlled stress rheometer.

Normalised dynamic viscosity and dynamic rigidity vs. normalised frequency for a Newtonian fluid in the medium gap geometry.

——— Exact , ····· Uncorrected (f_0=1, f_1=0, f_2=0),
····×···· Corrected for end effects (f_0=0·927, f_1=0, f_2=0),
—◇— Corrected for first order fluid inertia effects (f_0=1, f_1=3·016×10^{-2}, f_2=0),
—◆— Corrected for end effects and first order fluid inertia effects (f_0=0·927, f_1=2·725×10^{-2}, f_2=0),
—□— Corrected for second order fluid inertia effects (f_0=1, f_1=3·016×10^{-2}, f_2=2·918×10^{-4}),
—■— Corrected for end effects and second order fluid inertia effects (f_0=0·927, f_1=2·725×10^{-2}, f_2=2·576×10^{-4}).

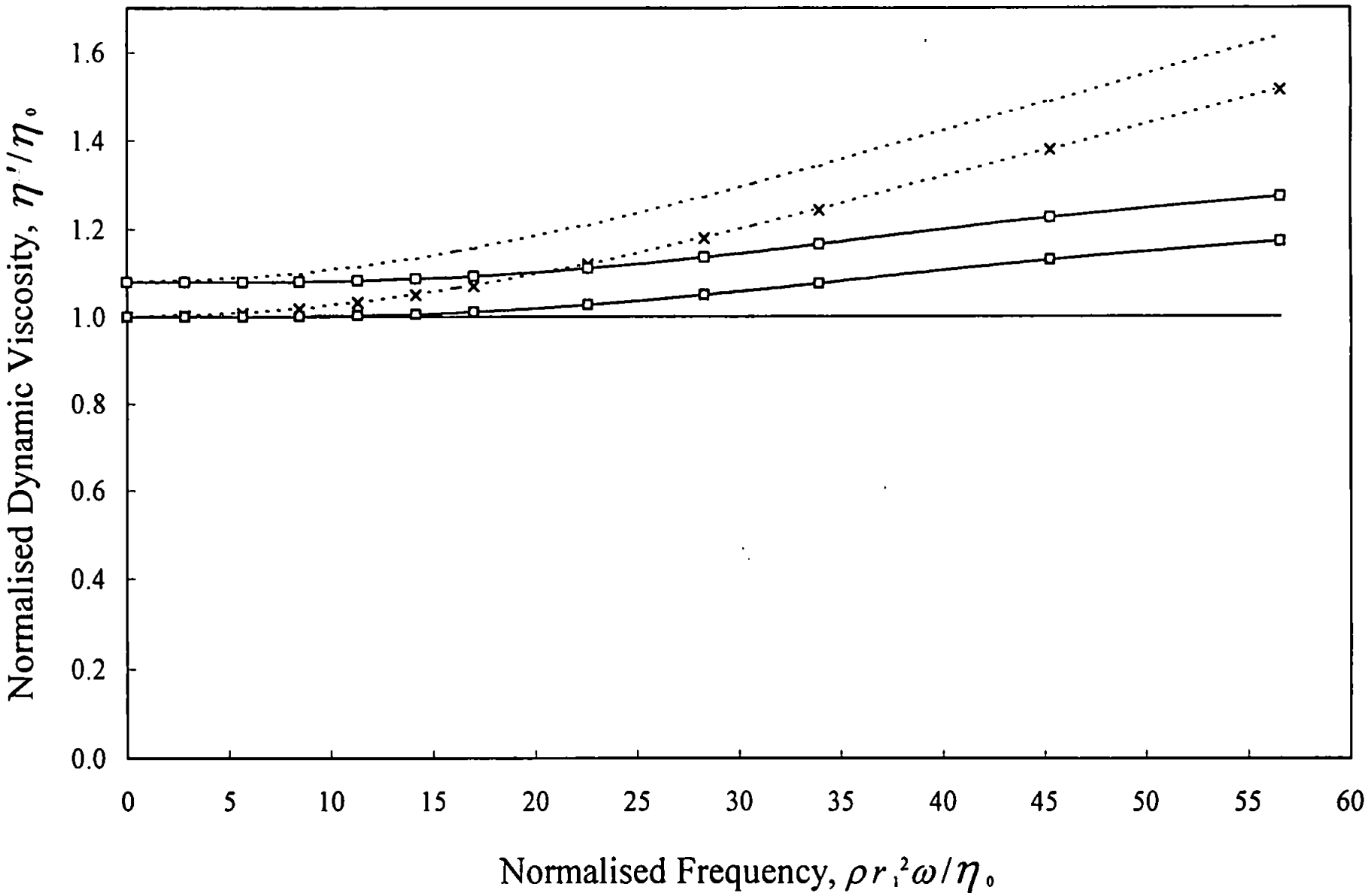
Normalised Dynamic Viscosity, η'/η_0
1.6
1.4
1.2
1.0
0.8
0.6
0.4
0.2
0.0
0
5
10
15
20
25
30
35
40
45
50
55
60
Normalised Frequency, $\rho r_1^2\omega/\eta_0$

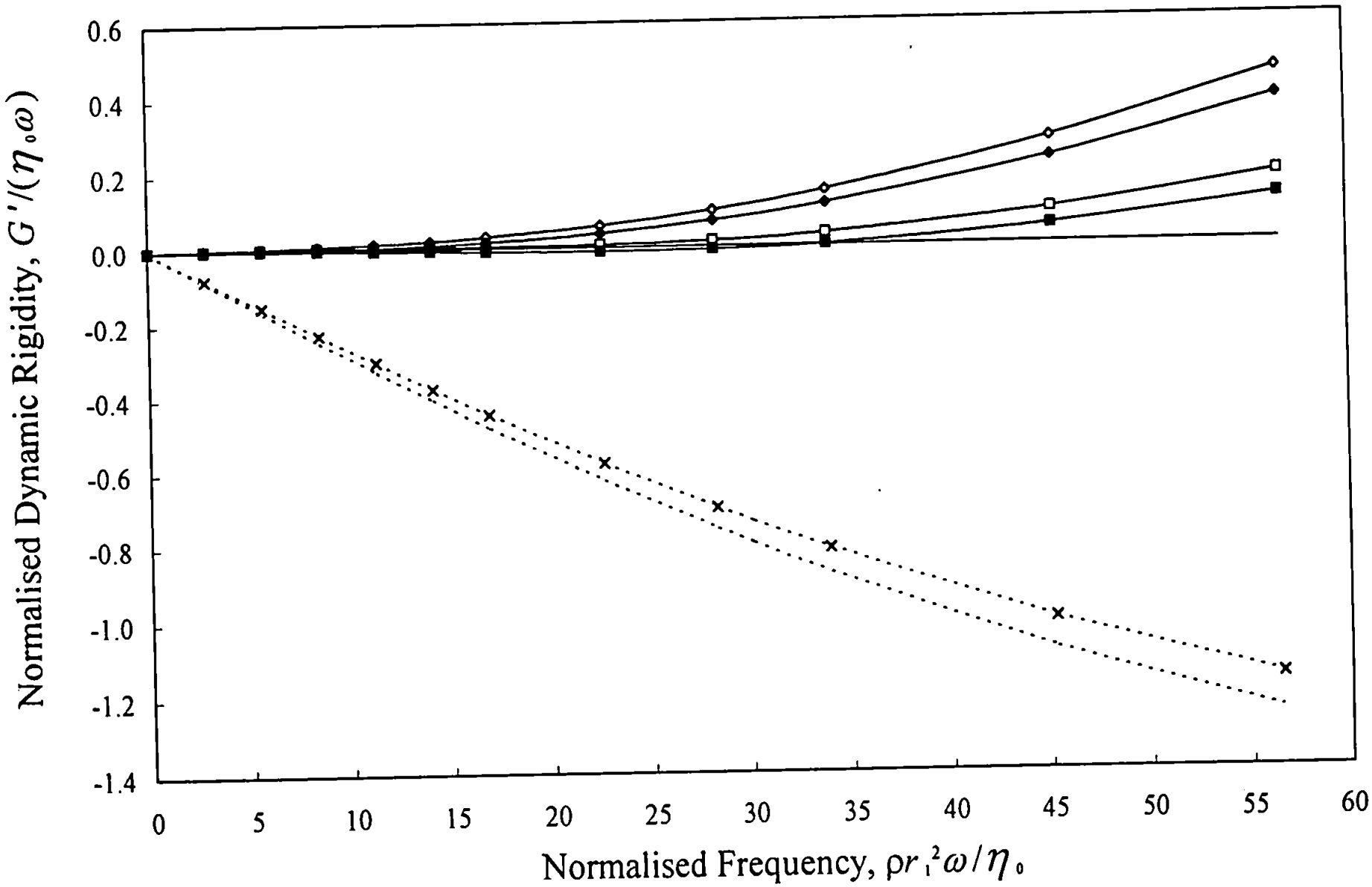
0.6
0.4
0.2
0.0
-0.2
-0.4
-0.6
-0.8
-1.0
-1.2
-1.4
0
5
10
15
20
25
30
35
40
45
50
55
60
Normalised Dynamic Rigidity, $G'/(\eta_0\omega)$
Normalised Frequency, $\rho r_1^2\omega/\eta_0$

Figures 8.5 and 8.6

Oscillatory shear flow simulations for a CSR controlled stress rheometer.

Normalised dynamic viscosity and dynamic rigidity vs. normalised frequency for a Newtonian fluid in the narrow gap geometry.

——— Exact , ····· Uncorrected (f_0=1, f_1=0, f_2=0),
····×···· Corrected for end effects (f_0=0·973, f_1=0, f_2=0),
—◇— Corrected for first order fluid inertia effects (f_0=1, f_1=4·152×10^{-3}, f_2=0),
—◆— Corrected for end effects and first order fluid inertia effects (f_0=0·973, f_1=4·021×10^{-3}, f_2=0),
—□— Corrected for second order fluid inertia effects (f_0=1, f_1=4·152×10^{-3}, f_2=4·088×10^{-6}),
—■— Corrected for end effects and second order fluid inertia effects (f_0=0·908, f_1=4·021×10^{-3}, f_2=3·937×10^{-6}).

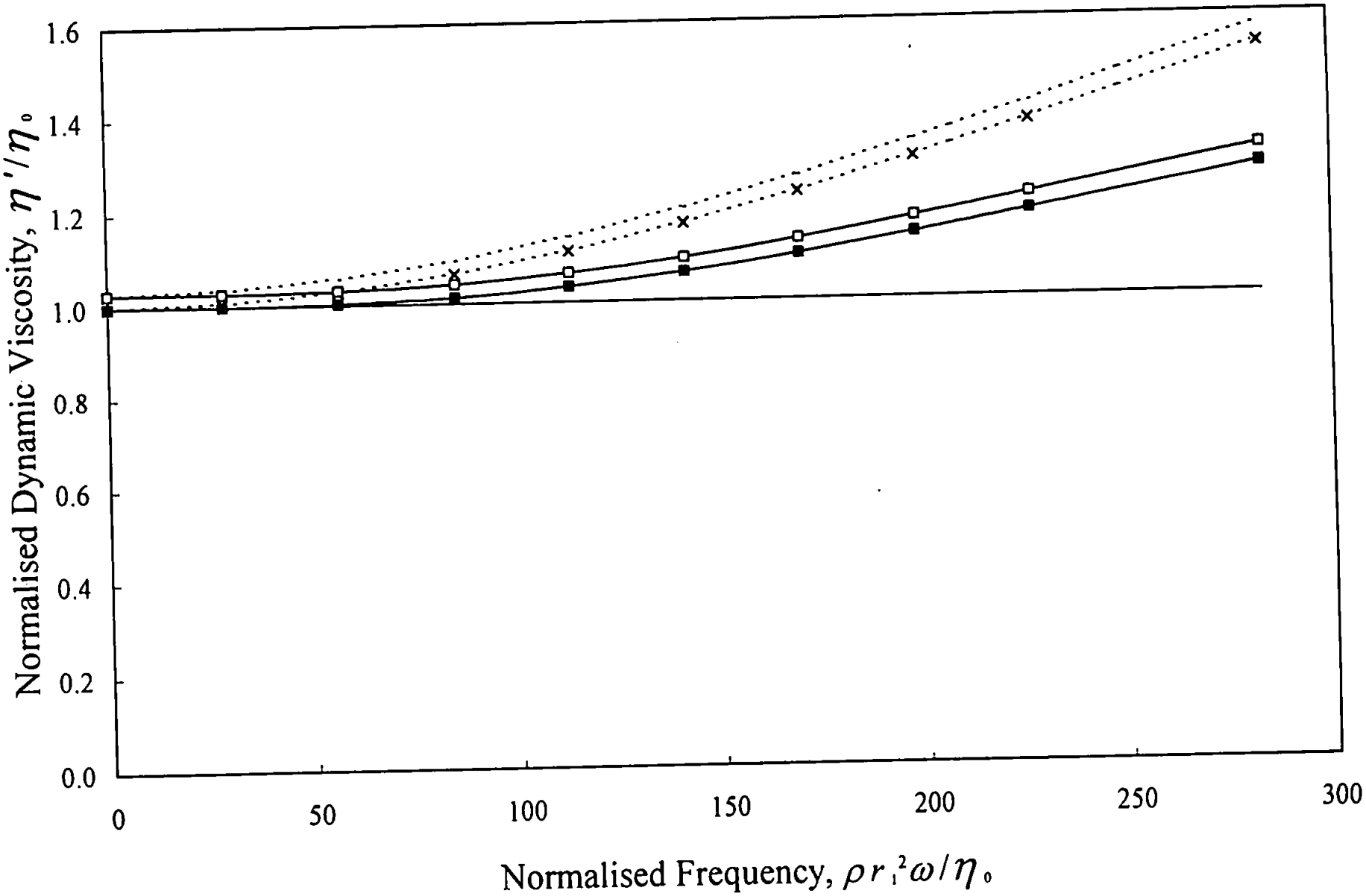
1.6
1.4
1.2
1.0
0.8
0.6
0.4
0.2
0.0
0
50
100
150
200
250
300
Normalised Dynamic Viscosity, η'/η_0
Normalised Frequency, $\rho r_1^2\omega/\eta_0$

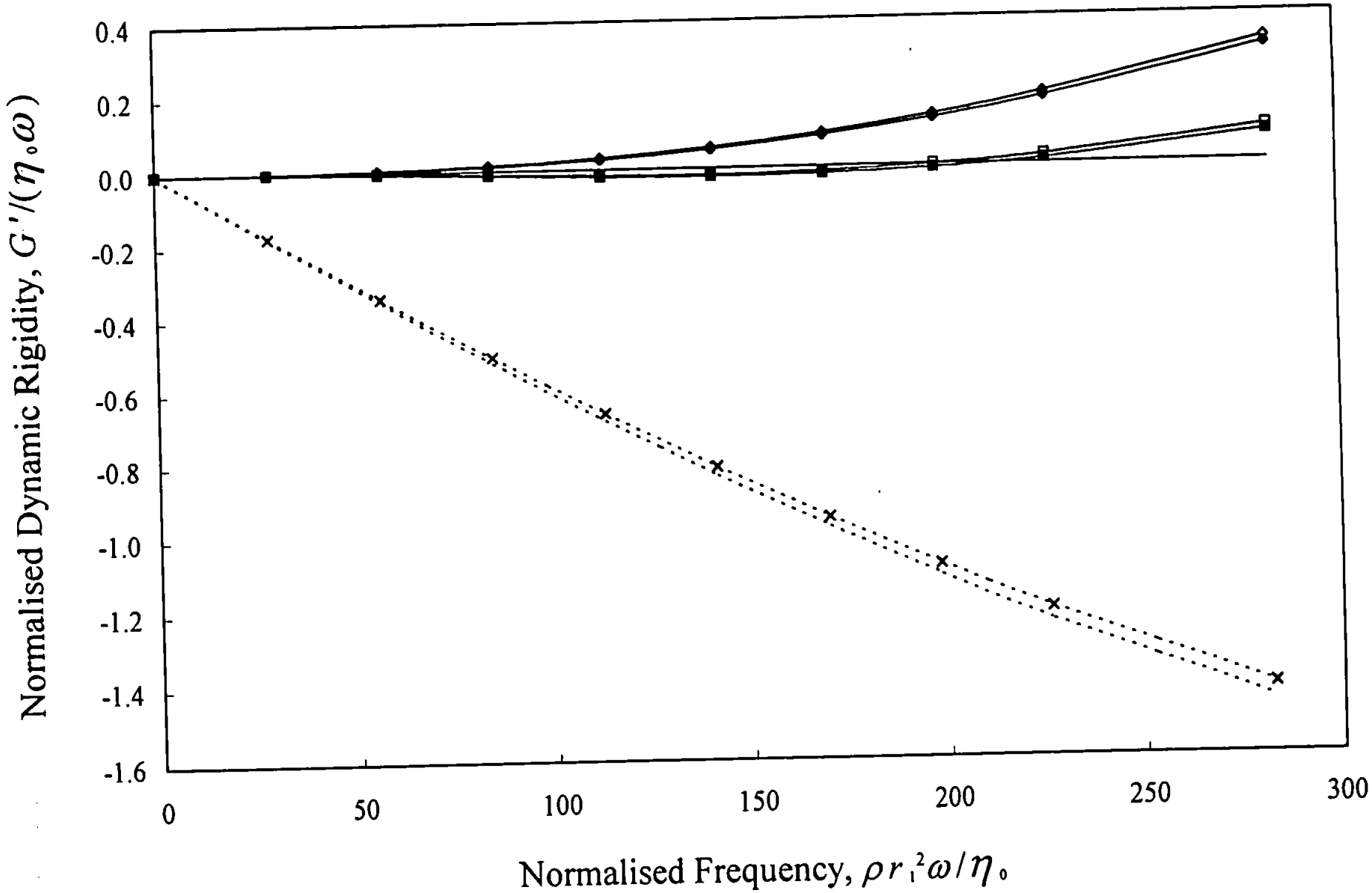
0.4
0.2
0.0
-0.2
-0.4
-0.6
-0.8
-1.0
-1.2
-1.4
-1.6
0
50
100
150
200
250
300
Normalised Dynamic Rigidity, $G'/(\eta_o\omega)$
Normalised Frequency, $\rho r_1^2\omega/\eta_o$

Figures 8.7 and 8.8

Oscillatory shear flow simulations for a CSR controlled stress rheometer.

Normalised dynamic viscosity and dynamic rigidity vs. Deborah number for a single element Maxwell model fluid in the wide gap geometry.

——— Exact , ····· Uncorrected (f_0=1, f_1=0, f_2=0),
····×···· Corrected for end effects (f_0=0·908, f_1=0, f_2=0),
—□— Corrected for second order fluid inertia effects (f_0=1, f_1=6·811×10^{-2}, f_2=1·919×10^{-3}),
—■— Corrected for end effects and second order fluid inertia effects (f_0=0·908, f_1=5·932×10^{-2}, f_2=1·612×10^{-3})

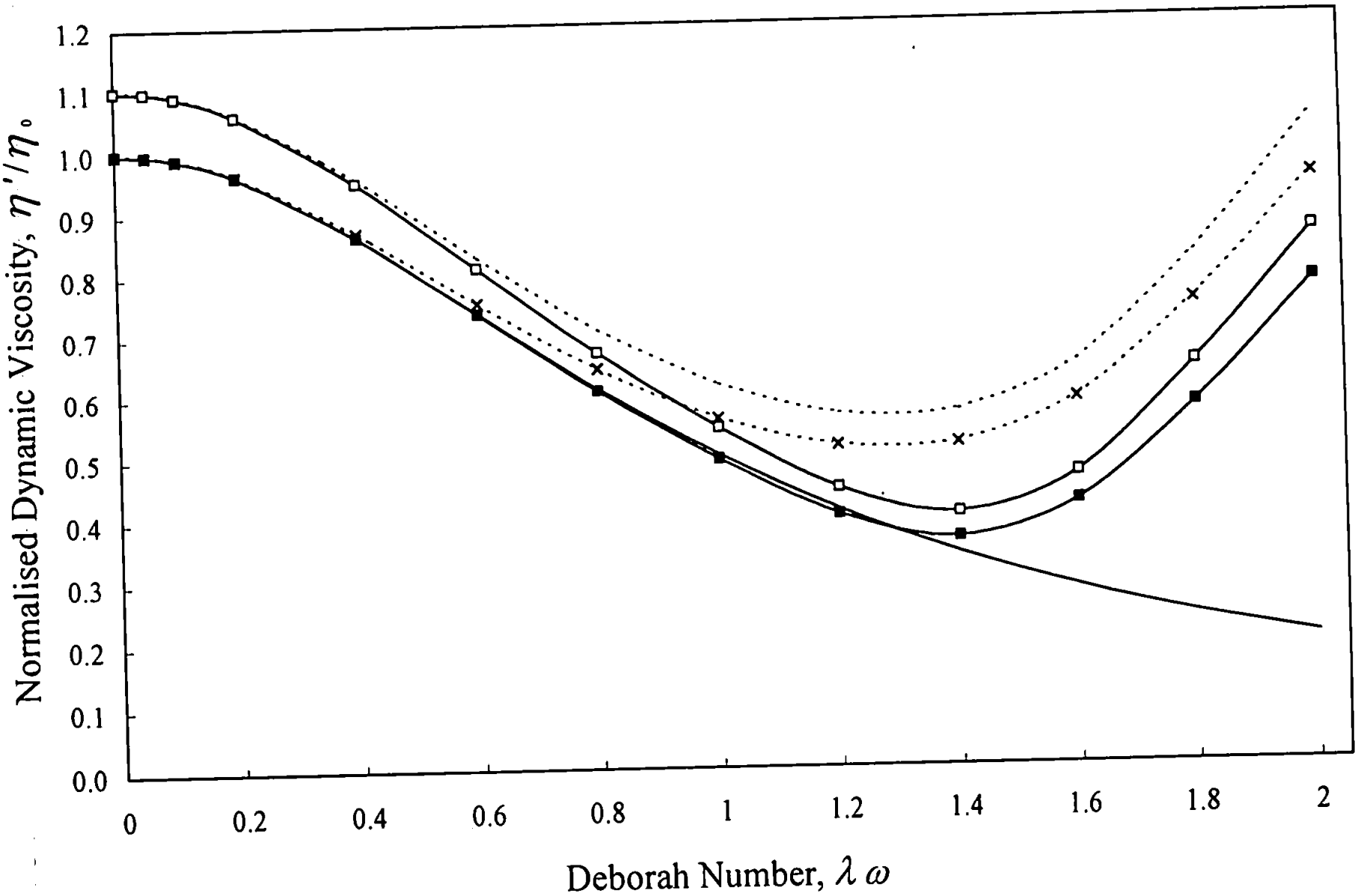
Normalised Dynamic Viscosity, η'/η_o
1.2
1.1
1.0
0.9
0.8
0.7
0.6
0.5
0.4
0.3
0.2
0.1
0.0
0
0.2
0.4
0.6
0.8
1
1.2
1.4
1.6
1.8
2
Deborah Number, $\lambda\omega$

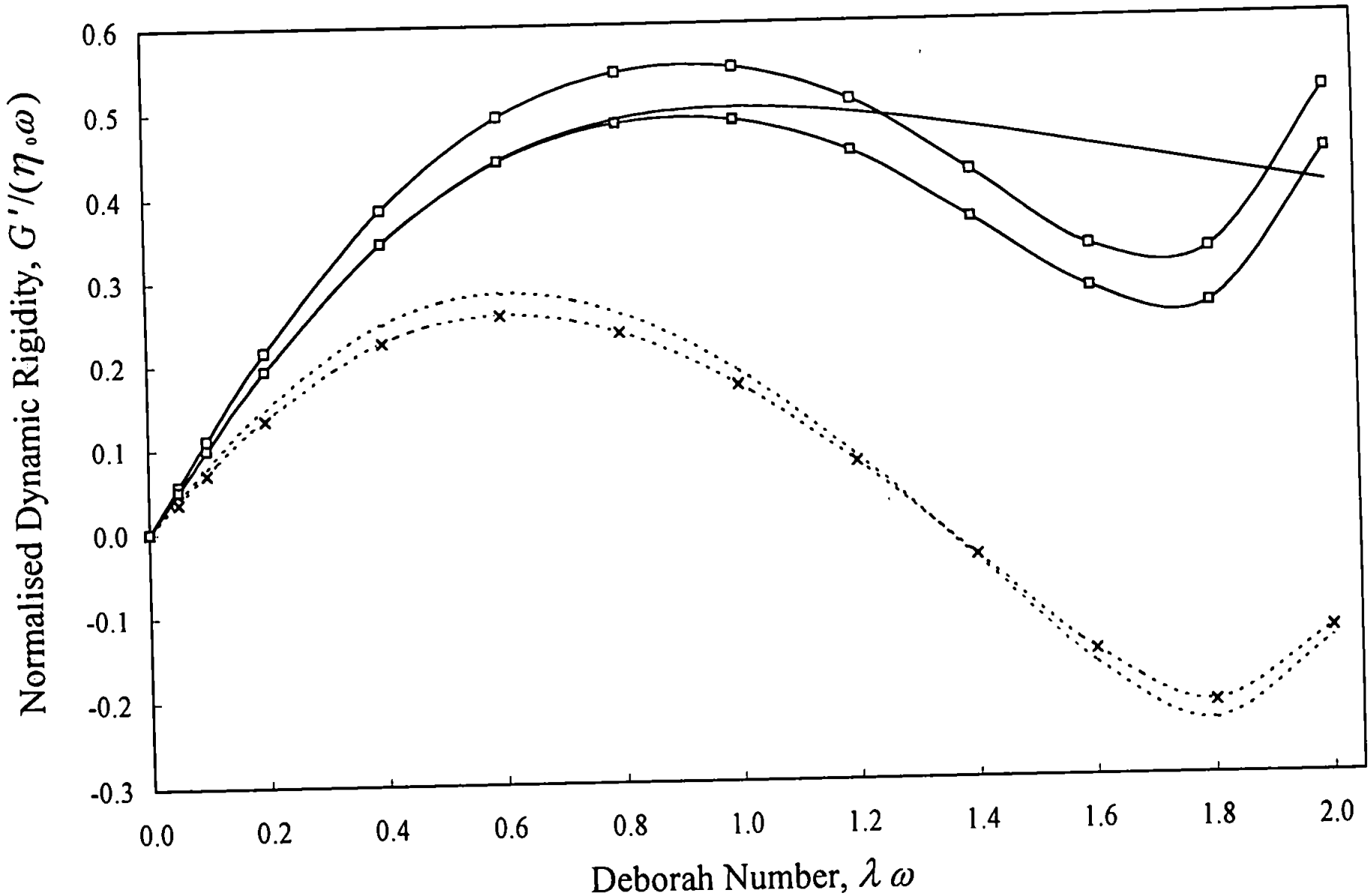
0.6
0.5
0.4
0.3
0.2
0.1
0.0
-0.1
-0.2
-0.3
Normalised Dynamic Rigidity, $G'/(\eta_o\omega)$
0.0
0.2
0.4
0.6
0.8
1.0
1.2
1.4
1.6
1.8
2.0
Deborah Number, $\lambda\,\omega$

Figures 8.9 and 8.10

Oscillatory shear flow simulations for a CSR controlled stress rheometer.

Normalised dynamic viscosity and dynamic rigidity data corrected for end effects and second order fluid inertia effects (f_0=0·908, f_1=5·932×10^{-2}, f_2=1·612×10^{-3}) vs. Deborah number for a range of R values in the wide gap geometry.

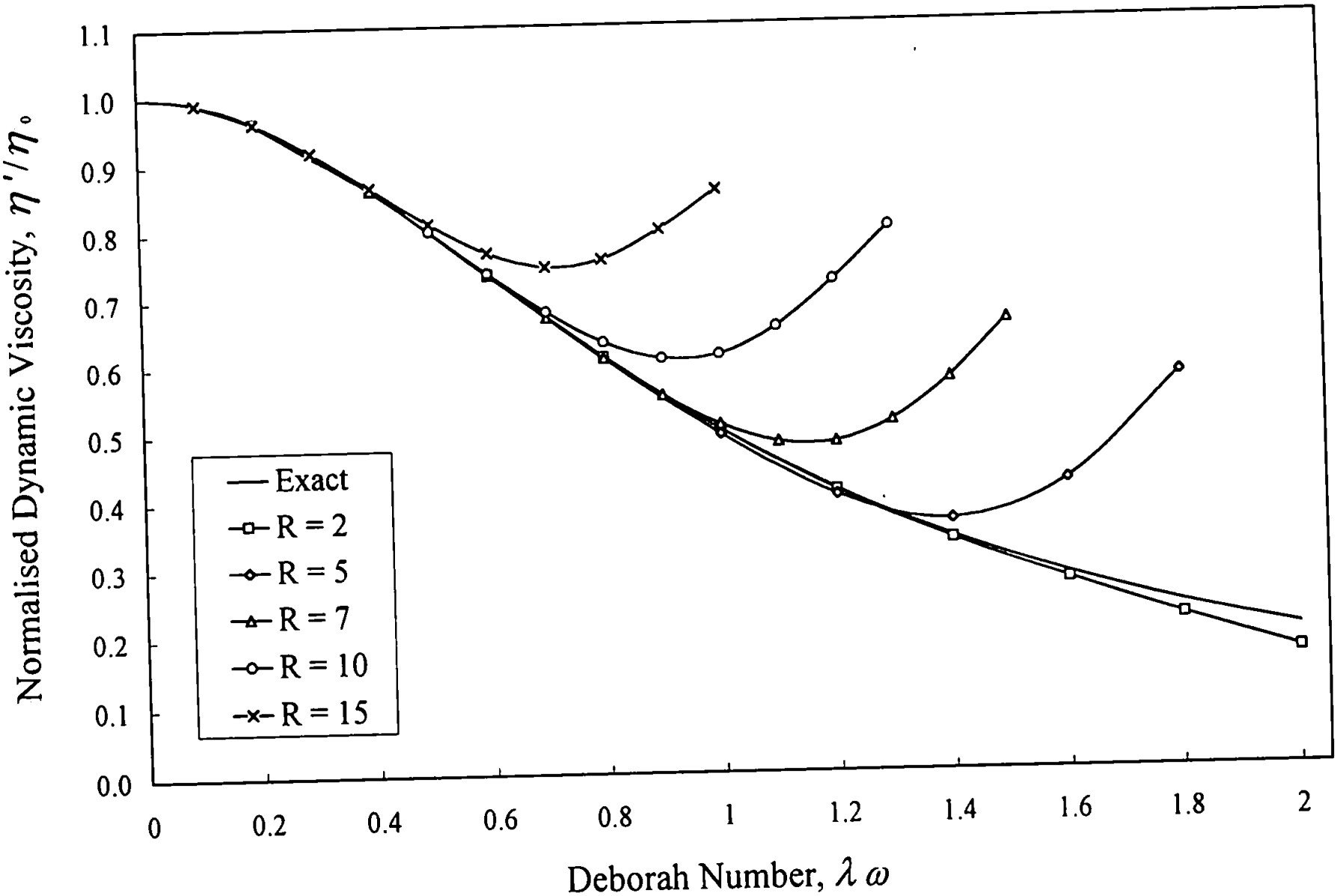
Normalised Dynamic Viscosity, η'/η_o
1.1
1.0
0.9
0.8
0.7
0.6
0.5
0.4
0.3
0.2
0.1
0.0
0
0.2
0.4
0.6
0.8
1
1.2
1.4
1.6
1.8
2
Deborah Number, $\lambda\omega$
Exact
R = 2
R = 5
R = 7
R = 10
R = 15

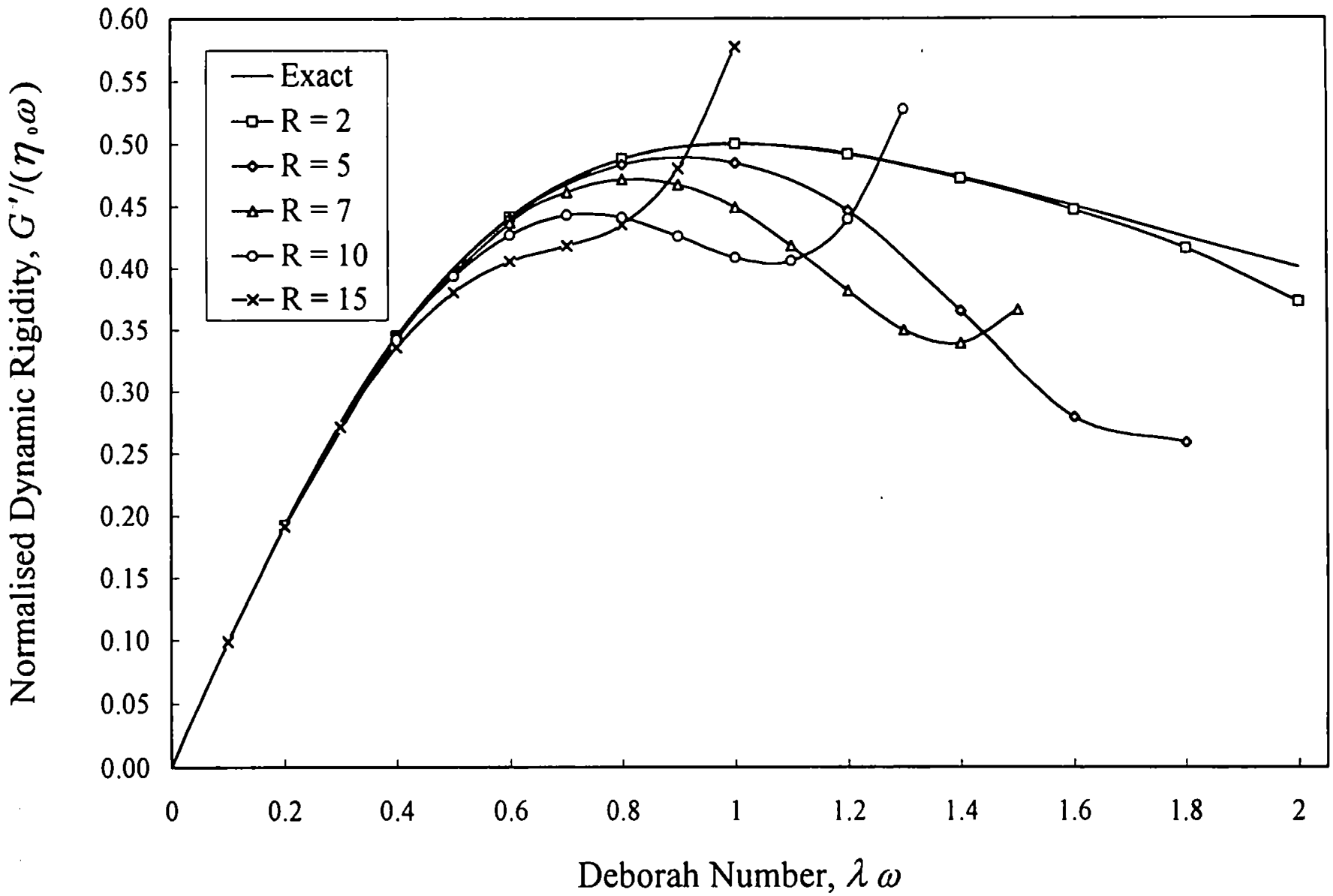
Exact
R = 2
R = 5
R = 7
R = 10
R = 15
0.60
0.55
0.50
0.45
0.40
0.35
0.30
0.25
0.20
0.15
0.10
0.05
0.00
0
0.2
0.4
0.6
0.8
1
1.2
1.4
1.6
1.8
2
Normalised Dynamic Rigidity, $G'/(\eta_o\omega)$
Deborah Number, $\lambda\,\omega$

Figures 8.11 and 8.12

Oscillatory shear flow simulations for a CSR controlled stress rheometer.

Normalised dynamic viscosity and dynamic rigidity data corrected for end effects and second order fluid inertia effects (f_0=0·927, f_1=2·725×10^{-2}, f_2=2.576×10^{-4}) vs. Deborah number for a range of R values in the medium gap geometry.

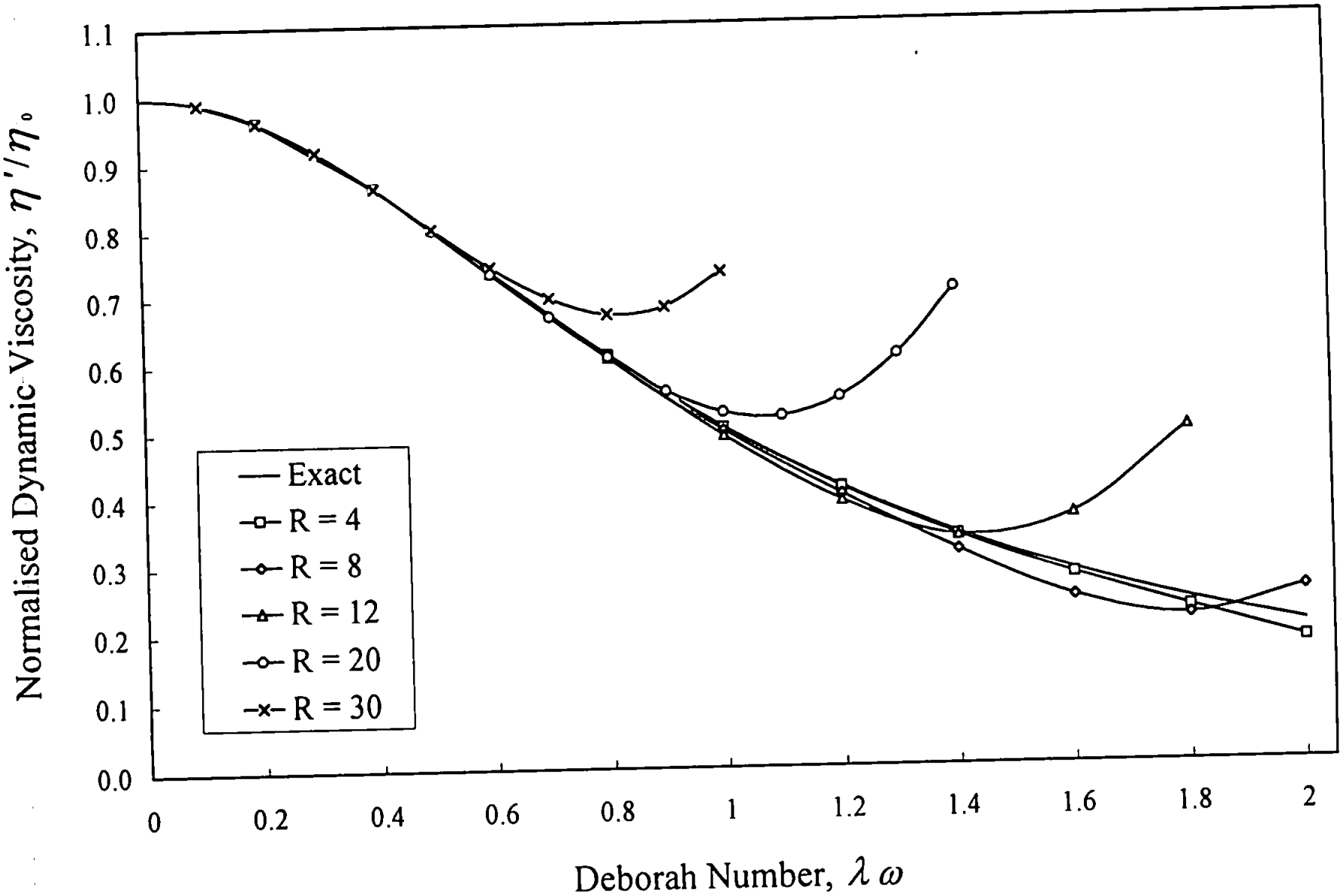
Normalised Dynamic Viscosity, η'/η_o
1.1
1.0
0.9
0.8
0.7
0.6
0.5
0.4
0.3
0.2
0.1
0.0
0
0.2
0.4
0.6
0.8
1
1.2
1.4
1.6
1.8
2
Deborah Number, $\lambda\omega$
Exact
R = 4
R = 8
R = 12
R = 20
R = 30

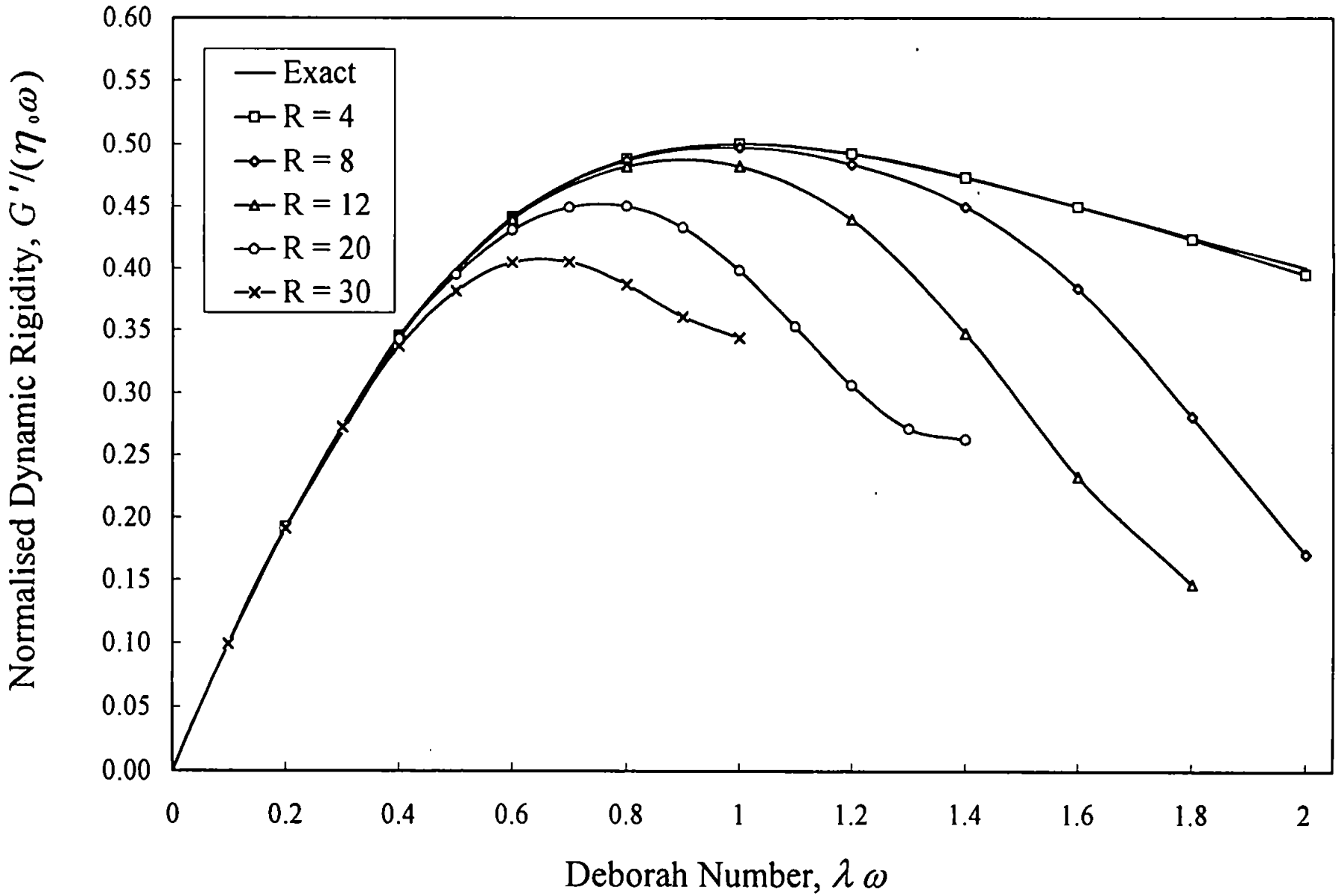
Exact
R = 4
R = 8
R = 12
R = 20
R = 30
0.60
0.55
0.50
0.45
0.40
0.35
0.30
0.25
0.20
0.15
0.10
0.05
0.00
0
0.2
0.4
0.6
0.8
1
1.2
1.4
1.6
1.8
2
Normalised Dynamic Rigidity, $G'/(\eta_o\omega)$
Deborah Number, $\lambda\,\omega$

Figures 8.13 and 8.14

Oscillatory shear flow simulations for a CSR controlled stress rheometer.

Normalised dynamic viscosity and dynamic rigidity data corrected for end effects and second order fluid inertia effects (f_0=0·973, f_1=4·021×10^{-3}, f_2=3·937×10^{-6}) vs. Deborah number for a range of R values in the narrow gap geometry.

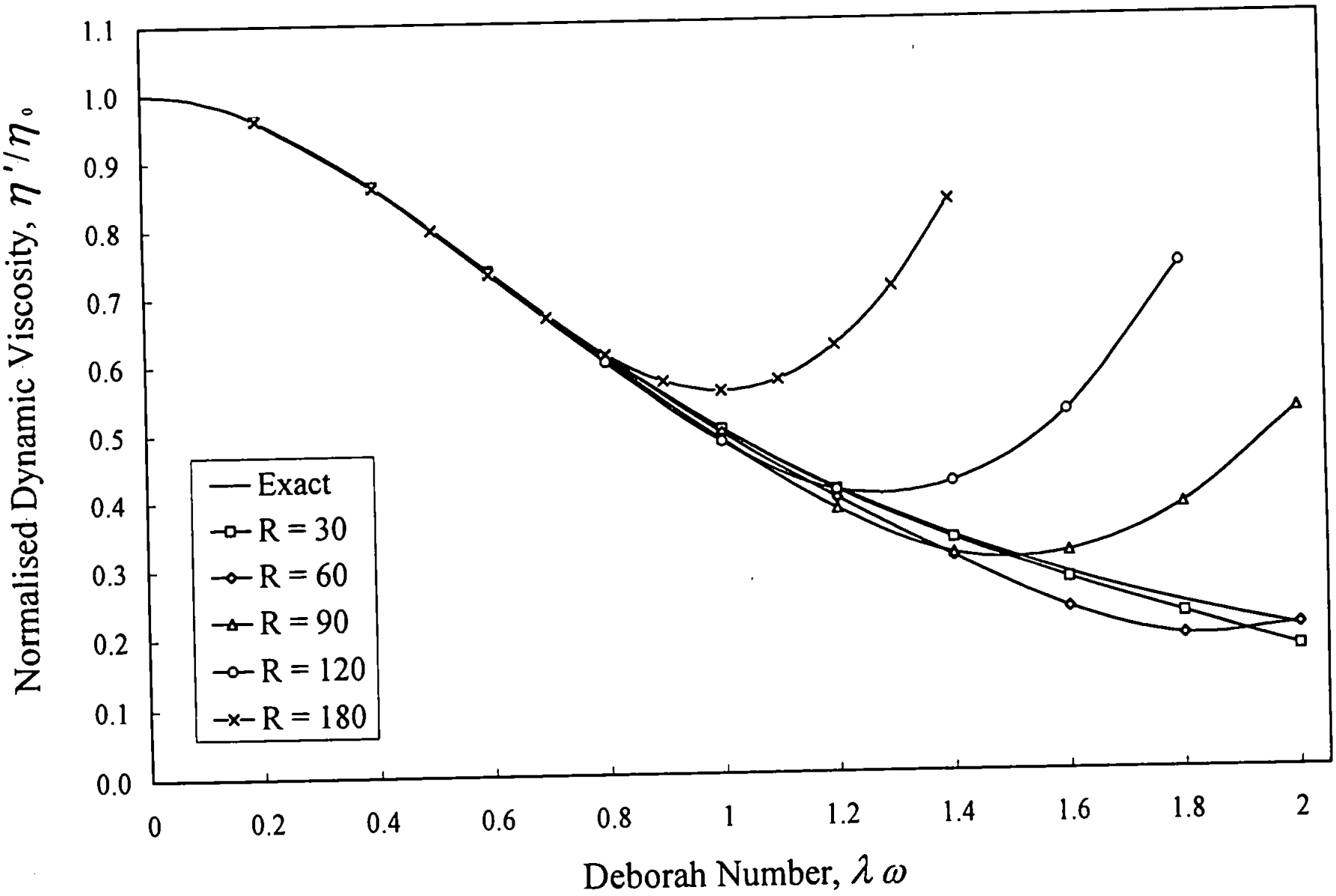
Normalised Dynamic Viscosity, η'/η_o
1.1
1.0
0.9
0.8
0.7
0.6
0.5
0.4
0.3
0.2
0.1
0.0
0
0.2
0.4
0.6
0.8
1
1.2
1.4
1.6
1.8
2
Deborah Number, $\lambda\,\omega$
Exact
R = 30
R = 60
R = 90
R = 120
R = 180

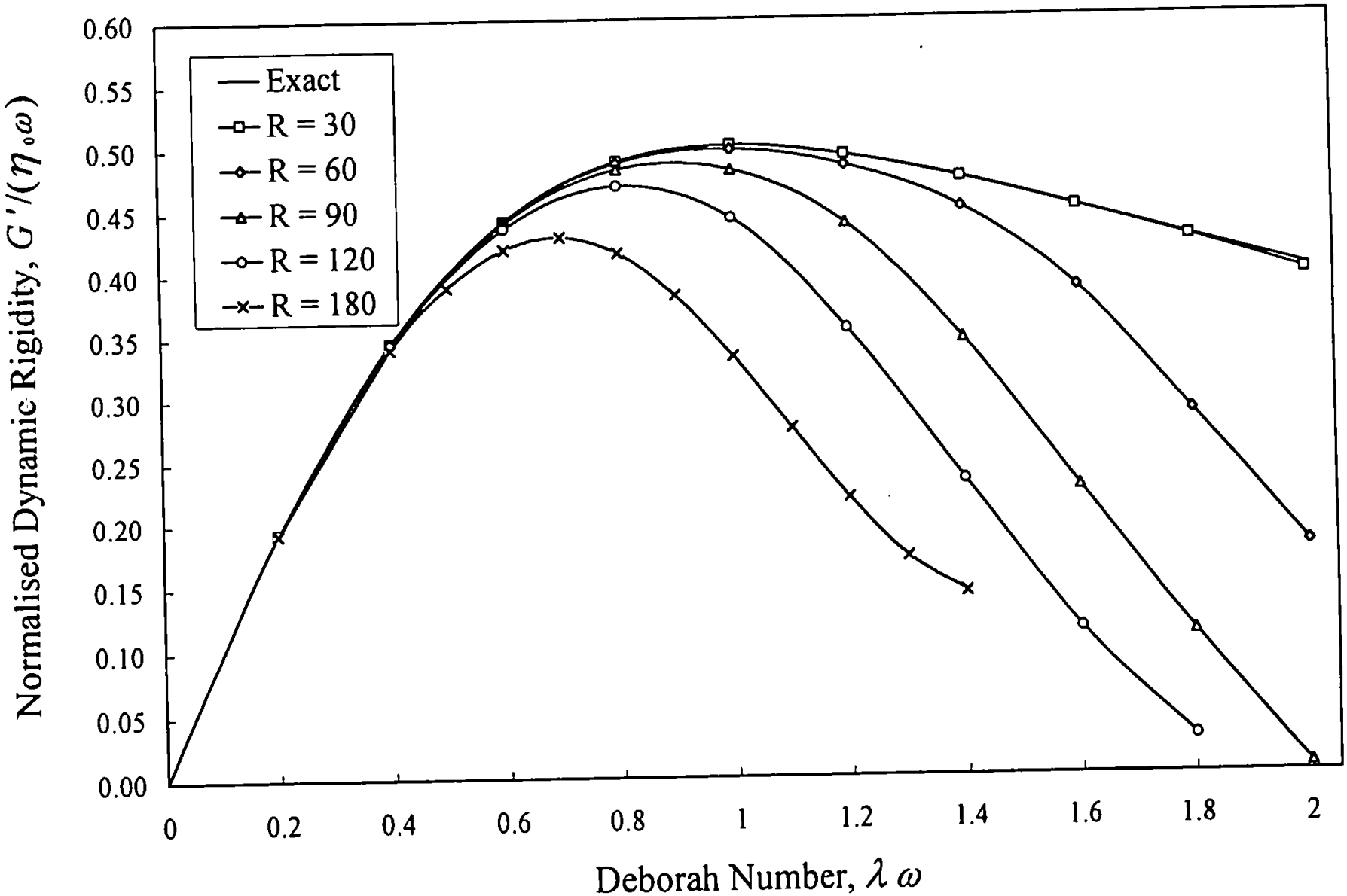
Exact
R = 30
R = 60
R = 90
R = 120
R = 180
Normalised Dynamic Rigidity, $G'/(\eta_o\omega)$
Deborah Number, $\lambda\,\omega$
0.60
0.55
0.50
0.45
0.40
0.35
0.30
0.25
0.20
0.15
0.10
0.05
0.00
0
0.2
0.4
0.6
0.8
1
1.2
1.4
1.6
1.8
2

Figures 9.1 and 9.2

Oscillatory shear flow simulations for a Weissenberg rheogoniometer with a torsion bar system.

Normalised dynamic viscosity and dynamic rigidity vs. normalised frequency for a Newtonian fluid in the medium gap geometry when $R = 10$.

——— Exact , ····· Uncorrected (f_0=1, f_1=0, f_2=0),
····×···· Corrected for end effects (f_0=0·927, f_1=0, f_2=0),
—□— Corrected for second order fluid inertia effects
(f_0=1, f_1=2·437×10^{-2}, f_2=5·452×10^{-2}, f_3=4·150×10^{-4}, f_4=7·068×10^{-4}),
—■— Corrected for end effects and second order fluid inertia effects
(f_0=0·908, f_1=2·248×10^{-2}, f_2=5·364×10^{-2}, f_3=3·739×10^{-4}, f_4=6·812×10^{-4}).

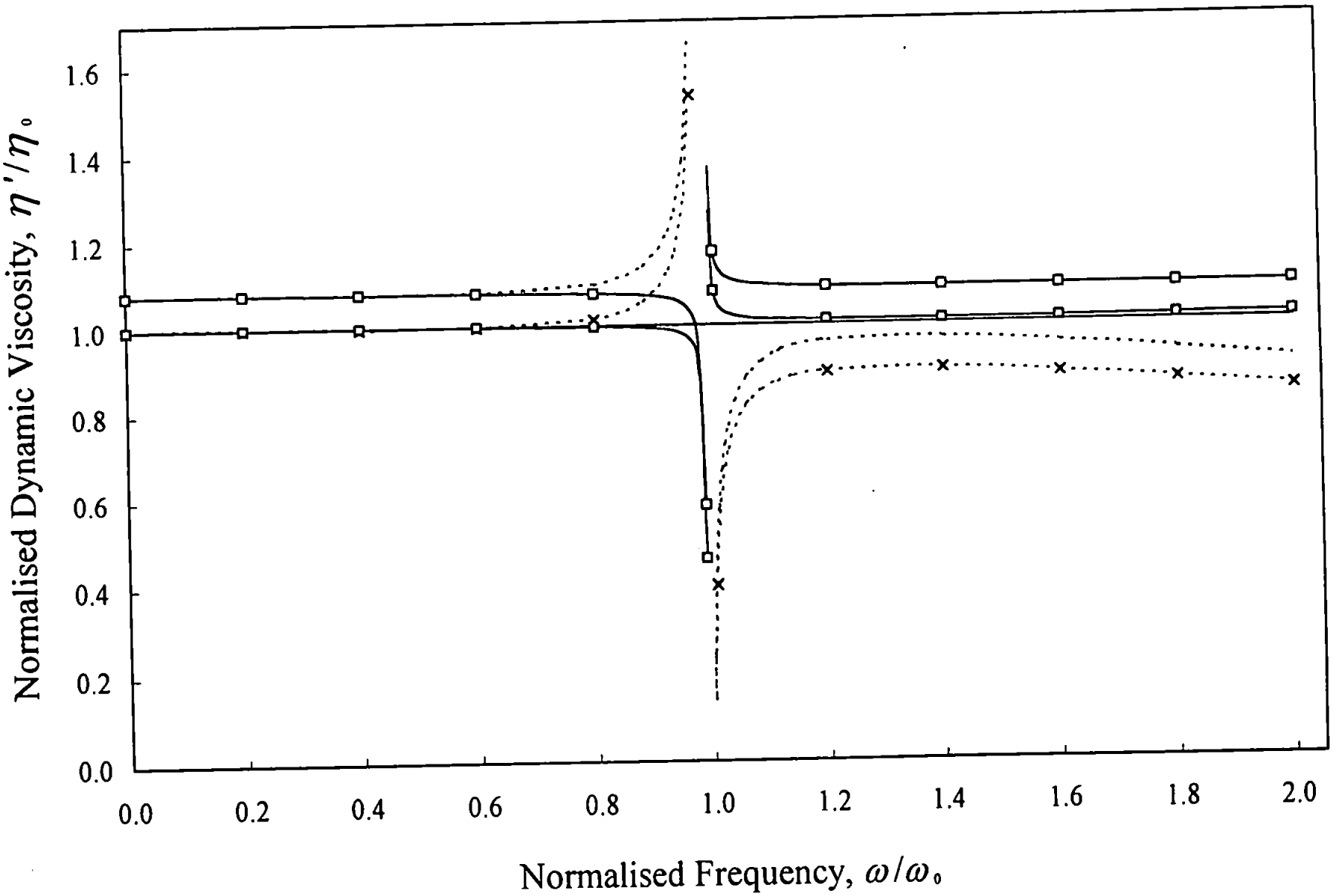
Normalised Dynamic Viscosity, η'/η_0
1.6
1.4
1.2
1.0
0.8
0.6
0.4
0.2
0.0
0.0
0.2
0.4
0.6
0.8
1.0
1.2
1.4
1.6
1.8
2.0
Normalised Frequency, ω/ω_0

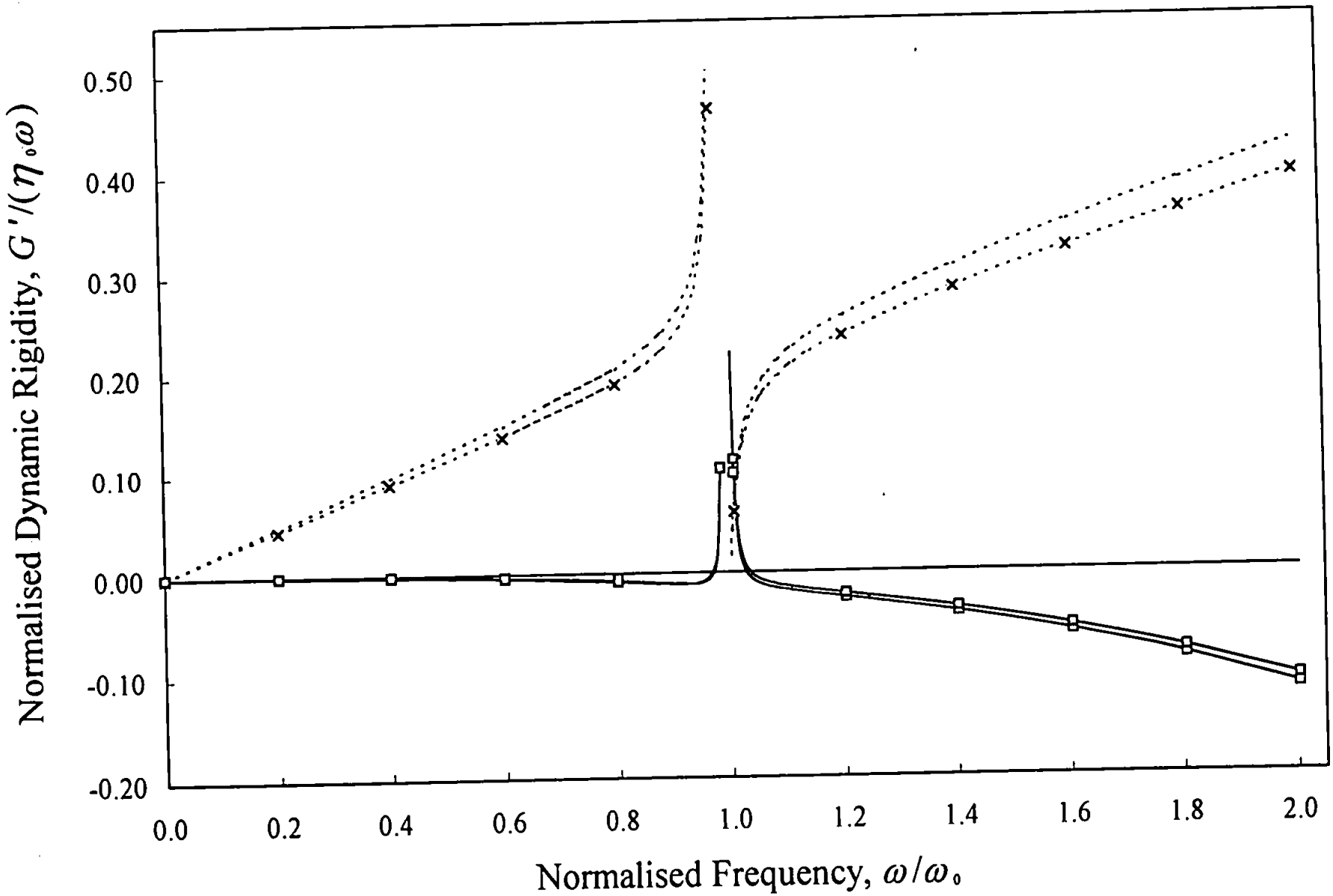
0.50
0.40
0.30
0.20
0.10
0.00
-0.10
-0.20
0.0
0.2
0.4
0.6
0.8
1.0
1.2
1.4
1.6
1.8
2.0
Normalised Dynamic Rigidity, $G'/(\eta_0\omega)$
Normalised Frequency, ω/ω_0

Figures 9.3 and 9.4

Oscillatory shear flow simulations for a Weissenberg rheogoniometer with a torsion bar system.

Normalised dynamic viscosity and dynamic rigidity vs. normalised frequency for a single element Maxwell fluid in the medium gap geometry when $R = 10$.

——— Exact , ····· Uncorrected (f_0=1, f_1=0, f_2=0),
····×···· Corrected for end effects (f_0=0·927, f_1=0, f_2=0),
—□— Corrected for second order fluid inertia effects
(f_0=1, f_1=2·437×10^{-2}, f_2=5·452×10^{-2}, f_3=4·150×10^{-4}, f_4=7·068×10^{-4}),
—■— Corrected for end effects and second order fluid inertia effects
(f_0=0·908, f_1=2·248×10^{-2}, f_2=5·364×10^{-2}, f_3=3·739×10^{-4}, f_4=6·812×10^{-4}).

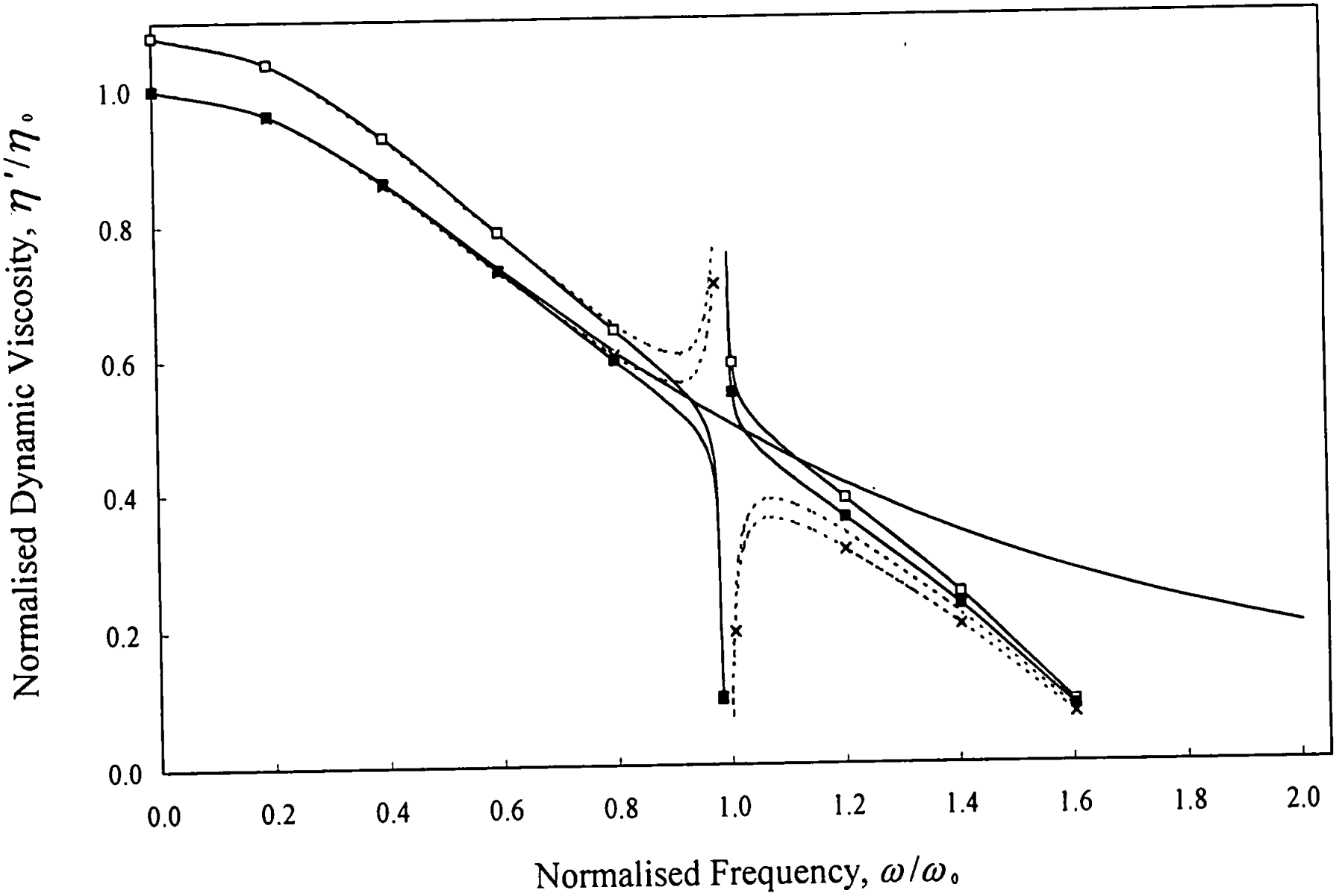
Normalised Dynamic Viscosity, η'/η_0
1.0
0.8
0.6
0.4
0.2
0.0
0.0
0.2
0.4
0.6
0.8
1.0
1.2
1.4
1.6
1.8
2.0
Normalised Frequency, ω/ω_0

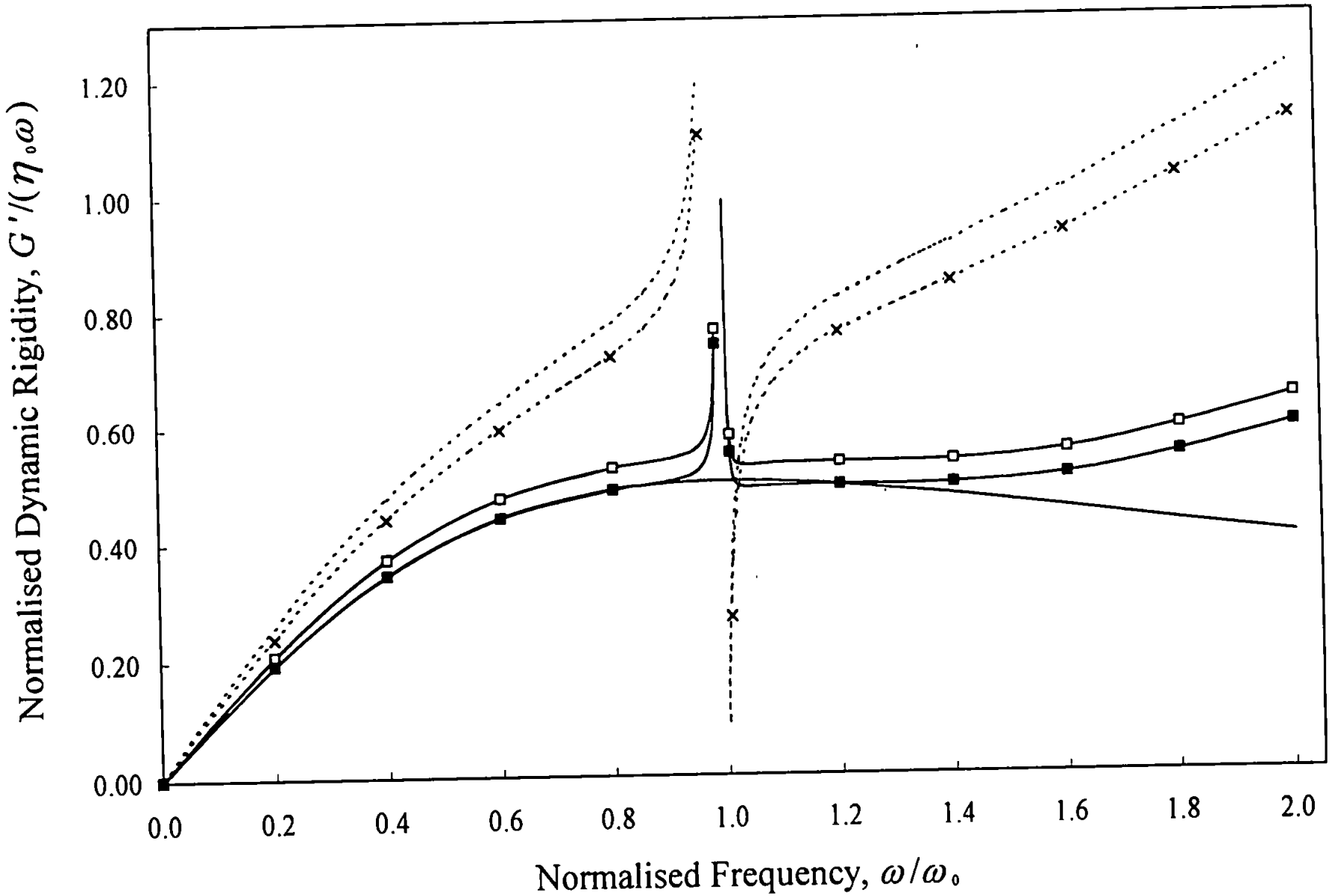
Normalised Dynamic Rigidity, $G'/(\eta_0\omega)$
1.20
1.00
0.80
0.60
0.40
0.20
0.00
0.0
0.2
0.4
0.6
0.8
1.0
1.2
1.4
1.6
1.8
2.0
Normalised Frequency, ω/ω_0

Figures 9.5 and 9.6

Oscillatory shear flow simulations for a Weissenberg rheogoniometer with a strain gauge torsion head system and a CSR controlled stress-rheometer.

Normalised dynamic viscosity and dynamic rigidity vs. normalised frequency for a Newtonian fluid in the medium gap geometry.

——— Exact , ···o··· CSR uncorrected (f_0=1, f_1=0, f_2=0),
····●··· Weissenberg uncorrected (f_0=1, f_1=0, f_2=0),
—o— CSR corrected for end effects (f_0=0·927, f_1=0, f_2=0),
—●— Weissenberg corrected for end effects (f_0=0·927, f_1=0, f_2=0),
—□— CSR corrected for end effects and second order fluid inertia effects (f_0=0·927, f_1=2·725×10^{-2}, f_2=2·576×10^{-4}),
—■— Weissenberg corrected for end effects and second order fluid inertia effects (f_0=0·927, f_1=2·248×10^{-2}, f_3=3·739×10^{-4}).

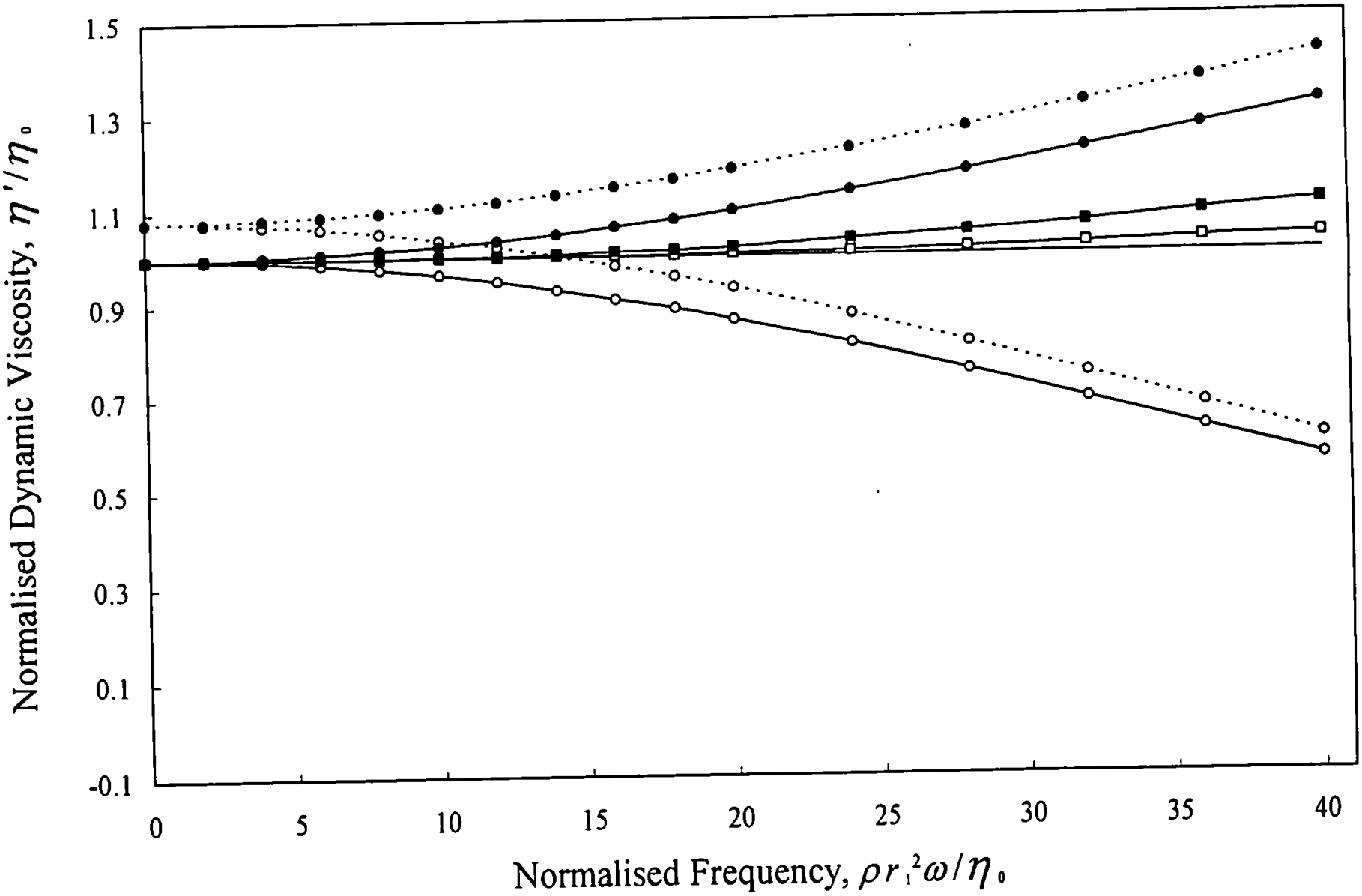
1.5
1.3
1.1
0.9
0.7
0.5
0.3
0.1
-0.1
0
5
10
15
20
25
30
35
40
Normalised Dynamic Viscosity, η'/η_0
Normalised Frequency, $\rho r_1^2\omega/\eta_0$

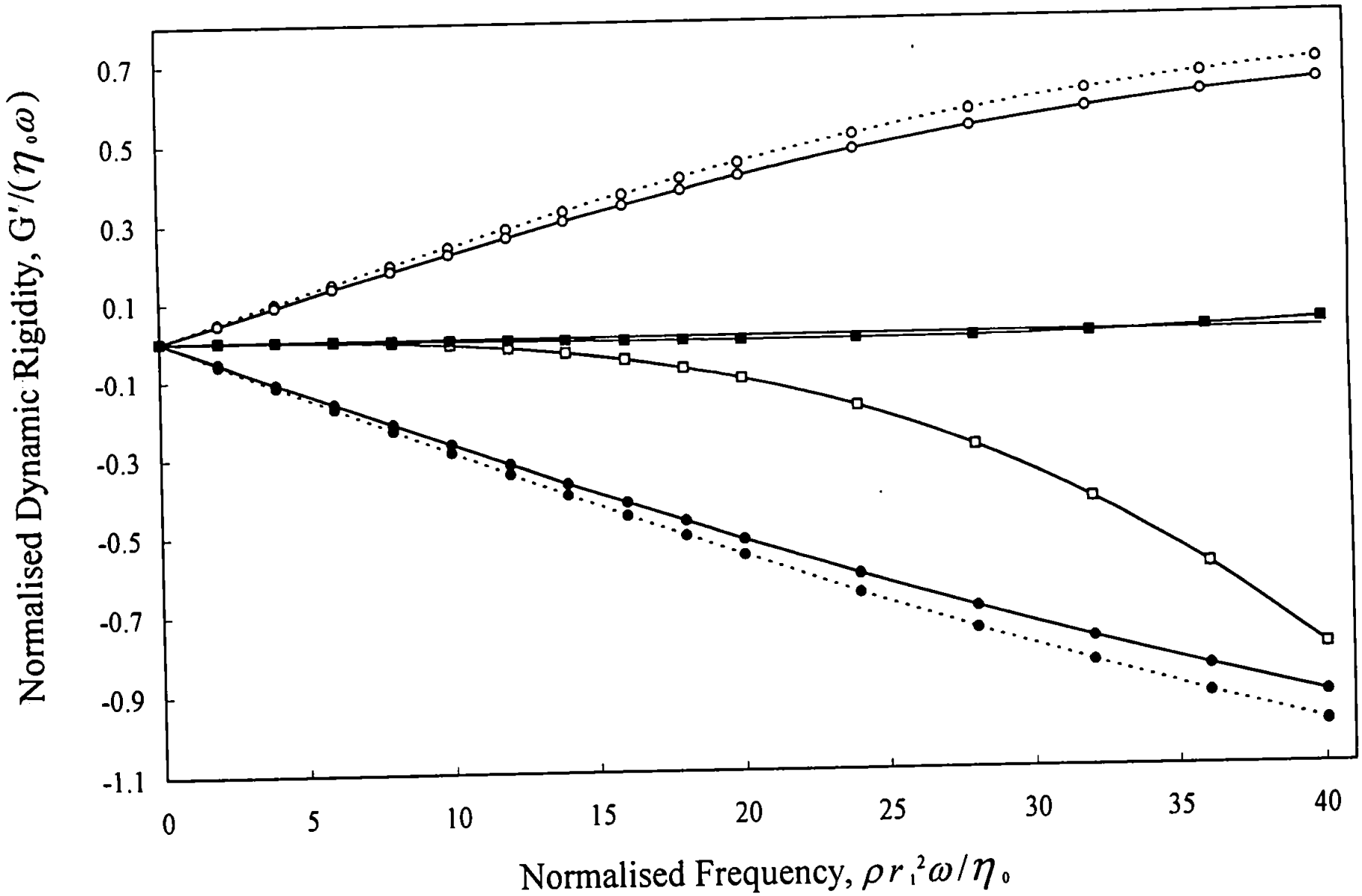
0.7
0.5
0.3
0.1
-0.1
-0.3
-0.5
-0.7
-0.9
-1.1
0
5
10
15
20
25
30
35
40
Normalised Dynamic Rigidity, $G'/(\eta_0\omega)$
Normalised Frequency, $\rho r_1^2\omega/\eta_0$

Figures 9.7 and 9.8

Oscillatory shear flow simulations for a Weissenberg rheogoniometer with a strain gauge torsion head system and a CSR controlled stress-rheometer.

Normalised dynamic viscosity and dynamic rigidity vs. normalised frequency for a single element Maxwell fluid in the medium gap geometry when $R = 10$.

——— Exact , ···o··· CSR uncorrected (f_0=1, f_1=0, f_2=0),
····●··· Weissenberg uncorrected (f_0=1, f_1=0, f_2=0),
—o— CSR corrected for end effects (f_0=0·927, f_1=0, f_2=0),
—●— Weissenberg corrected for end effects (f_0=0·927, f_1=0, f_2=0),
—□— CSR corrected for end effects and second order fluid inertia effects (f_0=0·927, f_1=2·725×10^{-2}, f_2=2·576×10^{-4}),
—■— Weissenberg corrected for end effects and second order fluid inertia effects (f_0=0·927, f_1=2·248×10^{-2}, f_3=3·739×10^{-4}).

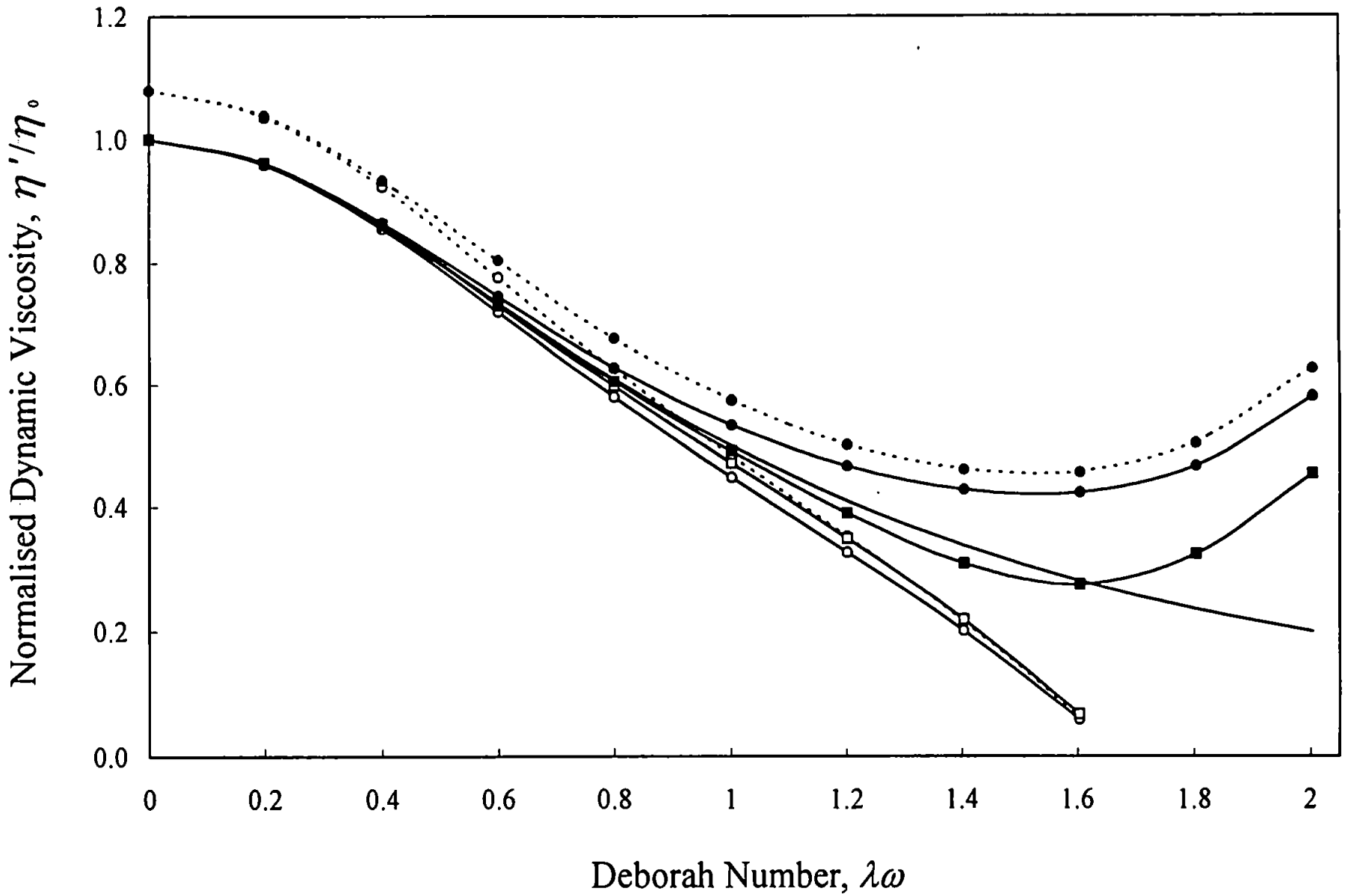
Normalised Dynamic Viscosity, η'/η_o
1.2
1.0
0.8
0.6
0.4
0.2
0.0
0
0.2
0.4
0.6
0.8
1
1.2
1.4
1.6
1.8
2
Deborah Number, $\lambda\omega$

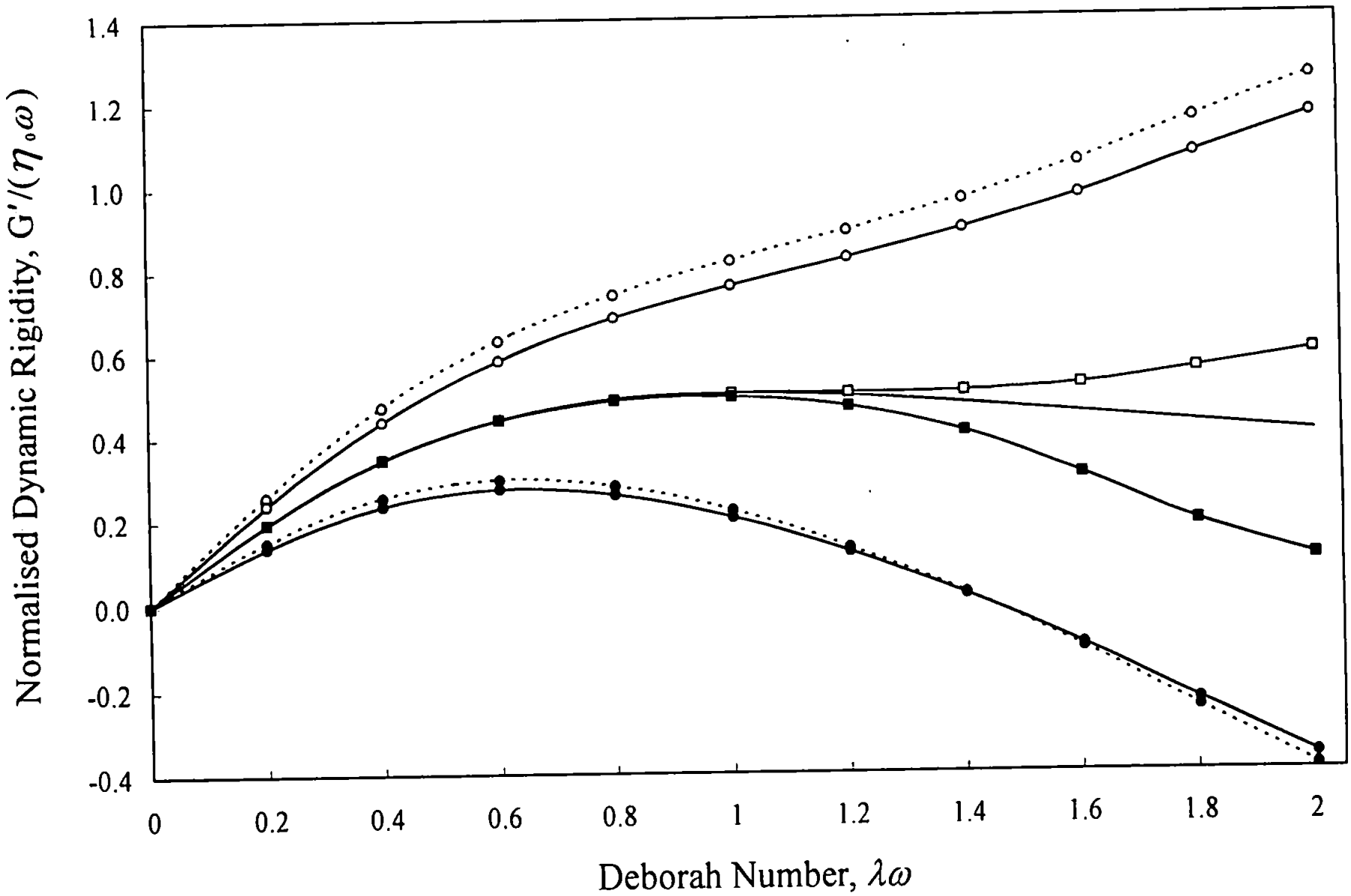
Normalised Dynamic Rigidity, $G'/(\eta_o\omega)$
1.4
1.2
1.0
0.8
0.6
0.4
0.2
0.0
-0.2
-0.4
0
0.2
0.4
0.6
0.8
1
1.2
1.4
1.6
1.8
2
Deborah Number, $\lambda\omega$